Additive Manufacturing Processes for High-Performance Ceramics: Manufacturing - Mechanical and Thermal property Relationship

by

Bhargavi Mummareddy

Submitted in Partial Fulfillment of the Requirements

for the Degree of

Doctor of Philosophy

in the

Materials Science and Engineering

Program

YOUNGSTOWN STATE UNIVERSITY

August, 2021

Additive Manufacturing Processes for High-Performance Ceramics: Manufacturing - Mechanical and Thermal property Relationship

Bhargavi Mummareddy

I hereby release this dissertation to the public. I understand that this dissertation will be made available from the OhioLINK ETD Center and the Maag Library Circulation Desk for public access. I also authorize the University or other individuals to make copies of this thesis as needed for scholarly research.

Signature:

Bhargavi Mummareddy, Student Date

Approvals:

Dr. Pedro Cortes, Dissertation Advisor Date

Dr. Eric MacDonald, Committee Member Date

Dr. Holly Martin, Committee Member Date

Dr. C. Virgin Solomon, Committee Member Date

Dr. Timothy Wagner, Committee Member Date

Dr. Salvatore A. Sanders, Dean of Graduate Studies Date

ABSTRACT

High Performance Ceramics materials (HPC's) have been of great interest in the industrial sector due to their superlative qualities such as lightweight, high mechanical and ablation properties, corrosion resistance, wear, and thermal resistances in harsh environments. The current aerospace, automotive, and maritime sectors require complex ceramic structures in applications related to propulsion engines, re-entry vehicles, heat engines, turbine components, high pressure injection systems, bearings, clutches, and actuators among many others. Despite their exceptional qualities, advanced ceramic structures require laborious work and expenses for their fabrication via conventional methods such as pressing and extrusion. Additionally, actual structural requirements are based on intricate configurations. The use of Additive Manufacturing has become a promising technology that could satisfy these requirements by producing complex structural components with tailored performance.

This present work has studied the 3D printing process of HPCs, as well as their mechanical, thermal, and physical properties. Here, a Vat Polymerization (VPP), Binder Jet Printing (BJP) and Material Jetting (MJ) additive manufacturing technologies were used to produce HPCs. The structure-property-processing relationship of silica, zirconia and aluminosilicates was investigated. A detailed study of the individual post-processing conditions and effects was incorporated in this research program to produce mechanically robust structures. The present work aims to provide a scientific and engineering platform to optimize the 3D printing and post-processing stages of ceramic materials.

The diffusion kinetics mechanism of post-processed ceramics printed via VPP at near fusion temperature were optically and theoretically investigated. An optical analysis of the manufactured samples assisted the understanding of the fusion process of the ceramic particles before and after sintering to produce near dense parts. Lastly, this program presents the conclusions observed in this work.

ACKNOWLEDGEMENTS

Firstly, I would like to thank my advisor, Dr. Pedro Cortes for all the guidance and extraordinary help through these years of my Ph.D. at YSU. If it is not your patience, time and effort I would not be what I am today. I am grateful that he always believed and gave me my comfort zone in the work, try different ideas, encouraged and taught me round abouts of research and much more. I would also like to thank my committee members, Dr. MacDonald, Dr. Martin, Dr. Solomon, Dr. Wagner for their support and reviews. Specially, Dr. MacDonald, I thank you for all the insights and help while writing the papers. It is always fun to work with you. A thank you goes to Dr. Linkous, for being there all the time answering my academic questions during my doctoral education.

I also acknowledge the collaborators, Dr. Jacob Adams from NCSU, Dr. Anton DuPlessis from Stellenbosch University and Dr. Jae-Won Choi from Akron University.

I would also like to thank Mr. Brian Hetzel at Fireline Inc, for offering help in research.

I also extend my gratitude to Jeremy McKnight, Dr. Deschenes & Mrs. Deschenes, Dylan Negro, Linda Adovasio and Ray Hoff for the enjoyable and perceptive discussions and extending their helping hand. I also acknowledge the people at Center of Excellence in Materials Science and Engineering, Center for Innovation in Additive Manufacturing at YSU, and Youngstown Business Incubator.

I also express my gratitude to my fellow graduate students, and lab mates without whom this journey was not fun filled and knowledgeable. Thank you all, for the chats we had during my time in the lab. Ellie, thank you for being the girl pal all the time.

I appreciate my cousin, Dr. Kalyan who always stood by my side taking up different roles as a friend, a cheerleader, and a guide from the beginning. I owe you one for being incredible, Kal.

Finally, to my family and friends, I would be always grateful for all your support and love. Specially, my parents, who believed in me all the time and backed me up in all the ups and

downs. I also acknowledge my sister Saranya, who always deals with my annoyance patiently. You people are the best that I could ever find, and I dedicate this work to you all. I am highly indebted to you all.

List of Acronyms

HPC - High Performance Ceramics

AM - Additive Manufacturing

VPP - Vat Phot Polymerization

SLA - Stereo Lithography

BJP – Binder Jetting Printing

MJ – Material Jetting

IPC - Interpenetrating Phase Composite

CAD - Computer Aided Design

NPJ - Nano Particle Jetting

DOD - Drop on Demand

C4 - Co-Continuous Ceramic Composite

TGA - Thermo Gravimetric Analysis

XRD - X-Ray Diffraction

CTE - Coefficient of Thermal Expansion

SEM – Scanning Electron Microscope

TEM – Transmission Electron Microscope

ANOVA – Analysis of Variance

BET – Brunauer -Emmet- Teller Analysis

SSS – Solid State Sintering

LPS – Liquid Phase Sintering

EDS – Energy Dispersive Spectroscopy

HIP – Hot Isostatic Pressing

NMR – Nuclear Magnetic Resonance

UTM – Universal Testing Machine

DLP – Digital Light Processing

CLIP – Continuous Liquid Interface Production

DPP - Daylight Polymer Printing

UV - Ultra-Violet

CIM - Ceramic Injection Molding

ABS – Acrylonitrile Butadiene Styrene

RI – Refractive Index

PEG – Polyethylene Glycol

PZT -Lead Zirconate Titanate

STL – Standard Tessellation Language

HV- Hardness Value

IPA- IsoPropyl Alcohol

CJ – Continuous Jet

CMC – Ceramic Metal Composite

DSC – Differential Scanning Calorimetry

DMTA – Dynamic Mechanical Thermal Analysis

TSS- Two Step Sintering

d_{20} – Particle diameter at 20% in cumulative distribution

d_{50} – Particle diameter at 50% in cumulative distribution

d_{90} – Particle diameter at 90% in cumulative distribution

SiO_2– Silicon Dioxide / Silica

Al_2O_3 – Aluminum Oxide / Alumina

ZrO_2 – Zirconium Dioxide / Zirconia

SiC – Silicon Carbide

Glossary

- **Layer thickness (µm):** The thickness the hopper/powder source is laid on the build platform.
- **Recoat Speed (mm/sec):** Speed with which the material source moves on to the build platform.
- **Binder set time (sec):** The time allowed for the binder to settle in the powder particles after the printhead moves on the powder bed.
- **Drying time (sec):** The time that the IR light passes on the print for the binder to cure in the printed samples.
- **Roller speed (rpm):** The rotational speed at which the roller moves on the powder bed to even the powder layer dropped by the hopper.
- **Roller-traverse speed (mm/sec):** The speed with which the roller moves on the powder bed to settle in the particles for avoiding large voids.
- **Emitter Output (%):** The intensity of the IR light which is used for curing the samples on the print bed.
- **Binder Saturation (%):** The amount of binder filled in the voids created in the powder layers. It can be defined as the ratio of the binder volume to the volume of voids.
- **Drop Volume (pL):** The volume of the binder droplet from each jetting unit in the print head.
- **Print Bed Temperature (^{o}C):** The temperature at which the print bed is maintained at.
- **Oscillator speed (rpm):** The speed at which the hopper vibrates on the powder bed to drop the powder.
- **Jet spacing (µm):** The space that is plugged in to maintain the distance between the jets for the binder droplets to purge in the powder bed.
- **Unimodal printing:** Printing using a single sized powder particle.
- **Bimodal printing:** Printing using two different sized powder particles.
- **Multimodal printing:** Printing using different sized powder particles varying from coarse to ultra-fine.

Table of Contents

Abstract……....iii

Acknowledgements…….……iv

List of Acronyms…….……....vi

Glossary…….....viii

Table of Contents……..…….……..ix

List of Figures……..……...xii

List of Tables……..……..xix

1. Research Motivation and Problem Statement....1

1.1: Introduction 1

1.2: High Performance Ceramics (HPC's) 3

1.3: Research Motivation and Problem Statement: 11

1.3.1: Objectives: 12

1.4: Organization 13

1.5: References: 14

2. Production of Metal Ceramic Structures using Vat Photo Polymerization 18

Overview: 18

2.1: Introduction 19

2.2: Literature Review 21

2.2.1. Printing Parameters....21

2.2.2. Materials 23

2.2.3. Interpenetrating Phase Composites (IPC)....26

2.3: Methodology....26

2.3.1. Printing and Sintering....26

2.3.2. Instrumentation 30

2.4: Results and Discussion 31

2.4.1. Curing: 33

2.4.2. Sintering: 37

2.4.3. Transformation to IPCs: 42

2.5: Conclusions 51

2.6: References 52

3. Binder Jetting Printing of High-Performance Ceramics....60

3.1: Introduction 61
3.1.1: Process parameters 62
3.2: Equipment: 67
3.3: Materials 68
3.3.1: Alumina-Silicate hollow microspheres 68
3.3.2: Fused Silica 79
3.4: Conclusions 92
3.5: References 93
4: Material Jetting 108
4.1: Introduction 109
4.1.1: Literature Review 112
4.2: Printing Technique and Testing 116
4.2.1: Printing Unit 116
4.2.2: Materials 117
4.2.3: Characterization 118
4.3: Results and Discussion 119
4.3.1: Applications 133
4.4: Conclusions 133
4.5: References 134
5: Sintering and Diffusion Kinetics in Silica and IPCs printed via Vat Polymerization 145
5.1: Introduction 146
5.1.1: Sintering in Ceramics. 153
5.2: Methods (Diffusion model) & Discussion 155
5.2.1: Theory 155
5.2.2: Mathematical model 163
5.3: Conclusions 166
5.4: References 167
6: Conclusions 178
Appendix A: Instrumentation 180
A1.Post Processing 180
A2. Analytical Characterization 182
A3. Mechanical Characterization 195
A4. Thermal Characterization 199

A5.References....200
Appendix B: Silicon Carbide....202
B1: Objectives....202
Silicon Carbide was printed via BJ-AM in order to investigate the effect of the bimodal and trimodal printing variations in the density of the manufactured materials.....202
B2: Printing Methodology....202
B3: Results and Discussion....203
B4: Conclusions....207
B5: References....208

List of Figures

Figure 1.1: (a) The Great Pyramid of Giza (b) Great wall of China (c) Flourescent mineral collection at Youngstown State University (d) Mesolithic age tool collection (e) Early Bronze age pottery……..…….……1

Figure 1.2: Bar-chart of stiffness (Young's modulus) of different materials…….……....2

Figure 1.3: Ashby diagram describing the characteristics of materials, where the technical ceramics stand top in terms of strength…….……...….4

Figure 1.4: Global technical ceramics market size of ceramic material……...…....6

Figure 1.5: Schematic diagram of the ceramic part fabrication…….……....7

Figure 1.6: Schematic diagram of additive manufacturing process of a sample being printed in a layer-by-layer fashion…….…….…8

Figure 1.7: Examples of 3D printed structures (a) A compressor component infiltrated from ceramics for air brakes in jet engines printed via BJP, (b) A component in passenger flights, (c) insulation part created for refractory application made from Vat polymerization, (d) Alumina lattice component created via SLA technique, (e) Calcium carbonate bone scaffold fabricated via SLA, (f) Sinusoidal antennae for dielectric applications created via NPJ…….…...10

Figure 1.8: Global technical ceramics market size of 3D printed ceramic materials…….….12

Figure 2.1: Schematic diagram of a typical stereolithography printing technology……...19

Figure 2.2: Industrial parts built via SLA. (a) Customized dental bridge. (b) Jig for a microelectronic device. (c) Prototype 3D component created on Formlabs……..……20

Figure 2.3: Experimental apparatus used in this work. (a) Form labs Form-2 SLA unit, (b) A complex geometry printed on Form labs, in the picture is a ceramic gyroid structure……..….27

Figure 2.4: CAD .stl files in Preform software showing the support system. The blue section displays the actual part that is sliced to be printed. The bottom white section displays the support system generated for printing the part on Formlabs unit……..28

Figure 2.5: Schematic figure of the parts printed on Form labs unit for mechanical testing. The figure shows the orientation that samples were printed on the SLA unit…….….29

Figure 2.6: Sintering profile actually used on the printed SLA ceramic parts in air at 1 atm to get crack-free samples……...……..…….…29
Figure 2.7: NMR spectrum of Formlabs Ceramic Resin…….…...…32
Figure 2.8: Particle size distribution of silica, the suspended powder in Formlabs resin…….…..33
Figure 2.9: Surface of the sample cured at 400°C. The SEM image shows the unbound silica particles after the resin was burnt off……..…34
Figure 2.10: Microscope image of a sample cured at 400°C in air at 100X magnification. (a) at 1°C/min. b) at 2°C/min. (c) at 5°C/min……..35
Figure 2.11: Microscope image of a sample cured at 400°C and cooled with a controlled ramp rate at 100X magnification. (a) at 1°C/min. (b) at 2°C/min. (c) at 5°C/min. The image also shows the delamination seen in the samples at different cooling rates……36
Figure 2.12: Microscope image of a sample cured at 400°C at 2°C/min at 50X magnification. (a) Actual image. (b) Graythresh image of the cured sample where the white speckles represent the particle after curing (right). ……..…….…37
Figure 2.13: Microscope image of a sample sintered at 1275°C in air at 100X magnification. (a) at 2°C/min. (b) at 5°C/min. (c) at 10°C/min…….…...39
Figure 2.14: Microscope image of a sintered silica sample at 50X magnification. (a) Actual image. (b) Graythresh image of the sintered sample where the white spots refer to the pores present in the sintered sample (right). …….……..…40
Figure 2.15: Microscope image of samples at 100X magnification showing a reduction in cracks from cured to sintered stage. (a) Surface of the samples after curing at 400°C at a curing rate of 2°C/min and cooling rate of 2°C/min. (b) Surface of the sample after sintering with a heating rate of 5°C/min and air cooled……..……...41
Figure 2.16: Surface of the samples sintered at 1275°C. (a) SEM image of the sintered sample. (b) The image shows a crack that shrinked during sintering…….……41
Figure 2.17: Relative density of the printed samples at different temperatures……..42
Figure 2.18: Transformed printed ceramic samples into interpenetrated phase composites (IPCs). a) cylindrical and rectangular samples used for the mechanical and thermal analysis. b) Low magnification of a transformed cylinder. ……...43
Figure 2.19: Optical micrographs of the transformed 3D printed ceramic samples into interpenetrated phase composites. (a) A micrograph of the infiltrated flexural sample at 30X. (b) A higher magnified image of the infiltrated sample showing a network of Aluminum and Alumina along with porosity……..…43

Figure 2.20: Surface of the transformed samples. (a) A low magnification SEM image of the transformed sample showing a contrast between the Alumina and Aluminum. (b) A high magnification SEM image showing unreacted silica resulting in porosity and a weak point leading to fracture……..44
Figure 2.21: Analytical test results of the sintered and transformed samples from this work. (a) XRD patterns of sintered and transformed samples. The image also shows the different elements present in the sintered stage and their transformation after the infiltration process. (b) EDS spectrum of the transformed sample at a fractured location. The spectrum shows the presence of Al, O and Si and below is the table describes the atomic weight % of the elements……..46
Figure 2.22: Phase diagrams shown for Al_2O_3-SiO_2 system from Thermo-Calc. (a) Gibbs free energy vs Temperature. (b) Phase diagram displaying mass % of Si vs Temperature. (c) Amount of Al present in each phase in the composite with respect to temperature……..47
Figure 2.23: Stress-strain graphs shown by green, sintered and transformed samples……48
Figure 2.24: A comparison chart of mechanical strength of samples printed via SLA in green and sintered stages along with the sample strength after the infiltration process. (a) Compressive Strength. (b) Flexural Strength……...49
Figure 2.25: The fractured surface of the transformed sample. The sample shows a diagonal brittle failure. The magnified image shows some non-transformed silica particles……...49
Figure 2.26: Hardness results of the sintered and transformed ceramics……50
Figure 2.27: Averaged CTE results of sintered and transformed samples tested between 25°C and 500°C……..51
Figure 3.1: Schematic diagram of Binder Jetting printing. The figure also shows the major components in the 3D printer. ……61
Figure 3.2: ExOne Innovent + Binder Jetting Printer Unit used in this research effort (left). Structure of the furan binder, used in this research work (right)……68
Figure 3.3: A test pattern created by the printhead where the 256 inkjets have dropped binder droplets to form lines……68
Figure 3.4: Micrograph of the as-received microspheres and their particle size distribution.……70
Figure 3.5: Shrinkage seen in the printed specimen after post processing. The image shows green part (left) and the sintered part (right)……71
Figure 3.6: Micrographs of the printed ceramic spheres. a) Green state. b) Sintered state. c) Magnified picture of the sintered state showing a necking between large particles…….72

Figure 3.7: XRD graph of the green and the sintered samples revealing increase in crystallinity on the sintered parts (XRD peaks in the sintered state show higher intensity than in the green state ~ 25˚)……..73
Figure 3.8: Mechanical properties of the printed and sintered hollow spheres. a) Compressive Strength. b) Flexural strength……..74
Figure 3.9: SEM micrograph of fractured samples showing fracture along the sintered spherical particles. (a) The fracture along the necking region. (b) A hollow sphere cracked after sintering…75
Figure 3.10: Specific fracture toughness of the sintered parts printed in different directions along with the schematic diagrams of the printing directions. (a) Fracture toughness results. (b) Schematic diagram of the parts built in different directions. (c), (d), (e) Fracture observed in the samples printed in the X, Y and Z directions respectively after machining in the notch (Indicated by the highlighted white lines)……./…….....76
Figure 3.11: CTE and hardness values of the microsphere 3D printed, and sintered samples manufactured in different directions. (a) CTE values seen along different directions. (b) Hardness values seen in different directions. The figure also shows the porous structures in the samples after hardness testing……...77
Figure 3.12: Abrasive wear observed on parts printed in Z-direction after subjecting to wear at different times…….....78
Figure 3.13: Optical analysis showing particle morphology of the Fused Silica powder as received……...82
Figure 3.14: Distribution graphs of Compressive Strength and shrinkage with respect to Binder Saturation and Traverse speed. (a) Shrinkage. (b) Compressive Strength……83
Figure 3.15: Sintered samples with 60% (left), 80% (right) binder saturation printed under a transverse speed of 2.5 mm/s. The samples on right shows a radial expansion after the post-processing stage….....84
Figure 3.16: Q-Q graph of the strength distribution……..…85
Figure 3.17: (a) Parallelepiped shaped part used for measuring surface contact angles. (b) Sessile drop forming due to the gravity and capillary effects at the syringe. (c) Sessile drop (ellipsoidal cap) formed from the binder (Glycerol) over the sample surface……87
Figure 3.18: Contact Angle measurements of the secondary binders on green silica samples……87
Figure 3.19: Average density of the sintered Silica samples with secondary binders at different concentrations……..…….....89

Figure 3.20: XRD of the sintered Silica samples with and without secondary binders……..90
Figure 3.21: Compressive Strength of the samples after addition of secondary binder. (a) Acetic Acid. (b) Dextrin……...……..91
Figure 3.22: SEM images of the samples after curing at 600^{O}C. (a) SiO_2 (b) SiO_2 with Acetic Acid (c) SiO_2 with Dextrin particles……..…..91
Figure 4.1: Schematic diagram of Material Jetting process…….…..109
Figure 4.2: (a) A paper circuit board build via silver epoxy. (b) A FET on textile showing the bending features. (c) A 3D printed signal conditioning circuit……..110
Figure 4.3: Samples printed using Polyjet printing with a glossy fisnish. (a) A printed propeller. (b) Human ear. ……...……....111
Figure 4.4: Samples printed using Nano-Particle Jetting (NPJ) technology. (a) Stainless Steel gears printed on XJet. (b) Lattice part printed for antennae applications. (c) Refractory parts fabricated for aerospace applications……..…..…..112
Figure 4.5: Ceramic Printing Unit used in this research (a) XJet Carmel 1400, based on Nano-Particle Jetting technique. (b) Schematic of the NPJ working…….116
Figure 4.6: Resin and powder properties of the Zirconia ink. (a) A SEM image of the Zirconia particles used in the resin. The image also shows the diameter of the largest particle (~150 μm). (b) A particle-size distribution histogram of the Zirconia powder. The powder was collected by evaporating the binder from the XJet ink. (c) XRD of the Zirconia printed sample……...117
Figure 4.7: Post-processing profiles used to sinter the printed green specimens. The profiles were named and designed according to the part geometry by Xjet. (a) Default, (b) Short, (c) Long, (d) Bulky, (e) Custom. ……120
Figure 4.8: Density of the samples sintered in different profiles. The figure also shows the standard deviation observed across the different densities……..…….…….……..120
Figure 4.9: XRD results of the printed samples sintered in different conditions. The samples sintered in the default and bulky profiles show highest peaks indicating higher crystallinity in comparison to samples printed in other conditions……121
Figure 4.10: XRD results of the printed samples sintered in different conditions. (a) Crystalline Vs Amorphous % in the samples. (b) Phase measurements observed in the sintered samples analyzed on TOPAS 3.0 using Reitveld analysis……....…122
Figure 4.11: TEM image of the sample sintered in custom profile. (a) TEM image of the sample showing crystalline phase. (b) A high magnified image of the crystalline phase showing the distribution of the grains in the samples. (c) Laue pattern of the sample indicating the crystalline

pattern……..…..……123
Figure 4.12: CTE analysis of the samples sintered in different thermal profiles. ……..124
Figure 4.13: Compressive Strength of the samples sintered in different post-processing profiles.125
Figure 4.14: SEM pictures of the surface of the compression samples taken at 210x magnification. (a) Surface of sample sintered under default profile where a homogenous layering was observed. (b) Surface of the samples sintered under the long profile, where defects such as pinholes were observed……....126
Figure 4.15: Flexural Strength of the samples sintered in different post-processing profiles……127
Figure 4.16: A representative SEM pictures of the surface of the flexural sample sintered in long thermal profile, taken at 330x magnification……128
Figure 4.17: Fracture Toughness of the samples sintered in different post-processing profiles..129
Figure 4.18: Mechanical properties of the lattice samples sintered in bulky and custom sintering profiles. (a) Compressive Strength of 0.6- and 0.8-mm unit cell lattice structures sintered in bulky profile. (b) Flexural Strength of 0.6- and 0.8-mm unit cell lattice structures sintered in bulky profile. (c) Compressive and Flexural strength of 0.8-mm unit cell lattice structures sintered in custom profile……....130
Figure 4.19: Lattice samples before and after compression testing. (a) A 0.8 mm unit cell lattice structure before testing. (b) A 0.8 mm unit cell lattice structure after compressive testing. A fracture was observed which extended along the struts along the unit cells…….…….....131
Figure 4.20: SEM image of the surface of the lattice structure after compressive testing. The crack initiated along the struts, causing the failure of the lattice samples ……..132
Figure 4.21: CT-Scan of zirconia parts before (left) and after a HIPing cycle (right). The HIPping process seems to close the observed internal crack on the printed specimens. The indentions on the outer edges are the embossed text describing the plane of each external surface and match as expected for the before and after images in each slice…..……..133
Figure 5.1: Schematic diagram of sintering process……...……...146
Figure 5.2: Densification mechanism as seen in sintering. (a) Loose powder as seen in green specimen. (b) Initial stage of sintering showing the particle adhesion. (c) Intermediate stage where samples are rounded eliminating porosity. (d) Final stage where sample is completely fused and sintered……..147
Figure 5.3: Schematic illustration of different sintering mechanisms depending on temperature.148
Figure 5.4: A schematic of mass -transport sintering mechanism seen in amorphous powders using a two-sphere model…….…..……...…..156

Figure 5.5: SEM images showing the micrographs of the silica samples at different temperatures during the sintering process. (a) At 400˚C. (b) At 800˚C. (c) At 1050˚C. (d) At 1225˚C……158
Figure 5.6: Particle Fusion observed at 1050˚C…….……159
Figure 5.7: Density and Particle size graph with respect to temperature……..160
Figure 5.8: SEM images showing the micrographs of the infiltration sintered samples. (a) Sintered fused silica sample before the infiltration process. (b) The transformed sample after infiltration.161
Figure 5.9: Evidence of the infiltration process. Grain size radius versus density graph seen after infiltration sintering (left). Grain distribution in the sample…….…….162
Figure 5.10Evidence showing the presence of silica and aluminum in the transformed samples. XRD of the transformed samples with peaks representing silica and aluminum. The figure also includes an SEM image of the transformed sample showing the unreacted silica particles.……...……..…....163
Figure 5.11: Schematic illustration of material flow using hyperboloid model……164
Figure 5.12: Graphical representation of diffusion flux and diffusion coefficient observed during sintering of silica samples……...……...…….165

List of Tables

Table 1.1: Applications of High-Performance Ceramics in different industries……5
Table 1.2: Additive Manufacturing techniques adapted for Ceramics in industrial development…9
Table 2.1: Shrinkage presented by SLA printed parts after curing at 400°C……37
Table 2.2: Shrinkage presented by SLA printed parts based on silica after sintering at 1275°C for 25 minutes at 10°C/min 1 atm pressure……40
Table 3.1: Shrinkage analysis observed in the printed hollow microspheres after sintering…..…..71
Table 3.2: Particle size distribution of Fused Silica powder used in this research……82
Table 3.3: Results of the Two-way ANOVA table for Binder Jetting Printing……85

1. Research Motivation and Problem Statement

1.1: Introduction

Ceramics have played an integral role in our daily life for centuries in the form of common products such as porcelain, glass and bricks. The history of ceramics dates back to 5000 BC where large structures like pyramids, giant monuments and cutting armories were made of ceramics. Figure 1.1 shows a range of ceramic structures from historic ages. For instance, the world's largest pyramid structure, Great Pyramid of Giza is a 2.3 million block limestone structure created by man with 8,000 tons of granite and 500,000 tons of mortar [1].

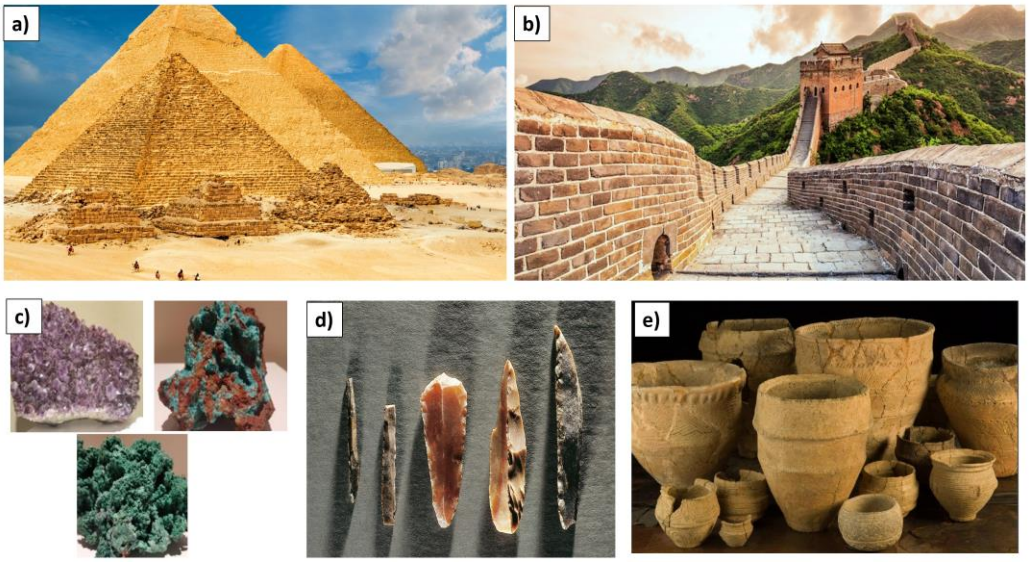

Figure 1.1: (a) The Great Pyramid of Giza [2] (b) Great wall of China [3] (c) Flouroscent mineral collection at Youngstown State University [4] (d) Mesolithic age tool collection [5] (e) Early Bronze age pottery [6].

The name ceramic derives from the Greek word κεραμοσ (keramikos) which means "of pottery" [7]. Ceramics are commonly made of two or three elements, found mostly as compounds of oxygen, carbon, boron, and nitrogen. These ceramics are mostly found in

crystalline or amorphous forms. Chemically, most ceramics are bonded by either covalent or ionic bonds [8]. Hence, these compounds are intrinsically hard and brittle. However, ceramics offer high resistance and good energy bearing in structural applications after firing them at high temperatures of at least 1000˚C. Ceramics are generally characterized by properties like strong and hard, inert to electrical conductivity and resistant to temperature, chemically inactive, and non-magnetic. Ceramics are used in a wide range of applications including refractory industries, machining and advanced applications in the automotive, medical and aerospace industries [9]. Figure 1.2 shows a bar chart of Young's modulus of different materials where it is observed that the stiffness of ceramics is comparable to that shown in metals.

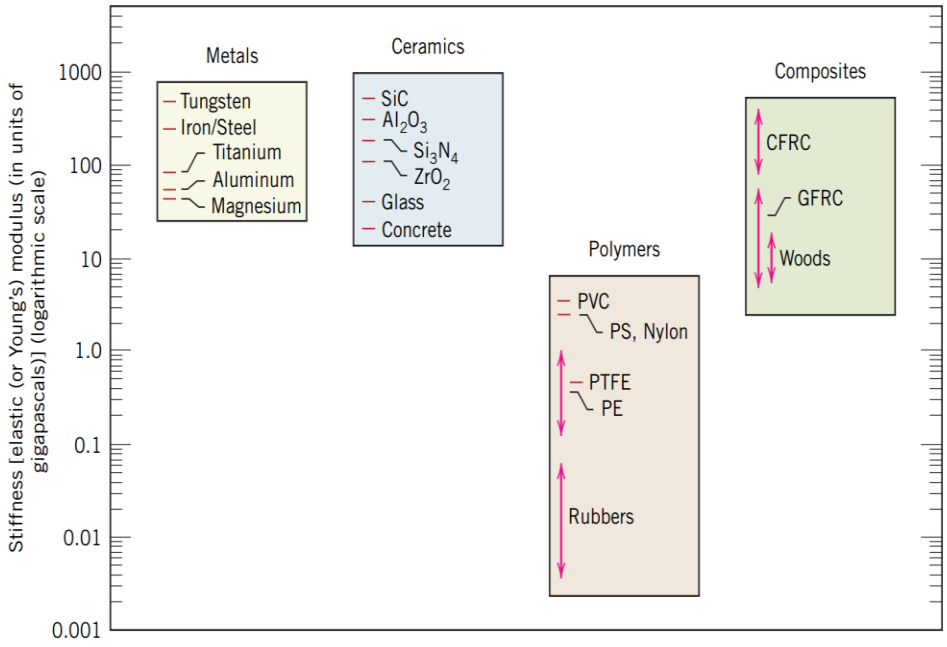

Figure 1.2: Bar-chart of stiffness (Young's modulus) of various materials [10].

Ceramics are classified into five different categories based on the type of chemical compounds present in them. They are described as [10]:

1. **Glasses** based on silica. Typically used as Pyrex, borosilicates in cooking, chemical glassware, and window glasses.

2. **Vitreous Ceramics** based on clay. These traditional ceramics are used as cutlery, piping fixtures, bricks and tiles.

3. **High Performance Ceramics**, based on oxides, nitrides, borides and carbides. These are employed in applications where high fracture toughness and wear resistance are required.

4. **Cement and concrete** based on a complex ceramic mixture of lime (CaO), silica (SiO_2) and alumina (Al_2O_3). These are used in most of the civil constructions.

5. **Natural ceramics** that occur in nature as rocks and minerals.

The use of ceramics for technical applications in industrial and biomedical industries was addressed after the industrial revolution [11–13]. Ceramics served with longer sustainability, superior mechanical and thermal performance while being chemically inert were under high importance [14]. Alternatively, High Performance Ceramics (HPC's) appeared to be promising materials in terms of mechanical performance and chemical resistance applications under harsh environmental conditions. These advanced engineering ceramics are capable of surviving at extreme temperatures (1400ºC and above) while offering high mechanical strength [15].

1.2: High Performance Ceramics (HPC's)

High Performance Ceramics (HPC's) are a class of ceramics which are also termed as 'engineering ceramics', 'technical ceramics' and 'structural ceramics'. The distinction between traditional ceramics and structural ceramics lies in their high resistance towards wear, thermal conduction, and mechanical performance at high temperatures. Hence, they are used in applications where high strength and wear resistance at severe temperatures is required. The high weight-to-

strength ratio is the most important characteristic shown by these technical ceramics (see Figure1.3).

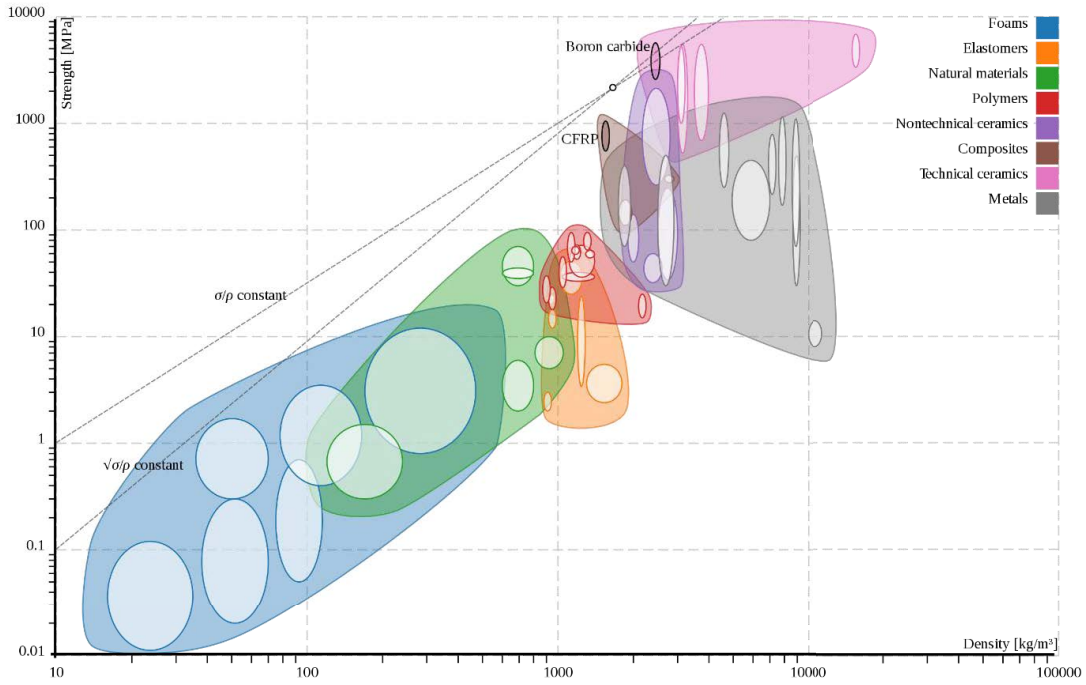

Figure 1.3: Ashby diagram describing the characteristics of materials, where the technical ceramics stand top in terms of strength [16].

As the mechanical performance and sustainability at higher temperatures has grown in the ceramic field, a paramount interest in developing structures out of HPC's has taken place in recent years. Several techniques in producing and processing these ceramics have been investigated and used in industrial applications. Some of the important parameters considered were the microstructure and post-processing due to their high influence in the final performance of material. With respect to all the characteristics, HPCs are employed in various industries for long sustainability and light weight features. Table 1.1 shows different applications where high-performance ceramics are used.

Table 1.1: Applications of High-Performance Ceramics in different industries.

Industry	Applications	Purpose
Aerospace	Re-entry vehicle nozzle Air frames Engines Ceramic tiles	High temperature and high stress Light-weight structures
Electronics	Resistors Antenna Capacitors Transducers and insulators Semi-conductors	Good dielectric capacitance Stability from porosity Resistance for conductivity Wear resistance
Bio-medical	Artificial bone scaffolds Implants Dentistry	Chemical inertness Capacity for strong bearing Wear resistance Corrosion resistance
Automotive	Rotating shafts Brake-rotor systems Heat engines	High shear stress and fracture strengths Sustainability at high temperatures
Refractory	Metal extrusion and die molds	High strength at even high temperatures
Tooling	Tooling tips	High hardness

According to a survey in 2015 on the market size of global technical ceramics, it was expected that the market size would soar to approximately $134.58 Billion by 2024 [17, 18]. Alumina among the different ceramics occupies the largest share, where the end products lie in machinery, automotive, electrical and electronics industries capturing 39.6% share among all the ceramics. Similarly, Zirconates, which are used as piezo electronics, dental and biomedical applications occupy a 11.4% growth in the ceramics global market. Figure 1.4 shows the expected significant growth in the ceramic market by at least 10.2% in the next five years. Titanates are expected to show a significant growth by over a 11.5% due to their usage in electronics and biomedical applications.

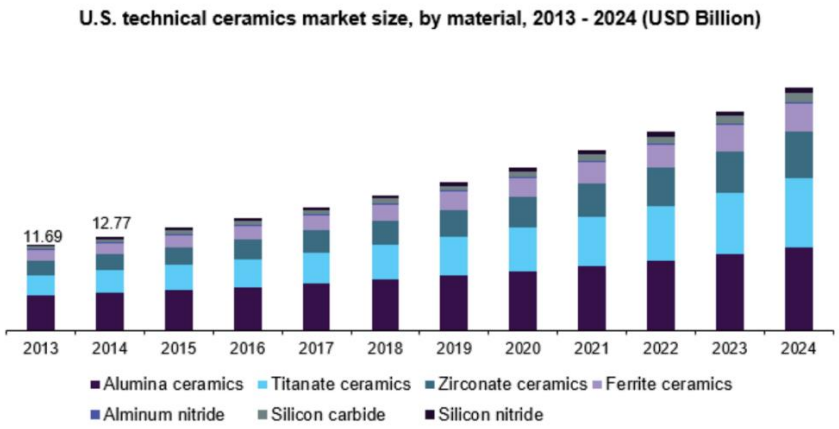

Figure 1.4: Global technical ceramics market size of ceramic material [18].

The survey also addressed the use of technical ceramics in the medical fields for their usage as dental implants, tissue, join and hip replacements. It was found that a market of about 8 billion during the year 2015 and it might increase tremendously in the coming years accounting the next 8-10 years.

With all the markets concentrating on newer technologies to utilize technical ceramics, it is expected that the North American Ceramic market might grow over 9.5% annually in terms of revenue. The survey reveals that the traditional ceramic market is mostly concentrated in manufacturing parts for automobile and electronic industries. This traditional manufacturing sector can be classified into different industries based on their production and R&D capacities i.e., “high”, “medium-high”, “medium-low” and “low-tech” industries [19]. The companies were built long back and have been a source of employment for labor intensive jobs in production. These industries majorly work on repetitive, low-skilled and manual based part production.

Present conventional fabrication techniques like pressing, ceramic injection, and ceramic extrusion are used to plastically deform ceramics to manufacture industrial structures [20]. A schematic of the manufacturing process of a ceramic part is shown in Figure 1.5. This

procedure is employed in most industries and repeated according to the requirement. Here, permanent dies to make the parts are installed in the industries which can be seen in high production industries [21–23].

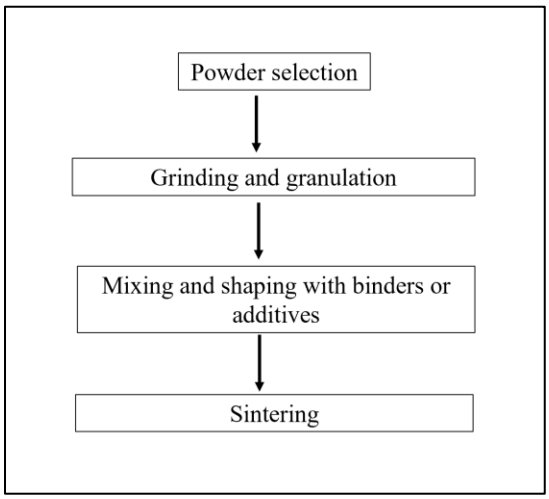

Figure 1.5: Schematic diagram of the ceramic part fabrication.

Although the market for this has been beneficial in terms of production, it lacks the innovation and customization of parts without material wastage. In the long-term, this might lead to a flattened business where the research lacks novelty. Indeed, these methods are limited for manufacturing simple geometries. These in fact require manual labor with a skill set on powder processing, and product molding and are accompanied by material wastage and high production costs. Furthermore, the industrial applications often require customization.

The solution to this issue is the alternative production technique for the production of customized ceramics structure known as additive manufacturing.

In Additive Manufacturing (AM), a layer of base material from a feedstock in the form of powder or resin suspension (or paste) is laid on the build plate/box and a source of binding agent is used for “gluing” the layers as well as the particles together. A Computer Aided Design (CAD) is sliced

into layers in each of these techniques to build a structure (see Figure 1.6). These additive manufacturing techniques have been recognized by ASTM F2792-12 for part building [24]. Some of the important advantages in adapting AM include precise fabrication, easy production of intrinsic structure of dense monolithic structures, and no material wastage. Different forms such as direct powder, slurry-based 3D printing, fused filament, and energy depositions are some of the industrial techniques used for producing complex parts [25, 26]..

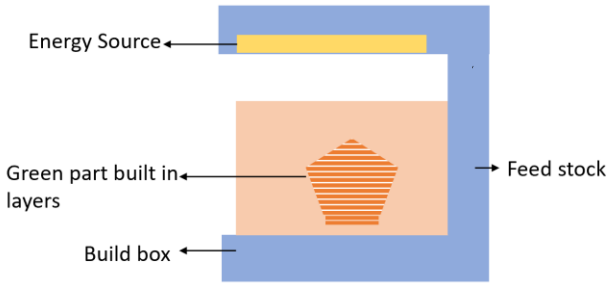

Figure 1.6: Schematic diagram of additive manufacturing process of a sample being printed in a layer-by-layer fashion.

With both advantages and challenges included in AM, research efforts to industrialize the used of AM is being in progress. Amir et al [27] in their review on Binder Jetting Additive Manufacturing reported a gradual increase in the research and publications using the technique. It was stated that around 31,000 publications were mapped by the end of 2019 where most were reported from the year 2014. A concentration on both metals and ceramics to study process parameters for building, optimization, post processing techniques, mechanical behavior and microstructure evaluation were some of the main topics considered in most papers. Along with the research, many companies have adopted 3D systems for producing parts. Presently six AM techniques are being used for the printing of ceramics and are described in Table 1.2.

Table 1.2: Additive Manufacturing techniques adapted for Ceramics in industrial development.

Additive Manufacturing Technique	**Source of Building**	**Technologies included**	**Companies building 3D systems**	**Technical Ceramics built**
Powder Bed Fusion	Laser Energy which melts/sinters the powder layer.	Selective Laser Melting (SLM) Selective Laser Sintering (SLS) Electron Beam Melting (EBM)	EOS, 3D Systems, Fuse 1 by Formlabs, Red Rock, HP	Zirconia, Alumina
Binder Jetting Printing (BJP)	Powder based techniques where a binder is filled in the powder layer voids and cured by a UV light.	-	ExOne, Tethon 3D, 3D systems, Z-Corp, Voxeljet	No limit on materials
Vat Polymerization (VAP)	Resin based building technique cured by an UV/Laser spot	StereoLithography (SLA), Digital Light Processing (DLP), Continuous Liquid Interface Production (CLIP), Daylight Polymer Printing (DPP)	Formlabs, Lithoz, Admatec, 3D CERAM Sinto	Silica, Zirconia, Alumina
Material Extrusion	Ceramic extruded continuous filament	Fused Filament Fabrication (FFF)	Nano-e, Xerion	Zirconia, Zirconia toughened Alumina, Alumina
Material Jetting (MJ)	Ink based technique cured by an UV light source	Drop on Demand (DOD), PolyJet, Nano Particle Jetting (NPJ)	Xjet, Object, Stratasys	Zirconia, Alumina.
Direct Energy Deposition (DED)	An electron beam or a laser source on a selectively deposited material	Electron beam Welding (EBW) Laser metal deposition (LMD) Electron beam free-form fabrication (EBF3)	AMBIT	Alumina, Zirconia, Hydroxyapatite [28]

Because customization of structural parts is enabled by 3D printing techniques, this process has gained great industrial interest with an emphasis on improving the mechanical properties and performance of ceramics as well as exploring their limitations [20]. An example of different applications in the medical, electronic, mold casting, dental, antennae and semi-conductor industries is shown in Figure 1.7.

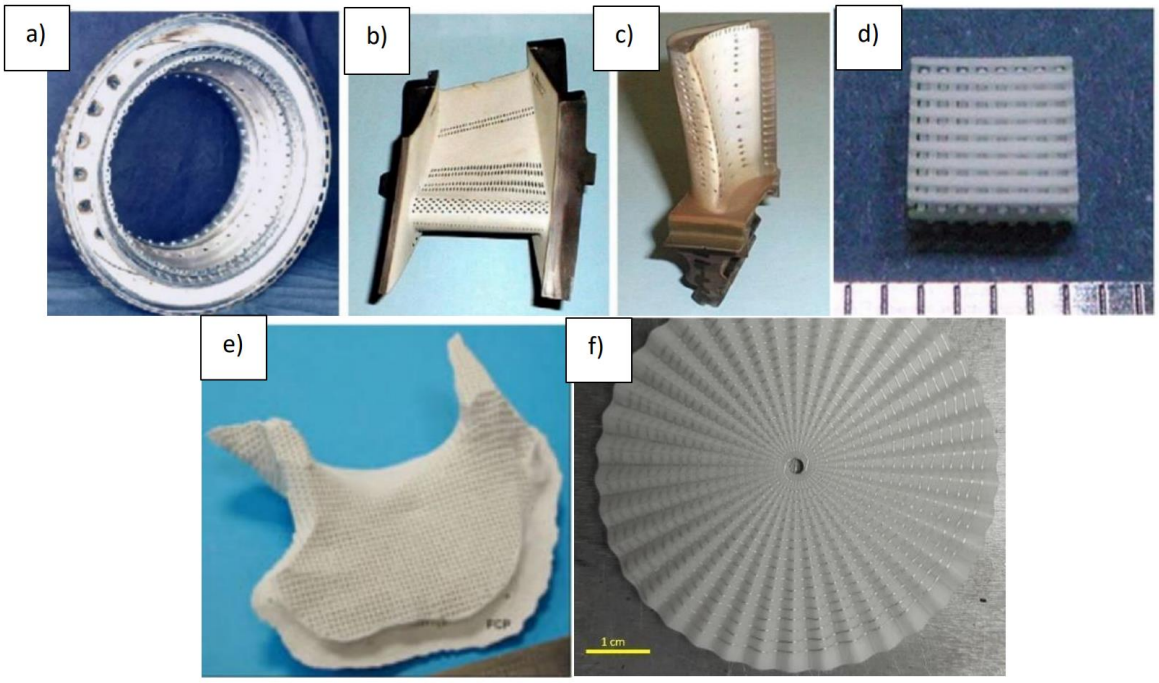

Figure 1.7: Examples of 3D printed structures (a) A compressor component infiltrated from ceramics for air brakes in jet engines printed via BJP, (b) A component in passenger flights, (c) insulation part created for refractory application made from Vat polymerization, (d) Alumina lattice component created via SLA technique, (e) Calcium carbonate bone scaffold fabricated via SLA, (f) Sinusoidal antennae for dielectric applications created via NPJ [29–31].

A survey on the ceramic market size built either traditionally or by advanced techniques forecasted the market size would soar to USD 407.72 billion by 2025 [32]. Jiang and team used

the Delphi approach, a multi-stage forecasting model to identify the future of additive manufacturing as a product by 2030 [33]. The model presented additive manufacturing in four different scenarios: 1) market explorer, 2) content provider, 3) service provider and 4) mass consumer. Each scenario indicated a growth in intellectual property, in creation of new business opportunities, and as a form of inexpensive mass production for customized products.

A report on 3D printing ceramics discussed the geographical market regions, the different types of ceramics using AM, and the industrial pros and cons along with variables like COVID-19, sales, material market and shipment losses. The report has predicted the AM adoption and market value of ceramic 3D printing by the year 2025 with all the ceramic AM techniques [34]. It is expected that the market might grow to $4.8 billion by the end of 2030 (see Figure 1.8). Hence, ceramic additive manufacturing can be considered as an opportunity for market growth.

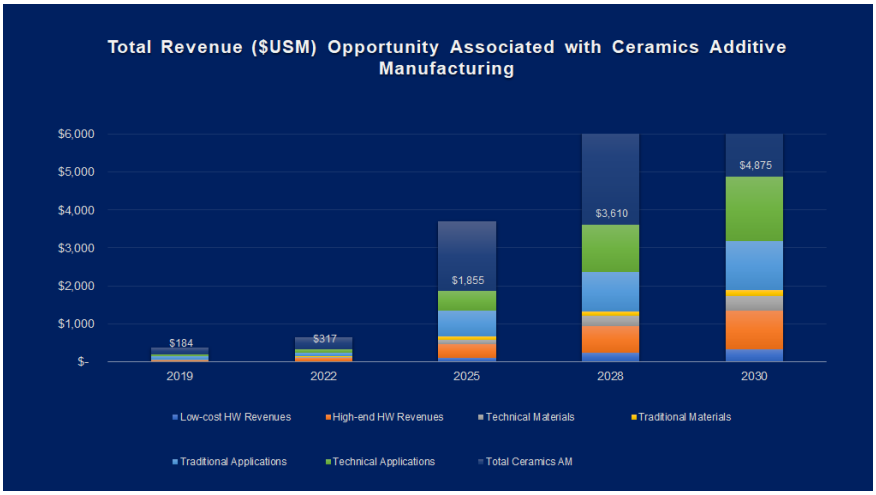

Figure 1.8: Global technical ceramics market size of 3D printed ceramic materials [35].

1.3: Research Motivation and Problem Statement:

Despite the advantages of these techniques, there are some limitations in the concentration of ceramics in AM techniques. Inherently, ceramic parts mostly require the unavoidable step of post processing. Additionally, 3D-printed parts are known to have inferior mechanical properties

than the parts manufactured using traditional processes. To overcome this disadvantage, the development of appropriate printing process parameters and post-processing treatments need to be investigated to obtain densified fracture-free parts in a single print. To date, there are limited studies addressing the mechanical and thermal performance of 3D printed HPCs. This work will provide an opportunity to establish the scientific and engineering foundations in studying HPCs using additive manufacturing.

In this research, three different additive manufacturing techniques: Stereolithography (SLA), Binder Jetting Printing (BJP) and Material Jetting (MJ) were investigated for fabricating specimens with high build density and dimensional accuracy. Printed structures with intricate geometries and high mechanical performance can provide a trust source to adapt AM in the industrial field. Indeed, this work could be used as a scientific and engineering platform for understanding the structural processing – property relationship of 3D printed HPCs.

1.3.1: Objectives:

The objective of this work is to utilize different additive manufacturing techniques and post processing techniques to understand the mechanical and thermal performance of fabricated HPC samples. This work provides an emphasis on: 1) Binder Jetting Printing -BJP; 2) Stereo Lithography -SLA, a process under the Vat Photopolymerization technology; and 3) Nano Particle Jetting -NPJ, a process under Material Jetting for printing near dense parts. The HPCs investigated in this work are: Fused Silica, Zirconia, and alumina-based powders. Future studies include transformation of oxides and carbides into co-continuous ceramic metal composites to obtain beneficial properties of both metal and ceramic phases in a single structure.

The specific objectives are as follows:

- Production of HPC samples via StereoLithography, Binder Jetting Printing and Material Jetting.

- Study the effect of powder particle size in the Binder Jetting Printing using XRD and microscopy as evaluating tools.
- Determine the printability of CAD model for building parts with or without support system.
- Study the post-processing effects on the mechanical and thermal properties of the printed parts.
- Study the microstructure of the samples before and after post-processing including the crystalline changes in the powder particles using XRD.
- Develop a diffusion model for a SiO_2- SiO_2 system.

1.4: Organization

The document is divided into 6 chapters.

- Chapter 1 discusses the introduction and motivation of the present research work.
- Chapter 2 discusses VPP polymerization and the results acquired on the silica-based samples. The chapter also discusses the production of metal-ceramic composites using SLA.
- Chapter 3 focuses on Binder Jetting and the different powders used for printing. An ANOVA analysis on printing parameters and post-processing were discussed. Along with this printability of different materials and their mechanical properties.
- Chapter 4 focuses on Nano Particle Jetted Zirconia and the effects of the post processing on their mechanical performance.
- Chapter 5 discusses a kinetic model developed to understand diffusion of a SiO_2- SiO_2 printed system via Stereolithography.
- Chapter 6 presents the conclusions from the present work in each printing technique along with future studies.

1.5: References:

1. Romer J (2007) The Great Pyramid: Ancient Egypt Revisited. Cambridge University Press, Cambridge
2. Pyramids of Giza | National Geographic. https://www.nationalgeographic.com/history/archaeology/giza-pyramids/. Accessed 16 Sep 2020
3. 6 Facts About the History of the Iconic Great Wall of China. https://mymodernmet.com/great-wall-china-facts/. Accessed 16 Sep 2020
4. Visit – Clarence R. Smith Mineral Museum. https://minerals.ysu.edu/visit/. Accessed 16 Sep 2020
5. Prehistoric Stone Tools Categories and Terms. https://www.thoughtco.com/prehistoric-stone-tools-categories-and-terms-171497. Accessed 24 Feb 2021
6. Tara-1024x619.jpg (1024×619). https://www.dayofarchaeology.com/wp-content/uploads/2012/06/Tara-1024x619.jpg. Accessed 16 Sep 2020
7. Ceramic - Wikipedia. https://en.wikipedia.org/wiki/Ceramic#cite_note-6. Accessed 13 Sep 2020
8. Ceramic property. https://depts.washington.edu/matseed/mse_resources/Webpage/Ceramics/ceramicproperty.htm. Accessed 13 Sep 2020
9. Ohji T, Jeong YK, Choa YH, Niihara K (1998) Strengthening and toughening mechanisms of ceramic nanocomposites. J Am Ceram Soc 81:1453–1460
10. Ashby MF, Jones DRH (2013) Ceramics. In: Eng. Mater. 2, 4th ed. Butterworth-Heinemann, pp 299–312
11. Lei J-F, Goldberg RK (2013) Special Issue on Seventy Years of Aerospace Research and Technology Excellence at NASA Glenn Research Center. J Aerosp Eng 26:197–201

12. Hagedorn Y (2017) Laser additive manufacturing of ceramic components: Materials, processes, and mechanisms. In: Laser Addit. Manuf. Mater. Des. Technol. Appl. Elsevier Inc., pp 163–180

13. Gasch M, Ellerby D, Irby E, Beckman S, Gusman M, Johnson S (2004) Processing, properties and arc jet oxidation of hafnium diboride/silicon carbide ultra high temperature ceramics. In: J. Mater. Sci. Springer, pp 5925–5937

14. Dever JA, Nathal M V., DiCarlo JA (2013) Research on High-Temperature Aerospace Materials at NASA Glenn Research Center. J Aerosp Eng 26:500–514

15. Ashby MF, Jones DRH (2012) Yield Strength, Tensile Strength, and Ductility. In: Eng. Mater. 1. Elsevier, pp 115–133

16. Ashby MM, Jones DRH (2012) Engineering Materials 1. Eng Mater 1. https://doi.org/10.1016/C2009-0-64288-4

17. Technical Ceramics Market Size Worth $134.58 Billion By 2024. https://www.grandviewresearch.com/press-release/global-technical-ceramics-market. Accessed 5 Jul 2020

18. Global Technical Ceramics Market Size | Industry Report, 2018-2024. https://www.grandviewresearch.com/industry-analysis/technical-ceramics-market. Accessed 5 Jul 2020

19. Radicic D, Pugh G, Hollanders H, Wintjes R, Fairburn J (2016) The impact of innovation support programs on small and medium enterprises innovation in traditional manufacturing industries: An evaluation for seven European Union regions. Environ Plan C Gov Policy 34:1425–1452

20. Wang JC, Dommati H, Hsieh SJ (2019) Review of additive manufacturing methods for high-performance ceramic materials. Int J Adv Manuf Technol 103:2627–2647

21. Ceramic Machining Services & More | Applied Ceramics, Inc. https://www.appliedceramics.net/services/. Accessed 12 Nov 2020

22. LSP Industrial Ceramics | Industrial and Technical Ceramics. https://lspceramics.com/. Accessed 12 Nov 2020

23. Ceramic Parts and Ceramic Products - Du-Co Ceramics Company. https://du-co.com/. Accessed 12 Nov 2020

24. ASTM Committee F42 (2012) ASTM F2792-12, Standard Terminology for Additive Manufacturing Technologies. ASTM Int. https://doi.org/10.1520/F2792-12

25. Chen Z, Li Z, Li J, Liu C, Lao C, Fu Y, Liu C, Li Y, Wang P, He Y (2019) 3D printing of ceramics: A review. J Eur Ceram Soc 39:661–687

26. Gokuldoss PK, Kolla S, Eckert J (2017) Additive Manufacturing Processes: Selective Laser Melting, Electron Beam Melting and Binder Jetting—Selection Guidelines. Materials (Basel) 10:672

27. Mostafaei A, Elliott AM, Barnes JE, Li F, Tan W, Cramer CL, Nandwana P, Chmielus M (2020) Binder jet 3D printing – Process parameters, materials, properties, and challenges. Prog Mater Sci 100707

28. Nam S, Jung I-H, Kim Y-M (2020) DED Type Laser Additive Manufacturing Technology of Oxide Ceramics. J Weld Join 38:469–478

29. Zhu Y, Allen G, Jones P, Adams J, Gittins D, Heard P, Skuse D (2014) Dispersion characterisation of CaCO. Compos Part A Appl Sci Manuf 60:38–43

30. Oh Y, Bharambe V, Mummareddy B, et al (2019) Microwave dielectric properties of zirconia fabricated using NanoParticle Jetting™. Addit Manuf 27:586–594

31. Chartier T, Chaput C, Doreau F, Loiseau M (2002) Stereolithography of structural complex ceramic parts. J Mater Sci 37:3141–3147

32. Ceramics Market Size, Share & Trends Analysis Report By Product (Traditional, Advanced), By Application (Sanitary Ware, Abrasives, Tiles), By End-Use; By Region, And Segment Forecasts, 2019 - 2025.

33. Jiang R, Kleer R, Piller FT (2017) Predicting the future of additive manufacturing: A

Delphi study on economic and societal implications of 3D printing for 2030. Technol Forecast Soc Change 117:84–97

34. SmarTech Analysis (2020) Report on Ceramics Additive Manufacturing Highlights New Dynamics within Potential 4.8 Billion Market by 2030. https://www.globenewswire.com/news-release/2020/04/21/2019566/0/en/SmarTech-Analysis-2020-Report-on-Ceramics-Additive-Manufacturing-Highlights-New-Dynamics-within-Potential-4-8-Billion-Market-by-2030.html. Accessed 12 Nov 2020

35. Ceramics 3D Printing Market Revenues to Top 3.6 Billion by 2028. https://www.smartechanalysis.com/news/ceramics-3d-printing-market/. Accessed 12 Nov 2020

2. Production of Metal Ceramic Structures using Vat Photo Polymerization

Overview:

This chapter provides details on 3D printing technology, Stereolithography and ceramic printing via this technique. Section 1 focuses on the introduction of stereolithography printing technique. Section 2 discusses the literature review discussing the research on this printing technique since the innovation. Section 3 presents the research methodology followed in the study and the instruments used to characterize the printed materials and their transformation into IPC's. Section 4 focuses on the results observed and sub conclusions drawn from each testing method. Section 5, at the end presents overall conclusions of the work.

2.1: Introduction

VAT Photo Polymerization (VPP) is a polymer based additive manufacturing technique recognized among the different ISO AM techniques [1]. In this process, a resin, mainly composed of monomers in a vat, is hardened on a build plate through a layer-by-layer process. Each layer when spread on the build plate is cured selectively by a light source or a low power laser until the final part is built (followed by a post processing stage). The VPP printing technology includes: Stereolithography (SLA), Digital Light Processing (DLP), Continuous Liquid Interface Production (CLIP) and Daylight Polymer Printing (DPP) [2].

Stereolithography (SLA) is a subdivision of the Vat Photo Polymerization (VPP), in which a UV or laser based light source cures the liquid photopolymer resin. After the printing process, the manufactured parts are subjected to a curing stage, where the polymer cross-links to form a solid network [3, 4]. The parts in this technique are built upside down using a support system as the build plate is immersed into the vat for each layer (see Figure 2.1).

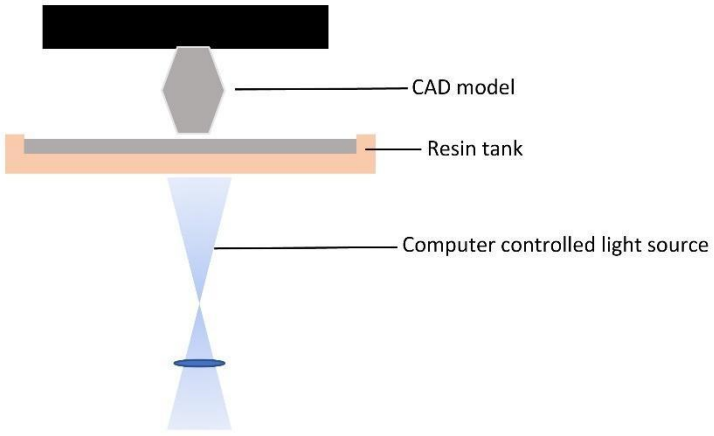

Figure 2.1: Schematic diagram of a typical stereolithography printing technology.

This technique was initially developed for rapid prototyping. Charles Hull at 3D systems in the earliest 80's developed a 3D printing (3DP) apparatus to convert the liquid polymer into solid objects [5, 6]. Although not designed to print huge parts in the beginning, the technique improved in terms of parameters used for printing layer thickness from 400 microns to 100 microns, with an

increased resolution. Along with this, acrylate-based epoxy resins were commercially available since the mid 90's [7, 8]. This solid freeform fabrication technique was then extended for printing different materials like ceramics, polymers and metals. This technique includes advantages like easy printing with respect to time and effort, simplifying complex parts printability, and the capability of printing in different colors. However, it has few limitations such as difficulties in producing large parts, presence of porosity, as well as high surface roughness on the printed parts. However, this technique is still industrially accepted for many rapid prototyping evaluations, dental and medical part fabrications [9, 10]. Subsequent improvements resulted in the incorporation of different materials such as acrylonitrile butadiene styrene (ABS), polypropylene and dyes on printers created by companies like 3D systems, Lithoz, Voxel jet, Stratasys, Formlabs, Admatec and Prodways [11–14]. VPP is currently used for the production of dies and jigs, jewelry, dental crowns, and in robotics including prototyping (see Figure 2.2).

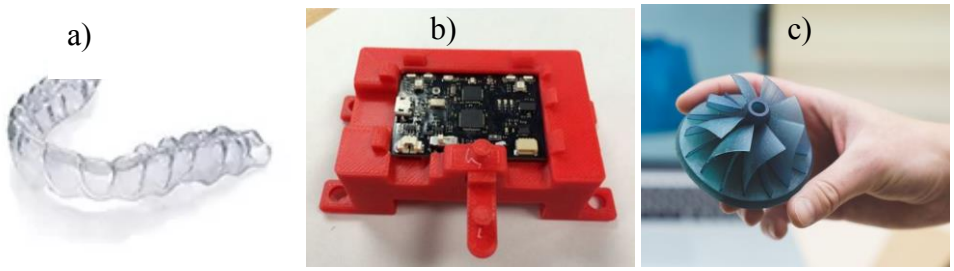

Figure 2.2: Industrial parts built via SLA. (a) Customized dental bridge [14]. (b) Jig for a microelectronic device [15]. (c) Prototype 3D component created on Formlabs [16].

Ceramic SLA first appeared in the late 90's where UV transparent powder particles of at least 40 vol % were suspended in a polymer based resin with photo initiators [17–20]. This resin is printed with a support system using the aforementioned printing process. These non-processed printed parts (commonly known as green parts) are then subjected to a thermal cycle to remove the polymer and finally to a sintering stage to consolidate the final part.

Since the 90's, there have been many studies where researchers have studied the behavior of different ceramic resins in order to obtain full dense parts for a wide range of commercial applications.

2.2: Literature Review

Traditionally, ceramics were fabricated through different techniques like Pressing, Ceramic Injection Molding (CIM), Investment casting, and Ceramic Extrusion. These techniques are based on pressure either with or without binder and with or without temperature. However, building intricate parts via these traditional techniques is difficult since a mold must be designed specially to fabricate the parts. Sometimes the parts have to be carved out of a block of ceramic pieces which accounts for waste material and time. If the parts need mass production, then further optimization and labor hours are required to design and fabricate them at lower production costs. However, the introduction of additive manufacturing has allowed the creation of intricate parts based on complex geometries. An additional advantage of additive manufacturing is the production of parts without the need for mold preparation. In specific, the SLA technology enables the production of complex parts suitable for medium batch production.

2.2.1. Printing Parameters

The SLA technique has been initially explored for polymer part building. The fundamental arrangement in stereolithography is an UV light through an oxygen-permeable window acting as a source of energy to form the covalent bonds between the molecules in a photopolymer resin to build a structure in a layer-by-layer fashion. The initial photopolymer resins were based on high molecular weight with low glass-transition temperatures, resulting in clear and rigid printed parts [21]. The photopolymers are basically monomers or oligomers which form longer chains when exposed to UV light or laser light. Photopolymerization can be optimized by parameters like light wavelength, and time of exposure [22]. In the earliest 90's, Griffith et al [17, 18] investigated the printability of ceramic suspended photopolymers based on a Newtonian resin with fine particle

loading (0.05 μm to 10 μm with 40-60 vol %) to print ceramic cores. These cores had a high burnout cycle as they were made of high carbon-based substances with a high degree of shrinkage.

In SLA, the printing process either goes top-down or bottom-up which describes the printing orientation. In the top-down approach, the CAD model is arranged and built upwards with the top of the structure being built first. In the bottom-down approach, the print starts at the bottom layers and the structure is inverted during the printing. In both orientations, the surface tension and the wiper blade movement of the resin plays a key role in recoating and maintaining a low surface roughness [23]. Additionally, since every layer is printed in quasi-static steps, a better surface quality is achieved in this 3D printing technique. In this technology, it is always required that a wiper blade moves along the print direction for each layer to maintain consistency in the recoating. The laser employed in most of the SLA units uses a Gaussian model where the intensity is less in the central portion of the beam and relatively higher at both ends to maintain symmetry in the prints [24]. Griffith et al [19] investigated the powder characteristics and light source intensities that could help in attaining better shape integrity properties using the Beer-Lambert's law for the ceramic resins; a work that was also extended to Alumina (Al_2O_3) and Silicon Nitride (Si_3N_4) [25, 26]. The Beer-Lambert's law is shown in Equation 2.1, where d is the particle size, is logarithm of exposed light, E0,volume fraction of suspended ceramic, and Q is scattering ability obtained from refractive index (RI). The study also reported that the printing parameters; cure depth (Cd), viscosity and layer thickness could be modified according to Beer-Lambert law. They reported that the cure depth is logarithmically proportional to the volume fraction of ceramic suspension and inversely proportional to the square of the refractive index. Here, lower cure depths are employed when printing ceramic resins in order to cure the ceramic parts [27]. It is recommended that the RI of the resin for printability should typically be in the range of 1.56 to 2.6 with the majority of the studies showing 1.5 when monomers are used [28, 29]. On the other hand, it is recommended that the particles filled in the resin should be of a smaller particle size and with a layer thickness higher than the particle size to see the particles randomly distributed along with the resin [27].

$$C_d = \frac{d}{\phi}\frac{1}{Q}\, ln\, ln\, \left[\frac{E_0}{E_c}\right] \qquad (2.1)$$

A control system connected to the SLA unit establishes the movement of the vat tank and the build platform. As mentioned before, the surface is recoated for each layer, and it is required that the wiper, vat tank and build plate work in correlation to avoid print failure or damage to the SLA unit. After the successful build, a post-processing step required specially for ceramics, the resin/binder is burned out, causing the layers to shrink. This could induce delamination among the printed layers. It is estimated that overcure may also occur which might be approximately 10 - 35% cause for the failure of prints [29]. Several studies using different powders such as Zirconia, silica, alumina are available for targeting specific industrial sectors such as the bio-medical, aerospace and refractory [10, 30–33].

2.2.2. Materials

Research on different industrial ceramic powders such as Zirconia, Alumina, Silica, metal oxides and borides has expanded its use in the Vat Polymerization technology in the production of complex parts. Griffith et al [18] for the first time worked on an aqueous based photo-curable ceramic suspension using a photo-initiator which bound the layers together. However, these aqueous binders can induce cracking and a quick drying, which affects the recoating [34]. On the other hand, non-aqueous resins, mainly composed of acrylates or epoxy resins, provide parts with higher strength. Non-aqueous resins have been investigated for printing non-oxide powders and metal powders, unlike aqueous ceramic suspensions which are only suitable for printing oxide powders. Similarly, studies using acrylate monomers, polyethylene glycol (PEG) and epoxy-based monomer resins have been investigated for loading ceramic powders to print via SLA.

The initial work from Griffith suggested the use of a minimum ceramic loading of 50 vol%. However, Liao [34] indicated that a higher amount of ceramic suspension would improve the final properties of the green and post-processed parts. Using also a higher ceramic loading content seems

to result in parts with less porosity, lower shrinkage, and a homogenous sintering distribution [35–38].

Chartier et al [39] demonstrated printing of alumina patterns with good resolution using monomeric resins and a high volume suspension content of alumina powder (60 vol %). The investigation included an optimization of curing depth and curing width in order to improve dimensional accuracy. Chen et al [40] also investigated the effect of ceramic loading varying between 78-89 wt% of Lead Zirconate Titanate (PZT) powder and evaluated the final parts for piezoelectric applications. An improved voltage stimulus was seen in the samples with 89% ceramic loading. However, the samples with high loading showed a non-homogenous distribution in the PZT with a high refractive index and lower adhesion properties with lower shrinkage. An interesting study by Johansson and team [41] have shown that non-reactive components in the photopolymer resins also reduce the shrinkage since the residual particles resulted in less porosity. A bimodal mixture containing micro and nano sized Al_2O_3 particles in a 1:1 ratio using acrylamide-based resin was printed to test the density properties of the manufactured parts, which resulted in a higher density than normal [42]. A comparison between the thermal and vacuum debinding was also included in this study, and a higher density was reported when the samples were vacuum debinded, which accounted for no exposure to oxygen. A study on the influence of drying and debinding methodologies was investigated by Zhou et al [43] using Alumina powders in attaining dimensional accuracy and a higher density. Zhou et al also used a liquid-based desiccant drying and two step debinding process on printed alumina and showed it was an efficient way for obtaining crack-free parts with improved densities (a relative density of 99.3% was obtained in these parts when printed via Stereolithography. The team also compared the mechanical properties of these printed samples to the samples fabricated via different techniques like gel-casting, injection molding, tape casting, slip casting and uniaxially pressed samples, and the printed samples seemed to have shown similar hardness values.

Additionally, Bae et al [44] have worked on molds based on fused silica for the refractory industry, and they have reported the presence of microcracks in the printed parts in green state, which seemed to disappear during the sintering stage at a temperature of 1500°C. This high sintering temperature resulted in an increased mechanical strength than that observed under lower sintering temperatures. Bae et al [44] also worked on the kinetics of crack development and reported that macrocracks occurred due to the presence of uncured resin in the ceramic samples. Esposito Corcione et al [38] also worked on prototyping silica molds for aluminum casting using SLA. Their results suggested that this technology could represent a non-expensive approach for the foundry industry.

Wang and Dommati have also studied the printing process of zirconia using SLA and have shown that complex geometries with high density (5.99 g/cm^3) can be fabricated. They reported a final shrinkage of approximately 24% from the initial dimensions [45].

Melchels et al [27] have shown stereolithography as one of the most powerful and versatile techniques to build implants and biodegradable tissue scaffolds as well as medical devices. The review provides a brief detail on the materials used for developing biomedical devices that can be used in medical imaging. Apart from that, SLA is majorly used in dental applications to create dental crowns and masticatory scaffolds. Alumina and Zirconia occupy a major portion in these frameworks for their polycrystalline behavior and mechanical toughness. A Weibull characteristic study on flexural strength of SLA fabricated alumina samples was reported by Dehurtevent et al [46]. They included a study on the viscosity of monomer resins with alumina particle suspension in varied concentrations. They reported that the samples with a relatively medium particle size (1.58 μm) and high solid suspensions resulted in a good density (3.86 g/cc) with high flexural strength (367.9 MPa). Additionally, from their studies they reported that SLA is suitable for creating complex shape dense parts like dental crowns; although, anisotropic shrinkage was observed. Zakery et al [47] has summarized the recent developments in the dental field using the SLA technology.

2.2.3. Interpenetrating Phase Composites (IPC)

Interpenetrating Phase Composites (IPCs) are a class of Co-Continuous Ceramic Composites (C4) which serve best for lightweight structures and long life applications [32]. Interpenetrating phase composites (IPCs) are attractive materials, due to the benefits of high-strength and reduced weight [39, 48–50]. IPCs are produced by reacting a molten metal with a sacrificial oxide structure to form C4 composites [51]. Breslin et al [52] conducted experiments on the production of IPC samples using silica templates and reported that the composites presented a phase distribution of 65% alumina and 35% aluminum with a modulus of rupture averaging about 470 MPa. Breslin has reported the presence of porosity during the transformation process due to the oxides present in the ceramic. Pavese et al [53] demonstrated the production of C4 composites from reactive metal penetration method and discussed the reduction of mechanical properties due to the high amounts of porosity present in the composites.

A mathematical model was investigated by Myers et al using a similar MATLAB code developed by Andreassen and Andreasen [54, 55]. In this method, a gray scale image of the transformed image is represented in numerical form using 0's, and 1's. The percentage of porosity, Alumina and Aluminum were denoted by this numerical technique.

2.3: Methodology

2.3.1. Printing and Sintering

Commercially available amorphous fused silica (SiO_2) ceramic photopolymer resin from Formlabs, Inc., (Somerville, MA, USA) was used in this research work to fabricate the investigated parts. The resin was tested for viscosity and refractive index on a Fungilab viscometer using a L3 spindle and an Abbe Mark II refractometer, respectively. The printing process was carried out on a Formlabs Form 2 SLA unit equipped with a 405 nm laser source, and a 50-micron layer thickness. Here, the resin was printed into different structures as shown in

figure 2.3, using. stl (Standard Tessellation Language) files designed on SolidWorks (CAD software) and sliced by the Formlabs Preform Software.

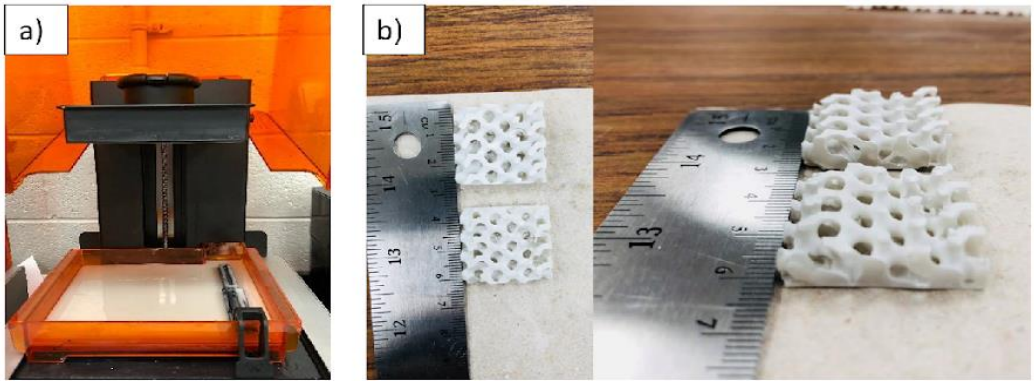

Figure 2.3: Experimental apparatus used in this work. (a) Form labs Form-2 SLA unit, (b) A complex geometry printed on Form labs, in the picture is a ceramic gyroid structure.

The preform software slices the .stl files into layers depending on the resolution, layer thickness, point density along with the type of resin indicated by the user. The support system on samples was added by the software to build the CAD model upside down (see figure 2.4). The build angle is also an important parameter as the liquid resin offers little surface tension and suction while pulling out the part during the recoating step. An optimized angle of 45˚ was suggested by the company, however the angles could be altered according to the part geometry. The samples have shown warpage and shift in the layers due to the Z-scaling.

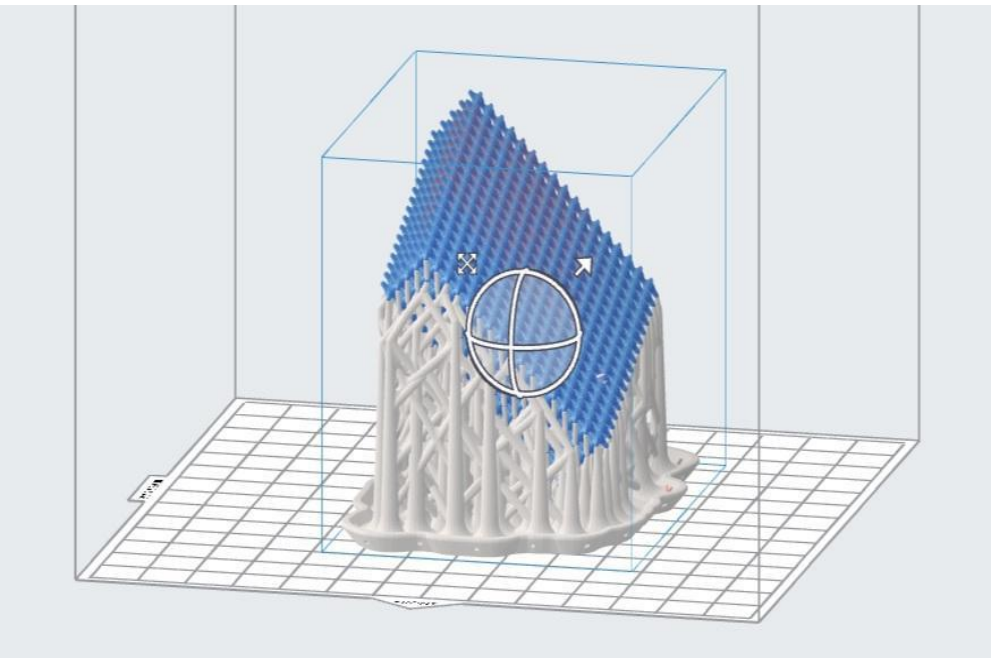

Figure 2.4: CAD .stl files in Preform software showing the support system. The blue section displays the actual part that is sliced to be printed. The bottom white section displays the support system generated for printing the part on Formlabs unit.

The models with support systems were arranged on a build platform of 14.5 cm x 14.5 cm build area with a capacity of building parts of 17.5 cm high. The build platform moves in the vertical direction according to the height of the 3D model whereas a resin tank filled with resin from a resin cartridge moves according to the .stl model. Here, cylindrical, and rectangular samples were printed in the flat XY plane with vertical Z orientations, in a top-down approach at a temperature of 35°C (see Figure 2.5). The printing was carried out at 50µm layer thickness with a laser spot resolution of 140 microns at a 405 nm wavelength. The cylinders and rectangular bars in this research were printed with a support system angled at 90◦which is the optimized angle observed for these flat parts. The printed samples were separated from the build plate and washed in Isopropyl alcohol (IPA) for at least 15 minutes in order to remove the excess resin. The parts were printed by bottom-up approach and thus they required a support system. These “green” parts

were sintered using the profile shown in Figure 2.6, where the samples were subjected to a maximum temperature of 1275°C in air at 1 atm pressure.

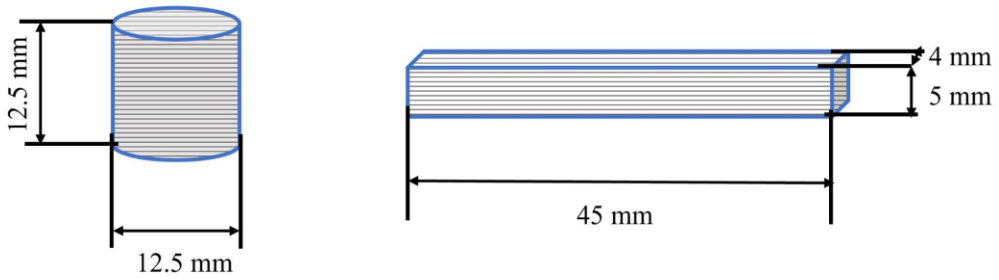

Figure 2.5: Schematic figure of the parts printed on Form labs unit for mechanical testing. The figure shows the orientation that samples were printed on the SLA unit.

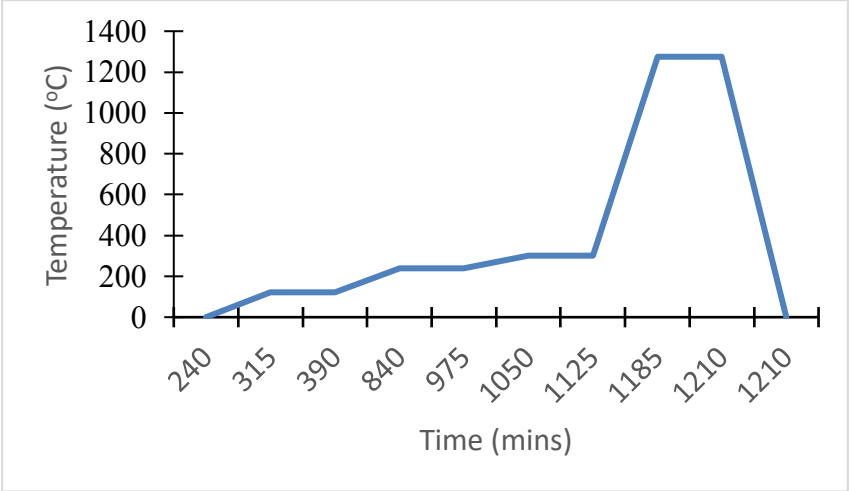

Figure 2.6: Sintering profile actually used on the printed SLA ceramic parts in air at 1 atm to get crack-free samples.

These sintered parts were then transformed into IPC's by submerging them into molten Aluminum (Al) through a proprietary process at Fireline, Inc. (Youngstown, OH) known as TCON where the following reaction takes place, see Equation 2.2.

$$3SiO_2 + 4Al \rightarrow 2Al_2O_3 + 3[Si]Al \qquad (2.2)$$

The specimens were submerged in the molten metal under a constant flow of argon at 1000°C to prevent oxidation and then cooled down to room temperature.

2.3.2. Instrumentation

Green, sintered and transformed parts were initially analyzed for density through the Archimedes principle in water. A TGA study in a TA 550 instrument was also performed on the resin to know the weight % of ceramic suspension. The ceramic particle size of the suspended powder was measured by a CILAS laser particle size analyzer that was capable of measuring the particle sizes up to 10 nm using a laser light source. The porosity of the samples in the cured and the sintered stages was measured using the MATLAB code, "graythresh" where the image was assigned with 0's and 1's for voids and particles, respectively [56]. The image after graythreshing contains the binary codes, and the percentages of each code represents the percent of voids and particles present in the image, respectively. At least 5 high-resolution images were used on each sample to calculate the porosity in the present work. The samples were then tested for mechanical strength at room temperature following ASTM standards on an Instron Universal Testing Machine. The compressive strength of the samples was tested at a strain rate of 1 mm/min following the ASTM C1424. Flexural strength was calculated using a 3-point bending set-up following ASTM C1161. Vickers Hardness testing was performed on the sintered and transformed parts using a Nanovea Hardness Testing equipment. A diamond tip (Barkovich, conical shape) indenter was used to indent the samples with 50 mN force. Following the mechanical testing, the samples were also tested for the linear coefficient of thermal expansion. The Coefficient of Thermal Expansion (CTE) of the samples was measured on a TA Q-400EM system following the ASTM E831. Optical examination to estimate porosity, microstructure and fracture mechanism was also included in this thesis. A Keyence VHX-7000 optical microscope and a Keysight FE-SEM equipped with EDS were used to evaluate the microstructural features of the samples. Green, sintered and transformed samples were analyzed to assess the build quality of the samples and composition. A Bruker X-Ray

Diffractometer equipped with a 40keV X-ray beam was used to observe the change in the crystallography of the samples at different stages. The samples were scanned under X-rays with a step rate of 0.02˚ for 30 seconds. Each scan was performed with a diffraction angle between 2θ =0˚ and 105˚ (see Appendix A1).

2.4: Results and Discussion

The as-received ceramic resin from Formlabs Inc., was tested for viscosity and refractive index before printing any samples. The resin had a 61.8 vol% fused silica suspended that was determined from the TGA analysis. This ceramic loading still stands on a higher suspended particles ratio resulting in a higher viscosity and the requirement for a high cure depth to obtain parts without delamination [57, 58]. A rotating spindle was used to measure the kinematic viscosity. In this process, the shear stress created by the rotation of the L3 spindle at a speed of 6 rpm was measured to be 5260 mPa.s at room temperature (25˚C). The obtained viscosity was taken under laminar flow, where the viscosity represents a relative mechanical turbulence [59]. The resin showed a shear-thinning behavior; thus when the printing started at 35˚C, the viscosity decreased enabling the recoating of the layers in the printing process [60]. The refractive index (RI) of the resin was affected by the kind of powder suspensions and the type of resin used. For the sake of photopolymerization, the cure depth, C_d should be smaller than the layer thickness for proper bonding and therefore, smaller RIs are always beneficial for the printing process [61]. A RI value of 1.6 was determined on the evaluated ceramic resin.

The chemistry of the resin was analyzed from the NMR spectra (see Figure 2.7). The spectrum shows R2-N groups, R-O-CH groups, RCH=CHR at ~ 2 ppm, 4 ppm and 6 ppm chemical shifts respectively. The peaks shown in the figure 2.7 correspond to Cd_3OD, NMR solvent used in this experiment.

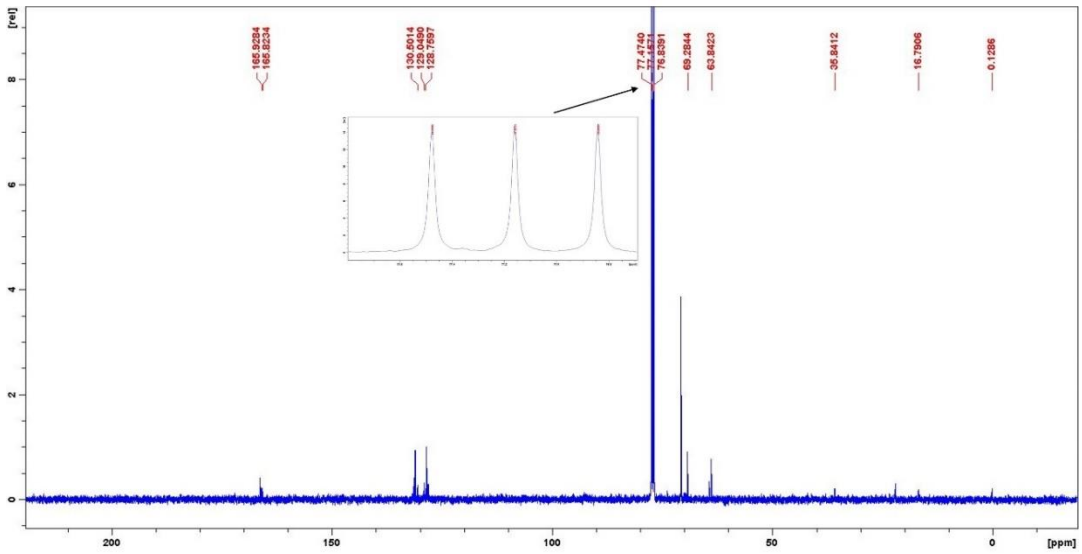

Figure 2.7: NMR spectrum of Formlabs Ceramic Resin.

A light source hardens the C=C to C≡C as well as replace the Van der Waals bonds from the monomer groups into a cross-linked polymer. The oligomers, consisting of a few units of monomers aid in forming the covalent bonds to induce polymerization under an UV-light source. The polymerization took place by a cationic mechanism [62].

The particles suspended in the resin were determined to be fused silica particles of an average size of 39.18 µm with a standard deviation of 17.46 µm (see Figure 2.8).

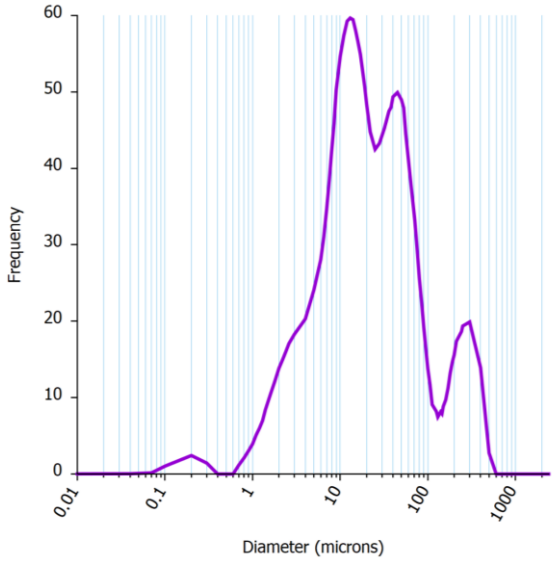

Diameter at %	d_{10}	d_{50}	d_{90}
Particle size (μm)	3.49	20.35	84.09

Figure 2.8: Particle size distribution of silica, the suspended powder in Formlabs resin.

2.4.1. Curing:

The samples were air dried after washing them in IPA and debinded at 400°C in air. At this stage the resin in the ceramic SLA samples evaporate leaving behind the ceramic samples in the built geometry (see Figure 2.9). This study involved heating up the samples up to 400°C in air at normal atmospheric pressure with different ramp rates: 1°C/min, 2°C/min and 5°C/min. Different ramp rates were set to understand the curing process that could lead to crack-free parts. As seen from the figure 2.10, the samples cured at lower ramp rates i.e., 1°C/min have shown lower number of cracks when compared to the samples cured at higher ramp rates (~2°C/min, 5°C/min). It was also observed that the silica printed samples when cured at 5°C/min turned flaky with loose particles and were easily destroyable. Studies by Kim et al [63] on sintered silicon carbide have resulted in similar features (procurement of high density specimens) when cured at low ramp rates.

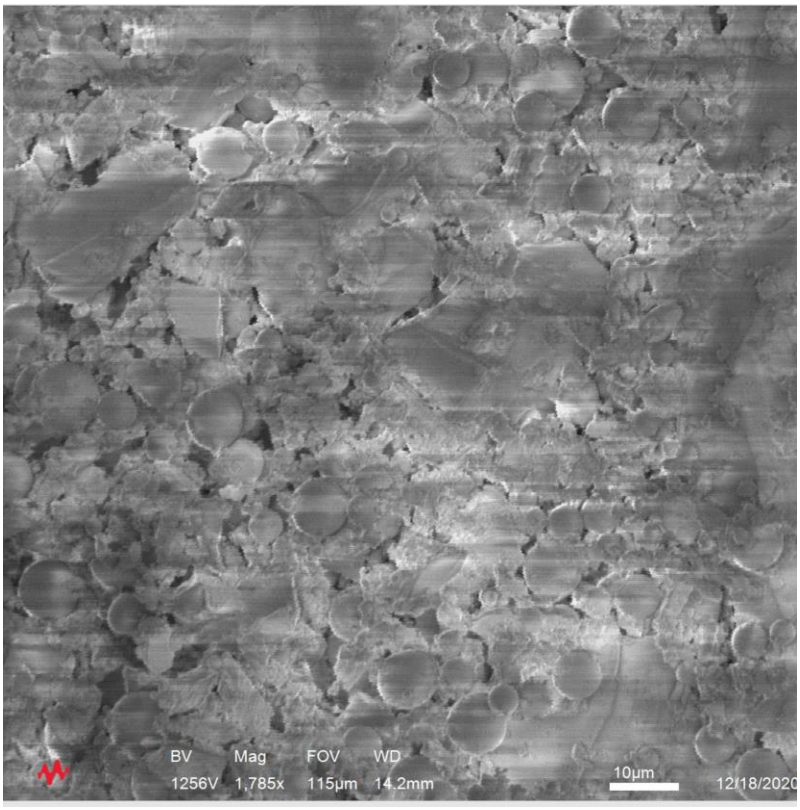

Figure 2.9: Surface of the sample cured at 400°C. The SEM image shows the unbound silica particles after the resin was burnt off.

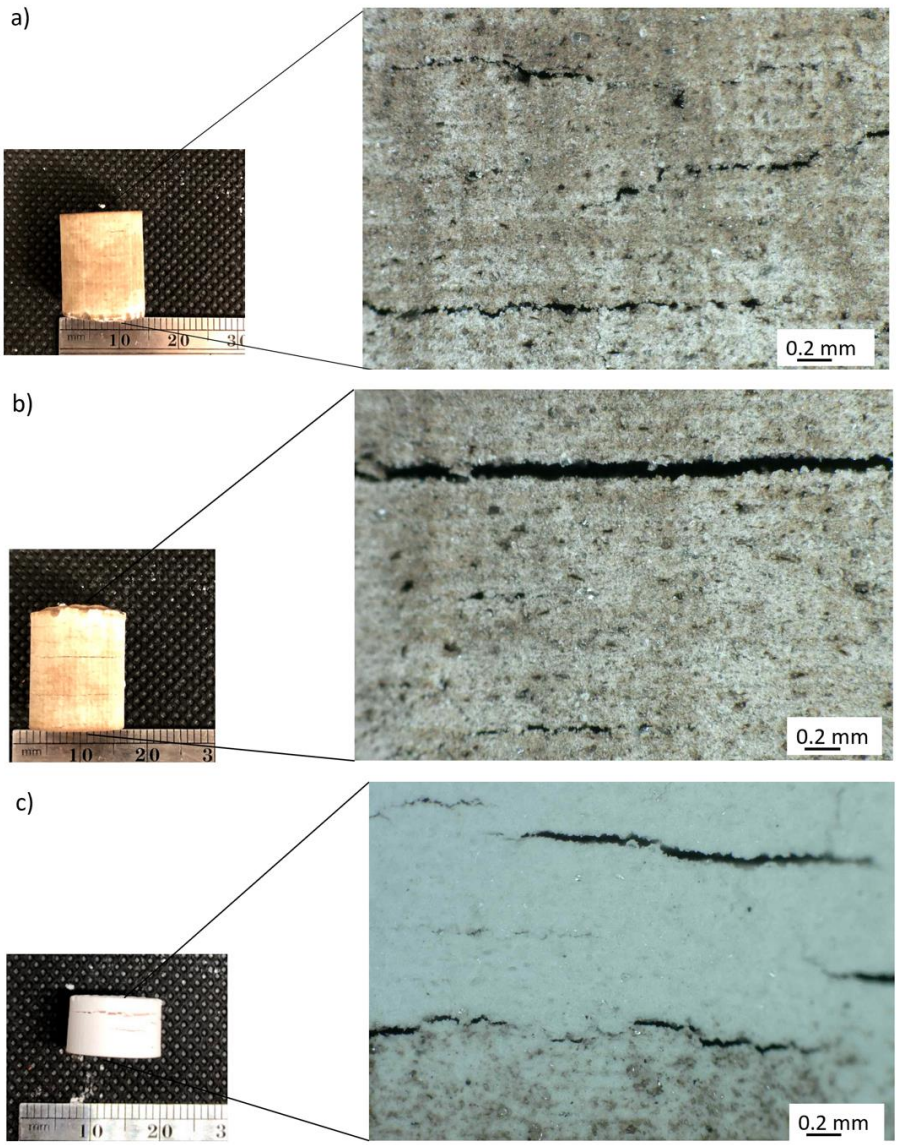

Figure 2.10: Microscope images of the samples cured at 400°C in air at 100X magnification. (a) at 1°C/min. b) at 2°C/min. (c) at 5°C/min.

The cooling stage also seems to affect the presence of cracks on the cured ceramics. It was observed that slowing the cooling ramp during the curing process resulted in fewer cracks than in those samples subjected to relatively fast cooling ramps (see figure 2.11). From the results seen in this work on cooling rates, it was understood that cooling rates play an important role in the sample densification. Tang et al [63] have reported similar results, where cooling rates played an important

role for the part densification. This mechanism was related by them to the thermal diffusivity of the material.

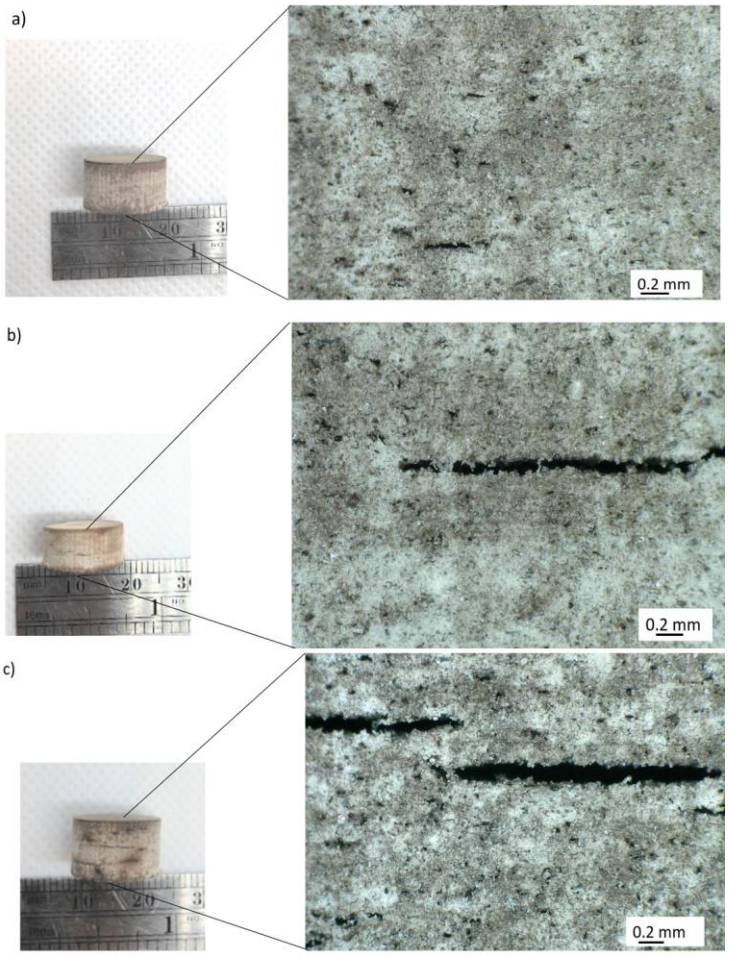

Figure 2.11: Microscope images of the samples cured at 400°C and cooled with a controlled ramp rate at 100X magnification. (a) at 1°C/min. (b) at 2°C/min. (c) at 5°C/min. The image also shows the delamination seen in the samples at different cooling rates.

The shrinkage of the cured parts has also been investigated in this work. Table 2.1 shows the average shrinkage measured in the samples after curing. It was here observed that the samples shrunk less than 2%, suggesting a limited contraction during the curing stage.

Table 2.1: Shrinkage presented by SLA printed parts after curing at 400°C.

Direction	Shrinkage (%)
X	1.13
Y	1.71
Z	1.19

The porosity was also recorded after the curing process. It was calculated after processing high-magnification images to a binary "graythresh" MATLAB code (see figure 2.12) [56]. The code showed that the samples had approximately 29% porosity. Similar results have been reported by Fu et al [64] when they tested the SLA printed samples for debinding and sintering analysis using a laser sintering method at different powers on Zirconia samples. They have associated the porosity with the debinding process and the printing parameters. Along with this, a reduction in weight and decrease in density were observed at the debinding stage. A similar decrease was observed in this work when the samples were debinded at 400ºC (see figure 2.17).

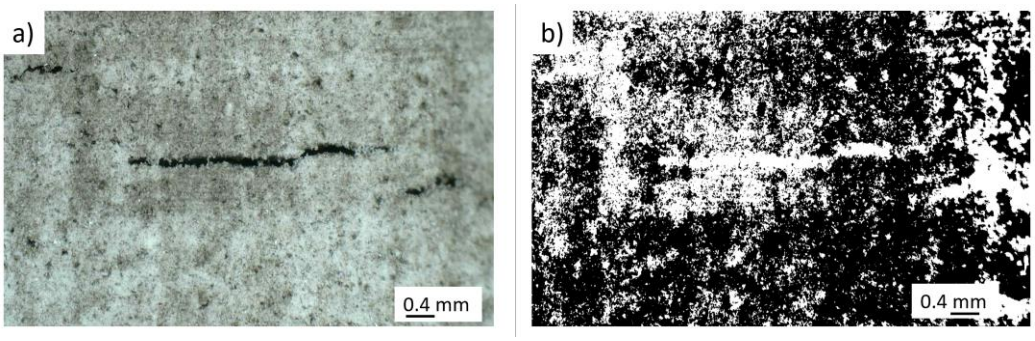

Figure 2.12: Microscope images of a sample cured at 400°C at 2°C/min at 50X magnification. (a) Actual image. (b) Graythresh image of the cured sample where the white speckles represent the particle after curing (right).

2.4.2. Sintering:

After curing the samples, these were sintered at 1275°C in air at 1 atm pressure for 25 minutes. A variability in the ramp rate was included during the sintering cycle where the ramp rates varied

among 2°C/min, 5°C/min and 10°C/min while air cooled (see Figure 2.13). As seen from figure 2.13, unlike the curing results, samples sintered with lower ramp rates still had delamination in the layers. However, the samples sintered in 5°C/min resulted in samples with relatively lower delamination with only 15 microns width whereas samples in 2°C/min, 10°C/min exhibited a delamination width of 78 microns and 95 microns respectively. Moghadam et al [65] showed similar results when refractory based ceramics are sintered at different heating rates. A higher mechanical strength and low porosity, shrinkage was reported in the samples when sintered at lower strength when the samples were sintered with high heating rates.

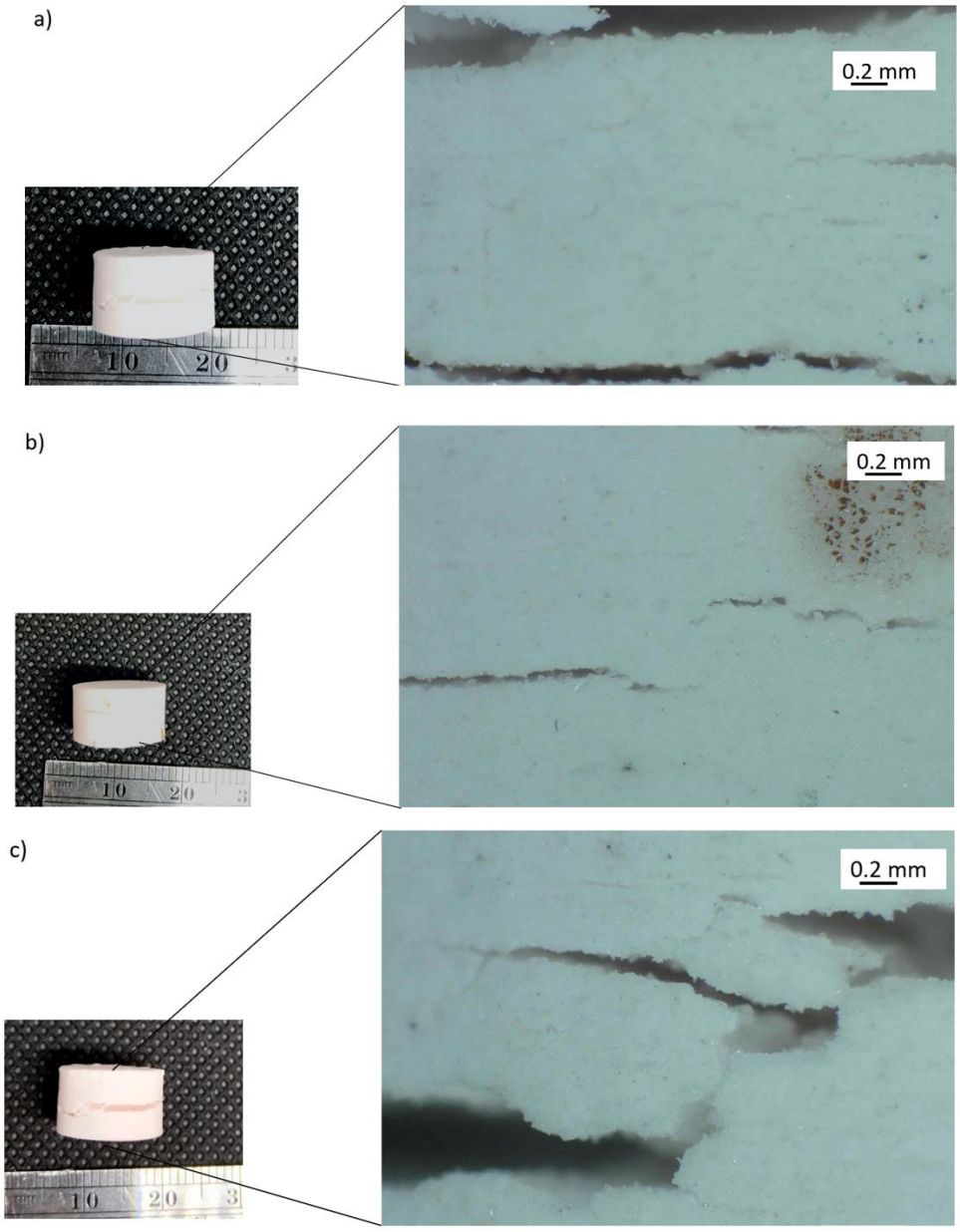

Figure 2.13: Microscope images of the samples sintered at 1275°C in air at 100X magnification. (a) at 2°C/min. (b) at 5°C/min. (c) at 10°C/min.

After the samples were sintered, shrinkage in all the directions was observed (see Table 2.2). Unlike the curing stage, the samples showed a higher degree shrinkage. Here, the Z direction showed the largest shrinkage, a mechanism associated with the printing parameters and layer arrangement,

adhesion [64]. Similar results have been recorded by Liravi et al [66] after performing the sintering studies.

Table 2.2: Shrinkage presented by SLA printed parts based on silica after sintering at 1275°C for 25 minutes at 10°C/min 1 atm pressure.

Direction	Shrinkage (%)
X	12.41 ± 1.59
Y	18.45 ± 3.06
Z	19.65 ± 2.14

The sintered samples were also evaluated with the binary graythresh code in MATLAB, and it was found that they displayed about 30% of porosity even after subjecting the silica samples to near fusion temperatures (see figure 2.14). The image shows the graythresh picture along with the sintered surface on which the binary encoding was made.

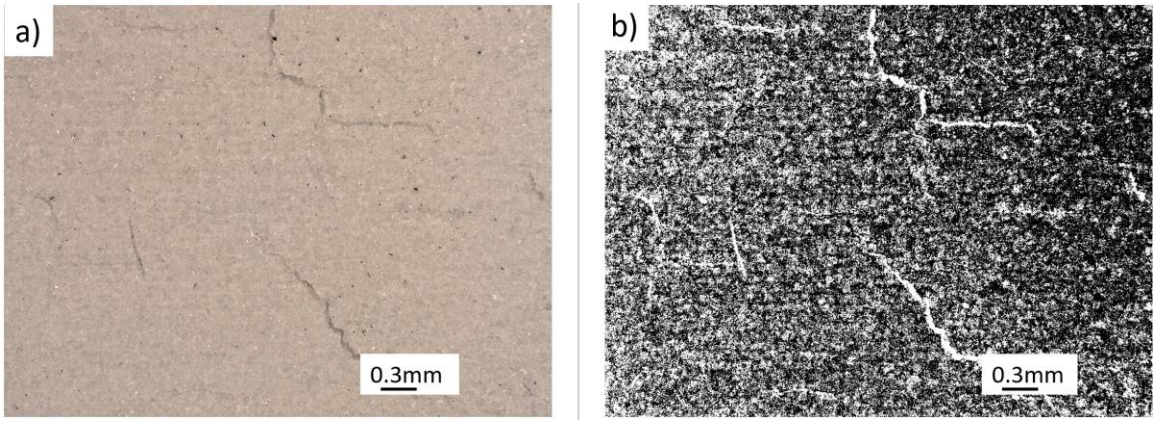

Figure 2.14: Microscope image of a sintered silica sample at 50X magnification. (a) Actual image. (b) Graythresh image of the sintered sample where the white spots refer to the pores present in the sintered sample (right).

As the samples were sintered at different ramp rates the change in crack length was recorded in this work, as it is in Figure 2.15. Nevertheless, the number of cracks and the crack size reduced from

the curing stage to sintering stage. High magnification images show a reduction in the crack length by 30% and number of cracks that appeared after the sintering stage, (see Figure 2.15). This crack reduction seems to be associated with the diffusion mechanism of the silica particles at high temperatures [67]. Figure 2.16 shows the SEM images of the surface of printed samples in green and sintered stages.

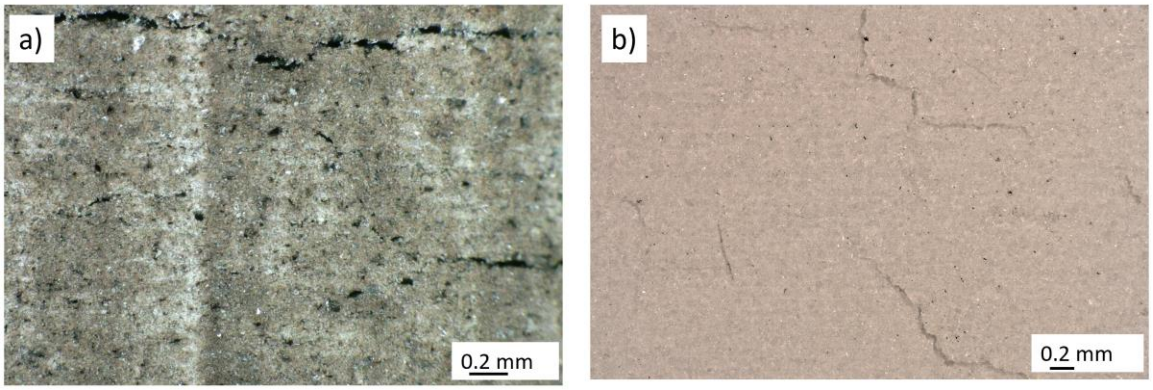

Figure 2.15: Microscope image of samples at 100X magnification showing a reduction in cracks from cured to sintered stage. (a) Surface of the samples after curing at 400°C at a curing rate of 2°C/min and cooling rate of 2°C/min. (b) Surface of the sample after sintering with a heating rate of 5°C/min and air cooled.

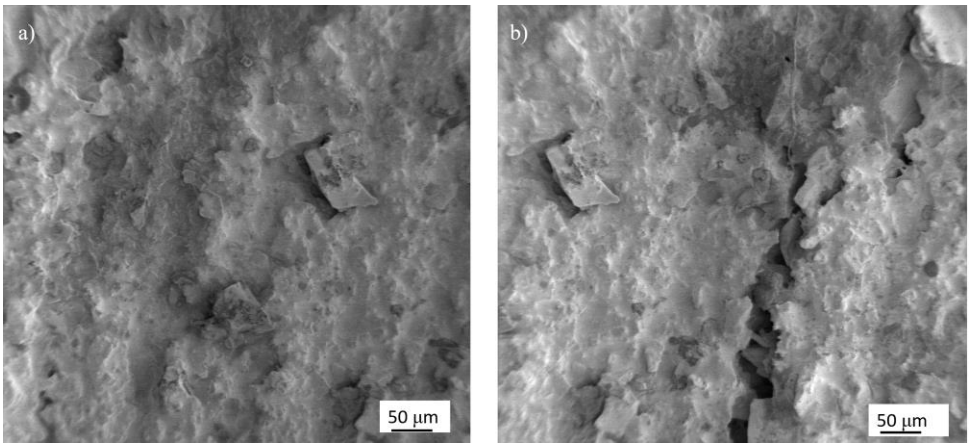

Figure 2.16: Surface of the samples sintered at 1275°C. (a) SEM image of the sintered sample. (b) The image shows a crack that shrinked during sintering.

The samples in the green state showed a density of 1.6 g/cc when tested using Archimedes principle. The density slightly lowered when all the resin is burnt when cured at 400°C and the unbound silica particles when sintered at 1275°C, diffused. The diffusion eventually led to an increase in the density (see figure 2.17). From this it can be suggested that a two-step process of curing and sintering can result in strong samples with lower number of defects. Besides, a low ramp rate in the curing stage and relatively high ramp rates in the sintering stage would work best for parts with resin.

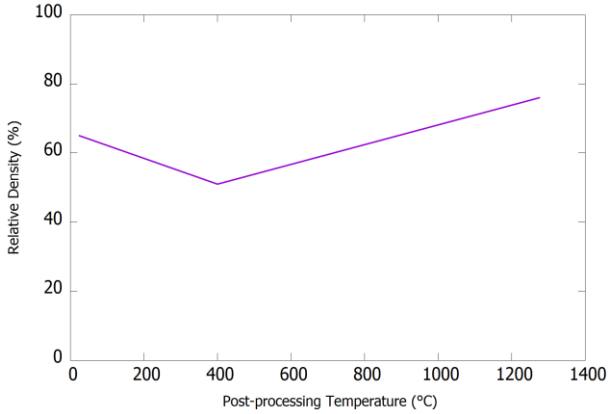

Figure 2.17: Relative density of the printed samples at different temperatures.

2.4.3. Transformation to IPCs:

After the samples were sintered, these were transformed into IPCs at Fireline Inc., by submerging them in molten metal by a TCON process in the flow of Argon gas. During this process, the samples underwent a chemical wetting process where the ceramic oxide acts as a backbone for the metal-ceramic composite. The transformed printed ceramic samples are shown in figure 2.18, where it can be observed that a near-shape conformation was obtained A closer examination displayed the presence of the continuous aluminum phase, indicated by the light grey zones, and the alumina phase, shown in dark gray color (see Figure 2.19). The samples also displayed a strong particle coalescence in the transformed stage and a strong network between Alumina and Silica (see figure 2.19). The figure also shows porosity in the system; however, the degree of porosity was considerably lower than those IPCs reported from binder jetted ceramic templates [50], suggesting

that the contact angle for wetting was greater than 90˚ [68]. Here, the density of the transformed samples was 3.30 g/cm^3, a value 0.66 g/cm^3 larger than that reported by Kyle et al [50]which were of the same composition printed via Binder Jetting. The SEM pictures of the transformed samples show the porosity and the Silica particles that were left behind after the transformation process figure 2.20 and 2.21 (b).

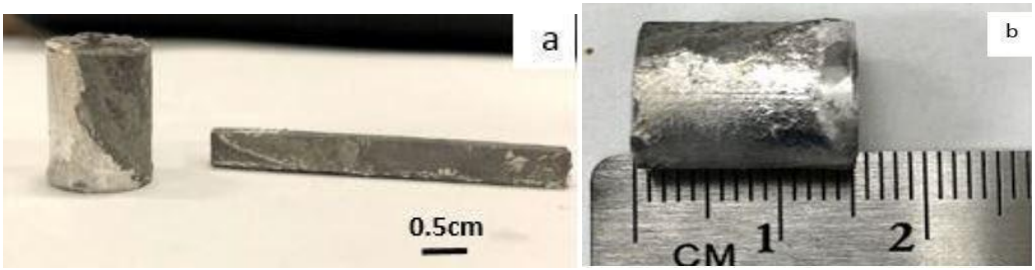

Figure 2.18: Transformed printed ceramic samples into interpenetrated phase composites (IPCs). a) cylindrical and rectangular samples used for the mechanical and thermal analysis. b) Low magnification of a transformed cylinder.

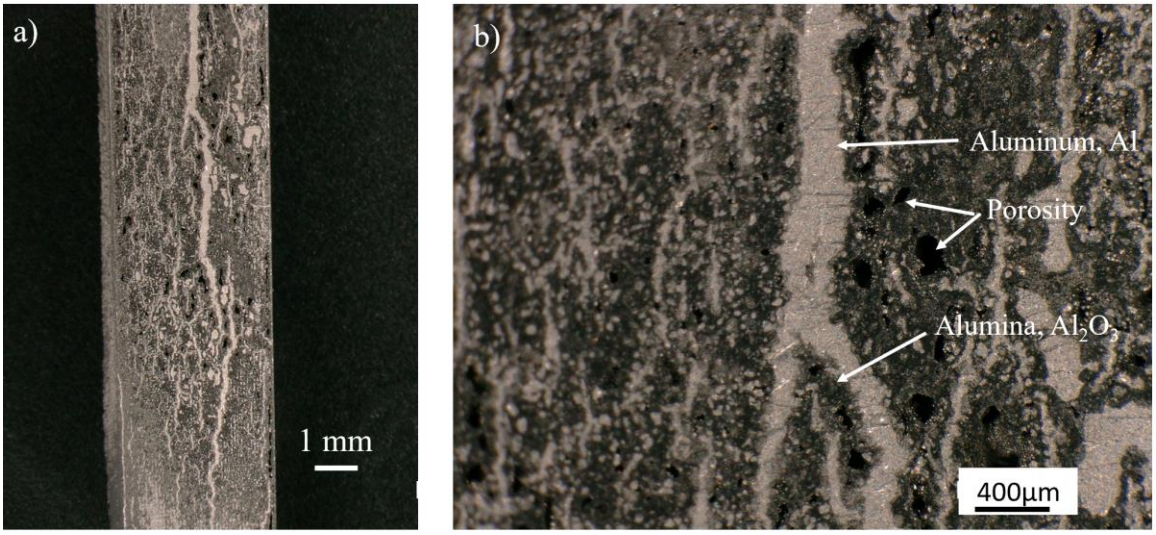

Figure 2.19: Optical micrographs of the transformed 3D printed ceramic samples into interpenetrated phase composites. (a) A micrograph of the infiltrated flexural sample at 30X. (b) A higher magnified image of the infiltrated sample showing a network of Aluminum and Alumina along with porosity.

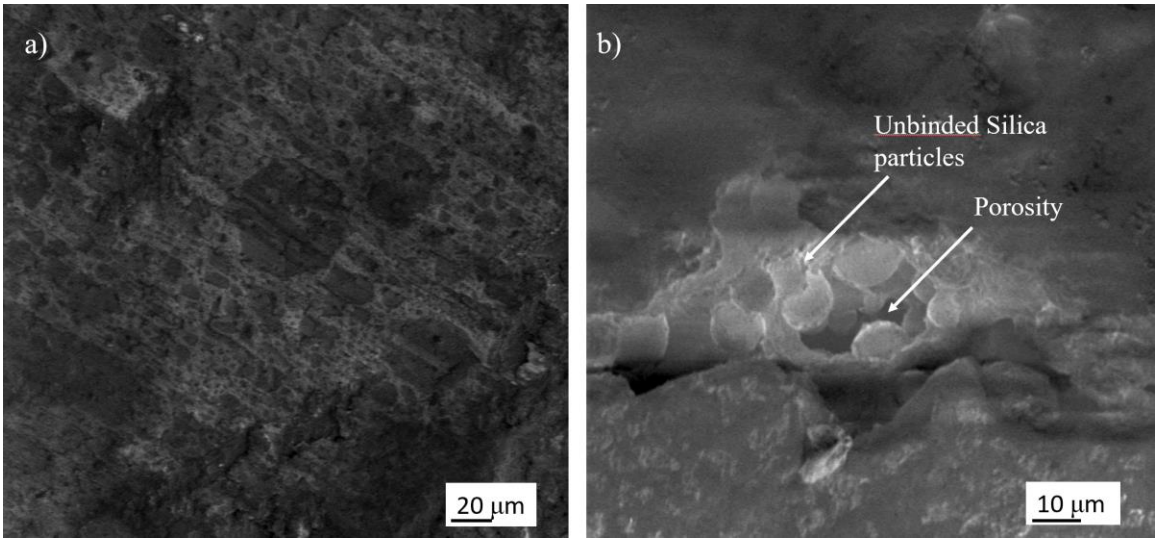

Figure 2.20: Surface of the transformed samples. (a) A low magnification SEM image of the transformed sample showing a contrast between the Alumina and Aluminum. (b) A high magnification SEM image showing unreacted silica resulting in porosity and a weak point leading to fracture.

An XRD analysis performed on the transformed ceramic parts revealed that the samples were composed of 42.1% of monoclinic alumina (Al_2O_3), 37.3% cubic aluminum (Al), 14.3% tetragonal silicon (Si), and 6.2% cubic silica (SiO_2), (see Figure 2.21). Included in figure 2.19, is the XRD of the sintered printed silica, which shows cristobalite and quartz phases. An EDS analysis was also performed on the transformed parts (see Figure 2.21); and it was observed that the parts were constituted by 51.77% Al, 47.21% O and 1.02% Si, a structural composition that appears to support the finding provided by the XRD.

a)

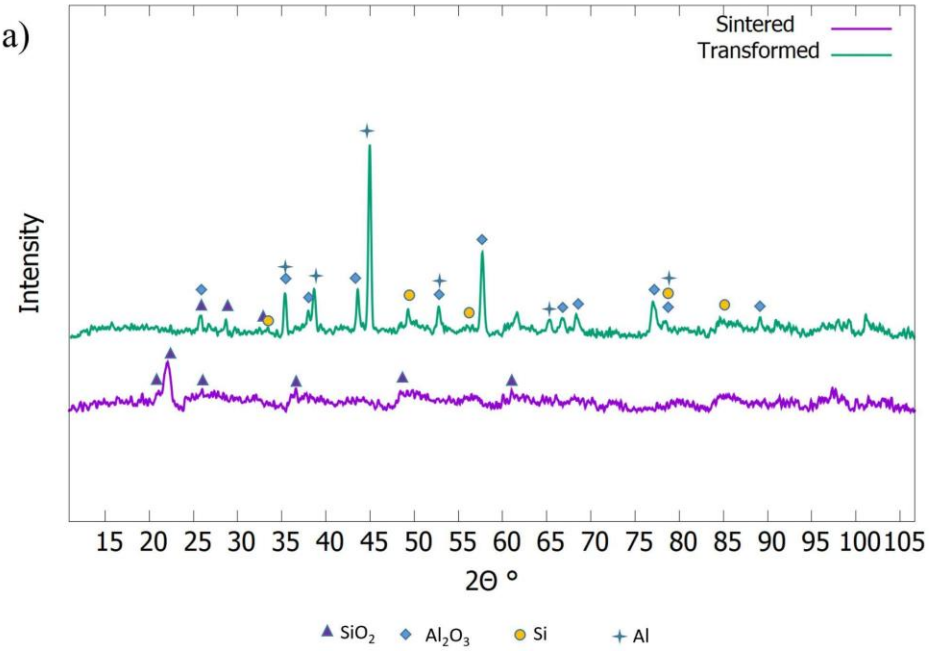
Sintered
Transformed
Intensity
15 20 25 30 35 40 45 50 55 60 65 70 75 80 85 90 95 100 105
2Θ °
SiO2
Al2O3
Si
Al

b)

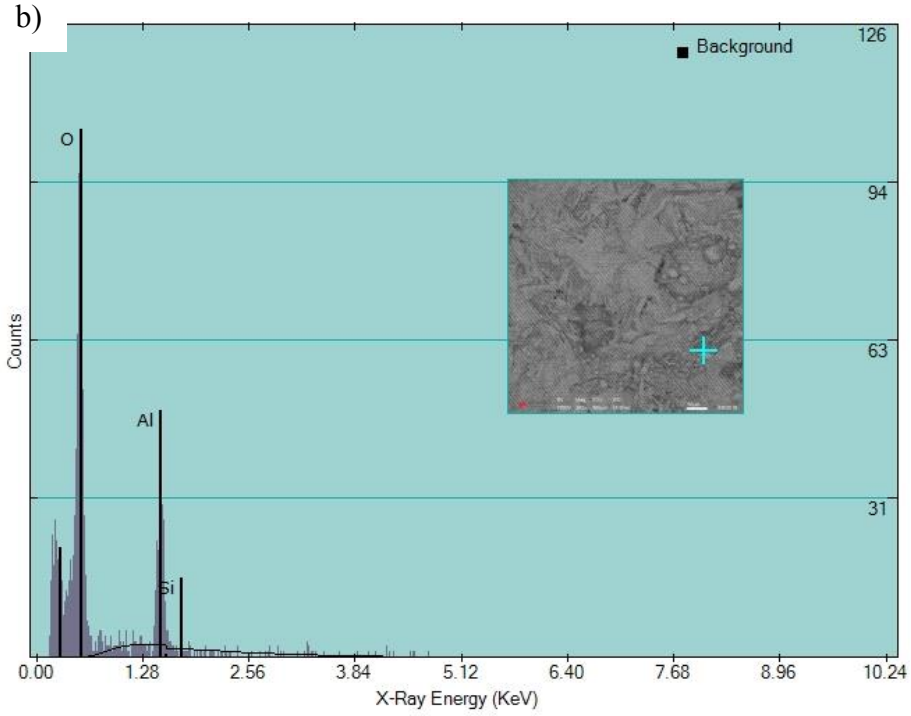
Background
126
94
63
31
O
Al
Si
Counts
0.00 1.28 2.56 3.84 5.12 6.40 7.68 8.96 10.24
X-Ray Energy (KeV)

Element	Weight %	Std. Dev.	Atomic %
O	66.66	4.18	77.14
Al	32.77	3.33	22.48
Si	0.57	0.54	0.37
Total	100.00		

Figure 2.21: Analytical test results of the sintered and transformed samples from this work. (a) XRD patterns of sintered and transformed samples. The image also shows the different elements present in the sintered stage and their transformation after the infiltration process. (b) EDS spectrum of the transformed sample at a fractured location. The spectrum shows the presence of Al, O and Si and below is the table describes the atomic weight % of the elements.

Here, a Thermo-Calc software, which used the composition weight % obtained from the EDS, was used to predict the phase diagrams of the transformed samples. These results were validated with the XRD. From figure 2.22(a) the samples had a negative Gibbs energy along the high temperatures throughout the reaction. The samples had the cristobalite phase of Silica and monoclinic alumina. This negative Gibbs energy (-320 KJ) was responsible for the red-ox reaction (Equation 2.2) to take place to produce Al_2O_3 and Al. During this reaction, the Silica particles act as reducing agent for the molten metal (aluminum). The infiltration takes place by capillary forces, which infiltrates the porous ceramic material [69]. In addition, figure 2.22(c) shows the amount of Al in all the phases of Silica as a function of the temperature. In this work, the silica presented a cristobalite phase around 1200ºC to 1500ºC, with an aluminum content of about 0.26-0.28.

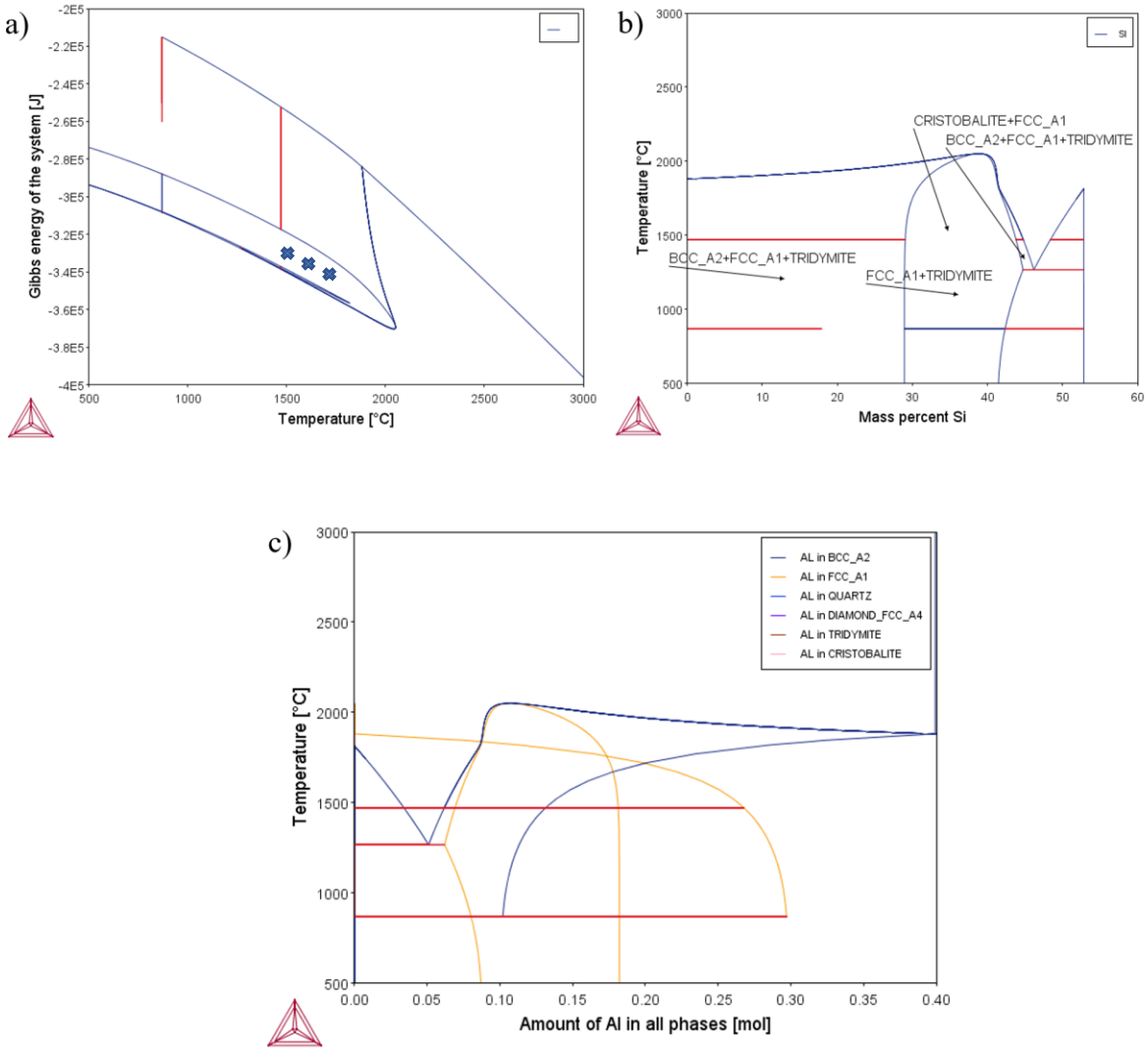

Figure 2.22: Phase diagrams shown for Al_2O_3-SiO_2 system from Thermo-Calc. (a) Gibbs free energy vs Temperature. (b) Phase diagram displaying mass % of Si vs Temperature. (c) Amount of Al present in each phase in the composite with respect to temperature.

Following the XRD and microscopic analysis of the samples, in all three categories; green, sintered, and transformed parts were evaluated under compressive and flexural conditions. It was observed here that the samples displayed a linear profile in the compressive stress-strain testing (see figure

2.23). The ceramic samples both in green and cured phases displayed a brittle failure while the transformed samples showed a shear fracture when tested in the vertical direction (Z).

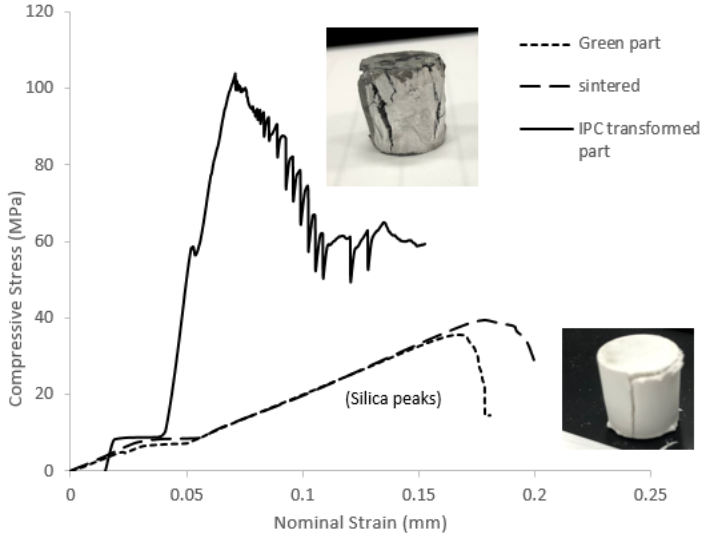

Figure 2.23: Stress-strain graphs shown by green, sintered and transformed samples [29].

The sintered ceramic samples showed an average compressive strength of 22 MPa, while the transformed samples yielded an average value more than four times higher than the sintered specimens (97MPa).

3-point flexural testing showed similar failure profiles than those observed under compression. A flexural strength of 21, and 92MPa was recorded for the sintered and transformed samples, respectively. It was here recorded that the strength of the transformed samples was more than two times higher than the strength obtained in the green and sintered samples printed in this research (see, figure 2.24). Optical microscopy showed that the flexural samples failed with a diagonal profile-fracture showing no traces of ductility. This fracture mechanism was observed in both the sintered and transformed specimens printed in the Y direction (see figure 2.25).

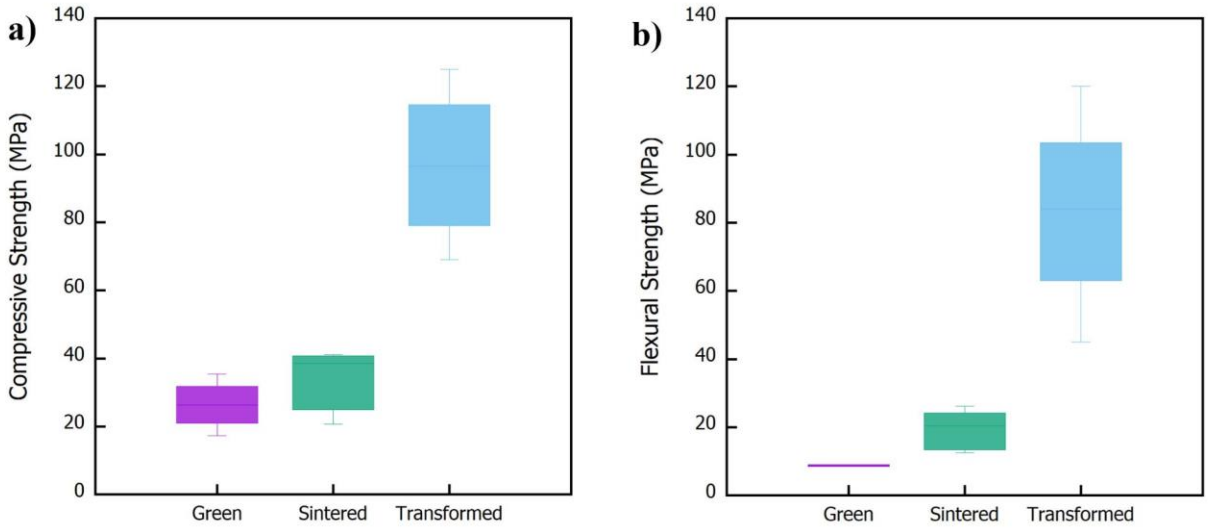

Figure 2.24: A comparison chart of mechanical strength of samples printed via SLA in green and sintered stages along with the sample strength after the infiltration process. (a) Compressive Strength. (b) Flexural Strength.

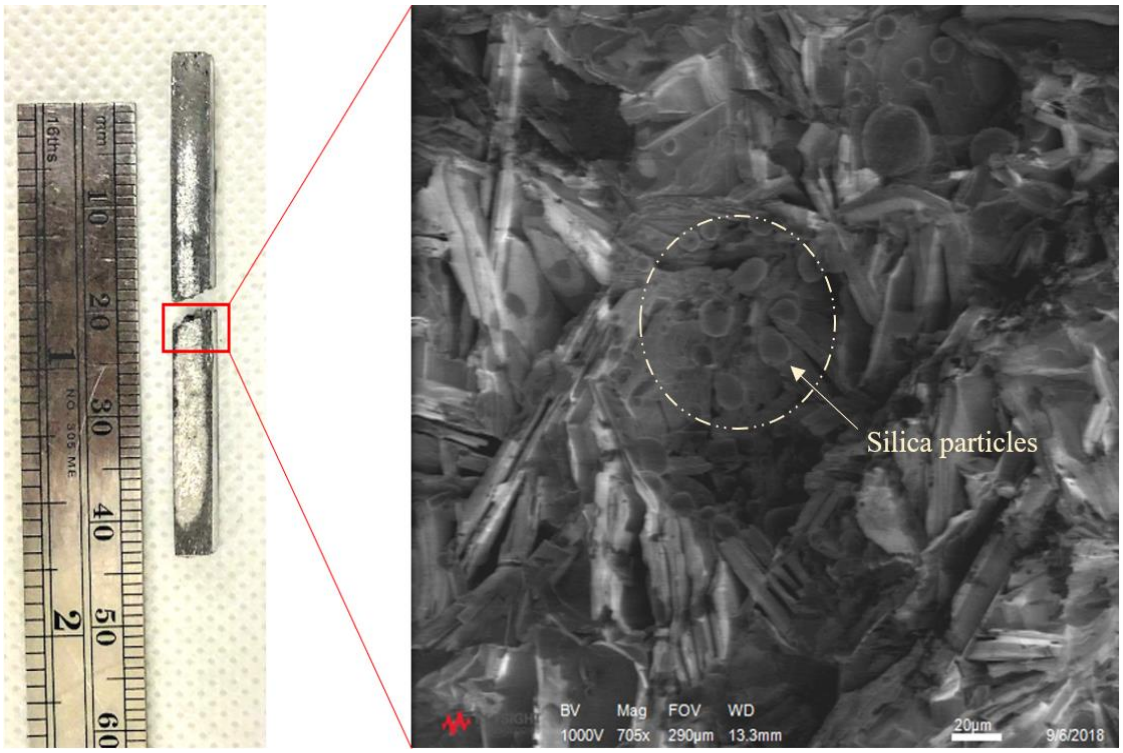

Figure 2.25: The fractured surface of the transformed sample. The sample shows a diagonal brittle failure. The magnified image shows some non-transformed silica particles.

From literature, the present samples have shown a higher strength than the transformed samples printed via Binder Jetting. It was recorded that the strength was higher by 2.6 times than similar composites printed via Binder Jetting [50].

Vickers Hardness testing was also performed on the sintered and transformed specimen, and the results were shown in Figure 2.26. From the figure, it was observed that the metal-ceramic composite resulted in a hardness greater than the observed on the sintered ceramic parts; a feature associated with the formation of continuum on the transformed parts. Here, any porosity from the sintering stage was filled out by the aluminum. The hardness of the composites appears to fall between the variability range reported on 3D printed ceramics such as alumina [67].

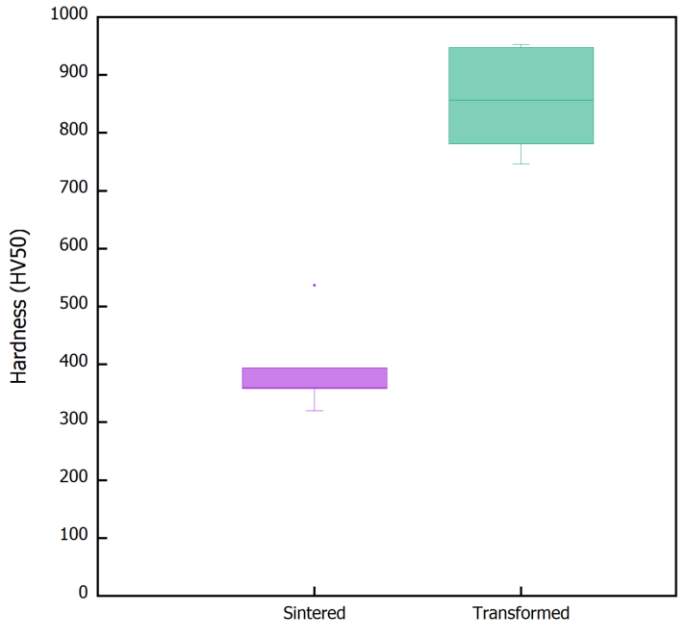

Figure 2.26: Hardness results of the sintered and transformed ceramics.

The Coefficient of Thermal Expansion (CTE) of the sintered and transformed 3D printed ceramics was evaluated in this research work (see figure 2.27). It was found that the CTE of the sintered parts yielded a value of about 24 $x10^{-6}$ K^{-1}, which is considerably higher than the reported CTE

values of silica samples built via conventional methods [70]. These results could be associated with the presence of cracks in the sintered samples, which could have interfered with the thermal conduction. In contrast, the CTE of the transformed parts resulted in an average value of 11.02 x 10^{-6} K^{-1}, which was two times lower than the aluminum alloy used on current composite tooling molds [71]. This is an attractive thermal performance for the composite tooling production field, since these materials can support high operational temperatures.

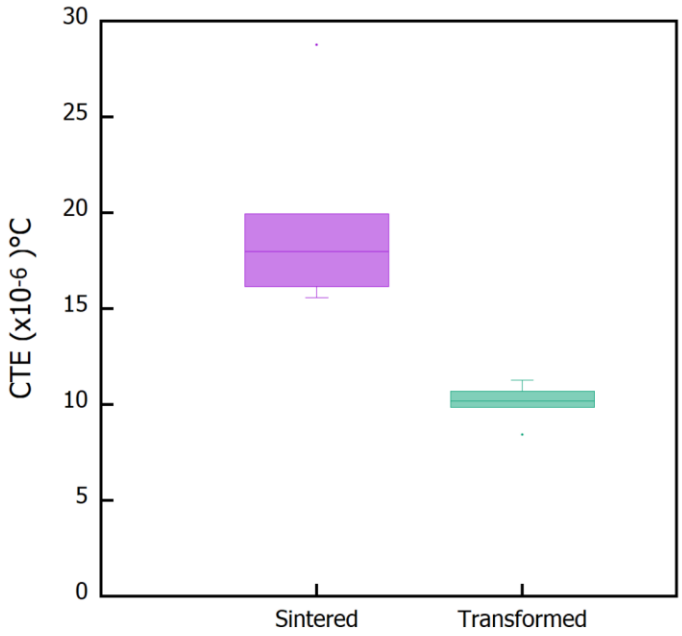

Figure 2.27: Averaged CTE results of sintered and transformed samples tested between 25°C and 500°C.

2.5: Conclusions

The transformation of the SLA printed ceramic samples to produce Interpenetrating Phase Composites (IPC's) seems to be a novel method which resulted in composite structures with good mechanical properties. The manufactured composites resulted in a compositional conformation of 42.1% alumina (Al_2O_3), 37.3% aluminum (Al), 14.3% silicon (Si), and 6.2% silica (SiO_2). The mechanical testing showed that the compression and flexural strength of the metal-ceramic composites were more than 2.6 higher than the recorded on the printed ceramics on their sintered

state. It has been shown that the mechanical performance of these interpenetrated composites is superior to that observed-on 3D printed transformed composites manufactured via binder jetting. The hardness testing also showed that the composites offer a superior hardness performance than shown by the sintered ceramics. It has also been shown that the coefficient of thermal expansion of the transformed ceramics is at least two times lower than the current composite tooling molds based on an aluminum alloy. A feature of interest in the production of carbon fiber reinforced epoxy systems. The current work suggests that these new composites could represent a promising structure for applications in transportation where complex configurations based on low volume production are required.

The future work includes testing these samples for high and low impact velocities and the performance when lattice structures are created in this method. This work reveals that the technique can be promising to build structural components.

2.6: References

1. ISO - ISO/ASTM 52900:2015 - Additive manufacturing — General principles — Terminology. https://www.iso.org/standard/69669.html. Accessed 15 Nov 2019
2. Photopolymerization - VAT, SLA, DLP, CDLP | Make. https://make.3dexperience.3ds.com/processes/photopolymerization. Accessed 16 May 2020
3. Licari JJ, Swanson DW (2011) Chemistry, Formulation, and Properties of Adhesives. In: Adhes. Technol. Electron. Appl. Elsevier, pp 75–141
4. Decker C (2011) UV-radiation curing of adhesives. In: Handb. Adhes. Surf. Prep. Elsevier Inc., pp 221–243
5. Khorram Niaki M, Nonino F (2018) What Is Additive Manufacturing? Additive Systems, Processes and Materials. pp 1–35
6. Reynolds GL (2006) Stereolithographic apparatus.

7. Ashley S (1994) Prototyping with advanced tools. Mech Eng 116:48
8. Mikhail PAVLOV, Matthias Hoebel, Felix ROERIG, Julius SCHURB (2019) EP2893994A1 - Method for manufacturing a metallic or ceramic component by selective laser melting additive manufacturing - Google Patents.
9. Kaza A, Rembalsky J, Roma N, Yellapu V, Delong W, Stawicki S (2018) Medical applications of stereolithography: An overview. Int J Acad Med 4:252
10. Bhargav A, Sanjairaj V, Rosa V, Feng LW, Fuh YH J (2018) Applications of additive manufacturing in dentistry: A review. J Biomed Mater Res - Part B Appl Biomater 106:2058–2064
11. Commercial, Professional, & Industrial 3D Printers | Stratasys. https://www.stratasys.com/3d-printers. Accessed 16 May 2020
12. Plastic 3D Printers I 3D Systems. https://www.3dsystems.com/3d-printers/plastic. Accessed 16 May 2020
13. Industrial 3D printing solutions | voxeljet. https://www.voxeljet.com/. Accessed 16 May 2020
14. 3Shape Dental System® - an Integrated CAD/CAM Solution for Labs. https://www.3shape.com/en/software/dental-system. Accessed 20 Nov 2020
15. Designing For 3D Printing Jigs and Fixtures. https://www.innosek.com/post/designing-for-3d-printing-jigs-and-fixtures. Accessed 20 Nov 2020
16. Online MJF 3D Printing service | Functional prototypes & low-run production parts | Get an instant quote | 3D Hubs. https://www.3dhubs.com/3d-printing/processes/mjf/. Accessed 4 May 2020
17. John W. Halloran;, Michelle Griffith, Tien-MinChu (2000) US6117612A - Stereolithography resin for rapid prototyping of ceramics and metals.
18. Griffith ML, Halloran JW (2005) Freeform Fabrication of Ceramics via Stereolithography. J Am Ceram Soc 79:2601–2608

19. Griffith ML, Chu TM, Wagner W, Halloran JW (1995) Ceramic Stereolithography for Investment Casting and Biomedical Applications. In: Int. Solid Free. Fabr. Symp. Texas ScholarWorks, University of Texas at Austin, pp 25–30

20. Yang L, Miyanaji H (2017) Ceramic Additive Manufacturing: A review of Current status and Challenges. In: 28th Annu. Int. Solid Free. Fabr. Symp. Center for Materials Science and Engineering, Mechanical Engineering Dept. and Chemical Engineering Dept., University of Texas at Austin, Austin, TX, pp 652–679

21. Davis J. Fred MRG (2011) Polymeric Materials for Rapid Manufacturing. In: Bártolo P (ed) Stereolithography Mater. Process. Appl., 1st ed. Springer Science & Business Media, pp 113–140

22. Andrzejewska E, Andrzejewski M (1998) Polymerization kinetics of photocurable acrylic resins. J Polym Sci Part A Polym Chem 36:665–673

23. Yao H, Wang J, Mi S (2017) Photo Processing for Biomedical Hydrogels Design and Functionality: A Review. Polymers (Basel) 10:11

24. Tarabeux J, Pateloup V, Michaud P, Chartier T (2018) Development of a numerical simulation model for predicting the curing of ceramic systems in the stereolithography process. J Eur Ceram Soc 38:4089–4098

25. Fan RN, Brunswick E, Assignee NJ, Du EI (1989) Solid imaging method using photohardenable compositions containing hollow spheres.

26. Halloran W. John (1997) Free Form Fabrication of Ceramic Stereolithography. Ann Arbor, MI

27. Melchels FP, Feijen J, Grijpma DW A review on stereolithography and its applications in biomedical engineering. https://doi.org/10.1016/j.biomaterials.2010.04.050

28. Melchels F, Feijen J, Biomaterials DG-, 2010 undefined A review on stereolithography and its applications in biomedical engineering. ElsevierPaperpile

29. Onuh SO, Hon KKB (1997) Optimising Build Parameters and Hatch Style for Part

Accuracy in Stereolithography. In: Int. Solid Free. Fabr. Symp. pp 653–660

30. Mummareddy B, Maravola M, MacDonald E, Walker J, Hetzel B, Conner B, Cortes P (2020) The fracture properties of metal-ceramic composites manufactured via stereolithography. Int J Appl Ceram Technol 17:413–423

31. Smith LL, Dai Z, Lee JC, Fotache CG, Cohen JM, Hautman DJ (2013) Advanced combustor concepts for low emissions supersonic propulsion. Trans ASME, J Eng Gas Turbines Power 135:815–827

32. Daehn GS, Breslin MC (2006) Co-continuous composite materials for friction and braking applications. JOM 58:87–91

33. Lopes AJ, MacDonald E, Wicker RB (2012) Integrating stereolithography and direct print technologies for 3D structural electronics fabrication. Rapid Prototyp J 18:129–143

34. Liao H (1997) Stereolithography Using Compositions Containing Ceramic Powders. University of Toronto

35. Zhang K, Xie C, Wang G, He R, Ding G, Wang M, Dai D, Fang D (2019) High solid loading, low viscosity photosensitive Al2O3 slurry for stereolithography based additive manufacturing. Ceram Int 45:203–208

36. Lasgorceix M, Champion E, Chartier T (2016) Shaping by microstereolithography and sintering of macro-micro-porous silicon substituted hydroxyapatite. J Eur Ceram Soc 36:1091–1101

37. Schmidt J, Altun A, … MS-J of the E, 2019 undefined Complex mullite structures fabricated via digital light processing of a preceramic polysiloxane with active alumina fillers. ElsevierSign in

38. Scalera F, Esposito Corcione C, Montagna F, Sannino A, Maffezzoli A (2014) Development and characterization of UV curable epoxy/hydroxyapatite suspensions for stereolithography applied to bone tissue engineering. Ceram Int 40:15455–15462

39. Chartier T, Chaput C, Doreau F, Loiseau M (2002) Stereolithography of structural

complex ceramic parts. J Mater Sci 37:3141–3147

40. Chen Y, Bao X, Wong CM, Cheng J, Wu H, Song H, Ji X, Wu S (2018) PZT ceramics fabricated based on stereolithography for an ultrasound transducer array application. Ceram Int 44:22725–22730

41. Johansson E, Lidström O, Johansson J, Lyckfeldt O, Adolfsson E (2017) Influence of Resin Composition on the Defect Formation in Alumina Manufactured by Stereolithography. Materials (Basel) 10:138

42. Wu H, Cheng Y, Liu W, He R, Zhou M, Wu S, Song X, Chen Y (2016) Effect of the particle size and the debinding process on the density of alumina ceramics fabricated by 3D printing based on stereolithography. Ceram Int 42:17290–17294

43. Zhou M, Liu W, Wu H, Song X, Chen Y, Cheng L, He F, Chen S, Wu S (2016) Preparation of a defect-free alumina cutting tool via additive manufacturing based on stereolithography – Optimization of the drying and debinding processes. Ceram Int 42:11598–11602

44. Bae C-J, Halloran JW (2011) Influence of Residual Monomer on Cracking in Ceramics Fabricated by Stereolithography. Int J Appl Ceram Technol 8:1289–1295

45. Wang JC, Dommati H (2018) Fabrication of zirconia ceramic parts by using solvent-based slurry stereolithography and sintering. Int J Adv Manuf Technol 98:1537–1546

46. Dehurtevent M, Robberecht L, Hornez JC, Thuault A, Deveaux E, Béhin P (2017) Stereolithography: A new method for processing dental ceramics by additive computer-aided manufacturing. Dent Mater 33:477–485

47. Zakeri S, Vippola M, Levänen E (2020) A comprehensive review of the photopolymerization of ceramic resins used in stereolithography. Addit Manuf. https://doi.org/10.1016/j.addma.2020.101177

48. Del Rio E, Nash JM, Williams JC, Breslin MC, Daehn GS (2007) Co-continuous composites for high-temperature applications. Mater Sci Eng A 463:115–121

49. Denry I, Kelly JR (2014) Emerging Ceramic-based Materials for Dentistry. J Dent Res 93:1235–1242

50. Myers K (2016) Structure-Property Relationship of Binder Jetted Fused Silica Preforms to Manufacture Ceramic-Metallic Interpenetrating Phase Composites. Youngstown State University

51. Ren X, Shao H, Lin T, Zheng H (2016) 3D gel-printing-An additive manufacturing method for producing complex shape parts. Mater Des 101:80–87

52. Breslin MC, Ringnalda J, Xu L, Fuller M, Seeger J, Daehn GS, Otani T, Fraser HL (1995) Processing, microstructure, and properties of co-continuous alumina-aluminum composites. Mater Sci Eng A 195:113–119

53. Pavese M, Fino P, Valle M, Badini C (2006) Preparation of C4 ceramic/metal composites by reactive metal penetration of commercial ceramics. Compos Sci Technol 66:350–356

54. Andreassen E, Andreasen CS (2014) How to determine composite material properties using numerical homogenization. Comput Mater Sci 83:488–495

55. Myers K, Juhasz M, Cortes P, Conner B (2015) Mechanical modeling based on numerical homogenization of an Al2O3/Al composite manufactured via binder jet printing. Comput Mater Sci 108:128–135

56. Zhang Y (2010) A Novel Image Processing Platform Development For Preprocessing Images With Two-Phase Microstructures Containing Isolated Particles.

57. Sun J, Binner J, Bai J (2019) Effect of surface treatment on the dispersion of nano zirconia particles in non-aqueous suspensions for stereolithography. J Eur Ceram Soc 39:1660–1667

58. Wang Z, Huang C, Wang J, Zou B (2019) Development of a novel aqueous hydroxyapatite suspension for stereolithography applied to bone tissue engineering. Ceram Int 45:3902–3909

59. Zhou W, Li D, Wang H (2010) A novel aqueous ceramic suspension for ceramic

stereolithography. Rapid Prototyp J 16:29–35

60. Song S, Park M, Lee J, Yun J (2018) A Study on the Rheological and Mechanical Properties of Photo-Curable Ceramic/Polymer Composites with Different Silane Coupling Agents for SLA 3D Printing Technology. Nanomaterials 8:93

61. Hu K, Wei Y, Lu Z, Wan L, Li P (2018) Design of a Shaping System for Stereolithography with High Solid Loading Ceramic Suspensions. 3D Print Addit Manuf 5:311–318

62. Purbrick MD (1996) Photoinitiation, photopolymerization and photocuring. J.-P. Fouassier. Hanser Publishers, Munich, 1995. pp. xii + 375, price DM198.00, sFr175.00, öS1466.00, US$138.00, £84.00. ISBN 3-446-17069-3. Polym Int 40:315–315

63. Tang YL, Kim JH, Shim JS, Kim S (2017) The effect of different cooling rates and coping thicknesses on the failure load of zirconiaceramic crowns after fatigue loading. J Adv Prosthodont 9:152–158

64. Fu X, Zou B, Xing H, Li L, Li Y, Wang X (2019) Effect of printing strategies on forming accuracy and mechanical properties of ZrO2 parts fabricated by SLA technology. Ceram Int 45:17630–17637

65. Ahmadi Moghadam H, Arab SM (2020) Effects of Heating Rate on the Thermal and Mechanical Properties of the Bauxite-Based Low-Cement Refractory Castables. J Mater Eng Perform 29:5968–5974

66. Liravi F, Vlasea M (2018) Powder bed binder jetting additive manufacturing of silicone structures. Addit Manuf 21:112–124

67. Rambo CR, Travitzky N, Zimmermann K, Greil P (2005) Synthesis of TiC/Ti-Cu composites by pressureless reactive infiltration of TiCu alloy into carbon preforms fabricated by 3D-printing. Mater Lett 59:1028–1031

68. Loehman RE, Ewsuk KG, Fahrenholtz WF, Lakshman BB (1997) Ceramic-metal composite formation by reactive metal penetration. Key Eng Mater 127–131:431–438

69. Maravola M, Cortes P, Juhasz M, Rutana D, Kowalczyk B, Conner B, MacDonald E (2018) Development of a low coefficient of thermal expansion composite tooling via 3D printing. In: ASME Int. Mech. Eng. Congr. Expo. Proc. American Society of Mechanical Engineers (ASME), p V002T02A090-V002T02A090

70. Maravola M (2018) Low Coefficient of Thermal Expansion Composite Tooling Manufactured via Additive Manufacturing Technologies. Youngstown State University

71. Ashkin D, Haber RA, Wachtman JB (1990) Elastic Properties of Porous Silica Derived from Colloidal Gels. J Am Ceram Soc 73:3376–3381

3. Binder Jetting Printing of High-Performance Ceramics

Overview

This chapter presents the research involved in printing high-performance ceramics via Binder Jetting Printing (BJP). Section 1 focuses on the introduction of the printing technique, the printing parameters, and the pros and cons of this technology. Section 2 elucidates the equipment and the materials used in this research program to print ceramic samples. Section 3 discusses three different ceramic powders printed in this work and their mechanical and thermal analysis. Each sub-section also presents the conclusions drawn on each material after printing. Finally, section 4 discusses overall conclusions and future work that discusses the benefits that can be drawn out from this 3D printing technology.

3.1: Introduction

Binder Jetting Printing (BJP) is one of the new age state-of- the art 3D printing technologies. It is a powder based additive manufacturing technique, where a binder is selectively dropped on the powder surface to bind the powder particles together. This AM method uses a CAD model to build a part glued by the binder by forming internal bonds and cured by a heating source (see Figure 3.1). Here the unbounded powder surrounding the part acts a support system to hold the component allowing the powder for reusing.

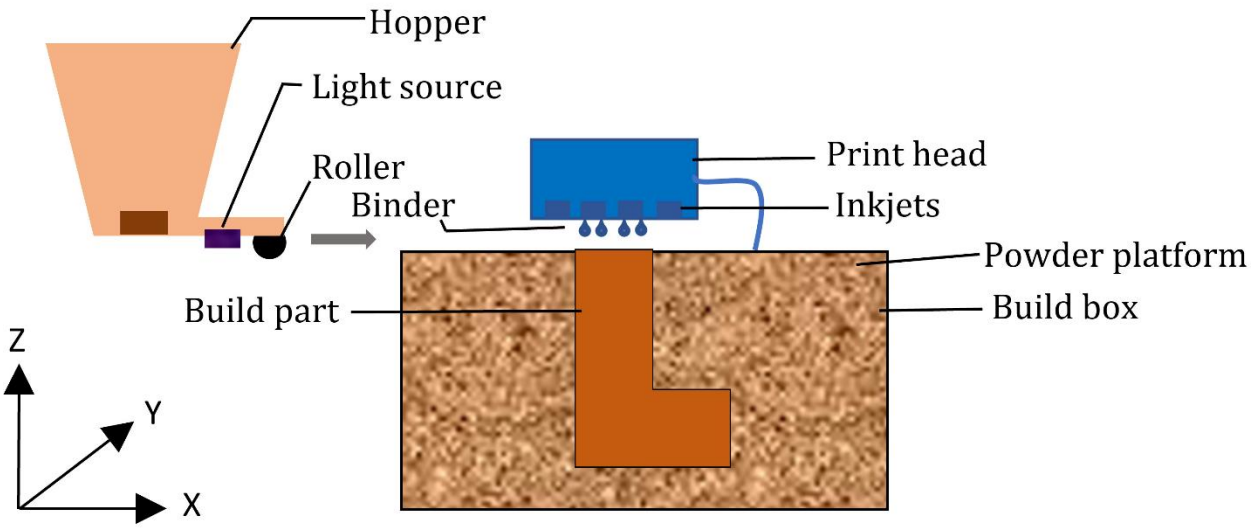

Figure 3.1: Schematic diagram of Binder Jetting printing. The figure also shows the major components in the 3D printer.

The binder jet technology was essentially built for rapid prototyping in late 1980's at Massachusetts Institute of Technology (MIT) by Sachs et al [1]. They investigated this technique for 3D printing detailed geometries and shells with alumina powder using colloidal silica binder for castings at high temperatures [1, 2]. Eventually, the technique due to the unique benefits of lower cost at higher build speed and printability with variety of powders made it suitable for several studies [3]. An illustration on the number of papers published since 2014 to 2019 with respect to advancement in Binder Jetting was shown by Mostafaei et al [4]. They reported that there were at least 170 papers

concentrated on BJ-AM while other 6500 papers published on the overall additive manufacturing field in the year 2019 [4]. The technique is also commercially explored by companies like Ex-One, Voxel-jet and 3D Systems [5–7]. A colored, multi-material, and hybrid structure BJP is an attractive feature that has been explored by commercial companies like Z-Corp and also by researchers such as Lehmus et al, Gibson et al [8, 9].

3.1.1: Process parameters

Printing a powder to form complex parts via BinderJetting Printing is a combination of several parameters. Some of the important printing parameters have been investigated for optimization and reliable part building.

Beginning from the powder, which is the base to start a print, its flow characteristics, geometry, and ambient conditions play a critical role in obtaining parts with less porosity [10][11]. Low porosity with good spread density leads to green parts with good density that impact the final mechanical properties of the printed part. This basic principle made researchers work with good flow-ability, and packing nature powders [12]. Spherical powder particles are supposedly used for better packing accounting to their geometry and theoretical density of 60% when distributed. A super ellipsoid simulation on different sized particles have shown particles with low aspect ratio difference displaying good distribution in horizontal planes [13]. Additionally, the interparticle forces in spherical powders result in an even distribution layering setup on the build plate when dropped from the automatic hopper feeding unit as such as those manufactured by ExOne [14]. Typically a particle size of 0.2 to 200 μm is used in BJP [3, 15, 16]. Generally, the powders are dropped on the build platform by gravity and acoustic source in a hopper feeder, and then distributed by a roller. Hence, the printing parameters such as roller-traverse speed, vibrator frequency, roller rotational speeds are also to be determined for each powder. A double smoothing method after powder laying was recommended by Shu et al [18]. An increase in the green density of 0.7 times was observed in alumina green parts when the powder was smoothened twice instead

once as seen in conventional binder jetting units. One more way to attain high dense parts was to increase the packing fraction of the powder particles by varying their sizes from coarse powders to ultrafine powders. Different sized and shaped particles are combined to result in greater densities[17, 18]. Bai et al [19] investigated the printability of copper, reviewing the advantages of unimodal and bimodal powder distributions in increasing density. A similar research by Liu et al [20] on copper powders has shown a 0.3 times increase in the tapped green density by adding 31% fine copper powder to coarse bronze powder. Multimodal prints also provided a good surface finish [21]. However the downside of using multimodal powders is the need for higher pressure during rolling for even distribution, fine powders reduce spread-ability, and it is hard for the binders to perforate in the multimodal system [22, 23].

The binder used in the printing process also plays a key role in the manufactured parts. Generally, low viscous printable binders are chosen. The essential requirement for selecting a binder is that it should act as a gluing agent. Two different mechanisms, in-bed and in-liquid are used in the BJP process. In the in-bed binding mechanism, a simple liquid is used as a hydrating initiator while a gluing agent (solid state) is already mixed in the powder whereas in the in-liquid mechanism the binding is totally dependent on the binder fluid [22, 24–27]. Some of the binders used in the in-bed process are dextrin, colloidal silicon agents, maldextrins, and starch [28, 29]. The in-bed printing process produces good parts, although no high density structures are obtained because of the addition of the gluing powders [24, 28]. Also, different variations such as wet and dry premixing are used. The wet premixing is similar to the slurry-based 3D printing, and it is reported to be advantageous over dry premixing as there is a less possibility for inkjet nozzle clogging [3]. However, these wet premixing were suitable for producing porous structures without inorganic contamination.

The in-liquid mechanism is a suitable technique where the binder is evaporated during the thermal debinding leaving behind a carbon residue. Some of the examples of in-liquid binders are polyvinyls, polysiloxanes, acrylic acids, and organic liquid binders [30–33]. Although the parts

printed via this mechanism have higher powder purity when compared to the parts in the in-bed mechanism. However, there was a high failure rate reported during the thermal debinding [34, 35]. Furthermore, inclusion of nanoparticles in the binders resulted in an increased density and strength[36, 37].

The inkjets equipped in the print head eject the binder (simple and high viscous) by either continuous jet (CJ) or drop-on-demand (DoD) techniques. These both jetting processes differ in the way of energy dispersion and frequency of the jetted binder [38, 39]. Between these two techniques, droplets generated by DoD techniques percolate easily into the powder layers due to the high pressures and geometry of the jets using conical shapes [12]. These ink jets are based on technologies such as liquid spark jetting, piezoelectric transducers, and fluid jetting tools. A downside of these high-pressure inkjet nozzles is that they create porosity and disturb the powder particle distribution when the droplets create satellite droplets. Liravi et al [40] reported that use of a medium viscous fluid can reduce the displacement of particles due to the density of the fluid.

Following the binder ejection, the geometry of binder droplets from the printhead onto the powder layers also makes an impact in lowering the porosity and even the distribution of the powder particles. The binder droplets are propelled out by pressure difference, gravity and surface tension between the powder and liquid. It generally penetrates by a capillary action [41, 42]. Miyanaji et al [41] have proposed a physics model for binder droplets for maintaining geometry and homogenous porosity of the prints from stainless steel and Ti-6Al-4V. Bai et al [43] investigated the contact angles made by binder droplets on the powder layers. They created an experimental set up to measure the dynamic contact angle and wettability using a sessile drop method.

Besides the factors like binder and powder selection, process parameters like binder saturation, layer thickness, printing orientation and traverse speed have also influenced the mechanical strength and thermal behavior of the final printed part.

The layer thickness can be defined as the thickness of the powder particles laid during the printing process. It is always suggested to maintain a layer thickness that is higher than the particle size. Sachs [44] from his study reports that a layer thickness three times larger than the average particle size is suitable for ceramic powders. Additional studies suggest that layer thickness should be selected in accordance with the binder saturation since the kinetics of the binder dropping changes [15, 45].

Binder Saturation can be defined as the ratio of the binder volume to the pore volume for each layer [46]. This is dependent on the powder packing nature which is usually around 50-70% when dropped from a hopper. Melcher et al reported an increase in density of Alumina/Copper oxide composites from 0.14 g/cc to 0.35 g/cc when the binder saturation was increased from 56% to 67%. A study on green part density and flexural strength as function of g the layer thickness was made by Suwanprateeb [15]. They suggested that the unoptimized layer thickness and binder saturation could lead to either unpenetrated loose powder particles or disintegrated parts with excessive binder.

Printing Orientation is the direction of the fabricating design. The general tendency of printing in Binder Jetting is the Z direction. However, Castilho [47] reported that there is a significant change in mechanical properties when printing in other directions, along with the geometrical accuracy of the specimen. The highest value of compressive strength has been in samples printed in the Y-direction, while the minimum in the X-direction. Furthermore, Li et al [45] studied the printing orientation effects on the print quality. A lower specific surface roughness was observed in the parts printed parallel to the X-Y plane, which seems to increase the mechanical strength.

Along with the printing parameters, one of the important steps in the BJP, is the post-processing state. The post-processing in BJP includes de-powdering, thermal debinding (curing) and sintering. Since, the BJP uses the unbound powder as support, after the print is completed, the unbound powder is separated from the printed *green* parts. In general, either manual brushing or a vacuum system is used to remove the loose powder, which is recycled. However, few studies have reported

additional techniques for removing the unbound powder such as: use of compressed air, and leaching and dissolving by a heat treatment [48–50]. In fact, Sachs [51], used a boiling fluid to clear the internal cavities in the printed samples.

Thermal debinding is the next post-processing step to de-powder the parts by subjecting them to a temperature where the liquid binder is evaporated. This step results in shrinkage and a reduction in the packing density. The next step is the final sintering stage, where the samples are subjected to the powder's near fusion temperatures where they undergo fusion. A solid-state sintering is observed during this step where surface energy and surface area are reduced. This step also includes larger shrinkage, low porosity (in comparison to green and debinded states), and high densities [3, 52, 53]. Specially with ceramics, sintering leads to strengthening and then to final structures. Sometimes, additives are added to the powders to improve sintering [54]. Further the samples are post processed to attain near-net densities using HIP, chemical vapor deposition techniques, polymer infiltration and metal infiltrations [55–58].

Many studies have used BJP for building structural composites in the medical, aerospace, automobile, electronic and tooling industries [36, 59–64]. Myers et al [65] have inspected printing silica of different particle sizes and transformed them into ceramic-metal composites (CMC's). Following the evaluation of the structure-mechanical performance of these Al-SiO_2 as functionally graded materials.

Although a considerable porosity and reduction in mechanical strength is commonly observed from the parts printed via BJP, it is still considered as a viable technology industrially for its ready-to-go build of complex geometries. In fact, the porous structures can be employed in bio-medical and dielectric applications [58, 66–68]. High Performance Ceramics (HPCs) have also been studied directly and indirectly by coating them with other binding or metal agents [69–71].

In this research, BJP has been used to study the following concepts:

1. Effect of the printing direction on the mechanical and thermal properties of alumina-silicate hollow microspheres.
2. Effect of the variability of the printing parameters on the mechanical properties for fused silica. The printing parameters here investigated were binder saturation, and roller-traverse speed.
3. Effect of a secondary binder addition on the mechanical properties for fused silica

3.2: Equipment:

This research was carried out on an ExOne Innovent + Binder Jetting Printer (see Figure 3.2). This unit uses furan (#7100037CL, BA005, ExOne, PA) as the in-liquid binding agent with a surface tension of 26.87 mN/m at room temperature in air, which has resulted in the production of robust green state ceramic-based parts (the chemical composition of the binder is included in Figure 3.2). The printer is equipped with a hopper of powder holding capacity of 1.107 kg, a roller, an IR light curing lamp, a build box of 65 x 160 x 65 mm (width x depth x length), and a printhead with 256 nozzles as observed in Figure 3.3. The printer uses three different fluid tanks for the binder, cleaner and waste that work with peristaltic pumps. The print head is capable of dropping tiny beads of binder measuring up to 10 pL. A print resolution of 30 microns is possible on this system. The built box moves by a pneumatic system and is controlled by a computer attached to the printer. A user application is used to plug-in different parameters such as recoat speed, roller speed, roller-traverse speed, binder saturation and job-process settings before starting the prints.

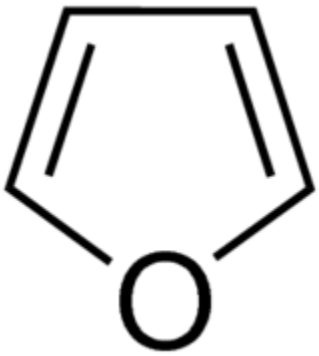

Figure 3.2: ExOne Innovent + Binder Jetting Printer Unit used in this research effort (left). Structure of the furan binder, used in this research work (right).

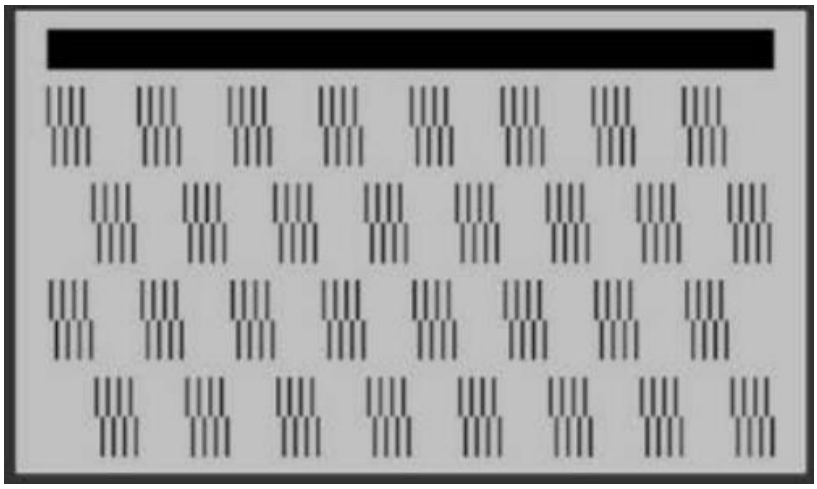

Figure 3.3: A test pattern created by the printhead where the 256 inkjets have dropped binder droplets to form lines.

3.3: Materials

3.3.1: Alumina-Silicate hollow microspheres

3.3.1.1: Objectives

The main objectives of printing hollow microspheres are described as follows:

- Study the printing process of lightweight hollow microspheres particles.
- Investigate the mechanical and thermal properties of samples printed in the X, Y and Z direction.
- Study the wear performance of the printed and post-processed hollow microspheres.

3.3.1.2: Printing Methodology

Lightweight ceramic hollow micro spherical particles synthetically made at SphereOne, Inc. (Chattanooga, TN) were used in this research. The microspheres had an average particle size of 75 microns with a bulk density of 0.40 g/cm^3 with a specific gravity 0.75 g/cm^3. The as-received powder was analyzed for XRF and it consisted of Al2O3 (~32%), SiO2(~ 42.5%) and traces of metal oxides (Fe, Ca, Ti). The powder was described to provide flame retardancy, refractory behavior, corrosion and abrasion resistance.

Samples using the microspheres were printed in the X, Y, Z directions on the ExOne Innovent + printer following the ASTM 52921. The samples were printed using the furan based aqueous binder with printing parameters of 60% binder saturation, 5 mm/sec roller traverse speed, and 150 μm layer thickness with a UV drying time of 20 seconds. As explained earlier, commonly 60% binder saturation with a low traverse speed and layer thickness that is double the particle size aids in attaining full dense specimens [2]. The printed samples were thermally debinded in a Yamato DX402A curing oven for six hours at 180˚C for obtaining *green state* samples (Appendix A). After the binder evaporation, the samples were sintered in air at 1275˚C at an initial heating ramp rate of 2 ˚C/min for 30 minutes, followed by an increased heating ramp rate of 10˚C/min and a dwelling time of 30 minutes to obtain the *sintered samples*. The samples were then air cooled with a cooling rate of 10˚C/min to room temperature.

3.3.1.3: Results and Discussion

The particle size analysis of the as-received material was performed in a CILAS 1190 particle analyzer system. The results showed that the material had an average diameter of 34.2µm with spherical morphology as seen in Figure 3.4. The spherical shape along with low specific gravity aids in enhancing the flowability and packing during the printing process [72]. Besides XRF analysis, XRD analysis on the microspheres showed the presence of 40.34% Alumina, 42.5% Silica, 6.2% Titanium Dioxide and traces of other metal oxides of K, Ca, and Fe with 9.7% with crystallinity in the as-received powder.

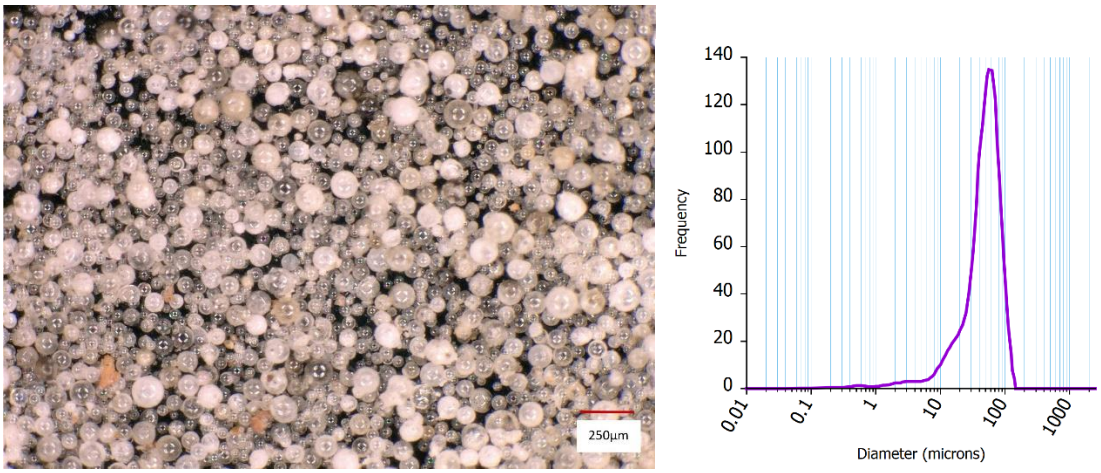

Figure 3.4: Micrograph of the as-received microspheres and their particle size distribution.

After the samples were printed and sintered, a shrinkage analysis was performed (see Table 3.1). The highest shrinkage was seen in the Z-direction (32.48%) (see Figure 3.5). This can be due to: (1) powder-binder interaction on the powder bed, (2) spacing that is created between the layers, (3) viscous flow during sintering involving damage to hollow spherical morphology. A ballistic effect was observed during the binder jetting process, where the powder particles are dislocated creating voids [73, 74]. A similar pattern was observed in 3D printed SiO_2 samples manufactured by Myers [65] and Parab et al [40, 75]. Myers reported a shrinkage of 13% in the Z direction and a minimum shrinkage of 10% in the X and Y directions when printed with silica powder of particle size 48 µm

[65]. The present paper displayed a lower shrinkage in the sintered samples, in comparison to Myers et al, however the microspheres due to the hollow particles resulted in higher degree of shrinkage.

Figure 3.5: Shrinkage seen in the printed specimen after post processing. The image shows green part (left) and the sintered part (right).

Table 3.1: Shrinkage analysis observed in the printed hollow microspheres after sintering.

Direction	Shrinkage (%)
X	28.80 ± 1.99
Y	26.72 ± 3.73
Z	32.48 ± 2.65

The printed green samples had a density of 0.34 g/cm^3 and after sintering the samples yielded a density of 1.002 g/cm^3; which is almost 3 times higher than that observed in the green parts. The samples showed some degree of porosity in both green and sintered states (see Figure 3.6). Nevertheless, the sintered samples displayed a porosity lower by 9.6% in comparison to green state samples. Liravi et al [40] observed that shrinkage and porosity are mostly dependent on the roller-traverse speed and the viscosity of the binder. Along with this, the smaller the drop size and lighter the binder, the lower the porosity. A MATLAB analysis was performed on SEM images of the

microsphere samples. Here the samples were transformed from RGB to grayscale using the "graythresh" and "im2bw" command. The final image is assigned with binary digits, '0' and '1' which is used to calculate the percentage of porosity and solid substance [76]. This resulted in a porosity of 32% in the sintered samples. This analysis was also used by Kyle et al [77], with a modeling error of 10% when predicting the 3D printed silica samples. It was also seen that the addition of metal oxides to printed ceramics can decrease their porosity as well as to elevate their strength properties [78]. Additives like metal-oxides can help in forming melt pools and coalescing the microspheres for higher density. Simultaneously, necking among the particles is seen, Figure 3.6. It is noteworthy, that the average particle size from green to sintered stages changed from 47.5 to 67.9 μm due to fusion of smaller particles to form larger particles (measured via Image J).

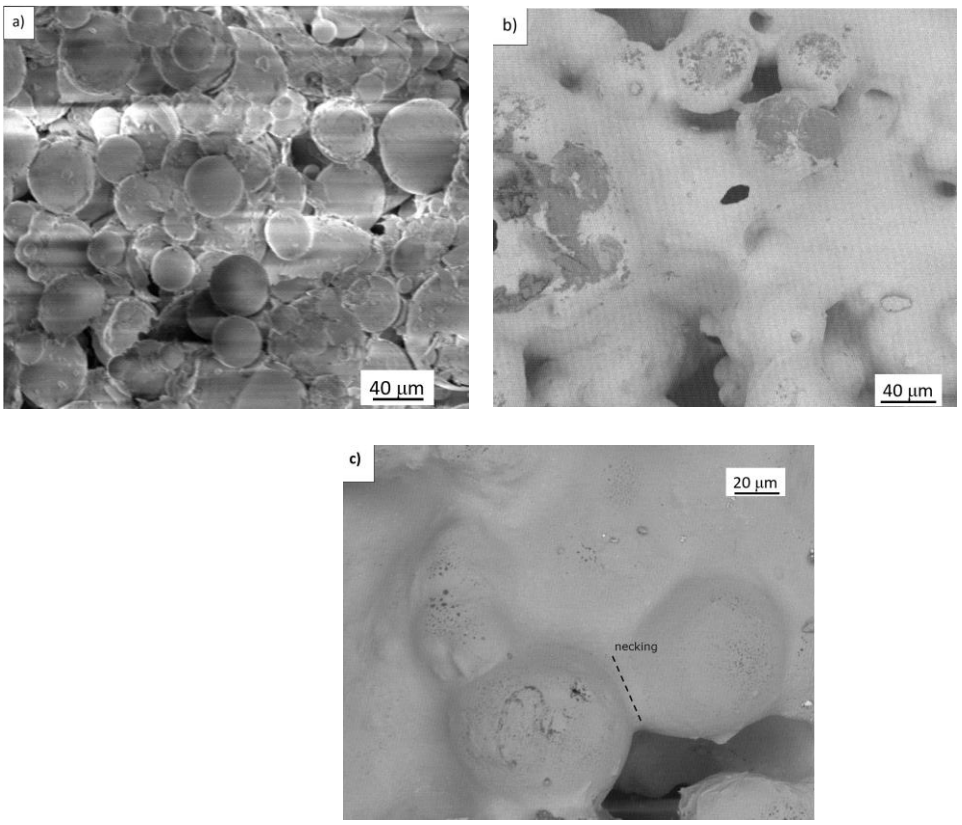

Figure 3.6: Micrographs of the printed ceramic spheres. a) Green state. b) Sintered state. c) Magnified picture of the sintered state showing a necking between large particles [79].

The sintered and green state samples were analysed using XRD (see Figure 3.7). From the XRD details, the sintered samples displayed a higher degree of crystallinity in comparison to green samples by 15.1%. The XRD analysis also showed the presence of 63.4% Alumina, 27.5% Silica with carbon, titanium and potassium oxides forming the remaining 9%. The silica present in the microspheres underwent an annealing process and thus transforming from sillimanite to mullite phase, maintaining an orthorhombic crystalline structure [80].

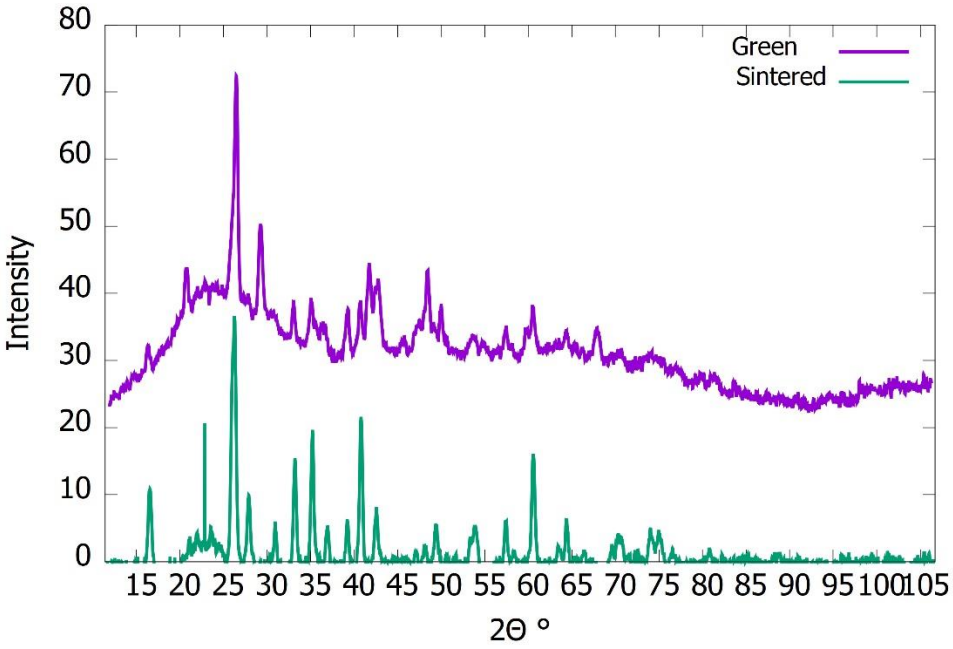

Figure 3.7: XRD graph of the green and the sintered samples revealing increase in crystallinity on the sintered parts (XRD peaks in the sintered state show higher intensity than in the green state ~ 25˚) [79].

Samples printed in the X, Y and Z directions were also evaluated for mechanical properties. Right angled cylinders of 12.5 x 12.5 mm (height x diameter) for compressive characterization and rectangular bars of 40 x 6 x 5 mm (length x breadth x height) for flexural characterization and 30 x 5 x 4 mm (length x breadth x height) for fracture toughness measurements were here manufactured. The sintered samples had a compressive strength 88% higher than the green state

samples, with an averaged value of 29.7 MPa across the three different printing directions. Although an overlap in the error bars was recorded among the X, Y and Z printing orientation, suggesting a limited statistical difference. The samples printed in the Y direction showed the highest compressive strength that can be associated with a larger diffusion among the particles in the columnar direction [81] (see Figure 3.8(a)).

An average flexural strength of 9.9 MPa was also recorded in the samples printed among the different printing directions (see Figure 3.8(b)). Although the flexural strength observed is 3 times lower than the compressive strength recorded in this work, the value is similar to that reported on mullite samples fabricated through conventional methods [63, 82]. Another reason contributing to the lower flexural strength might be due to the tensile and compressive loads acting on the same sample. The tensile loading mechanism in the bottom layers leads into a weakening and failure process at an early stage of loading. Castilho et al [47] have observed that a higher mechanical strength was seen in the Y direction. One of the contributing factors that affects the testing directionality is the formation of voids and contact surface while printing. Although the samples undergo homogenous sintering, voids formed during sintering are moved to the corners to round the fused particles leading to the formation of porosity [83, 84].

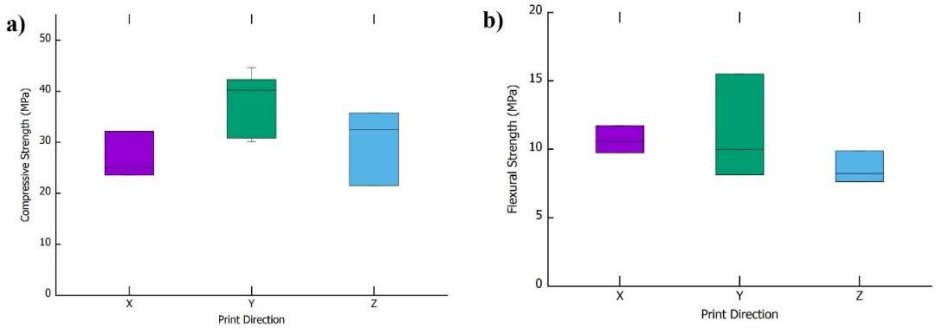

Figure 3.8: Mechanical properties of the printed and sintered hollow sphere samples. a) Compressive Strength. b) Flexural strength.

The fractured samples were optically analyzed under an SEM. The images displayed the absence of plasticity since a brittle fracture was seen. Also, the fracture initiated at the larger spheres and extended towards the fused zones (see Figure 3.9). A similar fracture mode was observed in both the compressive and flexural samples printed in the X, Y and Z directions.

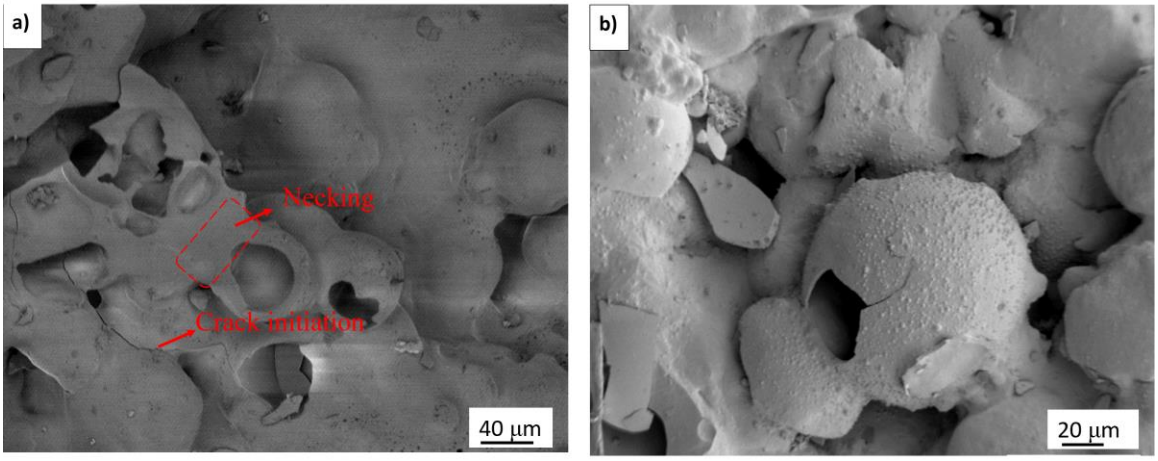

Figure 3.9: SEM micrographs of fractured samples showing fracture along the sintered spherical particles. (a) The fracture along the necking region. (b) A hollow sphere cracked after sintering.

Fracture toughness of the samples was performed by using a 3-point bending test using ASTM 1421 standard. Figure 3.10 shows a schematic build of the fracture toughness samples with a single edge notch. Here the samples printed in the X and Y directions showed the highest specific fracture toughness in comparison to the samples printed in the Z direction. It is also to be noted that the notch (0.05 mm thick) was machined after the sintering, which seemed to result in microcracks on the sample (see Figure 3.10 (c), (d), (e)). The area around the notch is the weakest point which can make the fracture propagate along the layers especially if the sample is printed in the z direction. The fracture toughness values obtained in this work were 30% lower than those reported on coupons fabricated via conventional methods [85]. The results obtained in this study suggest that slightest variation in the particle sizes (as seen in Figure 3.4) could improve the packing density and reduce the porosity with a probable chance to increase the fracture toughness.

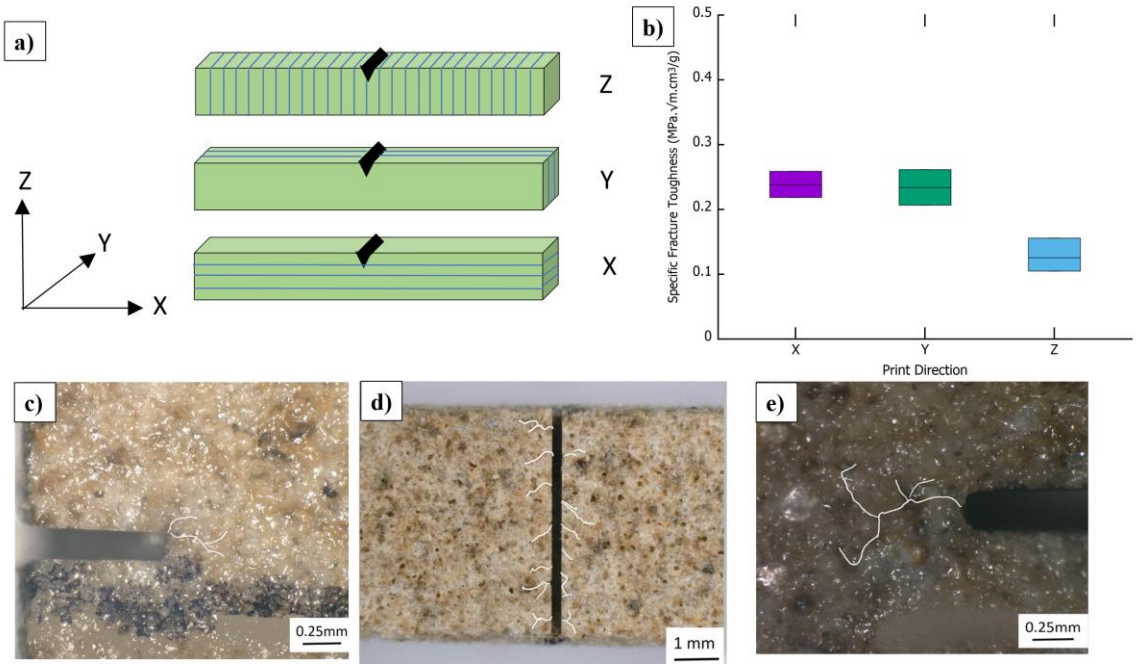

Figure 3.10: Specific fracture toughness of the sintered parts printed in different directions along with the schematic diagrams of the printing directions. (a) Schematic diagram of the parts built in different directions. (b) Fracture toughness results. (c), (d), (e) Fracture observed in the samples printed in the X, Y and Z directions respectively after machining in the notch (Indicated by the highlighted white lines).

The Coefficient of Thermal Expansion (CTE) of the sintered samples printed in different directions (6 x 5 x 6 mm -length x breadth x height) was performed using a quasi-static thermal profile. Although the samples printed in the Z direction showed a slightly higher CTE, the average CTE of the three different printing directions was about 4.8 x 10^{-6} C^{-1} (see Figure 3.11 (a)). Harrison et al [86] studied 3D printed Invar-36 and observed similar results with no significant changes across different printing directions. Bulk anisotropy instead of the hollow spheres could be one of the reasons contributing to the very low change in the thermal expansion. The values obtained in this work suggest that the materials are suitable structures for composite tooling application [87].

Included in figure 3.11, are the hardness results. Hardness testing performed in this study was performed on the X-Y polished plane on the sintered samples (10 x 8 mm (diameter x height)), and it was observed that these structures yielded a HV10 between 600 and 800 (see figure 3.11). This hardness value is 38.3% lower than that reported values in bulk mullite parts fabricated via slip casting [88]. Figure 3.10 shows that standard deviation error bars overlap across the different printing orientations, suggesting that the HV10 difference is not statistically significant. The lower averaged hardness of the part printed in the Y and Z -directions is probably due to measurements next to a pit or a layering interface. Also, the large standard deviation in the X -direction could be influenced by the variations of porosity across the surface.

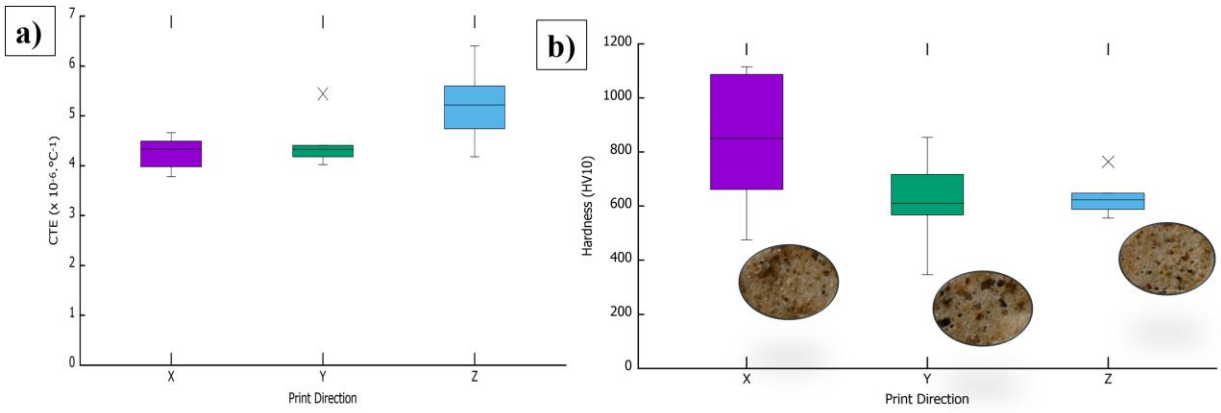

Figure 3.11: CTE and hardness values of the microsphere 3D printed, and sintered samples manufactured in different directions. (a) CTE values seen along different directions. (b) Hardness values seen in different directions. The figure also shows the porous structures in the samples after hardness testing.

The samples printed in the Z direction were tested for wear analysis using abrasion testing to record the height and volume loss. The wear was recorded at 5-, 15-, 30-, and 60-minutes intervals with an initial sample height recorded as 12.6 mm (see Figure 3.12). The largest degree of erosion was seen in the sintered samples in the first 5 minutes. The initial abrasion material lost can be associated with the loosely packed particles that are in and around the surface after the sintering

step. After the 60-minute period, the samples attained a plateau with a height loss of 1 mm and 8% volume loss. A wear factor of 0.0022 mg/mN was calculated using the following equation: K = W / (LF), where W is the wear mass loss in mg, L is the sliding distance in m (which was 5666 m for this study), and F, the applied load in N [89]. These 3D printed and sintered microsphere systems displayed an abrasion value 3 to 10 times lower than the reported on similar bulk mullite coated samples [89]. The results from the present work seem to suggest that these lightweight spheres represent an attractive material for brake rotors and surface coating applications, where features such as lightweight, hardness, and good abrasion performance is required.

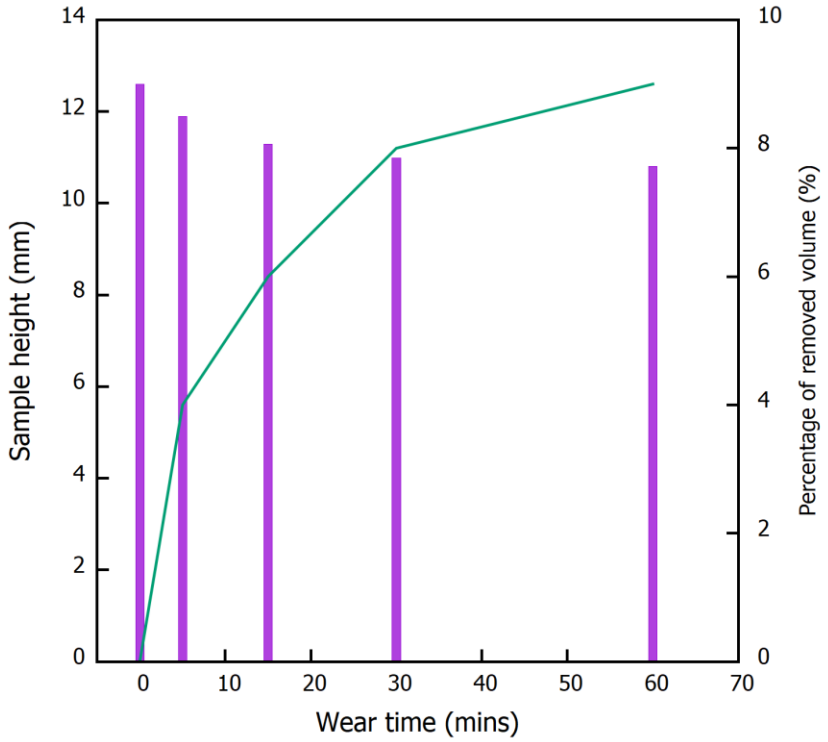

Figure 3.12: Abrasive wear observed on parts printed in Z-direction after subjecting to wear at different times.

3.3.1.4: Conclusions

The mechanical and thermal properties of the printed hollow micro spherical particles printed via Binder Jetting have been investigated in this study. An average shrinkage of 27.2% was observed

after the post processing stage The samples printed in this work reported an average compressive strength of 29.7MPa, a flexural strength of 9.9MPa and a fracture toughness of about 0.237 MPa $m^{1/2}$. Apart from the test results, some of the important characteristics observed in this study were:

1. The printed samples also showed high resistance towards corrosion, temperature, and high stresses. Along with these performances, their light-weight feature adds the advantage of using this material for applications such as armor strike face, coatings on re-entry vehicles and machining tools.
2. The low coefficient of thermal expansion reported in different directions showed that it can be a durable material for tooling applications. The abrasive performance observed here, also suggests that the investigated material is a good candidate for the applications where low wear and thermal expansion are required.

3.3.2: Fused Silica

3.3.2.1: Objectives

Fused Silica was investigated in this work addressing the following goals:

- Investigate the manufactured parameters of unimodal printing.
- Study the statistical significance and interaction effect of the following print parameters: binder saturation, and roller-traverse speed.
- Analyze the effects of incorporating secondary binders on the mechanical properties of fused silica.

3.3.2.2: Printing Methodology

Fused Silica (SiO_2) of 75µm average particle size powder was printed in an Ex-One Innovent + in the Z direction using a furan-based aqueous binder. Six sets of experiments varying the roller-traverse speed (2.5 mm/s, 5 mm/s) and binder Saturation (40%, 60%, 80%) were investigated. The roller speed (600 rpm), binder setting time (10s), and binder drying time (25s) were kept constant.

A persistent drop volume of 36.6 pL from each nozzle was used in this experiment. The printed parts were cured in the build box at 180°C for 6 hours to obtain the green parts. The samples were sintered at 1400°C for 6 hours at an average heating ramp rate of 6°C/min in air. The parts were allowed to air cool after the sintering cycle at a cooling rate of 10°C/min (control). The sintered parts were tested for compressive strength which were used to tabulate a factorial tree (design = 2x3, n=6 levels). A two-way factorial ANOVA method with no replications was used to understand the significance of each parameter used in this research (see Equation 3.1).

$$y_{ijk} = \mu + \tau_i + \beta_j + (\tau\beta)_{ij} + \varepsilon_{ijk} \quad , i = 1, .. , a, j = 1,\ldots, b, k = 1,\ldots, n \quad (3.1)$$

Where μ is the overall mean

τ_i is the effect of i th level of a factor A

β_j is the effect of j th level of a factor B

$(\tau\beta)_{ij}$ is the effect of interaction.

τ_i , β_j, $(\tau\beta)_{ij}$, ε_{ijk} are independent and identical random variables with normal distribution $\varepsilon_{ijk} \sim N(0, \sigma^2)$, where σ^2 is the variance.

Parallelepiped shaped parts were printed to measure the contact angle made by secondary binders: Water, Glycerol, Acetic acid, Dextrin, and Polysiloxane resin by capillary action on a Kruss Surface Tension measurement drop analyzer equipment using a syringe. A constant drop volume of 4 μL was dropped from a syringe needle on the silica green part surface in order to measure the contact hysteresis. At least 4 samples of the geometry were used to measure the contact angles made by selected binders in different angles (parallel, perpendicular, and 45°) with respect to the layering during the printing process. A fixed volume of liquid was dropped on the green parts to determine the contact angle made on the powder surface using the sessile drop method. Acetic Acid and Dextrin were selected as the secondary binders due to the lower contact angle made on fused silica samples [42, 90]. Water, and glycerol were not considered for the higher contact angles and polysiloxane resin for complexities in fabricating and relatively higher contact angles in comparison to dextrin and acetic acid. The parts with different concentrations of secondary binder

were then cured at 180°C, followed by the aforementioned sintering process. The sintered samples were mechanically tested to analyze the compressive stress-strain effect of the secondary binders. The compression test was carried out on a Instron Universal Testing Machine following ASTM C1421 standard using a 0.5 mm/min crosshead strain speed. Here, Equation 3.2 was used to determine the compressive stresses. The sintered specimens were optically characterized to investigate the microstructure and porosity features of the printed silica parts on a Keyence VHX-7000 optical microscope. The crystallographic changes in the samples were investigated via XRD analysis using a X8 Bruker Prospector XRD unit with 40kV X-Ray source ($2\theta = 0^{O}$ to 108^{O}). A Keysight benchtop FE-SEM with an electron beam source of 1keV was used in this work to observe the samples at a micro level (Refer Appendix A).

$$\sigma = F/A \qquad (3.2)$$

Where σ = Stress (MPa)

F = Applied Force (N)

A = Area

3.3.2.3: Results and Discussion

The fused silica used in this work was analyzed in a CILAS Laser particle analyzer and it was found that the average particle size was about 51μm (see Table 3.2). The microscopic study displayed that the fused silica exhibited an irregular morphology as observed in Figure 3.13. The layer thickness for printing this powder was adjusted to be 150 microns. Here, the thickness layer was selected to be three times larger than the particle size d to ensure a good printing spread-ability and a better particle distribution A density of 0.82 g/cc was observed in the green parts, and it increased to 1.12 g/cc after the post-processing stage. An average shrinkage of 12.28 % and 16.65 % were recorded along the diameter and height of the cylindrical samples after the post-processing stage, respectively. Kyle [65, 79] showed similar shrinkage values when fused silica was printed via BJP process.

Figure 3.14 shows the averaged volumetric shrinkage of the samples after the sintering process. It was observed that increasing the binder saturation results in an increase in shrinkage. It was seen that printing the parts at a traverse speed of 2.5 mm/s resulted in a higher shrinkage (40%) than that observed on the parts printed at 5mm/s due to the enhanced inertia forces from high packing densities [91, 92].

Similar shrinkage results have been reported by Miyanaji on 3D printed porcelain dental ceramics [93].

Table 3.2: Particle size distribution of Fused Silica powder used in this research.

d_{10} (μm)	d_{50} (μm)	d_{90} (μm)	Mean particle size (μm)
10.31	50.42	91.27	50.95

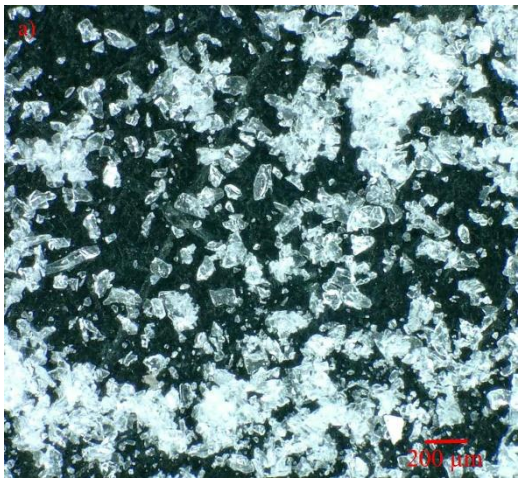

Figure 3.13: Optical analysis showing particle morphology of the Fused Silica powder as received.

The sintered samples from all the batches were tested for compressive strength and summarized as shown in Figure 3.14 (b). An average compressive strength of 12.4 MPa was obtained when the used traverse speed was 2.5 mm/sec and 5.21 MPa when the traverse speed was 5 mm/sec. Suggesting that a lower traverse speed induces a higher packing density in the samples, which

results in a higher compressive strength. This phenomenon was observed in both traverse speed testing. Similar results by Jimenezi et al [94] have shown that lowering the traverse speed (~ 6 mm/sec) produces higher density printed parts. A particle-based simulation has also revealed that green samples printed with a higher roller traverse speed resulted in prints with a high surface roughness [95, 96].

The figure also shows that increasing the binder saturation from 40% to 80% results in an increase of the sintering compressive strength. This was a phenomenon observed due to good polymerization without any ballistic effect in the samples [97, 98]. This is also due to the dominated behavior of the polymer bridges formed in the particles with less voids [99].

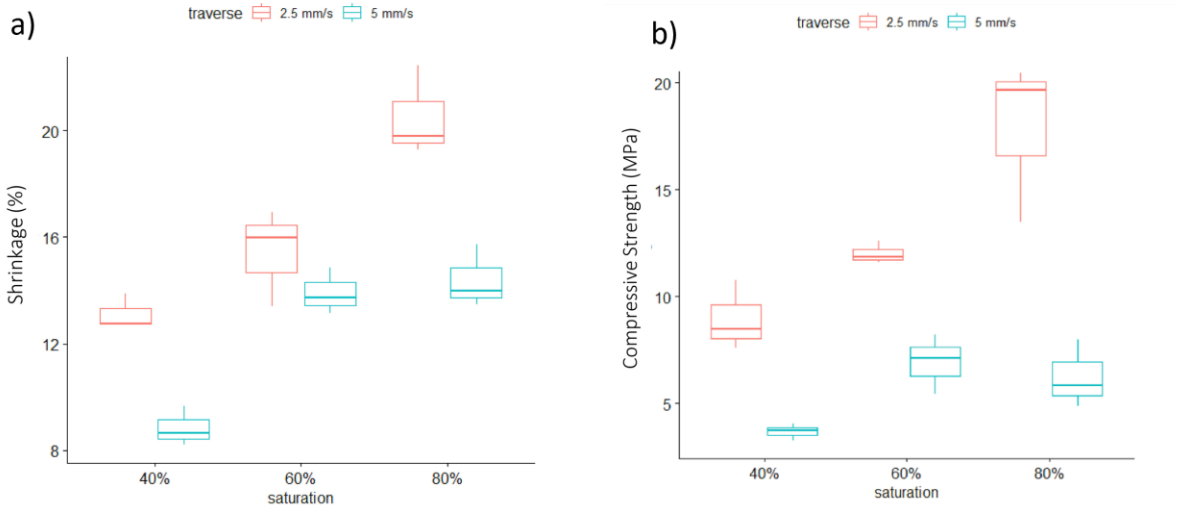

Figure 3.14: Distribution graphs of Compressive Strength and shrinkage with respect to Binder Saturation and Traverse speed. (a) Shrinkage. (b) Compressive Strength.

It is interesting to note, that although the samples printed with 2.5 mm/sec and 80% binder saturation exhibited the highest compressive strength, the samples presented a radial expansion as results of the high level of binder of saturation (see Figure 3.15). Hence, 60% binder saturation with 2.5mm/sec was selected to test the effect of the secondary binders.

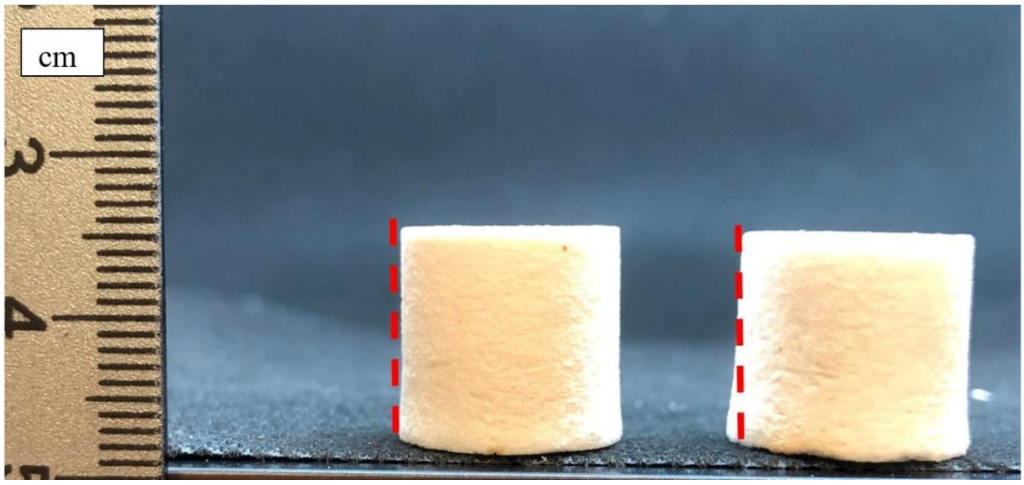

Figure 3.15: Sintered samples with 60% (left), 80% (right) binder saturation printed under a transverse speed of 2.5 mm/s. The samples on right shows a radial expansion after the post-processing stage.

The results of the two-way analysis of variance (ANOVA) are shown in table 3.3. This analysis evaluated the main effects of the binder saturation and traverse speed along with their interaction on the mechanical strength of the printed samples. Table 3.3 shows the statistical report with degrees of freedom, f-value and p-value. The f-value indicates that each testing parameter (binder saturation, traverse speed) is independent and different from each other, while p-value indicates that they were significant for the confidence interval (< 0.05) [100]. From the p-values, it seems that each analyzed parameter as well as their interactions have a significant impact on the compression stress of the samples, although the interaction appears to be more insignificant than the individual variables. Similar conclusions have been observed by Jimenez et al [94], when a broader statistical analysis was made on Alumina binder jetting printing. The large f- value of the transverse speed suggests a wide variance on the data. A Q-Q plot was used to understand the correlation and the presence of outliers in the results of printing parameters. The Q-Q plot shows that distributions have shown a straight line indicating the residuals follow a normal distribution. This also indicates that a low standard deviation among the results was found while varying the

print parameters [100, 101]. Additionally, there is no presence of extreme outliers and a positive correlation suggesting the data to be normally distributed.

Table 3.3: Results of the Two-way ANOVA table for Binder Jetting Printing.

Parameter	**Degrees of Freedom (df)**	**Sum of Squares (SS)**	**Mean Squares (MS)**	**F Value**	**P-value**
Traverse speed (mm/sec)	1	241.11	241.11	65.250	3.4e-06
Binder Saturation (%)	2	99.57	49.78	13.473	0.000856
Traverse speed: Binder Saturation	2	41.75	20.88	5.649	0.018667
Residuals	12	44.34	3.70		

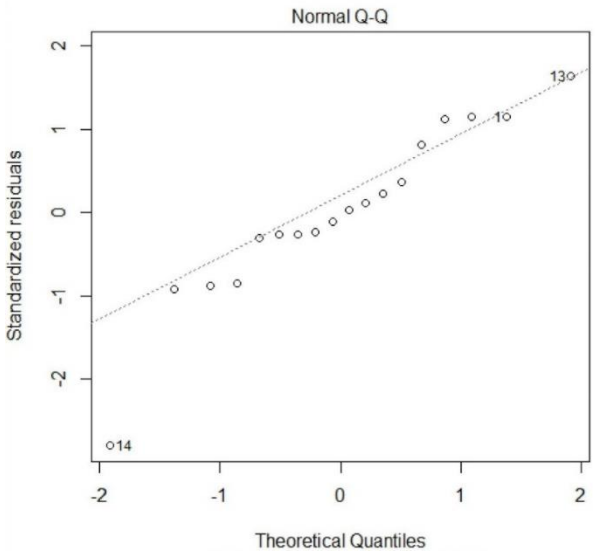

Figure 3.16: Q-Q graph of the strength distribution.

Parallelepiped shaped parts were chosen to investigate the surface tension of the studied binders (see Figure 3.17). An assumption was made that the binder makes a low contact angle (θ) with the powder surface would result in high wetting. This is accounted by the surface tension, external forces and the environment [102, 103]. The angles made between the solid surface and the liquid drop were measured for each binder. The contact angle here, was measured before there is a spontaneous penetration to avoid errors and the dispersion angle is measured from the sessile drop and ellipsoid cap formed by the binder on the surface (see Figure 3.17(b), (c)). Additionally, a pseudo line for maintaining symmetry in the drop was optically made [104]. Voids created at this stage when dropping micro-sized sessile drop were assumed to be absent as there is no presence of loose powder particles in the green parts.

The binders on the Fused Silica surface have experienced a spontaneous absorption resulting in different contact angles, Figure 3.18. However, they differ slightly from the liquid contact angles in air due to the surface and external factors like the porosity induced by the printing process [90]. Among all the binders, Acetic acid, polysiloxane resin and dextrin (dextrin + water in the ratio of 2:1) have yielded low contact angles relatively due to the viscosity changes [43, 105]. The figure shows that the contact angle seems to be independent of the printing orientation, suggesting that the wettability is rather governed by the pore-liquid diffusion interacting mechanism. It is interesting to note that parts infiltrated with Polysiloxane resin as a secondary parts do not need the post-processing stage due to the level of hardening achieved on the parts [105]. However, given its high viscosity and fast hardening, it was not further considered as a secondary binder.

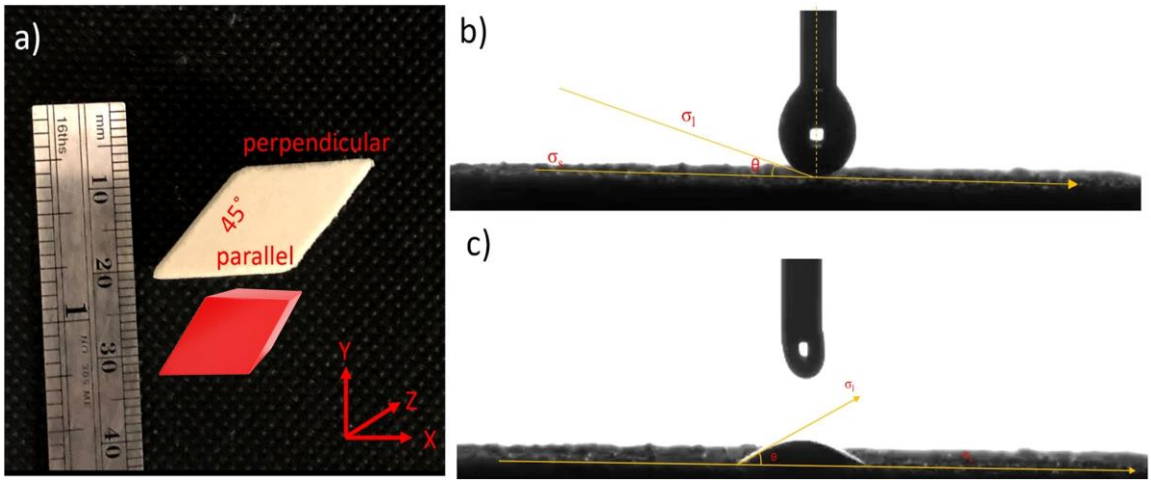

Figure 3.17: (a) Parallelopipe shaped part used for measuring surface contact angles. (b) Sessile drop forming due to the gravity and capillary effects at the syringe. (c) Sessile drop (ellipsoidal cap) formed from the binder (Glycerol) over the sample surface.

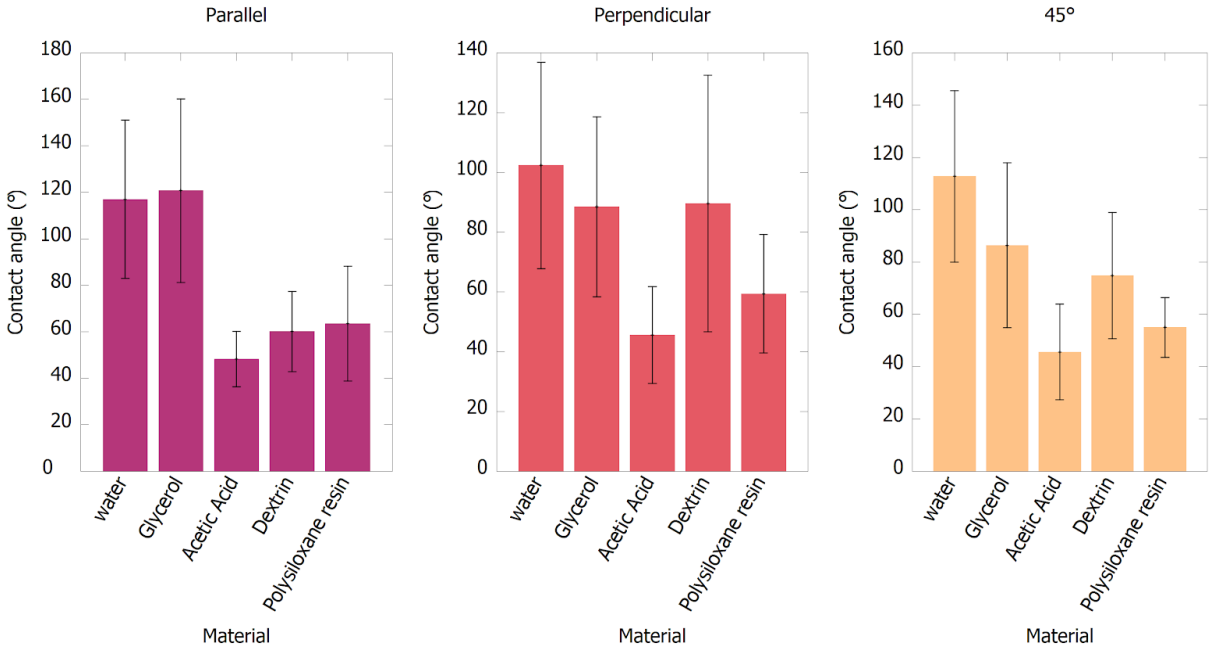

Figure 3.18: Contact Angle measurements of the secondary binders on green silica samples.

Due to the lower contact angle of the acetic acid and dextrin, these binders were decided to be further explored under different loading percentages. It is noteworthy that the samples reached a saturation point at 60% secondary binder loading where the absorption of the secondary binder reached equilibrium. Figure 3.19 shows the density of the printed samples subjected to different

secondary binder loading percentages at two different sintering times. The figure shows that after 400 minutes of sintering, the density slightly decreases due the binder evaporation. Indeed, at this time, the particles have not fused and the initiation of density enhancement begins after this stage [106, 107]. In contrast, increasing the sintering time more than 1000 minutes, allows for a particle diffusion mechanism that results in an increase in the density. From the figure, it seems that the incorporation of dextrin results in a higher density than the acetic acid system. It has been reported by Kuticheva [108] , that acetic acid reacts with the furan producing an acetylation process, which results in the production of unbound carbon residue. This makes the samples lose internal binding, resulting in a lower density and therefore in a lower strength. In contrast, the dextrin does not react with furan and fills the porosity of the printed parts adding weight to the sample and enhancing the internal binding [43].

The figure also shows that increasing the vol% of dextrin yielded the highest densities in the impregnated materials. Here, the 60% vol of dextrin appeared to have yielded a lower density than the 30 vol %, an effect probably related to a large presence of secondary binder at the surface of the sintered parts. The highest density of 1.43 g/cc was measured in the samples 30% dextrin loading by Archimedes principle, while the control samples without any seconding binder loading had a density of 1.12 g/cc. However, the samples theoretically have a 33% higher density with density as a binder [109].Unlike the expectations, the samples with dextrin have also shown an initial decrease in density when debinded but further improvement in density is seen after sintering.

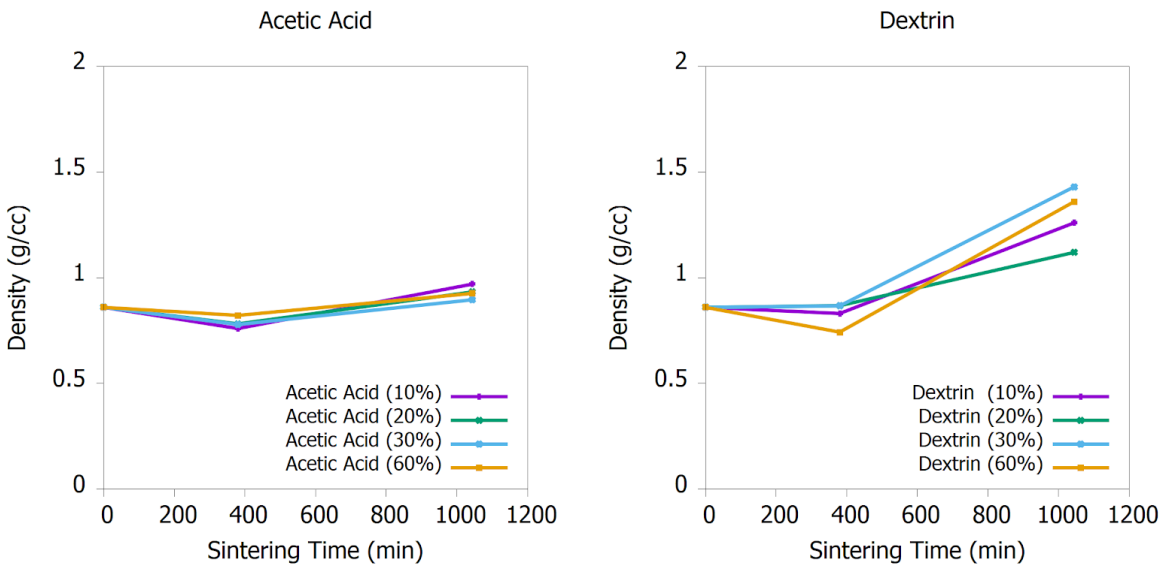

Figure 3.19: Average density of the sintered Silica samples with secondary binders at different concentrations.

The sintered samples were analyzed for crystallinity with and without the secondary binders (see Figure 3.20). It revealed that the samples had 85.2%, 72.2%, 91.1% crystallinity after sintering at 1400°C without secondary binder, and with acetic acid, and dextrin respectively. The highest peak displayed in all the XRD curves at 2θ= 23° is the cristobalite which intensified with the addition of dextrin [110]. The cristobalite in the silica structure is responsible for higher crystallinity and so higher strength [101]. The samples with dextrin loading inspite of the secondary powder particles accelerated the crystallization and there by strength [109, 111].The lower crystallization in the samples with acetic acid was because of the acylation as discussed earlier. Here the acetylation reaction breaks down the bonds/polymer bridges formed between the silica particles [99, 108]. This is in the following step leaves the samples with loose amorphous particles. The samples with dextrin have shown a higher crystallinity when 30% and 60% binder was included.

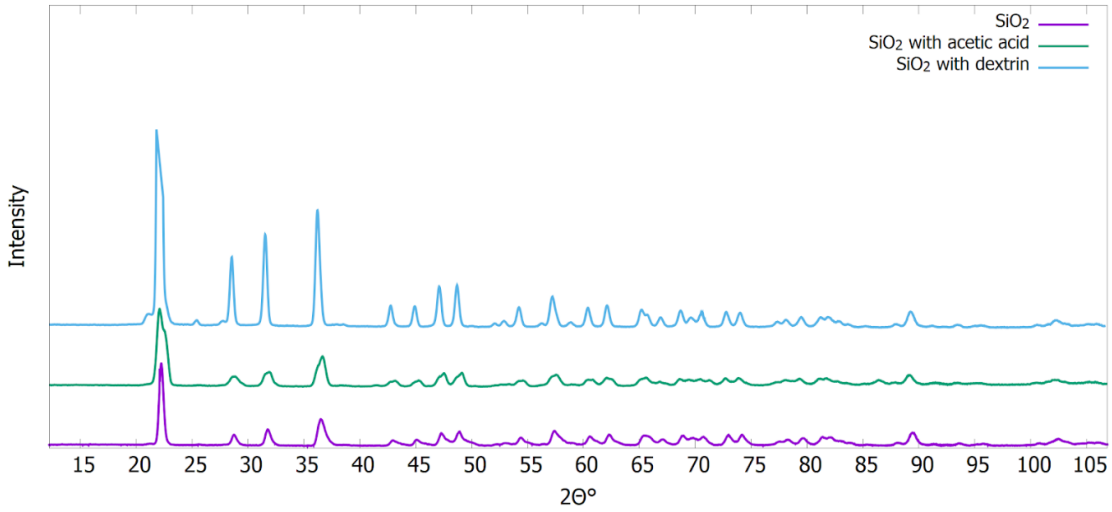

Figure 3.20: XRD of the sintered Silica samples with and without secondary binders.

The post-processed samples with secondary binders were tested for compressive strength (see figure 3.21). The results show that those samples containing dextrin exhibited a higher strength than those with acetic acid. The higher mechanical strength in the samples with dextrin loading was contributed by the higher crystallization and density as discussed earlier. It is interesting to note that increasing the concentration of acetic acid on the printed samples resulted in a decrease of compression strength on the parts. This could be associated with the reaction between furan and acetic acid, which could have weakened the system. In contrast, the inclusion of higher concentrations of dextrin on the printed parts resulted in an increase in the compression strength. One of the reasons for the higher compressive strength on the parts containing dextrin as secondary binder, is that it fills the voids in the silica specimen built via BJP (see Figure 3.22c).

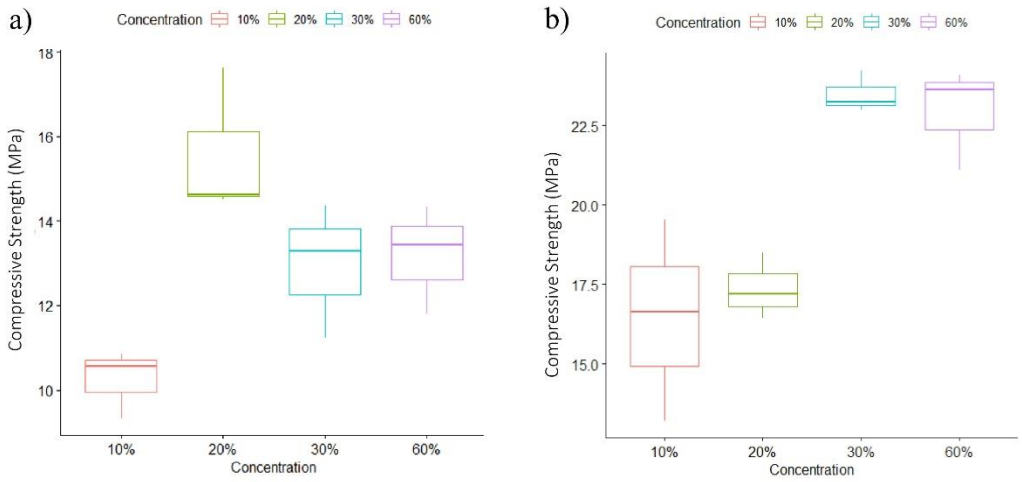

Figure 3.21: Compressive Strength of the samples after addition of secondary binder. (a) Acetic Acid. (b) Dextrin.

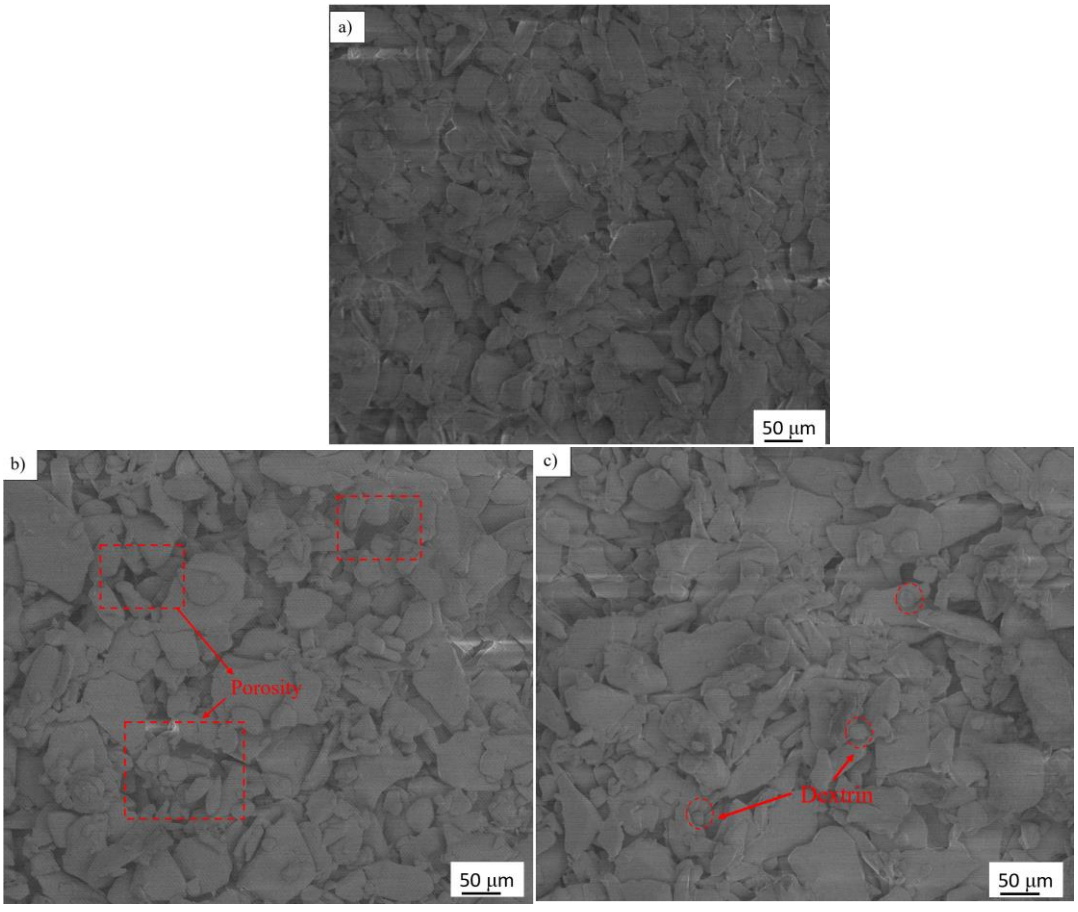

Figure 3.22: SEM images of the samples after curing at 600^{O}C. (a) SiO_2 (b) SiO_2 with Acetic Acid (c) SiO_2 with Dextrin particles.

3.3.2.4: Conclusions

The process parameters for binder jetting of fused silica were analyzed using a statistical analysis, and it was observed that the traverse speed has a more significant effect on the compressive strength of the printed parts in comparison to the binder saturation variable. Here, samples with 60% binder saturation and 2.5 mm/sec traverse speed displayed the highest compressive strengths among the set of experiments investigated here.

The inclusion of secondary binders was also investigated, and it was found that such incorporation enhances the mechanical strength of the printed samples. The strength seems to be related by the liquid-particle contact angle which is a measure of the surface tension and wettability. Among the five binders here investigated, dextrin and acetic acid were selected for testing the compressive strength. However, due to an acetylation reaction between the furan binder and the acetic acid, the samples containing acetic acid resulted in a low strength. In contrast, the inclusion of dextrin resulted in an increase of the compression strength. The sessile drop model used in this work only presents details from the drop propulsion from a syringe in microliters whereas the actual printing has a jetting system that has pico-sized ink droplets and real-time print parameters like binder drop spacing, droplet frequency, and pass speed also affect the printing. The results from the present study could assist in manufacturing stronger complex parts and guide in the use of additional binder systems for new materials in the BJP process.

3.4: Conclusions

A successful study on the effects of different parameters on mechanical properties of high-performance ceramic powders was made in this research. Hollow microspheres of low particle density yielded high density (~ 294%) and mechanical properties after sintering the printed coupons. The samples here printed were varied in print directions in the X, Y and Z. The results showed that the samples printed in Y directed yielded higher mechanical strength. Thermal properties were not very much affected by change in the print direction.

A statistical analysis performed in this research showed that slower traverse speeds result in parts with good geometric definition. Additionally, it was also observed that both binder saturation and roller-traverse speed are two important parameters that are needed to be watched when printing ceramic powders. A study on the effect of secondary binder addition showed that the ceramic samples (made of fused silica) were able to absorb up to 30% extra binder loading despite the voids. However, it was observed that a secondary binder with nano particles (dextrin, in this research) would help in attaining higher strength (~ 80%). It can be concluded from this study that a post-processing with an additional binder addition could help in improving mechanical strength. One of the reasons contributing to the increase in density is the particles of different particle size filling up the voids and thus less porosity.

Future studies on the Binder Jetting Printing include the following.

- A statistical analysis of all the different print parameters used while printing.
- The interaction effect of these parameters is also to be made as they can provide details on printing samples with geometric definition.
- A transformation of the fused silica samples printed via BJP can also help in industrial applications where complex geometries are required.

3.5: References

1. SACHS, E (1992) CAD-casting : the direct fabrication of ceramic shells and cores by three-dimensional printing. Manuf Rev 5:118–126

2. Emanuel M. SachsMichael J. CimaMichael A. CaradonnaJason GrauJames G. SerdyPatrick C. SaxtonScott A. UhlandJooho Moon (2003) Jetting layers of powder and the formation of fine powder beds thereby

3. Du W, Ren X, Ma C, Pei Z (2017) Binder jetting additive manufacturing of ceramics: A literature review. In: ASME International Mechanical Engineering Congress and

Exposition, Proceedings (IMECE). American Society of Mechanical Engineers (ASME)

4. Mostafaei A, Elliott AM, Barnes JE, et al (2020) Binder jet 3D printing – Process parameters, materials, properties, and challenges. Prog. Mater. Sci. 100707

5. (2015) Innovent ® 3D Printing System User Manual

6. Industrial 3D printing solutions | voxeljet. https://www.voxeljet.com/. Accessed 16 May 2020

7. The Best Industrial Metal and Plastic 3D Printers I 3D Systems. https://www.3dsystems.com/3d-printers?utm_medium=search&utm_source=google&utm_campaign=&utm_term=&utm_content=&gclsrc=aw.ds&&campaign=12567380320&content=507217267092&keyword=3d systems&gclid=Cj0KCQjwyZmEBhCpARIsALIzmnK-cS22MFiijaA_5f5weT7odJNNwfAu8h1WNorWJxRpPBmO8Mg2PMYaAjquEALw_wcB. Accessed 27 Apr 2021

8. Beaman JJ, Atwood C, Bergman TL, et al (2004) ADDITIVE/SUBTRACTIVE MANUFACTURING RESEARCH AND DEVELOPMENT IN EUROPE

9. Vaezi M, Chianrabutra S, Mellor B, Yang S (2013) Multiple material additive manufacturing - Part 1: A review: This review paper covers a decade of research on multiple material additive manufacturing technologies which can produce complex geometry parts with different materials. Virtual Phys. Prototyp. 8:19–50

10. Marcello R, Federica B (2004) Powder Flowability Characterising Techniques. Am Ceram Soc Bull

11. Daneyko A, Khirevich S, Höltzel A, et al (2011) From random sphere packings to regular

pillar arrays: Effect of the macroscopic confinement on hydrodynamic dispersion. J Chromatogr A 1218:8231–8248. https://doi.org/10.1016/j.chroma.2011.09.039

12. Seluga KJ (2001) Three Dimensional Printing by Vector Printing of Fine Metal Powders

13. Zhao S, Zhang N, Zhou X, Zhang L (2017) Particle shape effects on fabric of granular random packing. Powder Technol 310:175–186. https://doi.org/10.1016/j.powtec.2016.12.094

14. Pruitt B (1991) The design of an automated powder deposition system for a three-dimensional printing machine

15. Suwanprateeb J, Sanngam R, Panyathanmaporn T (2010) Influence of raw powder preparation routes on properties of hydroxyapatite fabricated by 3D printing technique. Mater Sci Eng C 30:610–617. https://doi.org/10.1016/j.msec.2010.02.014

16. Williams CB, Cochran JK, Rosen DW (2011) Additive manufacturing of metallic cellular materials via three-dimensional printing. Int J Adv Manuf Technol 53:231–239. https://doi.org/10.1007/s00170-010-2812-2

17. Nolan GT, Kavanagh PE (1992) Computer simulation of random packing of hard spheres

18. Yerazunis S, Cornell S, Nature BW-, 1965 undefined Dense random packing of binary mixtures of spheres. nature.comPaperpile

19. Bai Y, Wagner G, Williams CB (2017) Effect of particle size distribution on powder packing and sintering in binder jetting additive manufacturing of metals. J Manuf Sci Eng Trans ASME 139:. https://doi.org/10.1115/1.4036640

20. Liu J, ML Ryneson - US Patent 7 070,734, 2006 undefined Blended powder solid-

supersolidus liquid phase sintering. Google PatentsPaperpile

21. Bai Y, Wagner G, Williams CB (2015) Effect of Bimodal Powder Mixture on Powder Packing Density and Sintered Density in Binder Jetting of Metals. In: International Solid Freeform Fabrication Symposium. pp 758–771

22. Bredt J (1997) Binder stability and powder/binder interaction in three-dimensional printing.

23. Esnault V, Michrafy A, Heitzmann D, et al Processing fine powders by roll press. ElsevierPaperpile

24. Utela B, Storti D, Anderson R, Ganter M (2008) A review of process development steps for new material systems in three dimensional printing (3DP). J. Manuf. Process. 10:96–104

25. Salehi M, Maleksaeedi S, Sapari MA Bin, et al (2019) Additive manufacturing of magnesium–zinc–zirconium (ZK) alloys via capillary-mediated binderless three-dimensional printing. Mater Des 169:107683. https://doi.org/10.1016/j.matdes.2019.107683

26. Bredt J, Anderson T, DB Russell - US Patent 6 416,850, 2002 undefined Three dimensional printing materials system

27. Bredt J, Clark S, G Gilchrist - US Patent 7 087,109, 2006 undefined (2006) Three dimensional printing material system and method

28. Lam CXF, Mo XM, Teoh SH, Hutmacher DW (2002) Scaffold development using 3D printing with a starch-based polymer. Mater Sci Eng C 20:49–56. https://doi.org/10.1016/S0928-4931(02)00012-7

29. Suwanprateeb J, Chumnanklang R (2006) Three-dimensional printing of porous polyethylene structure using water-based binders. J Biomed Mater Res Part B Appl Biomater 78B:138–145. https://doi.org/10.1002/jbm.b.30469

30. Ziaee M, Crane NB (2019) Binder jetting: A review of process, materials, and methods. Addit. Manuf. 28:781–801

31. Reis N, Ainsley C, Derby B (2005) Viscosity and Acoustic Behavior of Ceramic Suspensions Optimized for Phase-Change Ink-Jet Printing. J Am Ceram Soc 88:802–808. https://doi.org/10.1111/j.1551-2916.2005.00138.x

32. Moon J, Grau JE, Knezevic V, et al (2004) Ink-Jet Printing of Binders for Ceramic Components. J Am Ceram Soc 85:755–762. https://doi.org/10.1111/j.1151-2916.2002.tb00168.x

33. Patterson R, Hollenberg DH., Desjarlais R, Alderfer George E. (1985) Ink jet printable coatings

34. Manogharan G, Kioko M, Linkous C (2015) Binder Jetting: A Novel Solid Oxide Fuel-Cell Fabrication Process and Evaluation. JOM 67:660–667. https://doi.org/10.1007/s11837-015-1296-9

35. de Gans B-J, Duineveld PC, Schubert US (2004) Inkjet Printing of Polymers: State of the Art and Future Developments. Adv Mater 16:203–213. https://doi.org/10.1002/adma.200300385

36. Kunchala P, Kappagantula K (2018) 3D printing high density ceramics using binder jetting with nanoparticle densifiers. Mater Des 155:443–450. https://doi.org/10.1016/j.matdes.2018.06.009

37. Bai Y, Williams CB (2018) Binder jetting additive manufacturing with a particle-free metal ink as a binder precursor. Mater Des 147:146–156. https://doi.org/10.1016/j.matdes.2018.03.027

38. Ansell TY (2021) Current Status of Liquid Metal Printing. J Manuf Mater Process 5:31. https://doi.org/10.3390/jmmp5020031

39. Sachs E, Gleason B, JG Serdy - US Patent 7 077,334, 2006 undefined (2006) Positive pressure drop-on-demand printing

40. Liravi F, Vlasea M (2018) Powder bed binder jetting additive manufacturing of silicone structures. Addit Manuf 21:112–124. https://doi.org/10.1016/j.addma.2018.02.017

41. Miyanaji H, Zhang S, Yang L (2018) A new physics-based model for equilibrium saturation determination in binder jetting additive manufacturing process. Int J Mach Tools Manuf 124:1–11. https://doi.org/10.1016/j.ijmachtools.2017.09.001

42. Marmur A (1988) Penetration of a small drop into a capillary. J Colloid Interface Sci 122:209–219. https://doi.org/10.1016/0021-9797(88)90304-9

43. Bai Y, Wall C, Pham H, et al (2019) Characterizing Binder-Powder Interaction in Binder Jetting Additive Manufacturing Via Sessile Drop Goniometry. J Manuf Sci Eng Trans ASME 141:. https://doi.org/10.1115/1.4041624

44. Sachs EM., Hadjiloucas C;, Allen S;, Helen J. Yoo (1998) Metal and ceramic containing parts produced from powder using binders derived from salt

45. Li S, Cao S (2012) Print parameters influence on parts' quality and calibration with 3DP-part I: Print parameters influence on parts' surface topography. In: Advanced Materials Research. Trans Tech Publications Ltd, pp 1639–1645

46. Castilho M, Gouveia B, Pires I, et al (2015) The role of shell/core saturation level on the accuracy and mechanical characteristics of porous calcium phosphate models produced by 3Dprinting. Rapid Prototyp J 21:43–55. https://doi.org/10.1108/RPJ-02-2013-0015

47. Castilho M, Gbureck U, Groll J, et al (2013) Fabrication of computationally designed scaffolds by low temperature 3D printing. Biofabrication 5:35012–35024. https://doi.org/10.1088/1758-5082/5/3/035012

48. Shanjani Y, De Croos JNA, Pilliar RM, et al (2010) Solid freeform fabrication and characterization of porous calcium polyphosphate structures for tissue engineering purposes. J Biomed Mater Res Part B Appl Biomater 93B:510–519. https://doi.org/10.1002/jbm.b.31610

49. Mondrinos MJ, Dembzynski R, Lu L, et al (2006) Porogen-based solid freeform fabrication of polycaprolactone-calcium phosphate scaffolds for tissue engineering. Biomaterials 27:4399–4408. https://doi.org/10.1016/j.biomaterials.2006.03.049

50. Song Q, Yan H, Liu K, et al (2018) Vertically Grown Edge-Rich Graphene Nanosheets for Spatial Control of Li Nucleation. Adv Energy Mater 8:1800564. https://doi.org/10.1002/aenm.201800564

51. Sachs EM., Cima MJ., Bredt JF;, Khanuja S (1992) Process for removing loose powder particles from interior passages of a body

52. Du W, Ren X, Ma C, Pei Z (2019) Ceramic binder jetting additive manufacturing: Particle coating for increasing powder sinterability and part strength. Mater Lett 234:327–330. https://doi.org/10.1016/j.matlet.2018.09.118

53. Nandwana P, Elliott AM, Siddel D, et al (2017) Powder bed binder jet 3D printing of

Inconel 718: Densification, microstructural evolution and challenges☆. Curr Opin Solid State Mater Sci 21:207–218. https://doi.org/10.1016/j.cossms.2016.12.002

54. Raju K, Yoon DH (2016) Sintering additives for SiC based on the reactivity: A review. Ceram. Int. 42:17947–17962

55. Andrievski RA (1998) The-State-of-the-Art of Nanostructured High Melting Point Compound-Based Materials. In: Nanostructured Materials. Springer Netherlands, pp 263–282

56. Duan W, Fan Z, Wang H, et al Electromagnetic interference shielding and mechanical properties of Si 3 N 4-SiOC composites fabricated by 3D-printing combined with polymer infiltration and pyrolysis. https://doi.org/10.1557/jmr.2017.245

57. Yin X, Travitzky N, Melcher R, Greil P (2006) Three-Dimensional Printing of TiAl3/Al2O3 Composites. Int J Mater Res 97:492–498

58. Mancuso E, Alharbi N, Bretcanu OA, et al (2017) Three-dimensional printing of porous load-bearing bioceramic scaffolds. Proc Inst Mech Eng Part H J Eng Med 231:575–585. https://doi.org/10.1177/0954411916682984

59. Maravola M, Cortes P, Juhasz M, et al (2018) Development of a low coefficient of thermal expansion composite tooling via 3D printing. In: ASME International Mechanical Engineering Congress and Exposition, Proceedings (IMECE). American Society of Mechanical Engineers (ASME), p V002T02A090-V002T02A090

60. Moon J, Caballero AC, Hozer L, et al (2001) Fabrication of functionally graded reaction infiltrated SiC-Si composite by three-dimensional printing (3DP^{TM}) process. Mater Sci Eng A 298:110–119. https://doi.org/10.1016/s0921-5093(00)01282-x

61. Trombetta R, Inzana JA, Schwarz EM, et al (2017) 3D Printing of Calcium Phosphate Ceramics for Bone Tissue Engineering and Drug Delivery. Ann Biomed Eng 45:23–44. https://doi.org/10.1007/s10439-016-1678-3

62. Uhland S, Holman R, DeBear B, et al Three-Dimensional Printing, 3DP™, of Electronic Ceramic Components

63. Du W, Ren X, Ma C, Pei Z (2019) Ceramic binder jetting additive manufacturing: Particle coating for increasing powder sinterability and part strength. Mater Lett 234:327–330. https://doi.org/10.1016/j.matlet.2018.09.118

64. Gaytan SM, Cadena MA, Karim H, et al (2015) Fabrication of barium titanate by binder jetting additive manufacturing technology. Ceram Int 41:6610–6619. https://doi.org/10.1016/j.ceramint.2015.01.108

65. Myers K (2016) Structure-Property Relationship of Binder Jetted Fused Silica Preforms to Manufacture Ceramic-Metallic Interpenetrating Phase Composites. Youngstown State University

66. Gaytan SM, Cadena M, Aldaz M, et al Analysis of ferroelectric ceramic fabricated by binder jetting technology

67. Vlasea M, Toyserkani E, Pilliar R (2015) Effect of Gray Scale Binder Levels on Additive Manufacturing of Porous Scaffolds with Heterogeneous Properties. Int J Appl Ceram Technol 12:62–70. https://doi.org/10.1111/ijac.12316

68. Gonzalez JA, Mireles J, Lin Y, Wicker RB (2016) Characterization of ceramic components fabricated using binder jetting additive manufacturing technology. Ceram Int 42:10559–10564. https://doi.org/10.1016/j.ceramint.2016.03.079

69. Travitzky N, Zimmermann K, Melcher R, Greil P (2006) From Polysaccharides to SiSiC Composites by 3D Printing. In: Narottam P. Bansal J.P. Singh Waltraud M. Kriven (ed) 107th, American Ceramic Society; Advances in ceramic matrix composites XI. American Ceramic Society, Baltimore, MD, pp 37–45

70. Winkel A, Meszaros R, Reinsch S, et al (2012) Sintering of 3D-Printed Glass/HAp Composites. J Am Ceram Soc 95:3387–3393. https://doi.org/10.1111/j.1551-2916.2012.05368.x

71. Sun W, Dcosta DJ, Lin F, El-Raghy T (2002) Freeform fabrication of Ti3SiC2 powder-based structures: Part I - Integrated fabrication process. J Mater Process Technol 127:343–351. https://doi.org/10.1016/S0924-0136(02)00284-4

72. Miyanaji H, Orth M, Akbar JM, Yang L (2018) Process development for green part printing using binder jetting additive manufacturing. Front. Mech. Eng. 13:504–512

73. Sacks MD, Bozkurt N, Scheiffele GW (1991) Fabrication of Mullite and Mullite-Matrix Composites by Transient Viscous Sintering of Composite Powders. J Am Ceram Soc 74:2428–2437. https://doi.org/10.1111/j.1151-2916.1991.tb06780.x

74. Bordia RK, Kang SJL, Olevsky EA (2017) Current understanding and future research directions at the onset of the next century of sintering science and technology. J Am Ceram Soc 100:2314–2352. https://doi.org/10.1111/jace.14919

75. Parab ND, Barnes JE, Zhao C, et al (2019) Real time observation of binder jetting printing process using high-speed X-ray imaging. Sci Rep 9:1–10. https://doi.org/10.1038/s41598-019-38862-7

76. Andreassen E, Andreasen CS (2014) How to determine composite material properties

using numerical homogenization. Comput Mater Sci 83:488–495. https://doi.org/10.1016/j.commatsci.2013.09.006

77. Myers K, Juhasz M, Cortes P, Conner B (2015) Mechanical modeling based on numerical homogenization of an Al2O3/Al composite manufactured via binder jet printing. Comput Mater Sci 108:128–135. https://doi.org/10.1016/j.commatsci.2015.06.031

78. Chandra D, Das GC, Sengupta U, Maitra S (2013) Studies on the reaction sintered zirconia-mullite-alumina composites with titania as additive. Ceramica 59:487–494. https://doi.org/10.1590/S0366-69132013000300021

79. Mummareddy B, Burden E, Carrillo JG, et al (2021) Mechanical performance of lightweight ceramic structures via binder jetting of microspheres. SN Appl Sci 3:402. https://doi.org/10.1007/s42452-021-04404-y

80. Wondraczek L, Heide G, Kilo M, et al (2002) Computer simulation of defect structure in sillimanite and mullites. Phys Chem Miner 29:341–345. https://doi.org/10.1007/s00269-002-0242-x

81. Farzadi A, Solati-Hashjin M, Asadi-Eydivand M, Osman NAA (2014) Effect of layer thickness and printing orientation on mechanical properties and dimensional accuracy of 3D printed porous samples for bone tissue engineering. PLoS One 9:. https://doi.org/10.1371/journal.pone.0108252

82. Snelling DA, Williams CB, Suchicital CTA, Druschitz AP (2017) Binder jetting advanced ceramics for metal-ceramic composite structures. Int J Adv Manuf Technol 92:531–545. https://doi.org/10.1007/s00170-017-0139-y

83. German RM, M. R (1996) Solid-state Sintering Fundamentals. In: Sintering Theory and

Practice. pp 67–141

84. Coble RL (1961) Sintering crystalline solids. I. intermediate and final state diffusion models. J Appl Phys 32:787–792. https://doi.org/10.1063/1.1736107

85. Salvini VR, Pandolfelli VC, Spinelli D (2018) Mechanical Properties of Porous Ceramics. In: Recent Advances in Porous Ceramics. InTech

86. Harrison NJ, Todd I, Mumtaz K (2017) Thermal expansion coefficients in Invar processed by selective laser melting. J Mater Sci 52:10517–10525. https://doi.org/10.1007/s10853-017-1169-4

87. Cortes P, Maravola M, Conner B, et al (2019) Production of Low Coefficient of Thermal Expansion Composite Tooling Manufactured Via 3D Printing. In: SAMPE 2019 - Charlotte, NC

88. Pitchford JE, Stearn RJ, Kelly A, Clegg WJ (2001) Effect of Oxygen Vacancies on the Hot Hardness of Mullite. J Am Ceram Soc 84:1167–1168. https://doi.org/10.1111/j.1151-2916.2001.tb00807.x

89. Viswanath B, Vijayarangan S (2010) A study of the low stress slicing abrasion wear behavior of mullite coatings. Int J Mech Mater Eng 5:

90. Shuttleworth R, Bailey GLJ (1948) The spreading of a liquid over a rough solid. Discuss. Faraday Soc. 3:16–22

91. Shrestha S, Manogharan G (2017) Optimization of Binder Jetting Using Taguchi Method. JOM 69:491–497. https://doi.org/10.1007/s11837-016-2231-4

92. Miyanaji H, Momenzadeh N, Yang L (2018) Effect of printing speed on quality of printed

parts in Binder Jetting Process. Addit Manuf 20:1–10. https://doi.org/10.1016/J.ADDMA.2017.12.008

93. Miyanaji H, Zhang S, Lassell A, et al (2016) Process Development of Porcelain Ceramic Material with Binder Jetting Process for Dental Applications. JOM 68:831–841. https://doi.org/10.1007/s11837-015-1771-3

94. Mendoza Jimenez E, Ding D, Su L, et al (2019) Parametric analysis to quantify process input influence on the printed densities of binder jetted alumina ceramics. Addit Manuf 30:100864. https://doi.org/10.1016/j.addma.2019.100864

95. Osman RB, van der Veen AJ, Huiberts D, et al (2017) 3D-printing zirconia implants; a dream or a reality? An in-vitro study evaluating the dimensional accuracy, surface topography and mechanical properties of printed zirconia implant and discs. J Mech Behav Biomed Mater 75:521–528. https://doi.org/10.1016/j.jmbbm.2017.08.018

96. Parteli EJR, Pöschel T (2015) Particle-based simulation of powder application in additive manufacturing. Powder Technol 288:96–102. https://doi.org/10.1016/j.powtec.2015.10.035

97. Xia M, Nematollahi B, Sanjayan J (2018) Influence of binder saturation level on compressive strength and dimensional accuracy of powder-based 3D printed geopolymer. Mater Sci Forum 939:177–183. https://doi.org/10.4028/WWW.SCIENTIFIC.NET/MSF.939.177

98. Fayazfar H, Salarian M, Rogalsky A, et al (2018) A critical review of powder-based additive manufacturing of ferrous alloys: Process parameters, microstructure and mechanical properties. Mater Des 144:98–128. https://doi.org/10.1016/J.MATDES.2018.02.018

99. Riechmann S, Wunnicke O, Kwade A (2021) The Effect of Binder Loading on the Pore Size of 3D Printed PMMA. Materials (Basel) 14:1–15. https://doi.org/10.3390/MA14051190

100. Montgomery CD, Runger G (2018) Design of Experiments with Several Factors. In: Applied Statistics and Probability for Engineers, 10th ed. John Wiley & Sons, pp 375–433

101. Kićević D, Gašić M, Marković D (1996) A Statistical Analysis of the Influence of Processing Conditions on the Properties of Fused Silica. J Eur Ceram Soc 16:857–864. https://doi.org/10.1016/0955-2219(96)80453-5

102. Yuan Y, Lee TR (2013) Contact angle and wetting properties. Springer Ser Surf Sci 51:3–34. https://doi.org/10.1007/978-3-642-34243-1_1

103. Snoeijer JH, Andreotti B (2008) A microscopic view on contact angle selection. Phys Fluids 20:057101. https://doi.org/10.1063/1.2913675

104. Schuster JM, Schvezov CE, Rosenberger MR (2015) Influence of Experimental Variables on the Measure of Contact Angle in Metals Using the Sessile Drop Method. Procedia Mater Sci 8:742–751. https://doi.org/10.1016/j.mspro.2015.04.131

105. Wong CP, Bollampally RS (1999) Thermal conductivity, elastic modulus, and coefficient of thermal expansion of polymer composites filled with ceramic particles for electronic packaging. J Appl Polym Sci 74:3396–3403. https://doi.org/10.1002/(SICI)1097-4628(19991227)74:14<3396::AID-APP13>3.0.CO;2-3

106. Chavez LA, Ibave P, Wilburn B, et al (2020) The Influence of Printing Parameters, Post-Processing, and Testing Conditions on the Properties of Binder Jetting Additive Manufactured Functional Ceramics. Ceramics 3:65–77.

https://doi.org/10.3390/ceramics3010008

107. Terrani K, Jolly B, Trammell M (2020) 3D printing of high-purity silicon carbide. J Am Ceram Soc 103:1575–1581. https://doi.org/10.1111/jace.16888

108. Kuticheva K V., Pevzner LM, Petrov ML (2015) Synthesis of 5-acetyl derivatives of alkyl 2-furoates and 3-(2-furyl)acrylates. Russ J Gen Chem 85:424–427. https://doi.org/10.1134/S1070363215020127

109. Pivinskii YE, Gorobets FT (1968) High-density fused-silica ceramics. Refractories 9:509–516. https://doi.org/10.1007/BF01284518

110. Li L, Fang Y, Xiao Q, et al (2014) Microwave Dielectric Properties of Fused Silica Prepared by Different Approaches. Int J Appl Ceram Technol 11:193–199. https://doi.org/10.1111/j.1744-7402.2012.02846.x

111. Ushigami Y, Kumano T, Haratani T, et al (2004) Secondary Recrystallization in Grain-Oriented Silicon Steel. Mater Sci Forum 467–470:853–862. https://doi.org/10.4028/WWW.SCIENTIFIC.NET/MSF.467-470.853

4: Material Jetting

Overview

This chapter discusses the research work performed in printed Zirconia via Material Jetting technology. Section 1 introduces the technology and the general procedure used to 3D print the samples via Material Jetting. An excerpt of different materials from literature and the printing parameters is presented in this section. Section 2 discusses the methodology and materials used in this research work. Section 3 presents and discusses the results obtained on the printed samples in terms of their mechanical and thermal performance. Section 4 presents the conclusion of this work.

4.1: Introduction

Material Jetting (MJ) is a 3D printing technology developed from well-known 2D-ink-printing methods. In this method, inks based on powder particles immersed in a liquid binder are jetted from nozzles to fabricate parts by a drop on demand mode [1, 2]. MJ initially started with wax printing in 1994 and was further developed into a multiple jets technology by 1996, followed by polymer printing from proprietary inks in 1998 [3]. From the early 2000s, further advancement concentrated on printing ceramic and metal inks, including production of parts using a heated print head. The technology commonly uses high viscous inks filled with ceramic powders (approximately 50% - 60%) based on nanoparticles to produce layers with high resolution and precision. Here, a UV exposure is applied to each layer to cure the ink. During the building process, a support material is jetted along the ceramic layers, which assist the production of parts with intricate geometries. A schematic representation of the MJ process is shown in figure 4.1. In general, the support material is constituted by salts which can be washed away by water. The green parts printed are post-processed according to the material specifications in order to obtain a final either ceramic or metal part. This printing technology includes advantages like high printing speeds, superior quality, accuracy and inclusion of different materials (polymers, ceramics, metals). This technique was commercialized by companies such as Objet from Stratasys, XJet, Xerox, and HP [4–7].

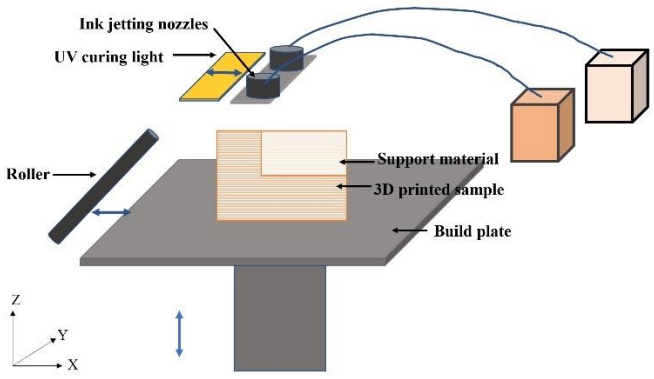

Figure 4.1: Schematic diagram of Material Jetting process.

Material jetting provides several advantages such as high accuracy in building specimens, low surface roughness, high dimensionality, low wastage, and wide printability with several materials. However, it also comes with few disadvantages such as long post-processing methods specially on ceramics, expensive units and inks, and slow printing process [2, 8].

Many times, this technique is classified based on the type of ink dropping, ink suspension. Material Jetting tends to be grouped under the ink-dropping and ink-suspension brand, and is typically classified into the following three categories:

(i) Drop-On Demand (DOD):

In this method, droplets of ink in the form of tiny beads are dropped on the build platform according to the CAD model. In general, DOD units consist of a cutter head either pneumatic or electronically operated with thermal actuators which cuts off the output of ink and support material. Viscosity is one of the major parameters that determines the flow in this method. This approach is used in waxes and polymers in general and avidly used in the field of electronics to print transistors, capacitors, inductors and wearables, OLEDS and energy storage systems (see Figure 4.2) [9–13].

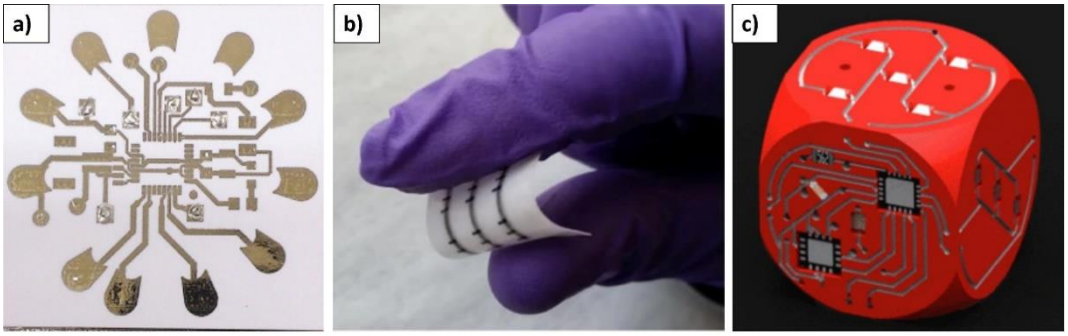

Figure 4.2: (a) A paper circuit board build via silver epoxy [14]. (b) A FET on textile showing the bending features [12]. (c) A 3D printed signal conditioning circuit [13].

(ii) Polyjet Printing:

Polyjet Printing was introduced by Object, a Stratasys base company [15]. In this technique, the photopolymer ink dropped from ink jets is cured into layers to form the

build part. A gel-like support material is used while printing complex parts [16]. A UV curing light is used to cure the ink beads formed from the liquid photocurable resin. This method has a capability for using wide variety of materials. Presently this technique is used to print microfluidic devices, biomedical based applications, mould preparations for castings and electronics for the features like surface finish, printing accuracy, and faster prints (see Figure 4.3) [17–19].

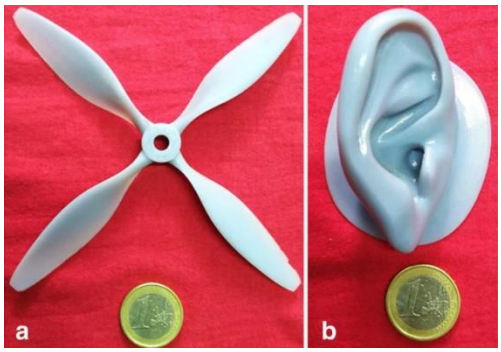

Figure 4.3: Samples printed using Polyjet printing with a glossy fisnish. (a) A printed propeller. (b) Human ear [18].

(iii) NanoParticle Jetting (NPJ):

Nano Particle Jetting is the 3D printing material jetting technique developed by Xjet. This technique uses a liquid ink containing nanoparticles of metal or ceramic powders that are expelled on a heated bed on a layer-by-layer process. During this process the ink is evaporated leaving the particles bound together in the shape of the CAD model. A post-processing is always required when using this technique as the particles need fusing to produce the final part. Presently, XJet produces stainless steel, zirconia and alumina inks that are printable using their Carmel unit, see Figure 4.4. The printing methodology is acclaimed to be used for dental crowns, hearing aids, surgical tools, and tool materials.

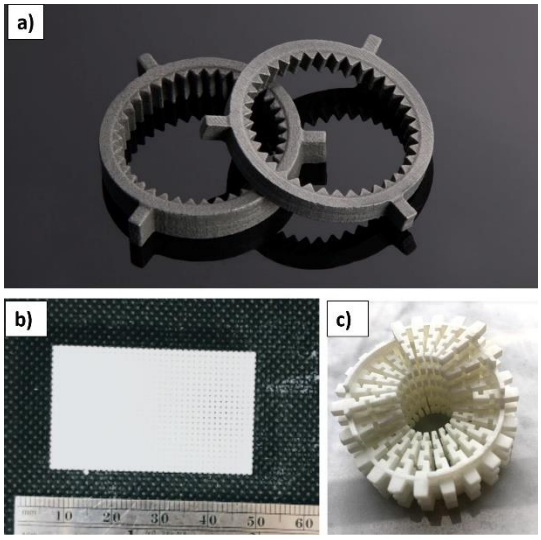

Figure 4.4: Samples printed using Nano-Particle Jetting (NPJ) technology. (a) Stainless Steel gears printed on XJet [20]. (b) Lattice part printed for antennae applications. (c) Refractory parts fabricated for aerospace applications.

4.1.1: Literature Review

Although material jetting was commercially introduced by Stratasys, it was Xiang et al [21] who developed the inkjet method for printing ceramics. From the initial efforts on printing solid oxide fuel cells using a piezoelectric drop on demand method, several improvements such as reliable dropping systems, repetition of printing, and post-treatments have been studied and incorporated to deliver reliable parts.

Ceramic Ink drop-generation and printing:

Previous research work on suspended ceramics inks use rheology as the main criterion for printing accurate and reliable parts. Derby et al [1] worked on ceramic inks and measured the feasibility of ink jet printing. These studies have included CFD measurements using drop velocity (μ), density (ρ), and surface tension (γ). Further rheological works have compared the droplet formation and detachment that is required for the ink jetting [22–24]. It has been concluded that a 40% volume suspension of ceramic powders with Newtonian behavior are the most suitable inks for an optimal 3D MJ printing [25]. As a part of these measurements, the Ohnesorge number (Oh) (Equation 4.1)

was identified as the appropriate characterization number for inkjet printing, where is the dynamic viscosity, γ, ρ, a are the surface tension, density, and characteristic length, respectively [26]. Fluid systems with 0.1≤ Oh ≤ 1 indicates a suitable number for inkjet printing without errors like formations of no-drop and satellite drops (unwanted drops) [1, 27].

$$Oh = \frac{\eta}{\sqrt{\gamma \rho a}} \qquad (4.1)$$

Along with the Ohnesorge number, an acoustic resonance from the nozzle or print head also plays an important role in the drop stabilization and printing. Generally, the nozzle in the printhead dampens the frequency of the droplet generation.

Presently, three different techniques classify the droplet generation from the printheads: (a) Continuous ink jet printing (CIJ), (b) Drop-on-Demand inkjet printing (DOD), and (c) Electro-static inkjet printing (EIJ) [28]. CIJ technique uses small sized drops which are deposited on the built platform by using two differently charged plates. The disadvantages using this method include generation of steam and satellite droplets, ink wastage and contamination along with droplet imprecision. DOD printing uses mechanical or electrical actuation to drop the liquid using surface tension/capillary forces as the driving process to deposit the ink. EIJ printing operates on the surface potential driving force and drops the ink droplets in the form of electro-sprays. The spraying threshold defines the droplet size to form individual drops. Martin et al [29] concluded that a proper understanding can only be obtained from physical observation of the droplet formation under the influence of shear rates, acoustic modes of print heads, drop formation, aerodynamics and electrostatic interaction of the drop. However, most of the systems use drop-on-demand printers for possible 3D inkjet printing.

The analysis of the formed drops and the interaction with solids, is commonly performed through the sessile drop method; where the liquid-solid interaction is function of the contact angles, gravity, time allowed for stability, velocity of drop arrival, direction of travel, and capillary forces

[26, 27, 30, 31].

Drop-on-Demand printing methodology uses capillary forces to form a drop. Here, the evaporation of the binder is the most common technique that is used for the next subsequent layer/drop to coalesce with the previous layers. Indeed, following the drop stabilization, the coalescence of adjacent drops is the next important concept in ink jetting. Davis [32, 33] proposed some limiting conditions for stabilizing the formation of an ink line. He worked on stabilizing the narrow liquid stream on the solid surface was formulated using fixed contact angles. Overlapping of drops to build a continuous line were to maintain a smaller drop diameter, drop spacing. A parallel line with irregular spherical caps is maintained by the width of bead and contact angle equilibrium without any hysteresis [34, 35]. It has been reported that a low deposition rate is required in order to reduce the drop curvature and to improve consistency [34]. Along with this, the dynamic viscosity created by the printing nozzles and high material density aids in rapid building rates [36].

Independently of the droplet generation process, these are evaporated by UV curing light. This process can produce a defect called “coffee staining”, which is caused by a receding drop with the next forming drop [37]. This creates a void between the drops without coalescence. The main reason for this condition, is the temperature and density difference along the drop, where the drop has a higher density and temperature at its center while decreasing along the edge. Deegan et al [37] developed a numerical model to compare the solute and dried solution. They observed a phenomenon where evaporation was seen on the edges of the drops resulting in the formation of a ring or a missing contact pinning base for the successive drop [38]. A solution that was provided to avoid the coffee staining was positioning a hole above the nozzle to leak out the high pressure formed due to the temperature. Apart from the ink viscosity and operational temperatures which define the production of reliable parts, the geometry and post-processing consideration also allow the production og samples with good geometry tolerance and definition.

A better understanding of all these parameters in the ink formation can be employed for layer-by-layer printing of CAD files.

Materials:

Although ink jetting method on introduction is most suitable for polymer printing, eventually solid suspensions were included using ceramics and metals [26–28, 30]. Noguera et al [39] studied the Newtonian flow of ink with at least 10% PZT micron sized powder and observed the viscosity effects the green part formation with printing layers of approximately 90μm. Additional studies have investigated temperature while printing that affected the line morphology during ink jetting [34, 40]. An optimal delay in the drop disposal and spacing combined with high temperatures (room temperature $\leq T \leq 60$) eliminated the coffee ring effect in the printing. It is also to be noted that the heating the substrate might bring back this coffee ring defect. Biswas et al [41] used a piezoelectric ink jetting method to print high-protein lysozymes using glycerol-water mixture. They did not observe any temperature effect on the ink despite any substrate change was seen at room temperature. Organic printable inks have also been developed to fabricate high-performance semi-conductors substrates [42]. Sekitani et al [43] used the inkjet technology to print metal contacts in organic semiconductors to improve performance and lower power consumption.

Ceramic components using Zirconia for intestinal capsule in imaging applications were printed using a polymer ink with 10 vol% solid loading [39]. Paraffin wax is one other binder used to print solid loadings using ink jet printing technology. This method allows higher solid loading and successfully print finite bodies [36, 44]. Mott et al [45] worked on producing alumina and zirconia inks using piezoelectric DOD ink jetting method. Functionally graded alumina-zirconia composite with 70% alumina and few restrained zirconia parts due to its high density. Seerden et al [36] printed 30-40 vol% alumina filled samples with high spatial resolution. The team used a hot-melt ink jet printing method using DOD printer.

Biomaterials is one of the other major applications using solid oxide loadings using collagen, hyaluronic acid, polymer hydrogels, PEG, gelatin, alginates, fibrin, and PMMA [23, 24, 46–49]. However, the bio-ink printing is made in controlled temperatures.

Although this technique was industrially used to print polymers by HP [50], this still needs to be developed for other materials.

4.2: Printing Technique and Testing

In this present research, a NanoParticle Jetting (NPJ) technique was used to fabricate fully dense bulk and lattice ceramics structures. A series of post-thermal treatments were investigated and related to the mechanical performance of the printed parts.

4.2.1: Printing Unit

An XJet Carmel 1400 unit was used in this research work (see Figure 4.5). This system uses a liquid dispersion method to drop both liquid suspensions, the nano-ceramic particle ink and the supporting material. The unit is capable of jetting ultra-thin layers (~10µm) with high spatial resolution (~20 µm). After the samples are built, the supporting material is generally disintegrated under flow of water without affecting the built part. The printed green samples are subsequently post-processed through a sintering cycle where the solid suspensions fused, and the liquid ink is evaporated to deliver the final dense samples.

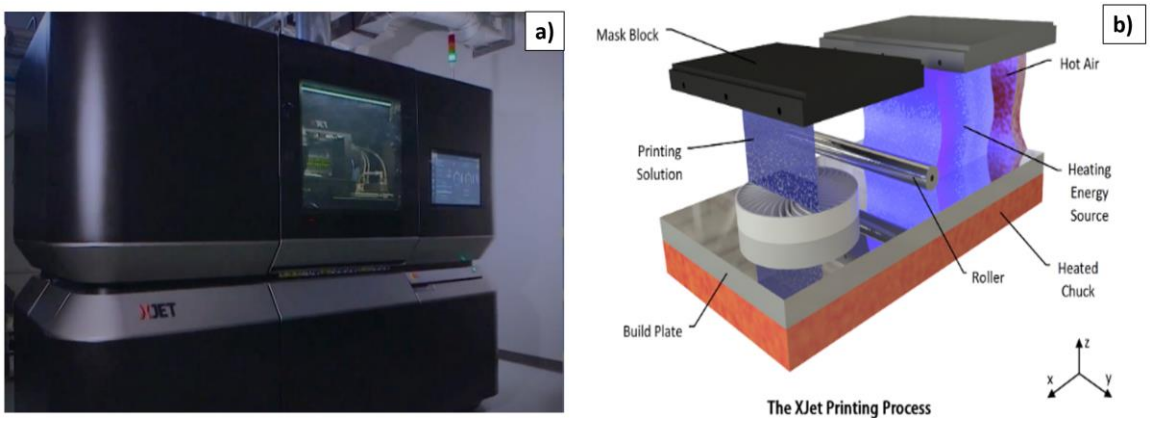

Figure 4.5: Ceramic Printing Unit used in this research (a) XJet Carmel 1400, based on Nano-Particle Jetting technique. (b) Schematic of the NPJ working [51].

This unit has a biggest build tray (500 X 280 cm^2) with a build height capability of 200 cm. The printing unit is equipped with 512 ink jetting nozzles that selectively disperse ink and twelve ink jets for dropping support material. The built plate is has the ability to heat up from 160°C to 230°C with a hot air dryer.

4.2.2: Materials

Zirconia suspended liquid inks were used in this research (Xjet Part# 7250001) along with support material (Xjet Part# 7250004), both provided by XJet ©. A 40.9 weight% solid zirconia suspension (from TGA analysis) was used in the ink with 96% zirconia stabilized with 4% yittria (Y_2O_3) with an average particle size of 10 microns (see Figure 4.6). Although Silica was evaluated for printing via AM techniques, Zirconia was selected for MJ process since NPJ is a proprietary technique. In fact, a first unit in the USA with only zirconia as a printable resin. However, in future silica inks can be worked for printing via MJ.

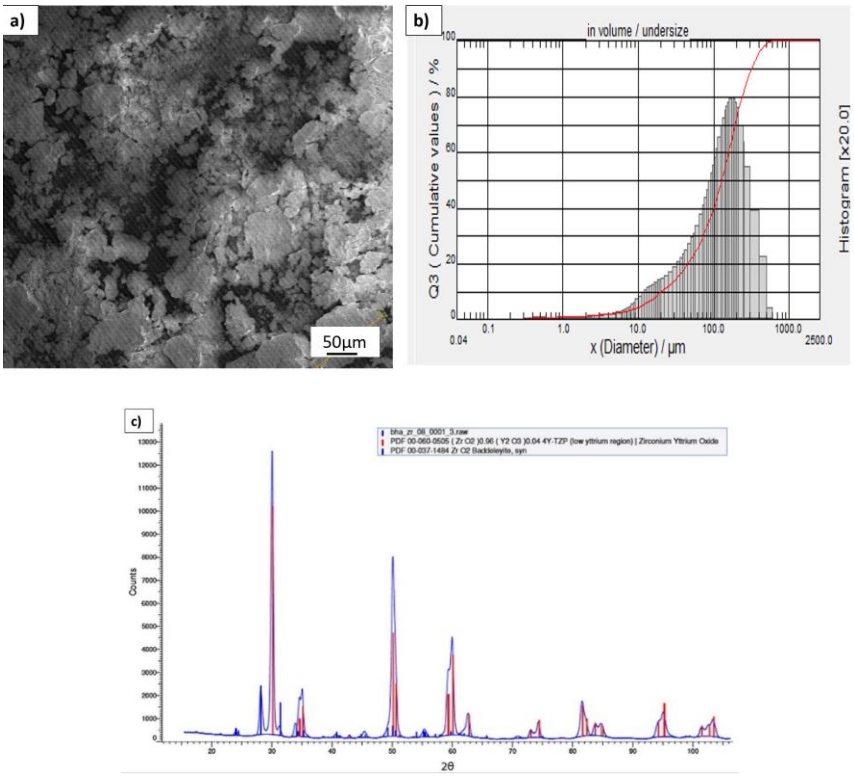

Figure 4.6: Resin and powder properties of the Zirconia ink. (a) A SEM image of the Zirconia particles used in the resin. The image also shows the diameter of the largest particle (~150 µm). (b)

A particle-size distribution histogram of the Zirconia powder. The powder was collected by evaporating the binder from the XJet ink. (c) XRD of the Zirconia printed sample [51].

From the literature, zirconia occurs in 3 different phases: monoclinic, tetragonal and cubic transforming according to the temperatures 1173^{o}C and 2730^{o}C while melts at 2690^{o}C [52]. However, only tetragonal and cubic phases of Zirconia are suitable for engineering and bio-medical applications due their high toughness, thermal, and chemical resistance under extreme conditions [53, 54].

4.2.3: Characterization

The printed specimens were sintered in a Mitutoyo atmospheric furnace (model CD-6" CSX/KJ-1700A). The particle size was analyzed on a CILAS 1190 laser particle size analyzer. The density of the samples was measured by the Archimedes principle. The ink used in this research was also tested using a TGA analysis to determine the weight % of solute present in the ink. Sintered samples were then evaluated to study their mechanical, optical, analytical and thermal properties. A Bruker Prospector X8 Diffractometer with 40kV X ray source was used to analyze the crystallographic details along with their phases. The phase quantification was performed on TOPAS 3.0 software using the XRD results. Optical and SEM analysis was made on a Keyence VHX-7000 optical microscope and on a Keysight FE-SEM, respectively. TEM analysis of the sample was performed on a JEOL 2100 Scanning/Transmission Electron Microscope. The TEM samples were prepared on a JEOL JIB-4500 SEM accompanied with Focused Ion Beam (FIB), Gas Injection Systems (GIS) allowing C and W depositions, and the Omniprobe nano manipulator.

Mechanical evaluation of the bulk and lattice structured parts was made on an Instron Universal Testing machine under quasi-static conditions (0.5 mm/sec) at room temperature. Here, the testing of the compressive and flexural strength of the bulk samples was based on the ASTM C1424 and ASTM C1161 standards, while the testing of the lattice samples followed the ASTM C364 and ASTM C1674 standards, respectively. In contrast, the fracture toughness testing was performed

following the ASTM C1421. A "a/w" ratio of 0.52 and a g(a/w) of 0.8875 were calculated for the fracture toughness samples with a single edge notch configuration.

Surface area measurements were made on a Micromeritics AutoChem 2920 system employing Brunauer-Emmett-Teller analysis (BET) using liquid nitrogen as medium with 30% N_2/He to measure the absorption of gas molecules by zirconia samples using the ASTM C1274 standard. The Coefficient of Thermal Expansion (CTE) measurements were carried out on a TA-Q400 EM unit. The samples were heated from room temperature (~ 25°C) to 550 °C in a quasi-static approach with a load of 0.5 N with a ramp rate of 2 °C /min, following the ASTM E831-06.

A Gibson-Ashby model for the open cellular structures was used to estimate the compressive strength of the lattice samples [55]. Equation (4.2) was used to calculate the compressive strength of the samples. Here σ_f^* is the crushing strength of the cellular material (MPa), σ is the strength of the cell-wall material (MPa), which in this case are the values from the solid compressive strength of zirconia, ρ refers to the density of the cellular structure (kg/m^3), ρ_s is the density of the cell-wall material (kg/m^3), and C, is a dimensionless constant (~0.65 for brittle crushing of ceramics).

$$\frac{\sigma_f^*}{\sigma} = C\left(\frac{\rho}{\rho_s}^{3/2}\right) \qquad (4.2)$$

4.3: Results and Discussion

Samples printed in three different orientations (0°, 45° and 90°) were sintered in different conditions, with a similar maximum sintering temperature of 1450°C (see Figure 4.7). Different sintering conditions were established by the company according to the geometry of the samples. The custom sintering profile was defined for this research using literature and experiments from samples printed via other AM techniques [56]. Analytical, optical and mechanical characterization of the samples in each orientation was also performed here. Across the diverse sintering profiles explored, it was found that an average shrinkage of 17.6% in the X and Y directions and 8.9% in the Z direction was observed on all after post-processed samples.

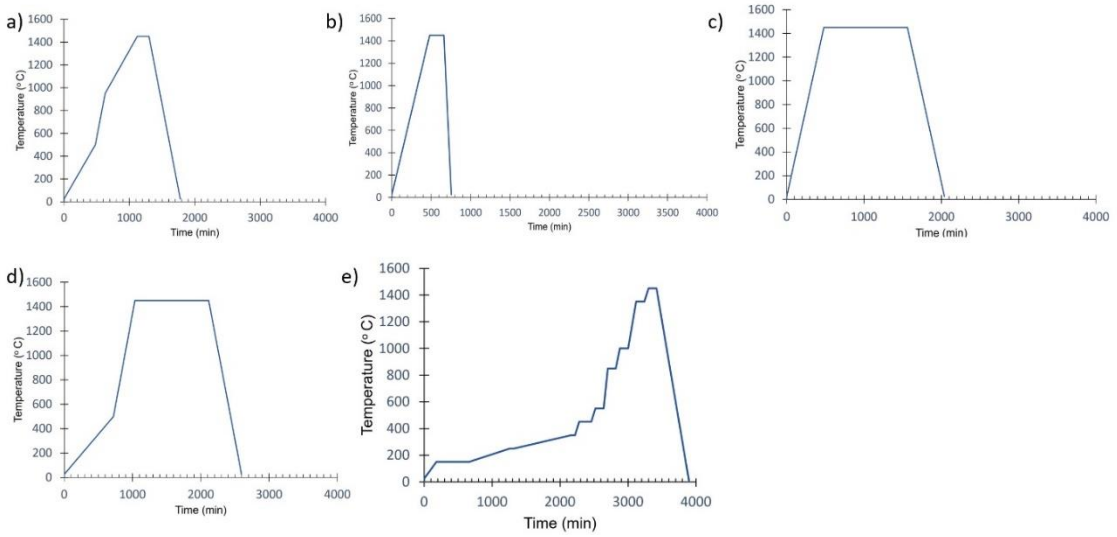

Figure 4.7: Post-processing profiles used to sinter the printed green specimens. The profiles were named and designed according to the part geometry by Xjet. (a) Default, (b) Short, (c) Long, (d) Bulky, (e) Custom.

After the post processing step, the samples were investigated for density with at least three samples under each sintering profile. An average density of 5.86 g/cc was found in the sintered samples whereas the green samples had a density of 4.36 g/cc (see Figure 4.8). This value is 1.34% lower than the theoretical value of conventionally manufactured zirconia.

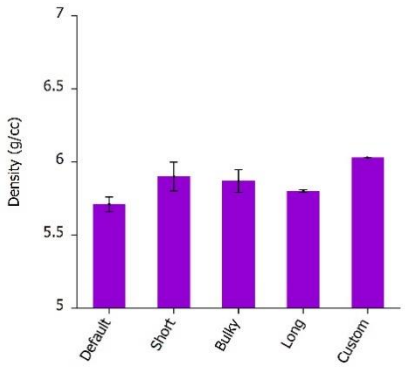

Figure 4.8: Density of the samples sintered in different profiles [57]. The figure also shows the standard deviation observed across the different densities from different sintering profiles.

The sintered samples were tested to evaluate the crystallinity and phases occurred during the different sintering conditions. The XRD showed that the sintered bulky samples had higher crystallinity in comparison to other sintering profiles (see Figure 4.9).

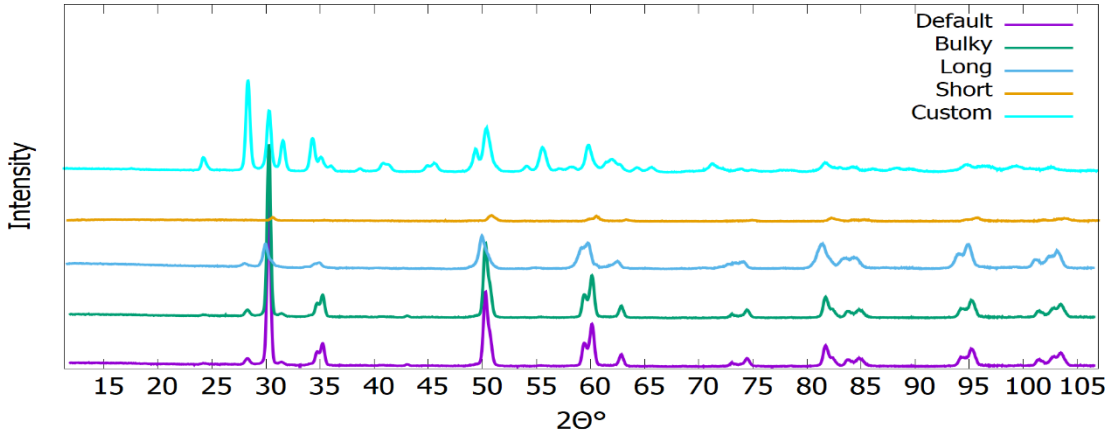

Figure 4.9: XRD results of the printed samples sintered in different conditions. The samples sintered in the default and bulky profiles show highest peaks indicating higher crystallinity in comparison to samples printed in other conditions.

A phase analysis on the sintered samples revealed that the zirconia material based on 75% crystalline and 25% amorphous phases with a monoclinic and tetragonal crystalline constitution as shown in Figure 4.10. A Rietveld analysis was performed on the samples sintered, and it was revealed that the samples following the custom sintered profile had a high amount of monoclinic crystalline phase. A factor that might be due to the long sintering cycle [58].

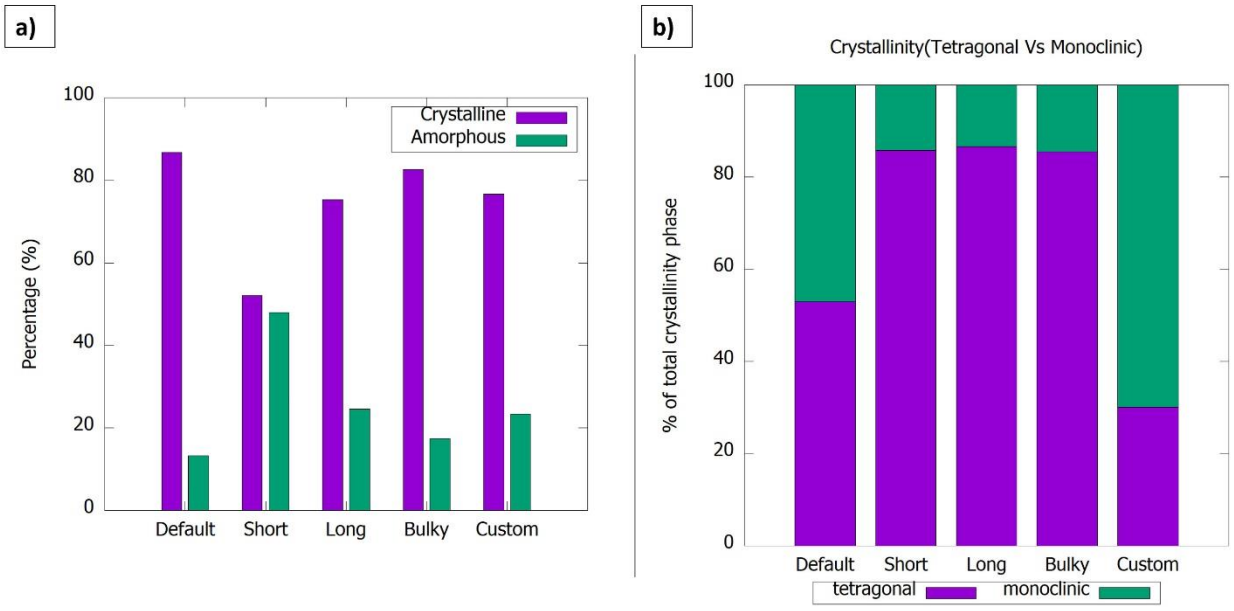

Figure 4.10: XRD results of the printed samples sintered in different conditions. (a) Crystalline Vs Amorphous % in the samples. (b) Phase measurements observed in the sintered samples analyzed on TOPAS 3.0 using Reitveld analysis.

TEM analysis was also performed on the sample sintered in the custom profile to understand the phase distribution in addition to the grain distribution (see figure 4.11). The TEM analysis shows the presence of strong crystalline phase supported by a Laue pattern. The crystalline phase shows the distribution of aligned grains which resulted in an adequate mechanical strength [59, 60].

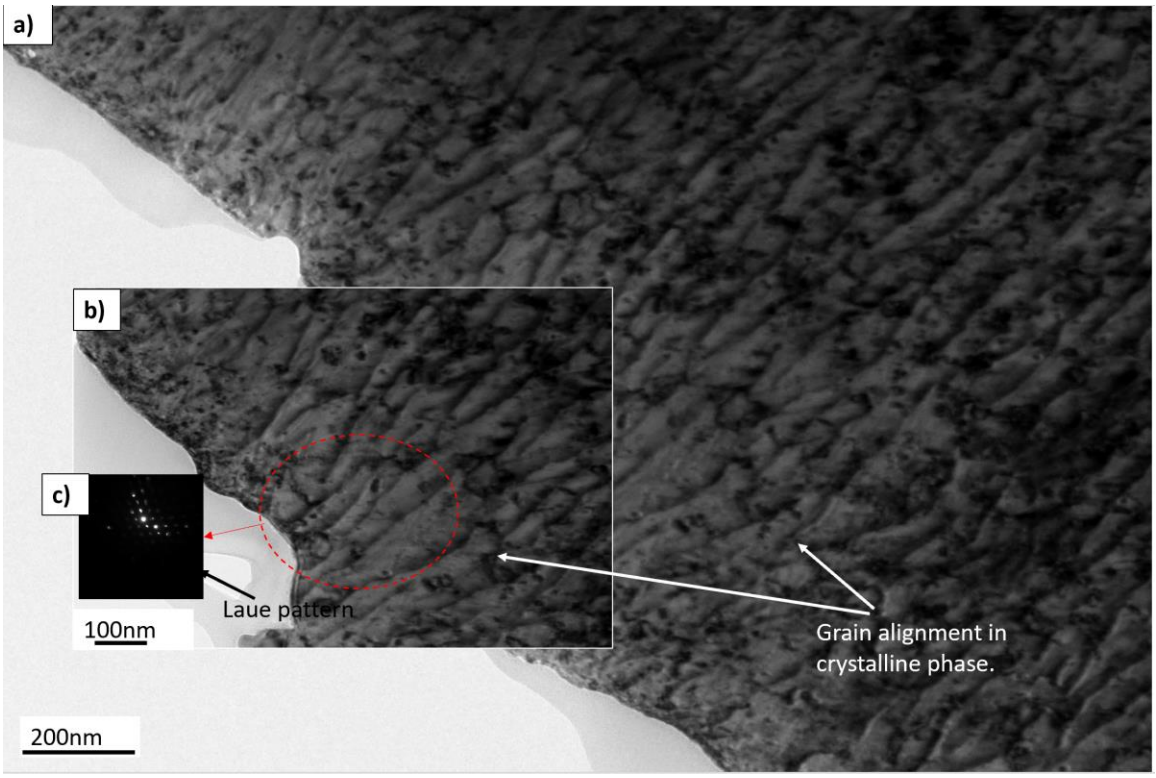

Figure 4.11: TEM image of the sample sintered in custom profile. (a) TEM image of the sample showing crystalline phase. (b) A high magnified image of the crystalline phase showing the distribution of the grains in the samples. (c) Laue pattern of the sample indicating the crystalline pattern.

BET analysis was carried out on the samples for determining the surface area of the investigated systems. It was observed that the samples had a surface area of 8.69, 5.73, and 0.72 m^2/g regarding the powder, green and sintered samples, respectively. From the BET analysis, the samples showed a reduction in the surface area from powder to green to sintered samples indicating the shrinkage and interdiffusion among the particles [60, 61].

A detailed discussion of the mechanical, thermal and morphological properties of the samples produced under the different sintering processes is presented in the following section.

The CTE analysis of the samples sintered in all the profiles showed an average value of 11.44 $\mu m/m.\ K^{-1}$ across the different post-thermal profiles (Figure 4.12). Here, the variation among the

different print orientations did not account for the CTE variations [62]. It is expected that there would be slight low or no variation in the CTE among all the directions. Figure 4.12 shows that the samples sintered under the custom profile displayed a higher CTE than the other sintering environments. This might be due to the higher temperatures and longer sintering times in the custom process. Paula et al [63] have reported that CTE values are highly dependent on the sintering process and temperatures, along with the addition of stabilizing elements or elemental oxides. Such conditions influence the phases formed in the sintered system. Daou [64] reported that one of the reasons for high CTEs could be also due to the presence of monoclinic phase, which could also induce an increase in the flexural and fracture toughness of the samples [65].

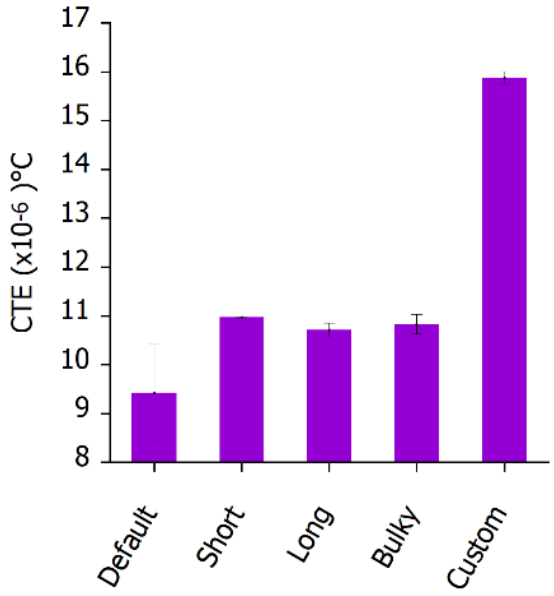

Figure 4.12: CTE analysis of the samples sintered in different sintering profiles.

An average compressive strength of 1565 MPa was seen in the samples sintered across the different profiles, with a higher strength on those systems printed in the 0˚orientation (see Figure 4.13). Osman et al [66] have also seen similar features and have related such mechanism to the layer adhesion in each orientation during the printing process. when samples were printed in different directions. The figure shows that the printed samples showed a 21% higher strength than the

samples fabricated via conventional methods [67]. The SEM analysis of the sintered samples under the long profile showed presence of pinholes, which could have led to a premature failure of the samples. The presence of pinholes might be due to the resin gasification in the samples during the sintering process. A similar pattern was observed by Aboushelib [68]. The reason behind this might be due to the fast-heating ramp which resulted in a binder evaporation. Such degasification appeared to have continued during the dwelling time. Figure 4.14 shows a microscopy analysis of the surface of the sintered samples describing the features of the investigated zirconia. The results show that the heating ramp during the sintering profile plays a key role in their mechanical performance.

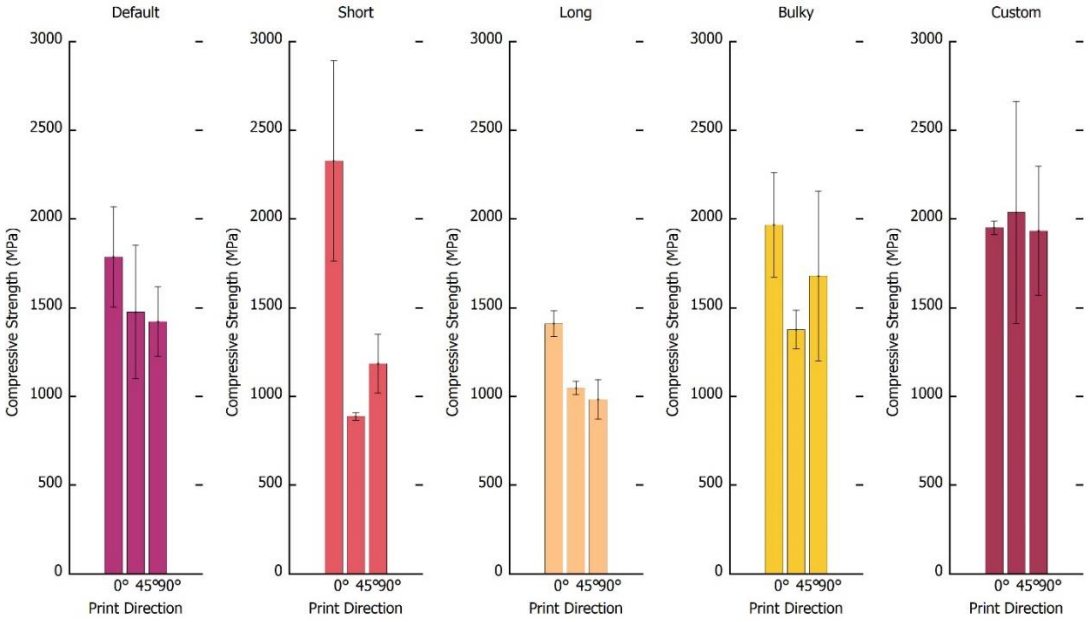

Figure 4.13: Compressive Strength of the samples sintered in different post-processing profiles [57].

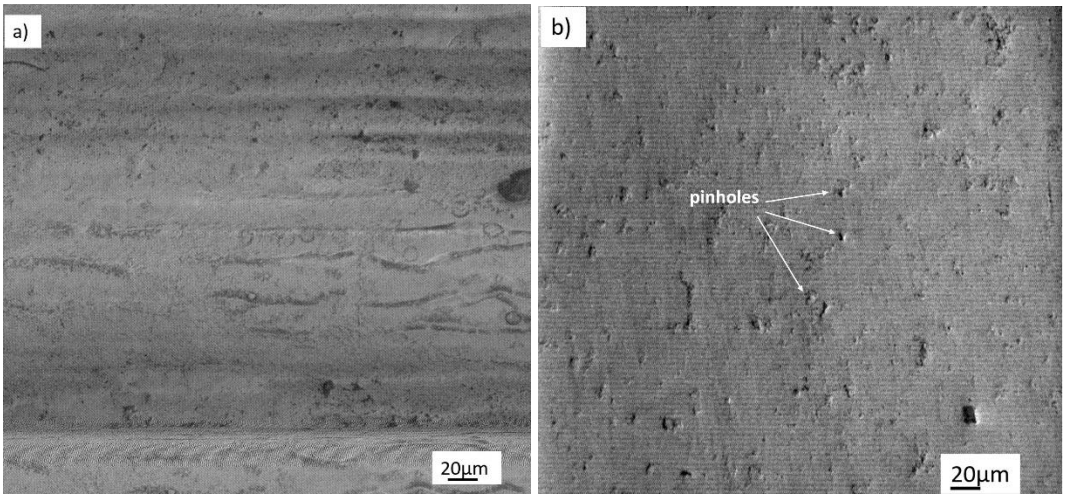

Figure 4.14: SEM pictures of the surface of the compression samples taken at 210x magnification. (a) Surface of sample sintered under default profile where a homogenous layering was observed. (b) Surface of the samples sintered under the long profile, where defects such as pinholes were observed [57].

An average flexural strength of 430 MPa was seen across all the sintered samples (see figure 4.15). The highest strength was observed in samples printed in the 0˚orientation as seen in the compression samples which can also be related to the reason reported by Osman et al [68]. In contrast to the compression results (where the highest strength was observed in custom sintering profile), the long sintering profile seems to have resulted in an adequate flexural strength. Optical analysis of the flexural parts did not exhibit any pinhole features as displayed in the samples printed during the compression testing (see figure 4.16). A difference in the surface finish of the samples was observed, and it is associated with the manufacturing process. It also seems that the samples printed in the XJet system had a high degree of variability during the washing stage, where the support system is removed by a salt solvent. A phenomenon where the samples either swell or erode due to the variabilities in the washing process. It is worth mentioning, that the samples printed in 90˚orientation and subjected to custom sintering profile did not show a homogenous mechanical performance as expected. It was seen that their flexural strength reduced to almost half of the value

recorded in 0˚ orientation. This can also be associated with the printing and post-processing variability. In fact, the variability was very peculiar in the samples printed in 0˚ orientation and sintered in the short thermal profile, where the strength in all the printing orientations was similar. This was different to the results seen in the compression testing where 0˚ orientation samples had a higher strength than the samples printed in the 45˚, 90˚ orientations. Additionally, relatively high standard deviations were observed in the flexural results of the 0˚ orientation samples sintered under the short thermal profile, highlighting the irregularities in the printing process. In overall this study shows a lower flexural strength with high variability than the recorded-on samples manufactured using conventional processing methods. This could be associated with the printing and washing process variability. However, the samples are still seem suitable for secondary loading applications.

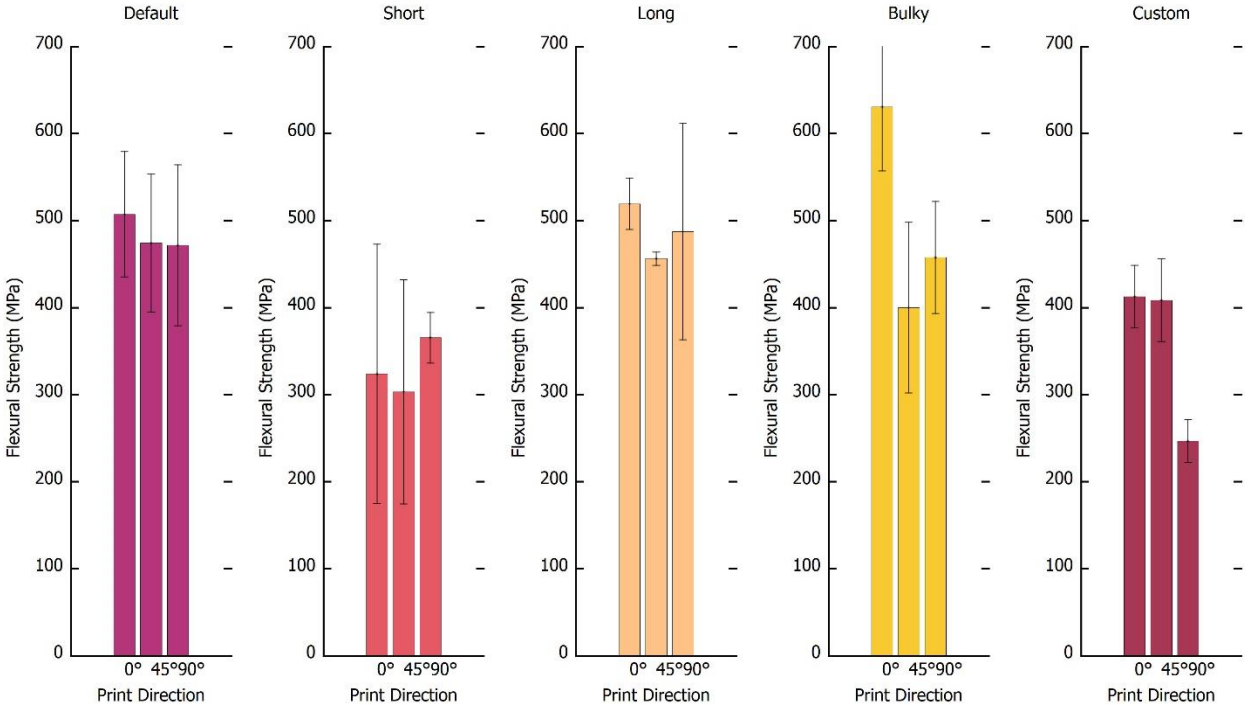

Figure 4.15: Flexural Strength of the samples sintered in different post-processing profiles [57].

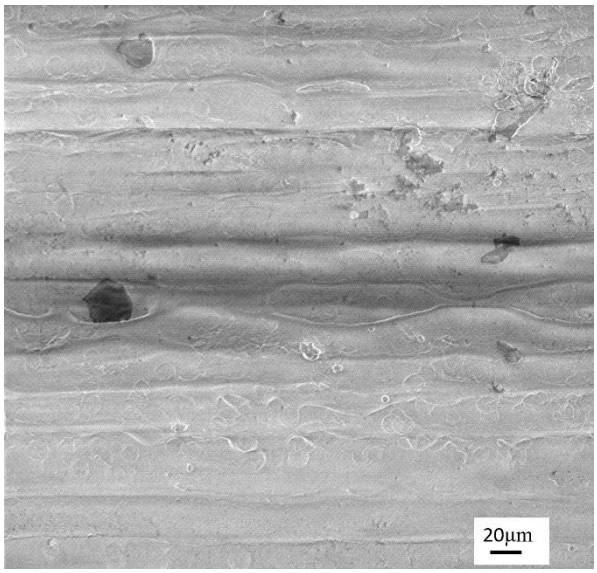

Figure 4.16: A representative SEM pictures of the surface of the flexural sample sintered in long thermal profile, taken at 330x magnification.

The fracture toughness of the printed and sintered samples was analyzed using a single-edge notch testing method. An average fracture toughness of 1.71 MPa√m was seen in the samples printed and sintered across all the thermal profiles (see figure 4.17). The samples displayed a shear fracture that propagated along the notch. Fracture toughness of the samples seen in this research was relatively lower by at least 2.4 times when compared to the samples fabricated using conventionally pressing methods [69]. From the figure 4.17, it was also observed that the fracture toughness does not depend on the printing orientation. Although, it was expected that the samples printed in 0˚ orientation would yield higher toughness than the samples in the 45˚, 90˚ orientations. This mechanism was also observed previously in the additive manufactured samples that were fabricated via BJP and extrusion based techniques [62, 70]. However, from the toughness values seen in the figure 4.17 it is assumed the presence of a high degree of inter-diffusion is achieved in the particles during the sintering process. This resulted in an even toughness value in all the printing orientations [62, 69]. The long and the bulky thermal profiles resulted in the samples with lower fracture toughness probably due to the higher crystallinity

based on a tetragonal phase as seen in the XRD. On the other hand, the average difference in the toughness between these two profiles and the rest of the sintering conditions was about 1MPa√m, a value that can be associated within the experimental testing. The highest fracture toughness was observed in the samples sintered in custom sintering profile, a mechanism related to the high presence of monoclinic crystal phase also seen by Ruiz and Readey [71].

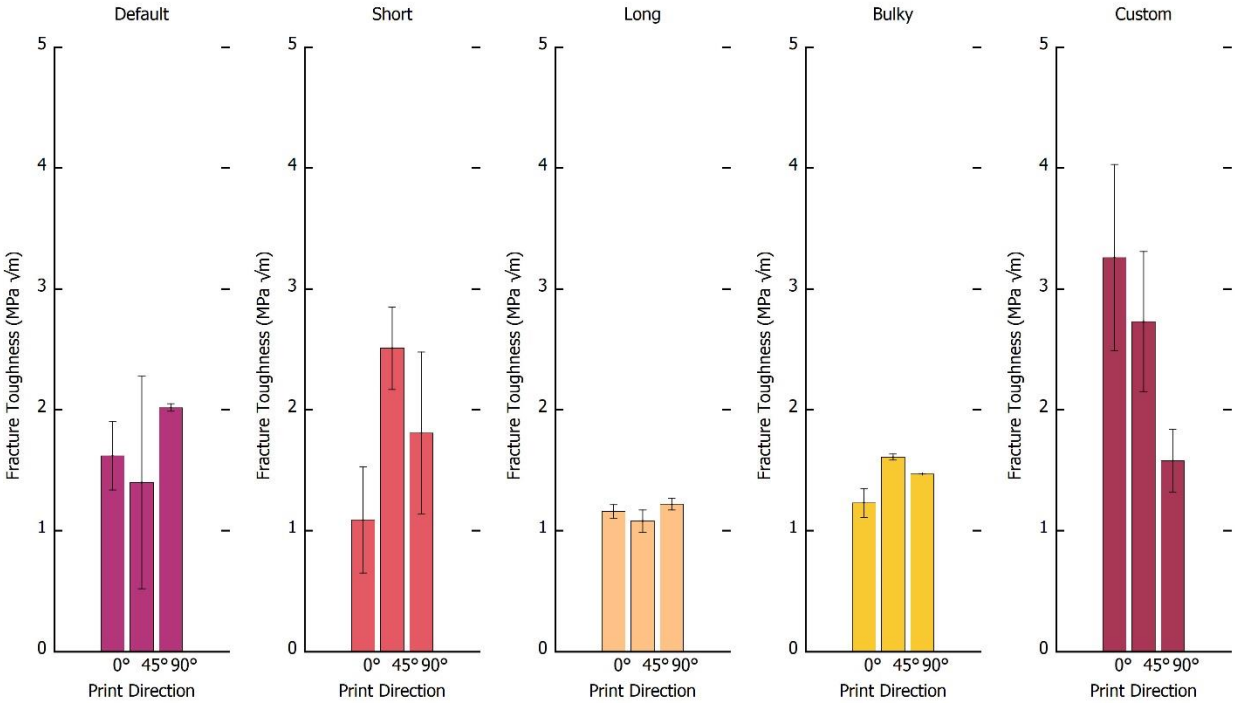

Figure 4.17: Fracture Toughness of the samples sintered in different post-processing profiles [57].

Along with this testing of bulk-solid samples, a mechanical characterization on lattice structures (in the 0˚ orientation) based on 0.6- and 0.8-mm unit cells was also performed (see Figure 4.18). Here, the lattice structures were sintered under the bulk and custom profile. These lattices showed a density of 4.92 and 5.71 g/cc for 0.6- and 0.8-mm unit cell lattice samples, respectively (when sintered in the bulk profile). The density increased to 5.87 and 6.03 g/cc when sintered under the custom sintering profile. However, a nominal density decrease was seen in the lattice samples in comparison to the sintered bulk samples. The samples with a unit cell size 0.6 mm had a nominal density of 69.2% while the samples with 0.8 mm had a density of 83.9%. An average

compressive strength of 175MPa and 225.99MPa were observed for the 0.6mm and 0.8mm unit cell lattice structures, respectively -when also sintered under bulk sintering profile (see figure 4.18 a, and b). A 0.8 mm unit cell sample was tested for the compressive test while sintering under the custom profile, and a strength of 382.8 MPa was observed (see figure 4.18c). It was observed that the samples displayed a brittle crushing mechanism, after testing them under compressive and flexural conditions (see Figure 4.19). The values observed in the lattice structures were about 5 times lower than that was recorded in the printed solid samples.

A 3-point bending was performed on these intricate geometry specimens and a flexural strength value of 60.6 MPa and 91.68 MPa were seen for 0.6- and 0.8-mm unit cell lattices when they were sintered in bulk sintering profile, similarly the 0.8mm unit cell samples had a flexural strength of 99.62 MPa when post-processed in the custom sintering profile. No data was recorded for the 0.6 mm unit cell due to technical issues with the machine.

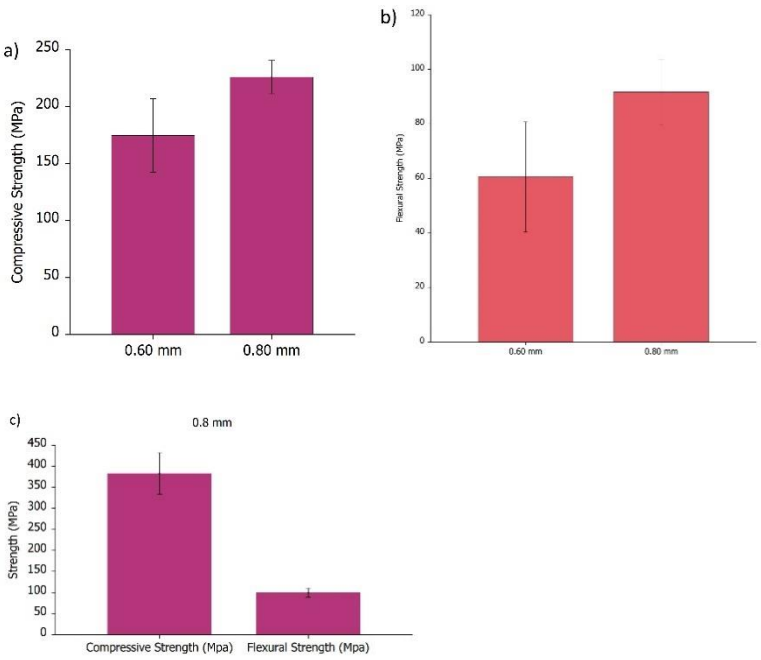

Figure 4.18: Mechanical properties of the lattice samples sintered in bulky and custom sintering profiles [57]. (a) Compressive Strength of 0.6- and 0.8-mm unit cell lattice structures sintered in bulky profile. (b) Flexural Strength of 0.6- and 0.8-mm unit cell lattice structures sintered in bulky

profile. (c) Compressive and Flexural strength of 0.8-mm unit cell lattice structures sintered in custom profile.

The results seen in the sintered samples under the custom profile were higher than the samples sintered in bulk profile which might be a result of the relatively longer sintering profile (about 57 hours). However, the flexural strength was similar in both profiles which can be accounted for the printing variability, and the effect of the open areas in the lattice structures that promotes the defects in the tensilemode during the flexural testing.

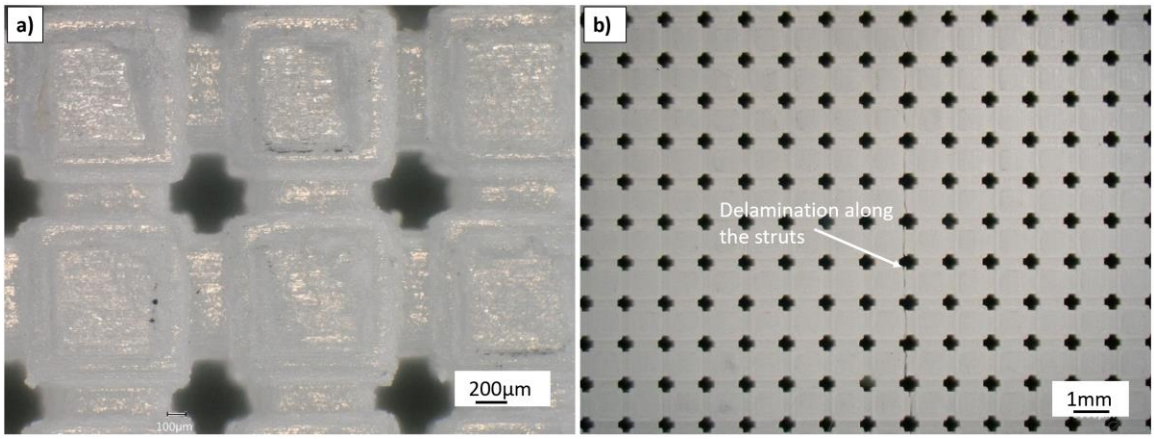

Figure 4.19: Lattice samples before and after compression testing. (a) A 0.8 mm unit cell lattice structure before testing. (b) A 0.8 mm unit cell lattice structure after compressive testing. A fracture was observed which extended along the struts along the unit cells.

Optical analysis of the samples showed that the failure initiates at the struts between the unit cells (see Figure 4.20). An estimation of the compressive strength was made using the Gibson-Ashby model for open cellular ceramics which indicated that their compressive strength varied by 10% in both bulky and custom profiles. The fluctuation might be due to the inter-diffusion variations across the sintering profiles [55]

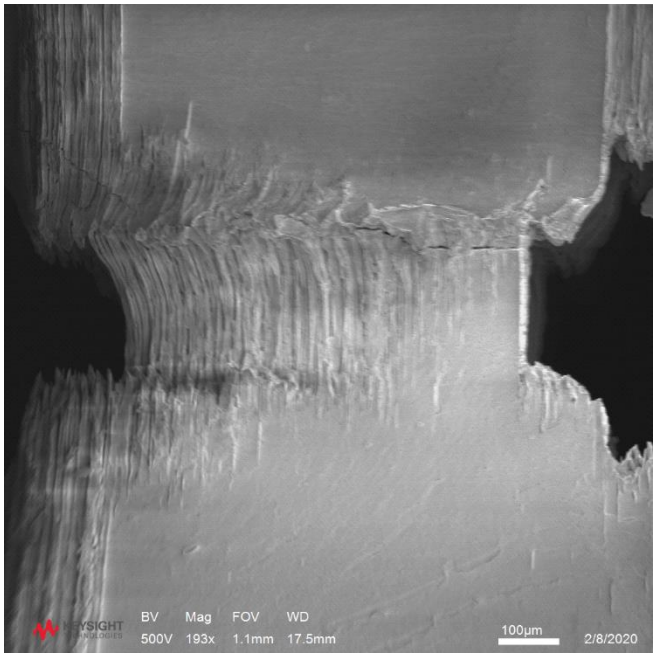

Figure 4.20: SEM image of the surface of the lattice structure after compressive testing. The crack initiated along the struts, causing the failure of the lattice samples [57].

The samples were also investigated for post-processing improvements using a Hot Isostatic Pressing (HIP) method. Here, the internal cracks in the samples printed in the 0° orientation and sintered in bulk sintering profile were investigated. The samples were subjected to 160 MPa pressure at 1350°C in an Argon atmosphere followed by a rapid cooling process. A CT scanning was used to observe the samples before and after the HIPing process using at least 3 samples (see figure 4.21). The 2-D images show a removal of the internal cracks of about 30 microns. This technique can be utilized to eliminate cracks, defects and delaminations, and to improve the structural density.

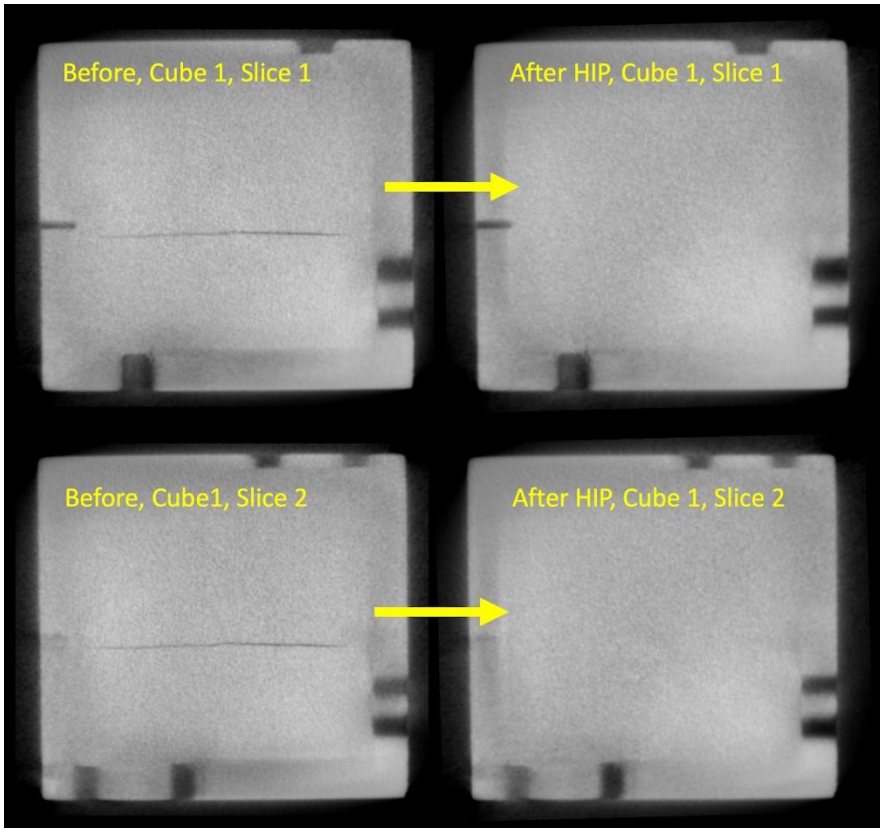

Figure 4.21: CT-Scan of zirconia parts before (left) and after a HIPing cycle (right). The HIPping process seems to close the observed internal crack on the printed specimens. The indentions on the outer edges are the embossed text describing the plane of each external surface and match as expected for the before and after images in each slice [57].

4.3.1: Applications

This state-of-art technology is presently used in the fields of orthodontics, dentistry, electronics and semiconductor industries. Dominant applications lie in digital printing of electronics, computer generated patterns using high frequency, graphic designs and high resolution jetting [42, 71, 72]. Unlike subtractive manufacturing where material is wasted, material jetting is used for low-cost productions and rapid production in thin-film devices, MEMs, sensors, energy-harvesting devices and low-temperature co-fired structures [73–75].

The samples printed in the present research were intended to be used in antenna applications. Measurements of microwave dielectric constants in electro-magnetic fields were measured and they

were suitable for antenna applications at room and high temperature conditions [51, 76–78]. Zirconia parts especially printed via NPJ can be employed in dental and high temperature applications due to their enhanced density and lower porosity based on intricate geometries.

4.4: Conclusions

Zirconia samples using NPJ were successfully printed and investigated for mechanical and thermal properties using different post-processing profiles. The samples were printed with a layer thickness as low as 10 microns and showed an average shrinkage of 17% after the sintering process.

All the sintered samples under the different profiles have shown a higher compressive and flexural strength in 0◦orientation while toughness samples exhibited high variability among the three printed directions. It was also shown that the samples sintered with slower ramp rates displayed higher strength and crystallinity than the samples sintered using higher ramp rates. It can also be concluded here that the samples had a high degree of diffusion among the particles where the orientation had affinity and high contact angle. The post-processing of the samples in each profile seemed to be dependent on the cleaning process where salts are removed. Leaving the salts behind, might be responsible for higher crystallinity. The residual stresses left in the samples after the thermal debinding and thermal prost-processing can also contribute to the failure in the sintered samples across the different profiles investigated.

The lattices printed here show that the technology can be used for accurately building intricate structures. The mechanical strength results displayed by the lattice structures were lower in comparison to the solid samples which might be due to the in-built hollow units. However, they appear to be mechanically robust enough to be used for electromagnetic applications.

HIPing was investigated on the sintered solid samples and it was observed that this post-processing technique can remove the internal cracks which were discovered via CT-Scan. It is also expected that this process can be applied to other AM printed ceramic samples to remove porosity and cracks in structural components and thereby improving the mechanical strength.

Future studies that need to consider in this research are as follows:

- Study the separation of support materials from the samples and their influence on the crystallinity of the samples.
- Analysis of the ink using DSC and DMTA which could provide details on the crystallization leading to higher strengths.
- Characterization of the samples under dynamic conditions as zirconia is a high-performance ceramic.
- Extend the use of the NPJ printed samples in different applications given its low degree of porosity, and the capability of producing intricate geometries.
- Fabrication of inks using different ceramic suspensions and characterization of their mechanical properties.

4.5: References

1. Reis N, Derby B (2000) Ink Jet Deposition of Ceramic Suspensions: Modeling and Experiments of Droplet Formation. MRS Proc 624:65. https://doi.org/10.1557/PROC-624-65

2. Material jetting - MJ, NPJ, DOD | Make. https://make.3dexperience.3ds.com/processes/material-jetting. Accessed 14 May 2021

3. The Evolution of Material Jetting 3D Printing - GrabCAD Blog. https://blog.grabcad.com/blog/2017/12/04/evolution-material-jetting-3d-printing/. Accessed 7 Jan 2021

4. Objet30 PolyJet 3D Printer | Stratasys. https://www.stratasys.com/3d-printers/objet30. Accessed 14 May 2021

5. Technology. https://www.xjet3d.com/technology/. Accessed 14 May 2021

6. Additive Manufacturing Innovation with 3D Printing - Xerox. https://www.xerox.com/en-us/innovation/insights/additive-manufacturing-3d-printing. Accessed 14 May 2021

7. HP Multi Jet 3D Printing Technology - The Latest 3D Printing Technology from HP | HP® Official Site. https://www8.hp.com/us/en/printers/3d-printers/products/multi-jet-technology.html. Accessed 14 May 2021

8. A Comprehensive Guide to Material Jetting 3D Printing - AMFG. https://amfg.ai/2018/06/29/material-jetting-3d-printing-guide/. Accessed 25 May 2021

9. Redinger D, Molesa S, Yin S, et al (2004) An ink-jet-deposited passive component process for RFID. IEEE Trans Electron Devices 51:1978–1983. https://doi.org/10.1109/TED.2004.838451

10. Zhang F, Saleh E, Vaithilingam J, et al (2019) Reactive material jetting of polyimide insulators for complex circuit board design. Addit Manuf 25:477–484. https://doi.org/10.1016/j.addma.2018.11.017

11. Liu Y, Cui T, Varahramyan K (2003) All-polymer capacitor fabricated with inkjet printing technique. Solid State Electron 47:1543–1548. https://doi.org/10.1016/S0038-1101(03)00082-0

12. Carey T, Cacovich S, Divitini G, et al (2017) Fully inkjet-printed two-dimensional material field-effect heterojunctions for wearable and textile electronics. Nat Commun 8:1–11. https://doi.org/10.1038/s41467-017-01210-2

13. MacDonald E, Salas R, Espalin D, et al (2014) 3D printing for the rapid prototyping of structural electronics. IEEE Access 2:234–242. https://doi.org/10.1109/ACCESS.2014.2311810

14. Andersson HA, Manuilskiy A, Haller S, et al (2014) Assembling surface mounted components on ink-jet printed double sided paper circuit board. Nanotechnology 25:094002. https://doi.org/10.1088/0957-4484/25/9/094002

15. What is Material Jetting and how does material jetting work? https://engineeringproductdesign.com/knowledge-base/material-jetting/. Accessed 29 May 2021

16. (49) PolyJet Technology - YouTube. https://www.youtube.com/watch?v=Som3CddHfZE. Accessed 29 May 2021

17. Castiaux AD, Pinger CW, Hayter EA, et al (2019) PolyJet 3D-Printed Enclosed Microfluidic Channels without Photocurable Supports. Anal Chem 91:6910. https://doi.org/10.1021/acs.analchem.9b01302

18. Pugalendhi A, Ranganathan R, Chandrasekaran M (2020) Effect of process parameters on mechanical properties of VeroBlue material and their optimal selection in PolyJet technology. Int J Adv Manuf Technol 108:1049–1059. https://doi.org/10.1007/s00170-019-04782-z

19. Udroiu R, Braga IC (2017) Polyjet technology applications for rapid tooling. In: MATEC Web of Conferences. EDP Sciences

20. » Systems. https://www.xjet3d.com/systems/. Accessed 9 Jun 2021

21. Xiang QF, Evans JRG, Edirisinghe MJ, Blazdell PF (1997) Solid freeforming of ceramics using a drop-on-demand jet printer. Proc Inst Mech Eng Part B J Eng Manuf 211:211–214. https://doi.org/10.1243/0954405971516194

22. Aegerter MA (2004) Ink-Jet Printing. In: Sol-Gel Technologies for Glass Producers and Users. Springer US, Boston, MA, pp 127–130

23. Skardal A, Atala A Biomaterials for Integration with 3-D Bioprinting. https://doi.org/10.1007/s10439-014-1207-1

24. Barui S (2021) 3D inkjet printing of biomaterials: Principles and applications. Med

DEVICES SENSORS 4:e10143. https://doi.org/10.1002/mds3.10143

25. Wong LY, Lim GH, Ye T, et al (2012) Jettable fluid space and jetting characteristics of a microprint head. J Fluid Mech 713:109–122. https://doi.org/10.1017/jfm.2012.440

26. Derby B (2011) Inkjet printing ceramics: From drops to solid. J Eur Ceram Soc 31:2543–2550. https://doi.org/10.1016/j.jeurceramsoc.2011.01.016

27. Reis N, Ainsley C, Derby B (2005) Viscosity and Acoustic Behavior of Ceramic Suspensions Optimized for Phase-Change Ink-Jet Printing. J Am Ceram Soc 88:802–808. https://doi.org/10.1111/j.1551-2916.2005.00138.x

28. Derby B (2015) Additive Manufacture of Ceramics Components by Inkjet Printing. Engineering 1:113–123

29. Martin GD, Hoath SD, Hutchings IM (2008) Inkjet printing - The physics of manipulating liquid jets and drops. J Phys Conf Ser 105:012001. https://doi.org/10.1088/1742-6596/105/1/012001

30. Schuster JM, Schvezov CE, Rosenberger MR (2015) Influence of Experimental Variables on the Measure of Contact Angle in Metals Using the Sessile Drop Method. Procedia Mater Sci 8:742–751. https://doi.org/10.1016/j.mspro.2015.04.131

31. Reis N, Derby B (2000) Ink Jet Deposition of Ceramic Suspensions: Modeling and Experiments of Droplet Formation. MRS Proc 624:65. https://doi.org/10.1557/PROC-624-65

32. Schiaffino S, Sonin AA (1997) Formation and stability of liquid and molten beads on a solid surface. J Fluid Mech 343:95–110. https://doi.org/10.1017/S0022112097005831

33. Davis SH (1980) Moving contact lines and rivulet instabilities. Part 1. The static rivulet. J Fluid Mech 98:225–242. https://doi.org/10.1017/S0022112080000110

34. Soltman D, Subramanian V (2008) Inkjet-printed line morphologies and temperature control of the coffee ring effect. Langmuir 24:2224–2231. https://doi.org/10.1021/la7026847

35. Stringer J, Derby B (2010) Formation and stability of lines produced by inkjet printing. Langmuir 26:10365–10372. https://doi.org/10.1021/la101296e

36. Seerden KAM, Reis N, Evans JRG, et al (2001) Ink-Jet Printing of Wax-Based Alumina Suspensions. J Am Ceram Soc 84:2514–2520. https://doi.org/10.1111/j.1151-2916.2001.tb01045.x

37. Deegan RD, Bakajin O, Dupont TF, et al (1997) Capillary flow as the cause of ring stains from dried liquid drops. Nature 389:827–829. https://doi.org/10.1038/39827

38. Deegan RD, Bakajin O, Dupont TF, et al (2000) Contact line deposits in an evaporating drop. Phys Rev E - Stat Physics, Plasmas, Fluids, Relat Interdiscip Top 62:756–765. https://doi.org/10.1103/PhysRevE.62.756

39. Noguera R, Lejeune M, Chartier T (2005) 3D fine scale ceramic components formed by ink-jet prototyping process. J Eur Ceram Soc 25:2055–2059. https://doi.org/10.1016/j.jeurceramsoc.2005.03.223

40. Farzadi A, Solati-Hashjin M, Asadi-Eydivand M, Osman NAA (2014) Effect of layer thickness and printing orientation on mechanical properties and dimensional accuracy of 3D printed porous samples for bone tissue engineering. PLoS One 9:. https://doi.org/10.1371/journal.pone.0108252

41. Biswas TT, Yu J, Nierstrasz VA (2019) Effects of ink characteristics and piezo-electric inkjetting parameters on lysozyme activity. Sci Rep 9:1–11. https://doi.org/10.1038/s41598-019-54723-9

42. Chung S, Cho K, Lee T (2019) Recent Progress in Inkjet-Printed Thin-Film Transistors. Adv. Sci. 6:1801445

43. Sekitani T, Noguchi Y, Zschieschang U, et al (2008) Organic transistors manufactured using inkjet technology with subfemtoliter accuracy. Proc Natl Acad Sci U S A 105:4976–4980. https://doi.org/10.1073/pnas.0708340105

44. Willems E, Turon-Vinas M, Camargo dos Santos B, et al (2021) Additive manufacturing of zirconia ceramics by material jetting. J Eur Ceram Soc 41:5292–5306. https://doi.org/10.1016/j.jeurceramsoc.2021.04.018

45. Mott M, Evans JRG (1999) Zirconia/alumina functionally graded material made by ceramic ink jet printing. Mater Sci Eng A 271:344–352. https://doi.org/10.1016/s0921-5093(99)00266-x

46. Berry DB, Yu C, Chen S (2020) Biofabricated three-dimensional tissue models. In: Principles of Tissue Engineering. Elsevier, pp 1417–1441

47. Patra S, Young V (2016) A Review of 3D Printing Techniques and the Future in Biofabrication of Bioprinted Tissue. Cell Biochem. Biophys. 74:93–98

48. Hewes S, Wong AD, Searson PC (2017) Bioprinting microvessels using an inkjet printer. Bioprinting 7:14–18. https://doi.org/10.1016/j.bprint.2017.05.002

49. Compaan AM, Christensen K, Huang Y (2017) Inkjet Bioprinting of 3D Silk Fibroin Cellular Constructs Using Sacrificial Alginate. ACS Biomater Sci Eng 3:1519–1526. https://doi.org/10.1021/acsbiomaterials.6b00432

50. Online MJF 3D Printing service | Functional prototypes & low-run production parts | Get an instant quote | 3D Hubs. https://www.3dhubs.com/3d-printing/processes/mjf/. Accessed 4 May 2020

51. Oh Y, Bharambe V, Mummareddy B, et al (2019) Microwave dielectric properties of zirconia fabricated using NanoParticle Jetting™. Addit Manuf 27:586–594. https://doi.org/10.1016/j.addma.2019.04.005

52. Scott HG (1975) Phase relationships in the zirconia-yttria system. J Mater Sci 10:1527–1535. https://doi.org/10.1007/BF01031853

53. Hannink RHJ, Kelly PM, Muddle BC (2000) Transformation toughening in zirconia-containing ceramics. J Am Ceram Soc 83:461–487. https://doi.org/10.1111/j.1151-2916.2000.tb01221.x

54. Li P, Chen I -W, Penner-Hahn JE (1994) Effect of Dopants on Zirconia Stabilization—An X-ray Absorption Study: I, Trivalent Dopants. J Am Ceram Soc 77:118–128. https://doi.org/10.1111/j.1151-2916.1994.tb06964.x

55. Ashby MF (1983) MECHANICAL PROPERTIES OF CELLULAR SOLIDS. Metall Trans A, Phys Metall Mater Sci 14 A:1755–1769. https://doi.org/10.1007/BF02645546

56. Ceramic Materials. https://www.lithoz.com/en/our-products/materials. Accessed 24 Jul 2021

57. Mummareddy B, Negro D, Bharambe VT, et al (2021) Mechanical properties of material jetted zirconia complex geometries with hot isostatic pressing. Adv Ind Manuf Eng 100052. https://doi.org/10.1016/j.aime.2021.100052

58. Sohn YH, Biederman RR, Sisson RD (1994) Isothermal oxidation of physical vapor deposited partially stabilized zirconia thermal barrier coatings. J Mater Eng Perform 3:55–60. https://doi.org/10.1007/BF02654499

59. Madhav Reddy K, Guo JJ, Shinoda Y, et al (2012) Enhanced mechanical properties of nanocrystalline boron carbide by nanoporosity and interface phases. Nat Commun 3:1–7.

https://doi.org/10.1038/ncomms2047

60. Madan DS, German RM (1990) Quantitative assessment of enhanced sintering concepts. Powder Metall 33:45–52. https://doi.org/10.1179/pom.1990.33.1.45

61. German RM, M. R (1996) Solid-state Sintering Fundamentals. In: Sintering Theory and Practice. pp 67–141

62. Mummareddy B, Burden E, Carrillo JG, et al (2021) Mechanical performance of lightweight ceramic structures via binder jetting of microspheres. SN Appl Sci 3:402. https://doi.org/10.1007/s42452-021-04404-y

63. Łada P, Miazga A, Konopka K, Szafran M (2018) Sintering behavior and thermal expansion of zirconia–titanium composites. J Therm Anal Calorim 133:55–61. https://doi.org/10.1007/s10973-017-6817-z

64. Daou EE (2014) The Zirconia Ceramic: Strengths and Weaknesses. Open Dent J 8:33–42. https://doi.org/10.2174/1874210601408010033

65. Juntavee N, Dangsuwan C (2018) Role of coefficient of thermal expansion on bond strength of ceramic veneered yttrium-stabilized zirconia. J Clin Exp Dent 10:e279–e286. https://doi.org/10.4317/jced.54605

66. Osman RB, van der Veen AJ, Huiberts D, et al (2017) 3D-printing zirconia implants; a dream or a reality? An in-vitro study evaluating the dimensional accuracy, surface topography and mechanical properties of printed zirconia implant and discs. J Mech Behav Biomed Mater 75:521–528. https://doi.org/10.1016/j.jmbbm.2017.08.018

67. Piconi C, Maccauro G (1999) Zirconia as a ceramic biomaterial. Biomaterials 20:1–25

68. Aboushelib MN, Kleverlaan CJ, Feilzer AJ (2008) Effect of zirconia type on its bond strength with different veneer ceramics. J Prosthodont 17:401–408.

https://doi.org/10.1111/j.1532-849X.2008.00306.x

69. Turon-Vinas M, Anglada M (2018) Strength and fracture toughness of zirconia dental ceramics. Dent. Mater. 34:365–375

70. Faes M, Vleugels J, Vogeler F, Ferraris E (2016) Extrusion-based additive manufacturing of ZrO2 using photoinitiated polymerization. CIRP J Manuf Sci Technol 14:28–34. https://doi.org/10.1016/j.cirpj.2016.05.002

71. Ruiz L, Readey MJ (1996) Effect of heat treatment on grain size, phase assemblage, and mechanical properties of 3 mol% Y-TZP. J Am Ceram Soc 79:2331–2340. https://doi.org/10.1111/j.1151-2916.1996.tb08980.x

72. Bracke P High Throughput Industrial Digital Printing

73. Chiu CH, Chiu WWW, Yang MH, et al (2007) Novel image trimming algorithm for use with ink jet printing fabrication. J Imaging Sci Technol 51:514–519. https://doi.org/10.2352/J.ImagingSci.Technol.(2007)51:6(514)

74. Haga KI, Kamiya Y, Tokumitsu E (2018) Direct imprinting of indium-tin-oxide precursor gel and simultaneous formation of channel and source/drain in thin-film transistor. In: Japanese Journal of Applied Physics. Japan Society of Applied Physics, p 02CB14

75. Lien DH, Kao ZK, Huang TH, et al (2014) All-printed paper memory. ACS Nano 8:7613–7619. https://doi.org/10.1021/nn501231z

76. Vaseem M, Ghaffar FA, Farooqui MF, Shamim A (2018) Iron Oxide Nanoparticle-Based Magnetic Ink Development for Fully Printed Tunable Radio-Frequency Devices. Adv Mater Technol 3:1700242. https://doi.org/10.1002/admt.201700242

77. Johnson K, Zemba M, Conner BP, et al (2019) Digital Manufacturing of Pathologically-Complex 3D Printed Antennas. IEEE Access 7:39378–39389.

https://doi.org/10.1109/ACCESS.2019.2906868

78. Rojas-Nastrucci EA, Weller T, Aida VL, et al (2014) A study on 3D-printed coplanar waveguide with meshed and finite ground planes. In: 2014 IEEE 15th Annual IEEE Wireless and Microwave Technology Conference, WAMICON 2014. IEEE Computer Society

79. Castro J, Rojas-Nastrucci EA, Ross A, et al (2017) Fabrication, Modeling, and Application of Ceramic-Thermoplastic Composites for Fused Deposition Modeling of Microwave Components. IEEE Trans Microw Theory Tech 65:2073–2084. https://doi.org/10.1109/TMTT.2017.2655057

5: Sintering and Diffusion Kinetics in Silica and IPCs printed via Vat Polymerization

Overview

This chapter discusses the mechanisms responsible for the diffusion process of ceramic systems based on silica during the sintering state and the transformation process of silica samples into interpenetrated composites (IPCs). Section 1 discusses the background of ceramics diffusion models and reviews previous models reported in the literature. Section 2 focuses on the theory behind particle fusion in silica and silica-aluminum samples. The theoretical and mathematical approach to define the kinetics of the sintering process are discussed in this section. Optical analysis of the samples was provided for more details on the sintering process. Section 3 concludes this chapter with the most important regarding the modeling of sintered ceramics.

5.1: Introduction

The production of 3D printed ceramics needs a mandatory post-processing step where samples are subjected to a thermal cycle, commonly called "sintering" (see Figure 5.1). Sintering consists of "*subjecting the material to higher temperatures, where it behaves as fluid aiding in forming coherent bonds between particles and so forming a strong solid structure"* [1]. This process predominantly occurs at the atomic/grain level leading to advantages like higher density, mechanical strength, and thermal resistance.

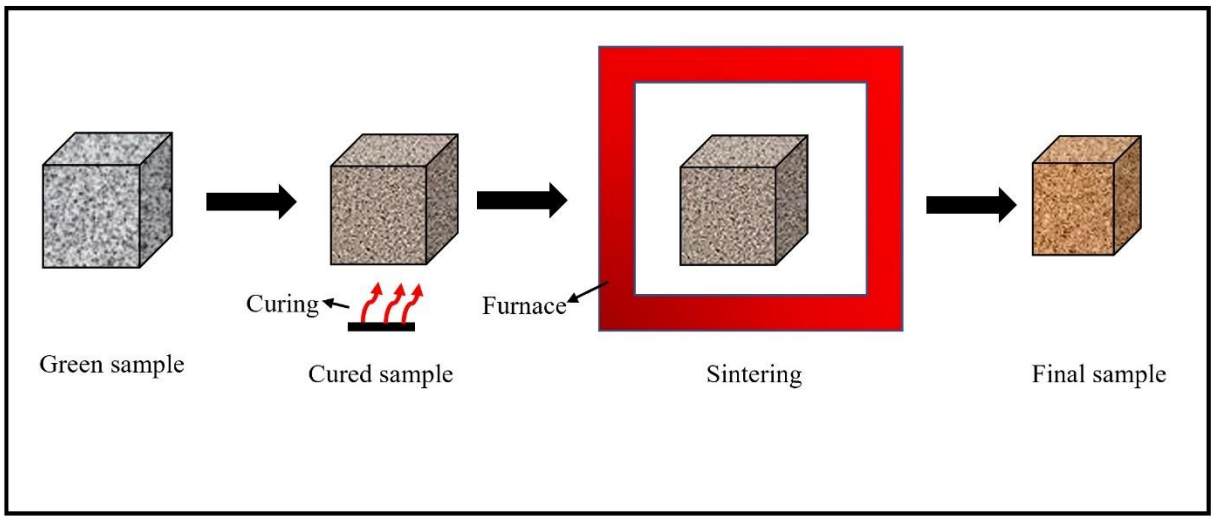

Figure 5.1: Schematic diagram of the sintering process.

There have been several studies from 1918 to illustrate the mechanisms of sintering and the transport mechanisms for densification of materials under the influence of different process parameters. Key controlling parameters like temperature, time, particle size, and sintering environment have been investigated for several kinetic models [2–6]. Some of the common changes observed in the sintered parts in comparison to green samples are (a) change in the dimensions of particle size with smaller grains, (b) higher density, (c) lower porosity. These features are responsible for enhancing the material properties like young's modulus, ductility, crystallinity, and resistance towards high temperatures. The structural retention in the sample is

also a result for maintaining equilibrium among the particles due to the chemical potential gradient that arises as a result of temperature step-up.

The densification mechanism in ceramics occurs in three different stages: initial, intermediate, and final [3, 4, 7–9]. In the initial stage, a minimal coarsening with small fusion between the particles takes place. This fusion process is called “neck growth”. In the intermediate stage, the fused samples move together to eliminate porosity and to yield an increase in the grain size. In the final stage, a saturation or an equilibrium in the particle movement has been achieved, where the pores are closed, and the sample is permanently densified. Figure 5.2 shows a schematic diagram of the densification process.

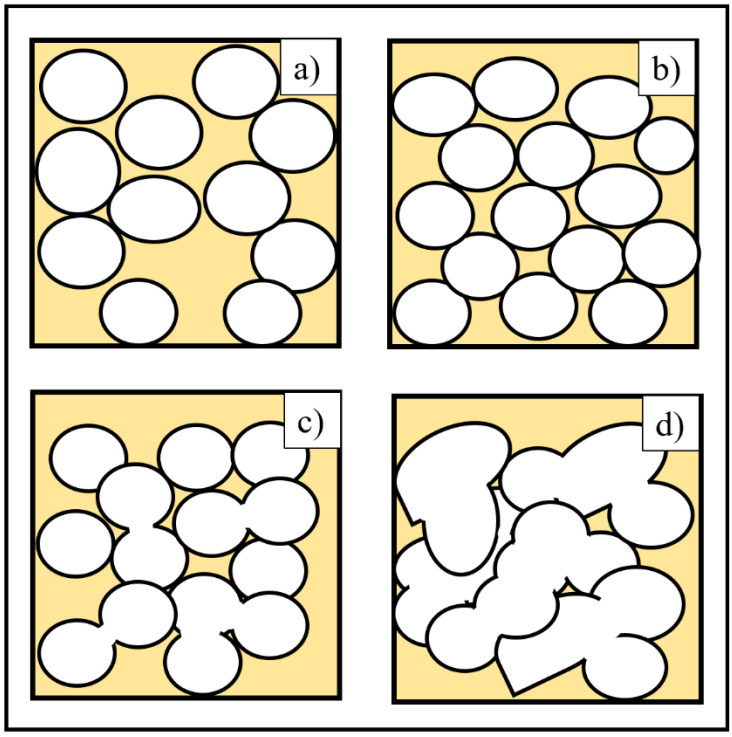

Figure 5.2: Schematic densification mechanism presented in the sintering process of ceramics [9]. (a) Ceramic powder constituted by loose particles. (b) Initial stage of sintering showing the particle adhesion. (c) Intermediate stage where samples pack together eliminating porosity. (d) Final stage where the sample is completely fused and sintered.

The surface energy developed between the particles moves them closer to develop curvature in the system. The surface energy is developed in different systems due to different reasons. In crystalline structures, it is due to the grain boundary motion, while in inorganic powders it is due to the viscous flow, plastic flow, and vapor transport. Similarly, in polymers and glasses the reason for grain transport is because of the viscous flow [10, 11]. Most of the time, it is also a combination of different mechanisms being responsible for the development of surface energy. The transport in the grains is defined by the Arrhenius relation, as shown in Equation 5.1. Here, N and N_o refer to the number of activated sites, Q is the activation energy, R is the gas constant, and T is the absolute temperature.

$$\frac{N}{N_o} = e^{-\frac{Q}{RT}} \qquad (5.1)$$

Different mechanisms of the sintering were classified into two different groups according to the densification patterns: Solid State sintering (SSS), and Liquid Phase Sintering (LPS) (see Figure 5.3) [11]. Although all the methods aim in getting solid cohesive bonded final part, the densification pattern in each method is different.

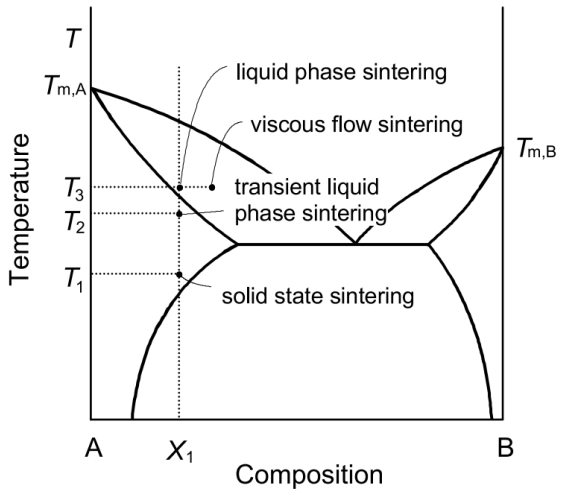

Figure 5.3: Schematic illustration of different sintering mechanisms depending on temperature[12].

Solid State Sintering is the bonding process where the particles are fused and densified below the melting temperature of the material. While in liquid phase sintering, the particles are bonded in a liquid phase above the melting point. In both phases the driving force is the reduction in the internal energy that leads to the movement/transport of the particles [10, 11, 13]. The transport mechanism takes place either by surface transport or bulk transport of the particles. Indeed, this driving force leads to either movement at an atomic level or a particle level leading to vacancies and grains, and grain boundaries that dislocate to form bonds. It is also to be noted that in surface transport no significant shrinkage has been observed since the mass flow occurs at the particle surface level.

Surface transport mechanism is generally observed at low temperatures, typically in metals, and metal oxides; this mechanism is further classified into: Evaporation-condensation, Surface diffusion, Volume diffusion.

a) **Evaporation- condensation:** Vapor transport is the mechanism observed when the particle surface evaporates causing the pore space to move or condense. Since the pores are reduced or dislocated, the particles move closer over time [9, 14]. This is a very slow process and usually dominated by some other transport mechanism. It was observed in the past in materials that are typically post-processed in the presence of H_2O, HCl, and halides [15–17] .

b) Surface Diffusion: This mechanism involves the motion of the atoms between the defects present or created such as vacancies, kinks, ledges, and additional atoms. This transport involves orientation of atoms in favor of sintering in the presence of temperature. Following the orientation, remaining atoms go along with them making the surface of the particles move. This is generally an initiating mechanism observed in many materials and responsible for smoothing of the materials [9].

c) **Volume Diffusion:** This mechanism involves transport of vacancies at crystal level or interparticle grain boundaries to enhance equilibrium [18]. This can be observed in samples that are generally compacted using force/pressure. This mechanism is mostly effected by the presence of external conditions including the usage of gas, pressure assistance.

Bulk transport mechanism is a mass transport mechanism that are active densification mechanisms seen in many common systems. This mechanism is highly influenced by the temperatures and responsible for stress development, pore movement, concave neck growth [9]. Bulk transport mechanisms can also be classified into three different mechanisms: Plastic flow, Grain boundary diffusion, Viscous flow.

a) **Plastic flow:** In this mechanism, vacancies under stress are moved causing a plastic deformation in the samples. A theoretical assumption in this mechanism is that the dislocations are climbed along the vacancies creating a new slip plane requiring no vacancy sink. Eventually the slip plane moves into the boundaries accounting for shrinkage [19, 20]. Along with the vacancy movement, necking between particles has also been observed with the exceeding stress around the necking zone. As the necking reaches maximum, a drop in the flow stress is equated with the shear stresses stopping the particle movement further and hence stopping the sintering mechanism [20–22].

b) **Grain Boundary Diffusion:** Grain boundary diffusion is a relatively dominant sintering mechanism in different materials. Here, the misoriented crystals or particles form a grain boundary which is removed mass-wise and replaced as a bond between the particles leading to new grain growth [8]. The main driving force for this process is the high energy developed along the grain boundaries.

c) **Viscous Flow:** Viscous flow is seen in the materials when they are subjected to high temperatures reaching their near-fusion temperatures [23]. This is generally seen in materials such as glasses, polymers, and amorphous materials.

In general terms, the sintering process includes a mixture of phases while temperature rises due to system variables like external pressure, surroundings and additives. Some of the effects of the variables are explained as below.

Pressure: Unlike the general pressure-less sintering, external pressure is used for post-consolidation of samples for netshaping and densification by eliminating porosity. This technique is generally used for coarse powders with only solid-state sintering where powder packing is low. During the pressure application, stress developed on the contact areas, or the necking areas leads to rounding of the particles thus leading to shrinkage, deformation of particles, and pore reduction. Some of the general pressure assisted sintering techniques are forging, powder/pellet extrusion, pressing, shockwave consolidation, hot isostatic pressing, and reactive processing [24–29]. However, the process includes few problems like easy contamination, expensive equipment, anisotropic shrinkage with stress areas [30–33].

External Atmosphere: An effect on stoichiometry by changing the purging gas was seen by Geach [34]. An off-stoichiometry in the ionic compounds to neutralize charge varied according to the change in the gas when sintering Urania. It was seen that when metal-oxides were sintered in oxygen, a slow sintering was observed while the usage of nitrogen as a purging gas sintering of the particles was seen at reduced temperatures. This is a phenomenon observed due to volume diffusion where dislocation in vacancies is seen [35, 36].

Additives: Addition of extra powders activates sintering leading a shift in the phase transformations of composites. This process is also termed as "*activaterd sintering*". It is a process where the diffusion rates of the powder is altered by forming large solubility bases. Although inhomogeneity in the final samples is observed, additive reduces the requirement of higher

temperatures. Dominant additives seen in ceramics are Cr, Y_2O_3, MgO, C, Nb, Al_2O_3, CaO, Ni, TiO_2. Important features that were observed in the samples after adding additives were reduction in surface energy, grain boundary mobility, stabilization in crystal structures, and control over grain growth [37–42].

Since sintering is an irreversible process, techniques like infiltration sintering, reactive sintering, induction heating, microwave heating, plasma/laser sintering, and electric discharge heating are used to densify the samples while enhancing the mechanical properties [43–49]. Despite the high sintering temperatures used in industry, the process commonly uses additives to enhance the sintering state.

A generic drive for sintering is considered to be the surface energy developed to reduce the pore size causing the particles to move. In each stage of the sintering process, the particles geometrically shrink in terms of the pore size and redefine the shape of the particle to reduce the curvature at any given interval until they reach an equilibrium. This is result of the internal energy difference caused by the high temperature [50]. Equation 5.2 describes the change of internal energy (U) in a system that can be used in the sintering state, where S is entropy, dW is work performed, N_i is the number of particles of the i^{th} component, N_c is total number of components, and μ_i is the chemical potential of the i^{th} component. It is worth noticing that dW is considered when external pressure or stress is applied on the system. The chemical potential change during this phase change occurs by Fick's laws of diffusion [50, 51]. The chemical potential which is given by Equation 5.3, where i_0 is the chemical potential in the standard state, k is Boltzmann constant (1.38×10^{-23} J/K), T is the absolute temperature, γ_i is the activity coefficient and X_i is the mole fraction of the composite.

$$dU = T\,dS - dW + \sum_{i=1}^{N_C} \mu_i\, dN_i \qquad (5.2)$$

$$\mu_i = \mu_i^0 + kT\, ln(\gamma_i X_i) \qquad (5.3)$$

Fick's law is used to measure the vacancy concentration gradient that is responsible for measuring the sintering rate and diffusion rate. Fick's first law can be used to explain the flux with respect to

the concentration gradient (see equation 5.4), where J represents the vacancies per unit time over the volume, D_v is diffusivity, and dC is the vacancy concentration over distance dx. This equation can be used for designing a sintering system with controlled movement rates in the system.

$$J = -D_v \frac{dC}{dx} \qquad (5.4)$$

In other words, the movement of particles/vacancies per volume in terms of flux can be defined with respect to the normalized molecular volume and area of the sample as shown in equation 5.5. Here, V is the volume of the sample, J is the flux, A is the area of the grain, and V_m is the molecular volume of the particle.

$$\frac{dV}{dt} = JAV_m \qquad (5.5)$$

5.1.1: Sintering in Ceramics.

Ceramics can be a complex system for quantitatively predicting the behavior and movement of atoms at different diffusion rates. The procedure for eliminating pores and attaining thermal equilibrium has been observed in the ceramic particles after subjecting them to the irreversible post-processing steps. These critical steps assist the densification and properties in ceramics [52]. However, improper sintering might also result in bad effects like destroying the advantageous properties in ceramics [53, 54]. A Two-Step Sintering (TSS) process has been suggested by Chen and Wang [55] to keep a control on the microstructure in order to attain high dense specimens. A ramp and hold step play a critical role in the sintering stage and allow the grains to rearrange within the sample while gaining density with time and temperature.

At a deeper level, the migration of the particles, grain boundaries and pores is due to the kinetics and temperature rise. The changes in surface energy, internal stresses and chemical potential act as driving forces behind this movement [56]. The predominant mechanism in the amorphous systems is by viscous flow phenomenon [4, 57].

Most of the time the grain boundary movement with respect to sintering temperatures is observed via quantitative microscopy techniques SEM/TEM. Additional experimental techniques such as X-ray absorption, mercury porosimetry, dilatometry, gas permeability, TGA, positron annihilation, differential thermal analysis and small angle neutron scattering are also used for evaluating the grain boundary movement [58]. Samples are commonly investigated for changes like defect growth, and dimensional changes.

Of particular interest is the sintering process of Alumina (Al_2O_3) since it is one of the most common ceramics used in the industry, although it is sensitive to oxygen inclusion. The sintering of alumina is a rate-controlled mechanism, which is sometimes achieved by the inclusion of additives for retarding grain growth [59, 60]. Galusek et al [61] observed that surface diffusion and grain-boundary diffusion played a crucial role in the grain migration in alumina sintering via small angle neutron scattering when yittria and zinc oxides were added.

Additional ceramics of great interest to the industry are cemented Carbides like tungsten carbide (WC), Titanium Carbides (TiC), FeC, and TaC which are hard to sinter. These ceramics utilize a liquid phase sintering process for densification [62, 63]. To control the microstructural changes in these ceramics, longer times in graphite crucibles is used depending upon the composition. It is also to be noted that densification in cemented carbides occurs before the initiation of liquid phase [64].

Silicon Carbide (SiC) is another important ceramic used in the industry, which is relatively difficult to sinter. During its sintering, the SiC is combined with additives like Al, Al_2O_3, Be, TiO_2, Y_2O_3 to reduce its sintering temperature [65]. A liquid phase sintering is observed with a low oxygen atmosphere to preserve carbon [65–67]. Most of the time, a solid-state sintering is seen in the carbides [63]. Silicon Nitride (Si_3N_4) is also an attractive ceramic, which has shown a glassy-viscous phase for densification at a processing temperature of 1600˚C [68]. The Si_3N_4 samples are sintered in boron nitride crucibles to avoid the loss of composition. However, Si_3N_4 includes sintering with a post-processing steps such as HIP, pressure sintering to eliminate porosity [69–71].

Zirconia can be considered as a special case in presenting a sintering phenomenon for the three different crystallographic phases. Although sintering is an irreversible process, after sintering and cooling zirconia, it can result in monoclinic, cubic and tetragonal phases [72, 73]. Kingery [4] reported a necking process in the particles at 2200˚C along with a linear shrinkage. He also reported the diffusion kinetics in zirconia spherical particles which underwent viscous flow diffusion mechanism for adherence.

Similar sintering process is adapted for ceramics like silica, barium titanate, boron carbides and nitrides as well as metal powders [4, 52].

Some of the challenges and offsetting concerns to deal with these post-processing include loss of microstructural control, warpage, microstructure coarsening, and distortion [74]. Hence a balance and control while sintering ceramics is an important step before examining and assessing any sintering cycle. This dissertation has established different sintering cycles used for different powder materials suitable for the AM techniques to obtain defect free specimens.

Given the aforementioned background on sintering, this research work seeks to establish a modelling sintering platform for structures manufactured via 3D printing. Here, the grain size, time and temperature were selected as the key parameters in the kinetics of the sintering process. A detailed analysis of the ceramic-metal infiltration process for fabricating IPCs is also presented in this chapter.

5.2: Methods (Diffusion model) & Discussion

The samples here considered were printed via a Vat polymerization technique. The silica samples printed were sintered and then infiltrated in molten aluminum to obtain Interpenetrating Phase Composites (IPCs) for further densification.

5.2.1: Theory

Silica powder suspended in a photo-polymer resin was 3D printed into bulk samples. The printed samples were cured to evaporate the binder leaving behind the fused silica particles. The silica

particles used in this work were of a mean diameter 39.18µm. The particles are then subjected to near-fusion temperatures for sintering (where solid bonds were formed). A shrinkage of 16.8 % was observed in the samples after sintering. Along with this, the porosity was reduced from 30% to 29% with near-full density of 79%. Parameters like surface energy, viscosity, temperature, pressure and volume played a key role in the homologous sintering [75]. Here, temperature and particle size were selected to be critical parameters to estimate the sintering kinetics. Additionally, the neck diameter, formed after fusion of the particles was taken into consideration for understanding the extent of diffusion and sintering.

In this work, a bulk transportation mechanism took place in the amorphous silica samples in green state when subjected to the near-fusion temperatures. Indeed, most of the amorphous powders follow a viscous flow diffusion mechanism for densification into final parts [4, 11]. It is worth noticing that no surface diffusion mechanisms were considered for convenience. The sintering model that is typically used on amorphous powders initiates by filling-in the material between the particles and approaching the centers, which results in a change in the curvature of the particles (Figure 5.4) [4].

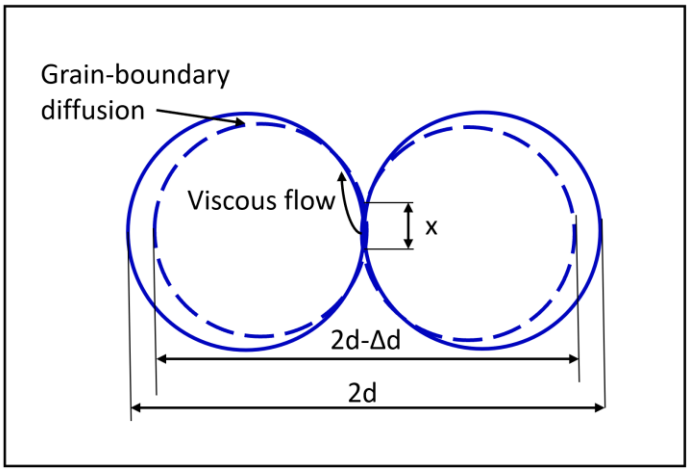

Figure 5.4: A schematic of mass -transport sintering mechanism seen in amorphous powders using a two-sphere model [76].

In the viscous flow, the pore size highly affects the final products. During the viscous flow, the sintering process can be divided into three steps as usual. (i) the green body is cured, (ii) After subjecting to a curing temperature, a liquid phase is formed and reaches a pyroplastic range where internal stresses develop, (iii) In the final stage, the particles along with temperature fuse together and cool down below the glass transition stage making the samples strong [77, 78]. These steps are also the fundations to optimize a firing profile. As mentioned before, one of the driving mechanisms in the sintering process is the chemical potential difference. This mechanism gives rise to a stress gradient that is associated with the epitaxial growth in the ceramics [79]. The rate of particle cohesion is directly proportional to the temperature until it reaches a minimum necking ratio (x/r) where it stabilizes any further grain growth [4].

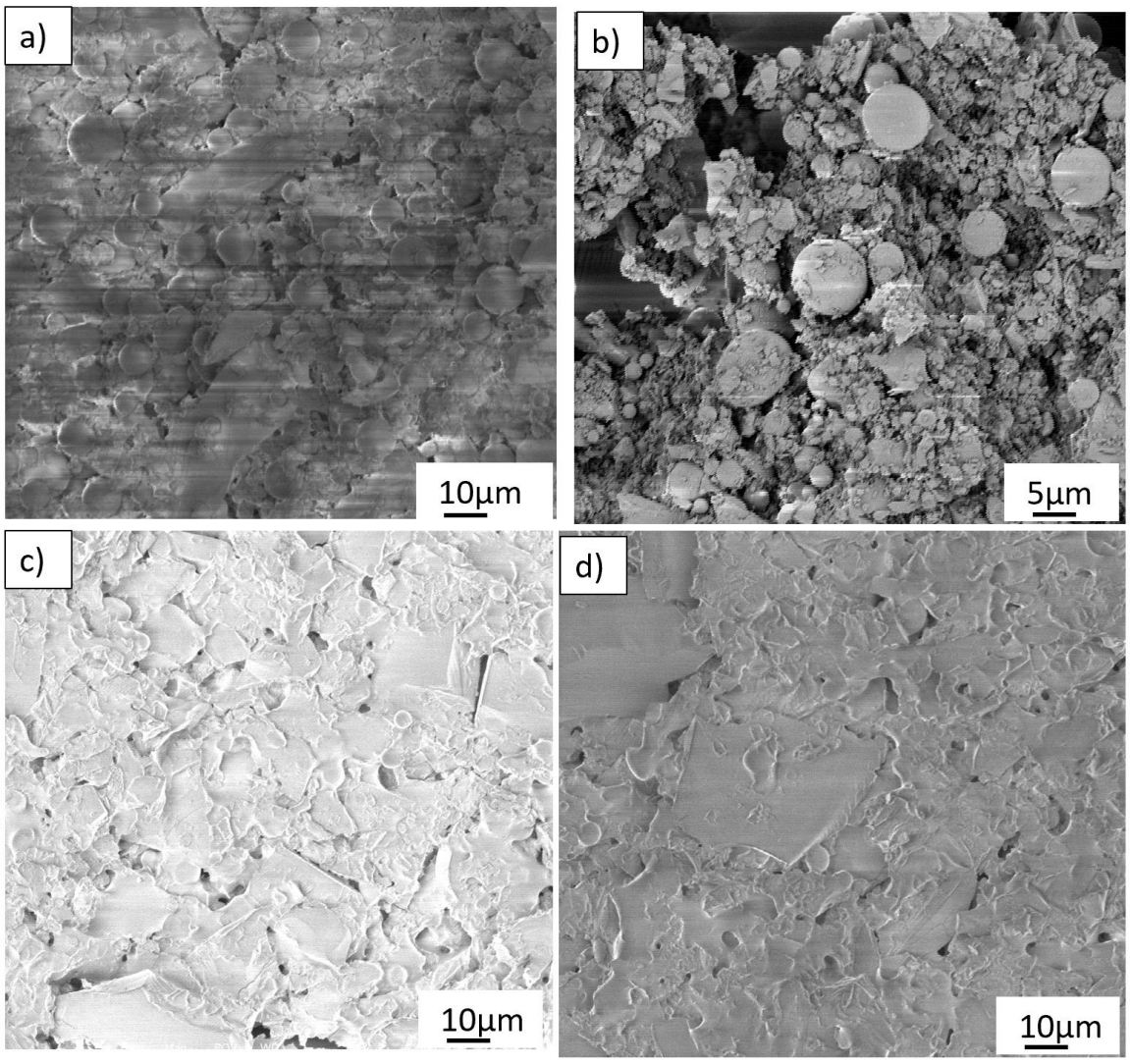

Figure 5.5: SEM images showing the micrographs of the silica samples at different temperatures during the sintering process. (a) At 400˚C. (b) At 800˚C. (c) At 1050˚C. (d) At 1225˚C.

In this work, the silica samples were observed for changes in particle size, density, and shrinkage after the sintering process. These changes were related to the sintering temperature. SEM images at nearly 2000x magnification were captured on an Keysight FE-SEM to observe the microstructural changes (see figure 5.5). At least 12 images were observed, and an average of the results was reported in this study. At 400˚C, the photopolymer acting as binder in the samples starts evaporating, adhering the powder particles together. From figure 5.5a, it can be seen that the

samples still have a spherical morphology as in the resin. The x/r ratio presented in this stage is a 0.12 with larger particle radius (32.65 microns). At 800˚C, the particles come together trying to eliminate porosity (see figure 5.5 b). At this stage, all the smaller pores congregate bringing the silica particles to one site. This results in larger pores that eventually migrate to the surface and produce a shrinkage in the sample. Although no significant fusion among the particles was seen, this can be described as the initial stage of sintering with a necking ratio of about ~ 0.11-12. At 1050˚C, the particles in the samples fuse together (see Figure 5.5c). The density of the samples increases at this stage and almost reaches the near fusion temperature. At 1275˚C, the samples reached their higher fusing stage with the necking ratio stabilizing at 0.09. Here, the density of the samples has increased eliminating most of the porosity and reached the highest shrinkage (see figure 5.5d). This temperature was assumed to be where the sintering process stops since the gradient in the necking ratio was zero and the samples reached the highest relative density of 79% of commercial silica. Figure 5.6 shows the necking ratio (0.09) making the particle size slightly higher than the size seen at 800˚C. As mentioned before, along with the particle size change, the porosity in the samples is eliminated by driving them to the corner in order to make the fusing particles rounded [10, 76].

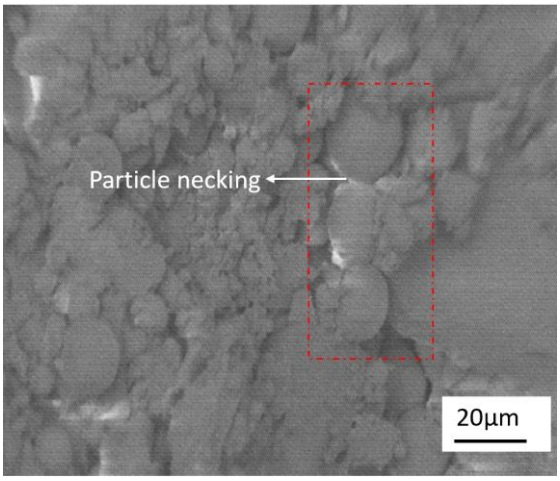

Figure 5.6: Particle Fusion observed at 1050˚C.

From figure 5.7, it can be observed that the density and particle size increased along with the temperature. This is also proportional to the exposure time. A similar pattern was observed in many other ceramic systems [3, 11, 76]. The main reason for the increase in the particle size is the migration of pores to the ends while the grains in the ceramics fuse together to form a bigger grain. This step also is responsible for the increase in density and shrinkage.

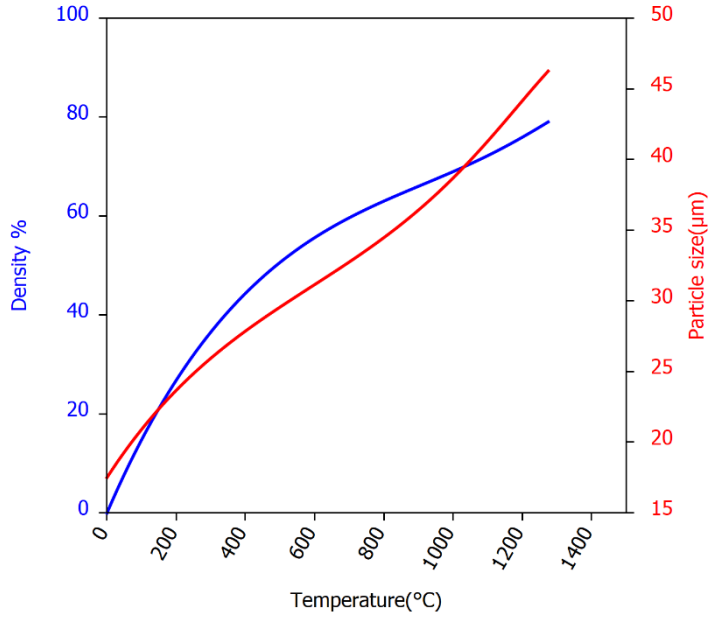

Figure 5.7: Density and Particle size graph with respect to temperature.

The solid silica samples after sintering underwent an infiltration process to increase their density and to produce a ceramic composite. They were submerged into molten aluminum between 1000˚C and 1250˚C in an Argon atmosphere [80, 81]. This is a two-step process where a material with high melting point is initially sintered, and then submerged into a relatively low melting point liquid phase material. Here, the fused silica sintered into solid and then submerged into a molten phase of aluminum (see Figure 5.8). The process initiates when the molten phase fills-in the open pores of the solid material followed by a chemical red-ox reaction taking place, which converts the silica into a composite. In this infiltration stage, the SiO_2 is chemically reacted with Al to form Al_2O_3 (see

Equation 5.6). The two main conditions for this chemical reaction to take place are (a) the solid structure needs to be open, and (b) The particle distribution needs to be interconnected and continuous. The solid silica samples require to have a porosity of at least 10% throughout the sample.

$$3SiO_2 + 4Al \rightarrow 2Al_2O_3 + 3[Si]Al \quad (5.6)$$

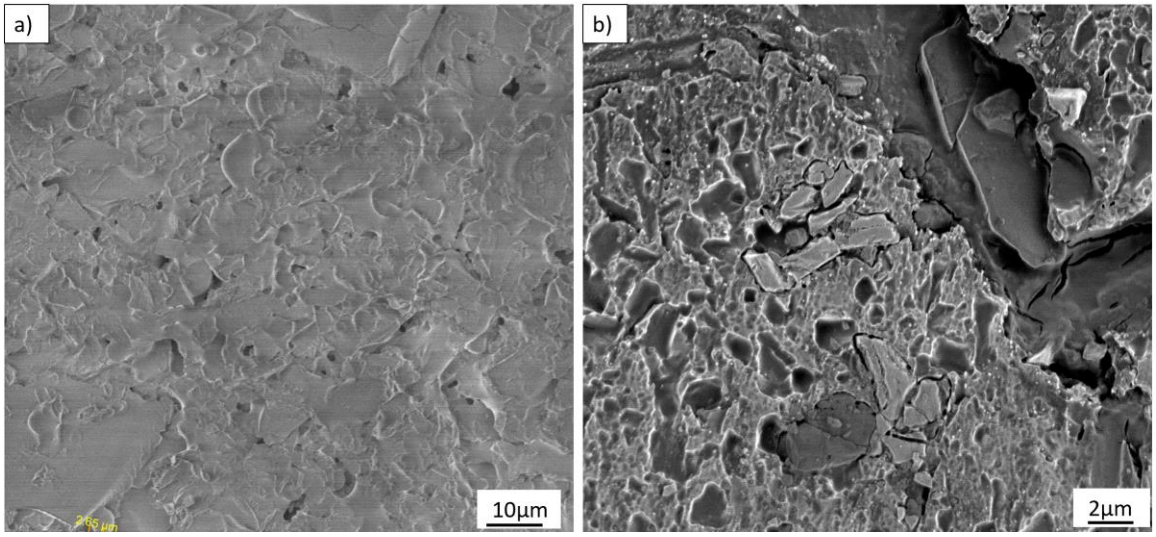

Figure 5.8: SEM images showing the micrographs of the infiltration sintered samples. (a) Sintered fused silica sample before the infiltration process. (b) The transformed sample after infiltration.

The infiltration process relies on the liquid wetting angle and uses the liquid-vapor surface energy as the driving force. Here, the liquid metal flows into the open pore by capillary forces [82, 83]. The depth of infiltration (h) is given in terms of surface energy and wetting angle along with the liquid viscosity, and governed by equation 5.7, where dP is the pore size, t is the time for infiltration, γ_{lv} is the liquid-vapor surface energy, θ is the wetting angle, η is the viscosity of molten metal [84].

$$h = \frac{\sqrt{d_P t\, \gamma_{lv} \cos\theta}}{4\eta} \quad (5.7)$$

Low wetting angles with external pressure are commonly maintained in order for the reaction to take place. Here, the argon atmosphere assists the infiltration of aluminum in silica. Dimensional growth is commonly observed during the transformation process along with the density (see figure

5.9a). The grain size and density increased by 1.7 and 2.06 times, respectively, after the infiltration process. A necking ratio of 0.14 was recorded in the samples after the infiltration process (see Figure 5.9b).

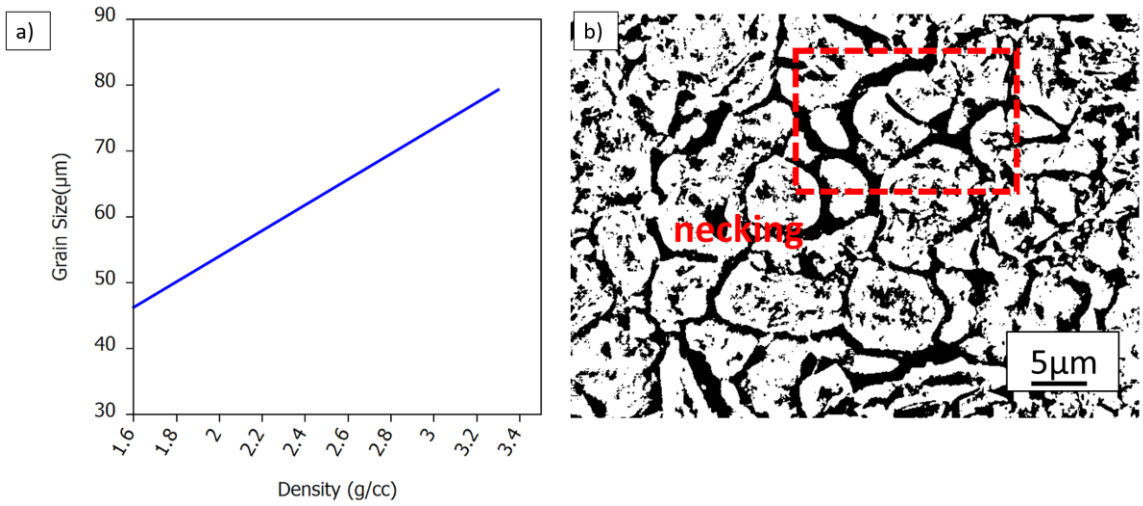

Figure 5.9: Evidence of the infiltration process. (a) Grain size radius versus density graph seen after infiltration sintering. (b) Grain distribution in the sample.

It is worth to be noted, that although the process helped in increasing density, the transformation of the samples is not complete. The final transformed samples still show the presence of silica (Figure 5.10). The XRD shows the presence of at least 6.2% silica in the transformed samples [44]. This might be due to the high contact angle during wetting and insufficient external pressure [84]. Gupta et al [85] have observed a similar mechanism in the SiC-Al system. The wetting system was here hindered by adhesion at the solid-liquid phase with γ_{sg} greater than γ_{lv}. This is termed as the work done by adhesion because of the non-wetting behavior of the solid and gas interfaces. Delannay et al [83] also explained the phenomenon of wetting non-metallic solids by liquid metals as the result of surface energies. In order to avoid any hindrances in the formation of composite, the wetting liquid should be greater than the bonding energy in the solid. The lack of full transformation can also be explained by physical adsorption governed by the Vander Waal forces.

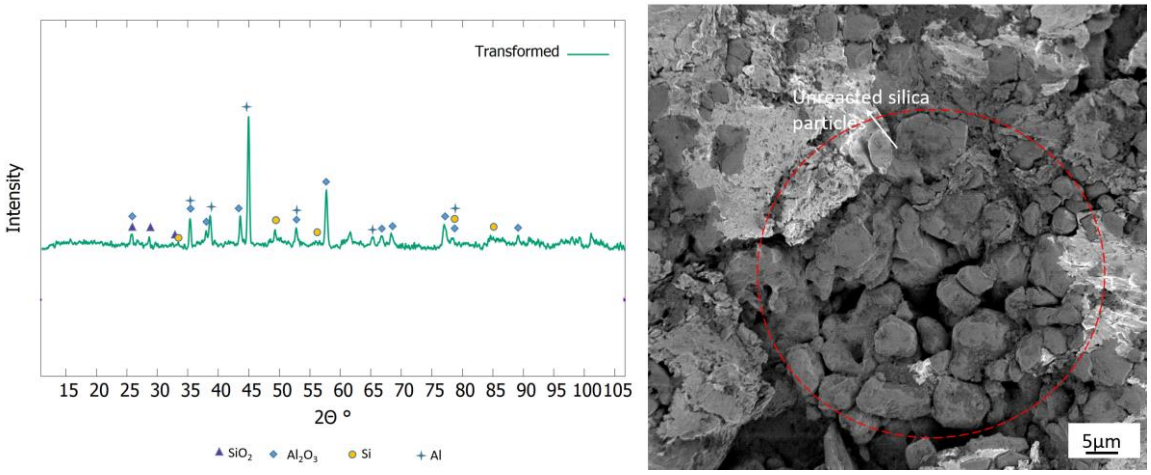

Figure 5.10: Evidence showing the presence of silica and aluminum in the transformed samples. XRD of the transformed samples with peaks representing silica and aluminum. The figure also includes an SEM image of the transformed sample showing the unreacted silica particles.

Adequate mechanical properties in the infiltrated samples have been recorded when the volume of the infiltrant is significantly less than the pore volume [49, 86]. However, the pore volumes were not measured here. But an increase in the mechanical properties were seen. In fact, the compressive strength of the silica samples increased from 21MPa to 92MPa after infiltration [44].

5.2.2: Mathematical model

A geometrical model using analytical calculations was considered to obtain the values for volume flow between particles, as well as the diffusion flux and kinetic diffusion constant.

Few assumptions that were considered for the model [87, 88]:

- The sintering process takes place under quasi-static conditions, and hence the diffusion gradient is steady.
- All the atoms are in equilibrium with only capillary stresses responsible for their movement.
- The stress at the grain boundaries is uniform.

- The heat source and sink for the internal energy is the grain boundaries, and vacancies present in the sample.

Here, monosized circular geometry particles were considered for an easier practical understanding following all the aforementioned assumptions. A hyperboloid model using two particles for the material cohesion and mass flow was selected for all the solid-state sintering of the fused silica particles (see Figure 5.11). The model only considered bulk material flow where shrinkage is observed directly but not the surface diffusion processes for easy calculations. It was considered that the viscous flow and the diffusion process, which induces fusion, took place at the grain boundaries of the particles. The viscous flow was based on a hyperboloid model, which can be used to measure the volume flow at any instance. Equation 5.8 describes the volume flow using the hyperboloid model.

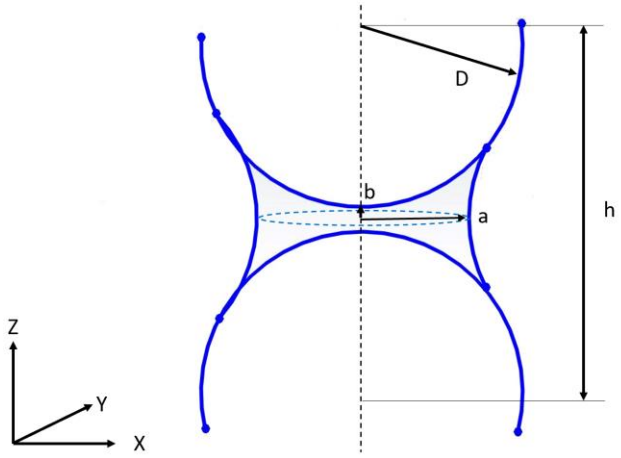

Figure 5.11: Schematic illustration of material flow using hyperboloid model.

$$V = \int_{-h/2c}^{h/2c} \pi a^2 (u^2 + 1)(c) du \qquad (5.8)$$

Where the surface generated for material flow is given as

$$\frac{x^2}{a^2} + \frac{y^2}{b^2} - \frac{z^2}{c^2} = 1 \qquad (5.9)$$

While a, b, and c are semi-principle axis with x= $a\sqrt{1+u^2}\cos v$.

Using the equation 5.4, and 5.5 the sintering process carried out in air was measured for volume (and therefore for the flux). The material particle size of the powder (as seen in laser particle analyzer, -refer to Chapter 2) was considered for the sintering modeling. The volume flow, diffusion flux, and diffusion coefficient were calculated at 400˚C, 800˚C, 1050˚C and 1275˚C. Figure 5.12 shows the detail of the diffusion flux and diffusion coefficients calculated in the material with respect to time along the sintering process (as described in Figure 2.6).

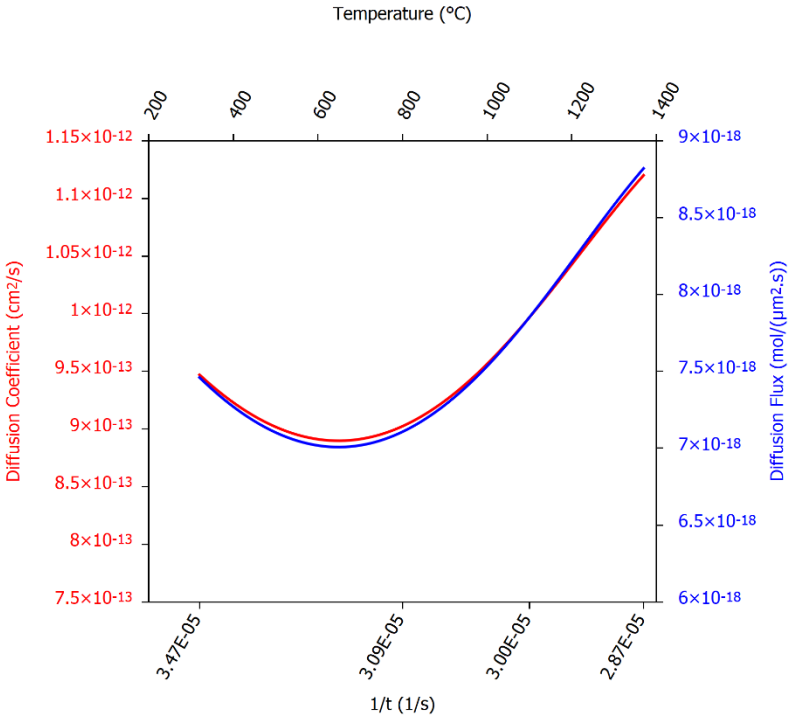

Figure 5.12: Graphical representation of diffusion flux and diffusion coefficient observed during sintering of silica samples.

From the calculations made in this research, the material diffusion constant for silica self-diffusion was determined to be 1.01± 0.01 x 10^{-12} cm^2/s (at 1050˚C). This was comparable to the measurements made by Yokoyama [89] using a through-diffusion experiment for silica in rhyolite phase. However, this value is 2 times higher when the Wilke-Chang correlation is used [90]. The

lower value seen here might be due to the sintering taking place in air, whereas the experiments carried by through -diffusion were in a saline atmosphere with pH 5.5 [89, 91–93]. This can also be noted by the flux values seen in the experiments made by Yokohama and Brady, Walther [89, 94, 95] in pH environments. The flux values in the absence of low pH environments were at least 10 times lower than in the presence of the acidic environments. The sintered samples had a Gibb's energy of about -320 kJ, which was obtained from Thermocalc (refer to Figure 2.22) [96].

Hence, the analytical measurements taken here with respect to time, temperature, and particle size were comparable to other studies, and can be validated by the values taken from the experimental methods.

5.3: Conclusions

A successful sintering process was observed in a solid-state sintering process. Similarly, an infiltration process of the sintered silica parts resulted in a consolidated metal-ceramic composite. A viscous flow in a bulk transportation phenomenon was responsible for the diffusion kinetics during the sintering. The necking ratio during this sintering process was stabilized at 0.09 at 1225˚C with an average shrinkage of 16.3% in all directions. The diffusion flux and diffusion coefficient at temperatures 400˚C, 800˚C, 1050˚C, and 1225˚C were determined. A diffusion flux constant for silica when sintering in air was found out to be $1.01 \pm 0.01 \times 10^{-12}$ cm^2/s in the case of self-diffusion in SiO_2. It was observed that not a full reaction took place during the transformation process, a mechanism associated with the high contact angle during metal wetting process and/or insufficient external pressure. However, a density increase by 2.6 times was observed in the transformed parts. The analytical study obtained in this work was comparable to the experimental work from other researchers. However, additional work is required to include the bulk transport mechanism present in the sintering process coupled with the metal-infiltration process.

5.4: References

1. Bordia RK, Kang SJL, Olevsky EA (2017) Current understanding and future research directions at the onset of the next century of sintering science and technology. J Am Ceram Soc 100:2314–2352. https://doi.org/10.1111/jace.14919

2. Kingery WD (1992) Sintering from Prehistoric Times to the Present. Solid State Phenom 25–26:1–10. https://doi.org/10.4028/www.scientific.net/ssp.25-26.1

3. Kingery WD (1959) Densification during sintering in the presence of a liquid phase. I. Theory. J Appl Phys 30:301–306. https://doi.org/10.1063/1.1735155

4. Kingery WD, Berg M (1955) Study of the Initial Stages of Sintering by Viscous Flow, Evaporation-Condensation, and Self-Diffusion*. J Appl Phys 26:1205–1217

5. Morris DG (1980) Compaction and mechanical properties of metallic glass. Met Sci 14:215–220. https://doi.org/10.1179/030634580790426436

6. Clyens S, Johnson W (1977) The dynamic compaction of powdered materials. Mater Sci Eng 30:121–139. https://doi.org/10.1016/0025-5416(77)90219-1

7. Kolar D, Kuczynski GC, Chiang SK (1984) On the Mechanism of Pore Coarsening. In: Materials Science Research. Springer US, Boston, MA, pp 81–88

8. Coble RL (1961) Sintering crystalline solids. I. intermediate and final state diffusion models. J Appl Phys 32:787–792. https://doi.org/10.1063/1.1736107

9. Kuczynski GC (1990) Self-Diffusion in Sintering of Metallic Particles. In: Sintering Key Papers. Springer Netherlands, pp 509–527

10. Randall M. German (1996) Sintering Theory and Practice | General & Introductory Materials Science | Subjects | Wiley

11. Bordia RK, Kang S-JL, Olevsky EA (2017) Current understanding and future research

directions at the onset of the next century of sintering science and technology. https://doi.org/10.1111/jace.14919/full

12. Kang SJ (2005) Sintering. Elsevier Ltd

13. JOHNSON DL (1968) SOLID-STATE SINTERING. Elsevier, pp 173–183

14. Rockland JGR (1967) The determination of the mechanism of sintering. Acta Metall 15:277–286. https://doi.org/10.1016/0001-6160(67)90203-9

15. Readey DW, Quadir T, Lee J (1987) Effects of Vapor Transport on Microstructure Development. In: Ceramic Microstructures ’86. Springer US, pp 485–496

16. READEY MJ, READEY DW (1986) Sintering of ZrO2 in HCl Atmospheres. J Am Ceram Soc 69:580–582. https://doi.org/10.1111/j.1151-2916.1986.tb04797.x

17. McIntyre RD (1968) The Effect of HCl-H2 Sintering on the Properties of Compacted Iron Powder. In: Iron Powder Metallurgy. Springer US, pp 249–254

18. Friedrich E, Schatt W (1980) Sintering of one-component model systems: Nucleation and movement of dislocations in necks. Powder Metall 23:193–197. https://doi.org/10.1179/pom.1980.23.4.193

19. Schatt W, Friedrich E (1987) Dislocation-Activated Sintering Processes. In: Sintering’85. Springer US, Boston, MA, pp 133–141

20. Morgan CS, Yust CS (1963) Material transport during sintering of materials with the fluorite structure. J Nucl Mater 10:182–190. https://doi.org/10.1016/0022-3115(63)90053-9

21. Brett J, Seigle L (1963) Shrinkage of voids in copper. Acta Metall 11:467–474. https://doi.org/10.1016/0001-6160(63)90173-1

22. Ogbuji LUJT (1990) Sintering Stress in Alumina: Finite Element Analysis

23. Kuczynski GC (1949) Study of the sintering of glass. J Appl Phys 20:1160–1163. https://doi.org/10.1063/1.1698291

24. KOCZAK MJ, KUHN HA (1974) Metal Powder Processing. Elsevier, pp 261–319

25. Fogagnolo JB, Robert MH, Ruiz-Navas EM, Torralba JM (2002) Extrusion of mechanically milled composite powders. J Mater Sci 37:4603–4607. https://doi.org/10.1023/A:1020648316319

26. Rabin BH, Korth GE, Williamson RL (1990) Fabrication of Titanium Carbide-Alumina Composites by Combustion Synthesis and Subsequent Dynamic Consolidation. J Am Ceram Soc 73:2156–2157. https://doi.org/10.1111/j.1151-2916.1990.tb05294.x

27. Chelluri B (1994) Dynamic magnetic consolidation (dmc) process for powder consolidation of advanced materials. Mater Manuf Process 9:1127–1142. https://doi.org/10.1080/10426919408934980

28. Misiolek W, German RM (1991) Reactive sintering and reactive hot isostatic compaction of aluminide matrix composites. Mater Sci Eng A 144:1–10. https://doi.org/10.1016/0921-5093(91)90204-Z

29. Atkinson H V., Davies S (2000) Fundamental aspects of hot isostatic pressing: An overview. Metall Mater Trans A Phys Metall Mater Sci 31:2981–3000. https://doi.org/10.1007/s11661-000-0078-2

30. Kwon O -H, Messing GL (1989) Gas Diffusion During Containerless Hot Isostatic Pressing of Liquid-Phase Sintered Ceramics. J Am Ceram Soc 72:1011–1015. https://doi.org/10.1111/j.1151-2916.1989.tb06260.x

31. Xu J, McMeeking RM (1992) An analysis of the can effect in an isostatic pressing of

copper powder. Int J Mech Sci 34:167–174. https://doi.org/10.1016/0020-7403(92)90081-Q

32. Lee D-H, Kim H-E, Cho S-J Microstructure and Fracture Toughness of Hot-Pressed Silicon Carbide Reinforced with Silicon Carbide Whisker

33. Lis J, Pampuch R (1994) SINTERABLE CERAMIC POWDERS PREPARED BY SHS, THEIR DENSIFICATIONS AND FINAL PRODUCTS. In: Advanced Materials '93. Elsevier, pp 603–608

34. Geach GA (1959) Recent british developments in the theory of sintering. Powder Metall 2:104–114. https://doi.org/10.1179/pom.1959.2.3.007

35. Schatt W, Friedrich E (1985) Dislocation activated sintering processes. Powder Metall 28:140–144. https://doi.org/10.1179/pom.1985.28.3.140

36. DeHoff RT (1989) Stereological Theory of Sintering. In: Science of Sintering. Springer US, pp 55–71

37. Madan DS, German RM (1990) Quantitative assessment of enhanced sintering concepts. Powder Metall 33:45–52. https://doi.org/10.1179/pom.1990.33.1.45

38. German RM, Rabin BH (1985) Enhanced sintering through second phase additions. Powder Metall 28:7–12. https://doi.org/10.1179/pom.1985.28.1.7

39. Aldinger F (1974) Controlled porosity by an extreme kirkendall effect. Acta Metall 22:923–928. https://doi.org/10.1016/0001-6160(74)90059-5

40. Savitskii A (1999) Liquid-Phase Sintering of the Systems With Interacting Components. In: Advanced Science and Technology of Sintering. Springer US, pp 19–28

41. Masteller MS, Heckel RW, Sekerka RF (1975) A mathematical model study of the

influence of degree of mixing and powder particle size variation on the homogenization kinetics of compacted blends of powders. Metall Trans A 6:869–876. https://doi.org/10.1007/BF02672310

42. Mummareddy B, Negro D, Bharambe VT, et al (2021) Mechanical properties of material jetted zirconia complex geometries with hot isostatic pressing. Adv Ind Manuf Eng 100052. https://doi.org/10.1016/j.aime.2021.100052

43. Bertrand P, Bayle F, Combe C, et al (2007) Ceramic components manufacturing by selective laser sintering. Appl Surf Sci 254:989–992. https://doi.org/10.1016/j.apsusc.2007.08.085

44. Mummareddy B, Maravola M, MacDonald E, et al (2020) The fracture properties of metal-ceramic composites manufactured via stereolithography. Int J Appl Ceram Technol 17:413–423. https://doi.org/10.1111/ijac.13432

45. Prochazka S (1975) Sintering of Silicon Carbide. In: Mass Transport Phenomena in Ceramics. Springer US, Boston, MA, pp 421–431

46. Liu G, Li J (2013) High-gravity combustion synthesis: A fast and furnace-free way for preparing bulk ceramic materials. J. Asian Ceram. Soc. 1:134–142

47. Katz JD (1992) Microwave sintering of ceramics. Annu Rev Mater Sci 22:153–170. https://doi.org/10.1146/annurev.ms.22.080192.001101

48. Kang S-JL (2010) Liquid phase sintering. In: Sintering of Advanced Materials. Elsevier, pp 110–129

49. Li SJ, Queyroux F, Boch P (1994) Particulate composites in the Al2O3-SiO2-TiO2 system by infiltration processing. J Eur Ceram Soc 13:3–9. https://doi.org/10.1016/0955-2219(94)90052-3

50. Balluffi RW, Allen SM, Carter WC (2005) Irreversible Thermodynamics: Coupled Forces and Fluxes. In: Kinetics of Materials. John Wiley & Sons, Inc., pp 23–39

51. Tyrrell HJV (1964) The origin and present status of fick's diffusion law. J. Chem. Educ. 41:397–400

52. Sutharsini U, Thanihaichelvan M, RameshSingh (2017) Two-Step Sintering of Ceramics. Sinter Funct Mater. https://doi.org/10.5772/68083

53. Pang X, Qiu J, Zhu K, Du J (2012) (K, Na)NbO3-based lead-free piezoelectric ceramics manufactured by two-step sintering. Ceram Int 38:2521–2527. https://doi.org/10.1016/J.CERAMINT.2011.11.022

54. Mancuso E, Alharbi N, Bretcanu OA, et al (2017) Three-dimensional printing of porous load-bearing bioceramic scaffolds. Proc Inst Mech Eng Part H J Eng Med 231:575–585. https://doi.org/10.1177/0954411916682984

55. Chen I-W, Wang X-H (2000) Sintering dense nanocrystalline ceramics without final-stage grain growth. Nat 2000 4046774 404:168–171. https://doi.org/10.1038/35004548

56. Gatea HA (2020) The Effect of Sintering Temperature on the Electrical Properties and Particle Size of the Compound Ferroelectric PZT Prepared by Wet Chemical Methods. IOP Conf Ser Mater Sci Eng 928:072007. https://doi.org/10.1088/1757-899X/928/7/072007

57. Burke JE (1963) Progress in Ceramic Science.

58. German RM (1996) Sintering Measurement Techniques. In: Sintering Theory and Practice. Wiley, pp 23–66

59. Bennison SJ, Harmer MP (1990) Effect of Magnesia Solute on Surface Diffusion in Sapphire and the Role-of Magnesia in the Sintering of Alumina. J Am Ceram Soc 73:833–

837. https://doi.org/10.1111/J.1151-2916.1990.TB05122.X

60. HEUER AH (1979) The Role of MgO in the Sintering of Alumina. J Am Ceram Soc 62:317–318. https://doi.org/10.1111/J.1151-2916.1979.TB09496.X

61. Galusek D, Ghillányová K, Sedláček J, et al (2012) The influence of additives on microstrucutre of sub-micron alumina ceramics prepared by two-stage sintering. J Eur Ceram Soc 32:1965–1970. https://doi.org/10.1016/J.JEURCERAMSOC.2011.11.038

62. Nelson RJ, Milner DR (2014) DENSIFICATION PROCESSES IN THE TUNGSTEN CARBIDE-COBALT SYSTEM. http://dx.doi.org/101179/pom19721530014 15:346–363. https://doi.org/10.1179/POM.1972.15.30.014

63. Pötschke J, Gestrich T, Richter V (2018) Grain growth inhibition of hardmetals during initial heat-up. Int J Refract Met Hard Mater 72:117–125. https://doi.org/10.1016/J.IJRMHM.2017.12.016

64. Schreiner M, Schmitt T, Lux B, Lassner E (1984) Origins of discontinuous grain growth during liquid phase sintering of WC-Co cemented carbides. Powder Met Int; (Germany, Fed Repub of) 16:4:

65. Raju K, Yoon DH (2016) Sintering additives for SiC based on the reactivity: A review. Ceram. Int. 42:17947–17962

66. Kim T-E, Youn CHO K, Khishigbayar K-E Effect of heating rate on the properties of silicon carbide fiber Effect of heating rate on the properties of silicon carbide fiber with chemical-vapor-cured polycarbosilane fiber with chemical-vapor-cured polycarbosilane fiber Effect of heating rate on the properties of silicon carbide fiber with chemical-vapor-cured polycarbosilane fiber. J Adv Ceram 6:59–66. https://doi.org/10.1007/s40145-017-0218-4

67. PROCHAZKA S, SCANLAN RM (1975) Effect of Boron and Carbon on Sintering of SIC. J Am Ceram Soc 58:72–72. https://doi.org/10.1111/j.1151-2916.1975.tb18990.x

68. Hirosaki N, Okada A (1992) Gas-Pressure Sintering Map for Silicon Nitride-Based Materials. Hot Isostatic Press Theory Appl 143–148. https://doi.org/10.1007/978-94-011-2900-8_23

69. Podobeda LG (1979) Effect of impurities on the properties of silicon nitride materials. Sov Powder Metall Met Ceram 1979 181 18:59–63. https://doi.org/10.1007/BF00791895

70. Kang S-JL, Greil P, Mitomo M, Moon J-H (1989) Elimination of large Pores During Gas-Pressure Sintering of β′-Sialon. J Am Ceram Soc 72:1166–1169. https://doi.org/10.1111/J.1151-2916.1989.TB09702.X

71. Crosbie GM, Nicholson JM, Stiles ED (1989) Sintering factors for a dry-milled silicon nitride-yttria-alumina composition. undefined

72. Daou EE (2014) The Zirconia Ceramic: Strengths and Weaknesses. Open Dent J 8:33–42. https://doi.org/10.2174/1874210601408010033

73. Scott HG (1975) Phase relationships in the zirconia-yttria system. J Mater Sci 10:1527–1535. https://doi.org/10.1007/BF01031853

74. German RM (1996) Sintering Practice. In: Sintering Theory and Practice. Wiley, pp 450–506

75. Bron VA (1964) Some crystal-chemical relationships in the activated sintering of highly refractory oxides in the solid phase. Sov Powder Metall Met Ceram 1964 15 1:339–344. https://doi.org/10.1007/BF00774114

76. German RM, M. R (1996) Solid-state Sintering Fundamentals. In: Sintering Theory and Practice. pp 67–141

77. Salem S, Salem A (2013) Mechanisms of Momentum Transport in Viscous Flow Sintering. Sinter Appl. https://doi.org/10.5772/53259

78. FUNK J (1982) DESIGNING THE OPTIMUM FIRING CURVE FOR PORCELAINS. Des Optim FIRING CURVE Porc

79. Clarke D (1985) GRAIN BOUNDARIES IN POLYPHASE CERAMICS. J Phys Colloq 46:C4-51-C4-59. https://doi.org/10.1051/JPHYSCOL:1985404

80. Denmeade J (2013) Investigation of novel precursor routes for incorporation of oxynitride spinel phases into ceramic-metallic composites formed via the TCON process

81. Peters K-M, Cravens RM, Hemrick JG ADVANCED CERAMIC COMPOSITES FOR IMPROVED THERMAL MANAGEMENT IN MOLTEN ALUMINUM APPLICATIONS

82. Snoeijer JH, Andreotti B (2008) A microscopic view on contact angle selection. Phys Fluids 20:057101. https://doi.org/10.1063/1.2913675

83. Delannay F, Froyen L, Deruyttere A (1987) The wetting of solids by molten metals and its relation to the preparation of metal-matrix composites composites. J Mater Sci 1987 221 22:1–16. https://doi.org/10.1007/BF01160545

84. Randall M. German (1996) Novel Sintering Techniques. In: Sintering Theory and Practice . Wiley, pp 373–420

85. Gupta M, Ibrahim IA, Mohamed FA, Lavernia EJ (1991) Wetting and interfacial reactions in Al-Li-SiC p metal matrix composites processed by spray atomization and deposition. J Mater Sci 1991 2624 26:6673–6684. https://doi.org/10.1007/BF00553692

86. Mortensen A, Cornie JA (1987) On the infiltration of metal matrix composites. Metall Mater Trans A 1991 186 18:1160–1163. https://doi.org/10.1007/BF02668570

87. Geguzin YE, Boiko YI (1982) Self-diffusion coefficients obtained in model sintering experiments. Sov Powder Metall Met Ceram 1982 214 21:271–273. https://doi.org/10.1007/BF00806758

88. German RM (1979) Some sources of activation energy errors in sintering experiments. Powder Metall 22:29–30. https://doi.org/10.1179/POM.1979.22.1.29

89. Yokoyama T (2013) Diffusivity of dissolved silica in rock pore water at 25°C as characterized by through-diffusion experiments. Water Resour Res 49:8299–8309. https://doi.org/10.1002/2013WR013794

90. Wilke CR, Chang P (1955) Correlation of diffusion coefficients in dilute solutions. AIChE J 1:264–270. https://doi.org/10.1002/AIC.690010222

91. Applin KR (1987) The diffusion of dissolved silica in dilute aqueous solution. Geochim Cosmochim Acta 51:2147–2151. https://doi.org/10.1016/0016-7037(87)90263-8

92. Rebreanu L, Vanderborght JP, Chou L (2008) The diffusion coefficient of dissolved silica revisited. Mar Chem 112:230–233. https://doi.org/10.1016/J.MARCHEM.2008.08.004

93. Tén BY (2004) Calculation of SiO 2 Diffusion Coefficients Based on Kinetic Curves of Silica Grain Dissolution. Glas Ceram 2004 613 61:111–113. https://doi.org/10.1023/B:GLAC.0000034061.78803.A4

94. Yokoyama T (2013) Characterization of the reaction and transport properties of porous rhyolite and its application to the quantitative understanding of the chemical weathering rate. Geochim Cosmochim Acta 118:295–311. https://doi.org/10.1016/J.GCA.2013.05.011

95. Brady P V., Walther J V. (1990) Kinetics of quartz dissolution at low temperatures. Chem Geol 82:253–264. https://doi.org/10.1016/0009-2541(90)90084-K

96. Breslin M (1994) Transformation Kinetics of Al2O3/Al Co-Continuous Ceramic/Metal

Composite Materials (C4) Produced by a Displacement Reaction Between Liquid Al and Fused SiO2. The Ohio State University

6: Conclusions

Different Additive Manufacturing (AM) technologies were here investigated to print high-performance ceramic coupons (aluminosilicates, silica and zirconia). The samples were printed via Vat Photo-Polymerization (VPP), Binder Jet Printing (BJP), and Material Jetting (MJ); and the powder particle size and crystalline nature before and after printing was investigated.

Near dense final parts were obtained (79% in VPP, 68% in BJP, 97% in MJ) across the different AM processes investigated. In addition to standard samples, intricate geometries with unit cell structures were analyzed for printability. It was observed that process parameters such as printing direction, particle size, and post-processing techniques strongly affected the mechanical performance of the printed samples. It was also observed that the particle-binder interaction plays a critical role on the structural performance and conformation of the manufactured systems. Several post-processing conditions were studied in this work, and the optimal sintering parameters and environment for the individual material in terms of porosity and defects was established. It was observed that for a successful sample manufacturing in all the investigated techniques a slow heating and cooling ramp was required to achieve dense parts. In fact, it was shown that a two-step sintering process (ramp and hold with cooling cycles) results in denser structures.

The mechanical and thermal properties of ceramic samples printed via each AM technique seem to provide a comparable performance to those parts fabricated using conventional manufacturing methods. A full densification process with limited porosity remains a challenge when producing printed parts via VPP and BJP. SEM micrographs of the ceramic samples showed a certain degree of porosity after the post-processing stage. The densification of these printed parts was achieved by subjecting the parts into a transformation process to yield Interpenetrated Phase composites (IPCs).

The purpose of this work is to contribute to the scientific and engineering field by providing a robust study of the printing parameters and post-processing conditions to yield 3D printed ceramic

structures. This work could be of great benefit to the aerospace, automotive, defense, electronic and maritime field where lightweight high performance ceramics are currently required.

Appendix A: Instrumentation

This document discusses the characterization techniques used in this work. Analytical and mechanical characterization of the samples which include before and after analysis, which provide a roadmap in understanding the printability and pos-thermal processes. In this work, several instruments were used to know the fundamental features such as particle size and crystallographic arrangement, as well as to provide an understanding of the effects of the post-processing stage into the mechanical and thermal performance of the parts.

A1. Post Processing

Ceramics always require an unavoidable step of subjecting them to high temperatures/ near-fusion temperatures for the particles to adhere and densify. Concurrently, the powders show increase in crystallinity and phase formation during the temperature variations. In this work two high temperature sintering ovens were used to sinter the printed samples.

A1.1. Yamato DX402A

A curing oven operated in atmospheric conditions that has the capability of reaching a maximum of 300˚C. A glass wool insulation is used in this oven with a PID controller and K-type thermocouple. This oven is used in this research to cure samples printed via Binder Jetting Printing (BJP).

A1.2. Blazir Zirconia

This is a dental furnace that has a maximum temperature capability of 1530˚C. The equipment has the capacity for including innumerable ramp and dwell steps (figure 1).

Figure A1: Blazir Zirconia Dental Furnace [1].

A1.3. Kejia Furnace, KJ -1700 A

This is an atmospheric furnace with Molybdenum Disilicate (MoSi2) heating elements with a maximum temperature that can go up to 1600˚C. The equipment is capable of upto 30 programs for ramp and dwell steps. And the chamber is made of Alumina Fiber, that is capable to withstand the higher temperatures.

Figure A2: High Temperature Atmospheric Furnace used in this work to sinter Silica, Zirconia specimen.

A1.4. Grinding and Polishing

Grinding and Polishing are the initial steps used to prepare a sample for mechanical and optical analysis. This involves the mechanical grinding/polishing stage of the samples to achieve a smooth finish so the microstructure of the grains and the phases in the sample are clearly visible. In this research a Struers Planopol polishing machine equipped with different sets of SiC grained polishing sheets were used (see Figure 3). The polishing sheets had a grain of size with 180, 240, 400, 800, 1200, 1400 microns using water as medium. A mirror finish is always desired when it is the case with metals, but ceramics are polished so that a smoother surface is observed. The final step of the polishing is made using a diamond suspension with particle size from 0.1µm - 3µm on a cloth to attain mirror/glazed finish.

Figure A3: Polishing machine at YSU.

In this research, the sample were also grinded to get an even surface for various mechanical testing. Finely polished samples (where the grinding and polishing took place up to diamond suspension) were characterized optically under optical and electron microscope.

A2. Analytical Characterization

A2.1. Laser Diffraction Analyzer

This spectroscopy method is used to determine the size distribution in loose powder particles. It is a replacement to the traditional techniques like sieve analysis. The technique works based on the

Fraunhofer principle of light scattering (see Figure 4), measuring the angular variation and intensity of the laser beam source on the dispersed particle to determine the volumetric size of the particles.

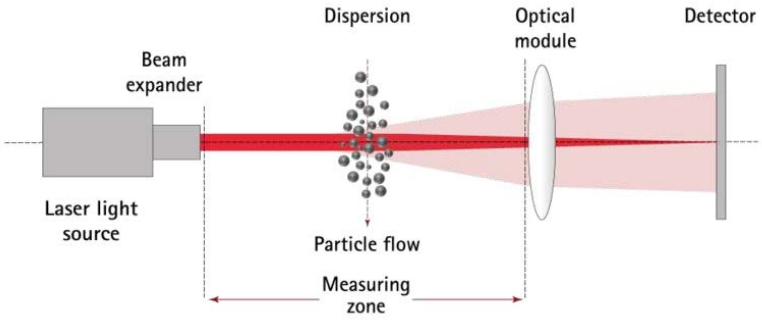

Figure A4: Fraunhofer principle of light scattering that is used in Laser Particle size Analyzer set up [2].

The instrument used in this research was CILAS 1190 capable to measure 0.4 microns to 2.5 mm particle sized particles supported with a Size expert software. It consists of a laser beam, a pump that enables titration of the powder particles in a liquid medium (which is water), and a computer that collects all the data based on the intensity of the light source on the particles (see Figure 5).

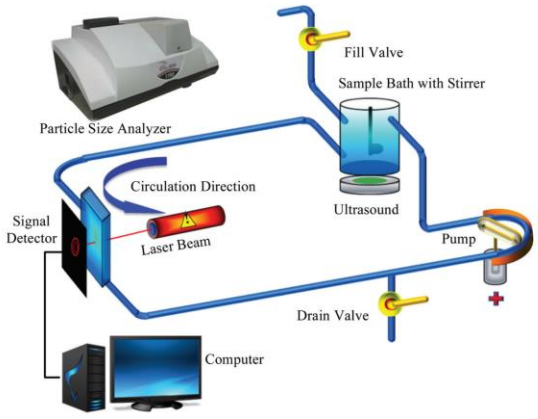

Figure A5: Schematic diagram of CILAS 1180 laser particle analyzer [3].

A2.2. Viscometer

Viscometer is a specialized instrument to measure the dynamic viscosity (η, units: cP or mPa.s) of any liquid. The technique involves a quantitative measure of shear stress of the thesing fluid. In this research, a dynamic shear rheometer, Fungilab, Viscolead Advance was used (see Figure 6). It

consists of various stainless-steel spindles (L, R, H models) shaped in cylinders with different diameters. The rotational cylinders drag the liquid in various speeds to introduce torque to determine the shear rate. Spindle L3 was used in this work to measure the viscosity of the ceramic resin used in StereoLithography.

Figure A6: Fungilab, Viscolead Viscometer used in this research [4].

A2.3. Refractometer

Refractive index of any mixture is the measure of the light refraction of the substance through any transparent medium where refraction refers to the deflection of light between two substances due to density difference. The material index is measured at a constant temperature. It consists of a LED light source that is focused on a prism surface, which passes through the material. The critical angle of reflection is then determined by a high-resolution sensor. Figure 7 shows the schematic of a refractometer that works based on Snell's law, Equation 1. Here, n is the refractive index, 1 refers to the incident angle, and 2 refers to the refracted angle. The refractometer used in this research was a Reichert Abbemark II unit.

$$n_1 \, sin\theta_1 = n_2 \, sin\theta_2 \qquad (1)$$

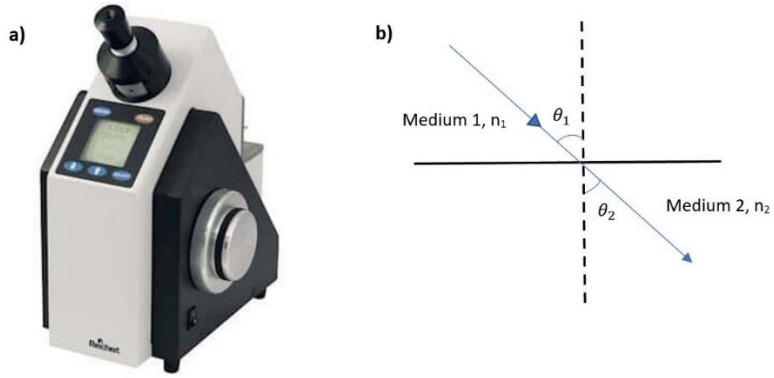

Figure A7: (a) AbbeMark Refractometer [5] (b) Schematic diagram of Snell's law showing refraction of a light ray in two different mediums.

A2.4. Thermo Gravimetric Analysis

Thermo Gravimetric analysis simply is a method to know the mass change of any sample along time and temperature. It is used to know the phase transition in solutions as well as the oxidation and reduction in materials. The results serve as a basis for selection and formulation of new materials. The instrument has a ultra-high sensitive precision pan made either of Aluminum/Alumina to hold the sample and a computer to program the temperature. A TA -TGA 2950 measurement device was used in this research to calculate the weight loss % of the resin used in StereoLithography and Material Jetting, as shown in Figure 8.

Figure A8: TA-TGA 2950 analytical instrument used in this research.

A2.5. X-Ray Diffraction

X-Ray Diffraction is an analytical method used to learn the crystalline structure and composition along with unit cell dimensions of any material. X-Rays are irradiated onto the sample and the array of atoms are scattered in order to constructively and destructively form elastic waves that are seen as the diffraction pattern reflection. The interference observed here is determined by the Bragg's law, Equation 2, where X is the incident angle, d is the distance between diffracting planes, is the beam wavelength and n is an integer. The equipment consists of an X-ray tube, a goniometer and an X-ray detector. The X-rays are generated in a cathode-ray tube where electrons are bombarded on to the target material to produce X-ray spectrum. The spectrum consists of K_{α}, K_{β}, L_{α} wavelengths that are filtered and detected by a rotating detector. Generally, the target materials used are Cu, Fe, Mo, Cr. The X-rays generated are collimated onto the specimen and the spectrum after absorption is converted into signals that are detected as peak intensity, Figure 9. XRD is used to measure the material purity and percentage of amorphous and crystalline phases.

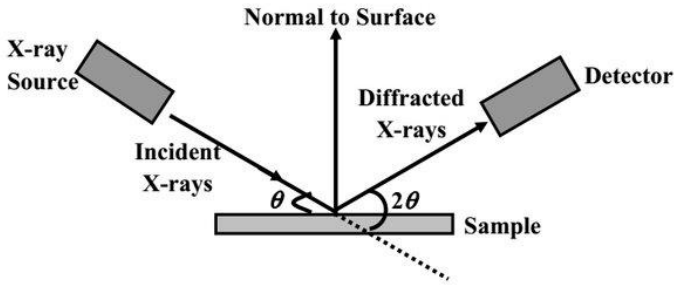

Figure A9: Schematic diagram of working of X-Ray Diffraction [6].

$$2d \sin\theta = n\lambda \qquad (2)$$

In the present research, Bruker Prospector CCD Diffractometer using 40kV source is used, as shown in Figure 10. A rotation angle of 0° to 110° is used with a scanning step of 0.02° for a period of 30 seconds. The spectrum detected is matched to the peaks and d-spacing from the data available in the American Mineralogist Crystal Structure Database to identify the material of interest. Here,

the data used to interpret the crystalline structures was from Powder Diffraction Files (PDF) made by the International Centre for Diffraction Data (ICDD).

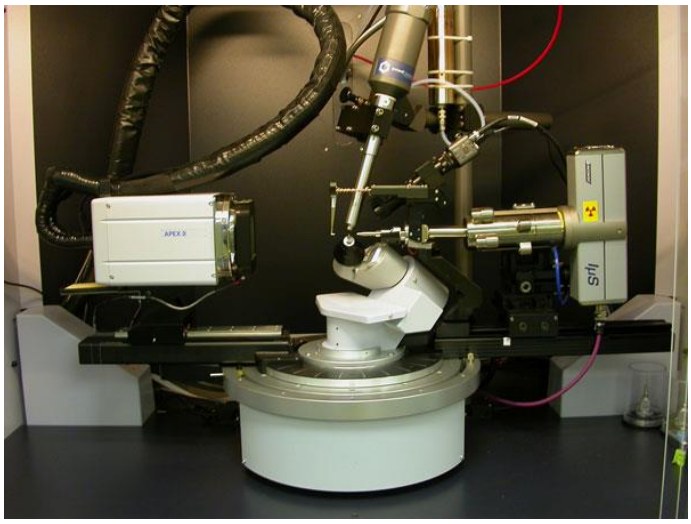

Figure A10: Bruker Prospector X8 XRD unit used in this research.

A2.5.1. Phase Analysis (Reitveld Fitting Analysis)

Phase analysis in this research was performed by the Reitveld method. The Rietveld method is a technique where the XRD spectrum calculated is fitted to the experimental data. Unit cell dimensions of the crystal structure is used to quantify the phases. The experimental data is refined to fit the analytical data and simulated to give different phases present. The present research used the TOPAS 3.0 software to simulate the data to analyze the phase percentages.

A2.6. X-Ray fluorescence Study (XRF)

XRF analysis is a similar analysis like XRD where the difference lies in the extent of chemical composition determination. XRF determines the chemical composition by the X-ray beam irradiated on the sample. The characteristic X-ray energy emitted after the absorption of the incident X-rays is used to characterize the elements present in the sample. K and L energy levels in the electron energies play a key role in the whole process, however samples under Z<12 (lighter elements) cannot be determined in this technique. This is because of the usage of a scintillating detector generally made up of Rh requires a higher intensity of X-ray reflection that is not seen in

lighter elements. The XRF instrument used in this research was a S2 Ranger with a capacity of 28 sample holding (see figure 11). XRF in combination with the XRD reveals the elemental analysis, and phase analysis.

Figure A11: XRF unit used in this research [7].

A2.7. NMR Spectroscopy

Nuclear Magnetic Resonance (NMR) spectroscopy is used to qualitatively analyze materials and to characterize the molecular structure of organic composites. The sample was exposed to a magnetic field so the nuclei in the sample are electrically charged in order to detect the energy transfer in the external magnetic field. The energy transfer is observed as a spectrum where the values are plotted between the resonance intensity and chemical shift. Then, each chemical shift is matched with its corresponding chemical groups. This system also provides the stoichiometry of the material. In this research, a 400 MHz multinuclear NMR, Bruker Advance with an inverse probe was used.

A2.8. Brunauer-Emmett- Teller (BET) Analysis

BET is a method to analyze the surface area (m^2/g) of a material with respect to partial pressures. The instrument uses liquid nitrogen to dry the samples at elevated temperatures and measure the

volume of gas adsorbed by the sample surface. However, only monolayers are considered for dynamic gas adsorption.

In this research, a Micromeritics AutoChem 2920 BET testing system was used, and it employed a 30%N_2/He gas mixture as the adsorbent material. A schematic BET unit is shown in Figure 12. ASTM C1274 standards were used to determine the partial pressures as well as the specific surface area in this work.

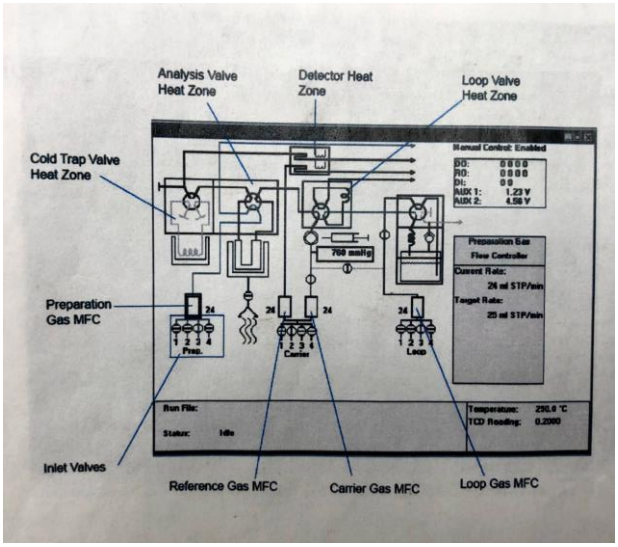

Figure A12: Schematic Figure of BET working.

A2.9. Microscopy

Microscopy is a common technique used to analyze objects. In general, the microstructure, micro-sized powder particles and fracture profiles are observed in a microscope. Most of the time, grinded and finely polished samples are observed to understand the features in the system.

A2.9.1. Light Microscopy

An optical microscope is a system with an eye piece, objective lens, illumination system, and a specimen stage. Light rays are focused through a condenser lens to attain maximum illumination and then the advantage of light is used to magnify the image through the objective and lens, and the eyepiece (see figure 13). A magnified image is seen at this point. Different techniques of

microscopy like polarized, reflected and transmitted light microscopes were used depending on the type of light used and the movement of the light.

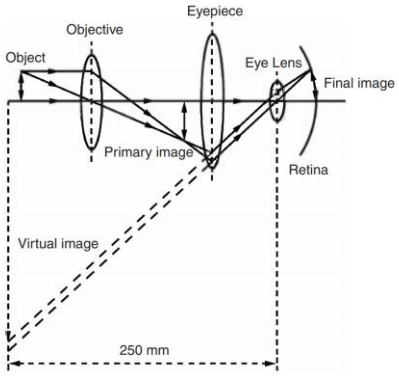

Figure A13: Schematic figure showing working principle of light microscope.

In this research, a reflected light microscope was used to observe the opaque ceramic samples. A Keyence VHX-7000 series microscope was used in this work to analyze microscopic features in the ceramics (see figure 14). The microscope is capable of magnifying samples from 20x -2000x magnification along with bright and dark features.

Figure A14: Keyence VHX-7000 microscope representation used in this research [8].

A2.9.2. Scanning Electron Microscopy

A Scanning Electron Microscope (SEM) is a sophisticated electron microscope which uses an electron beam to generate the image. Kinetic energy created by the electrons is scattered on the

surface of the sample and diffracted electrons produce signals according to the energy. Secondary and backscattered electrons are used to observe the morphology and topography of the samples. The major parts in the SEM include an electron source, lenses, scanning coil, detector, power supply, a vacuum system, and a display unit (see Figure 15). An electron source is the major component which uses thermal heat/voltage to generate electrons for forming a beam in low vacuum conditions to focus on the sample. Generally, three types of electron sources: Tungsten filament, LaB_6 crystal, and field emission gun are used for electron generation. A condenser lens is used to focus the beam of electrons through a column where a narrow beam is formed into a spot. The spot is then deflected onto the surface of the sample which is later detected by a detector. The detector differentiates the secondary electrons, back scattered electrons and characteristic X-rays depending upon the voltage speed and density of the specimen.

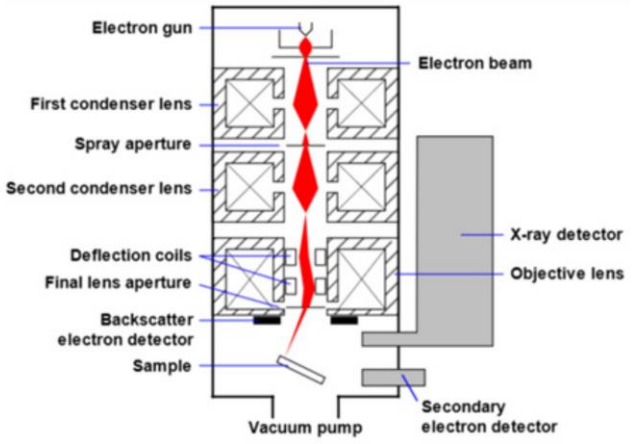

Figure A15: A schematic showing the working of the SEM [9].

A Keysight FE-SEM using a field emission gun, and a JEOL JIB-4500 multi-beam SEM using LaB_6 crystal electron source were used in this work to analyze the samples (see Figure 16).

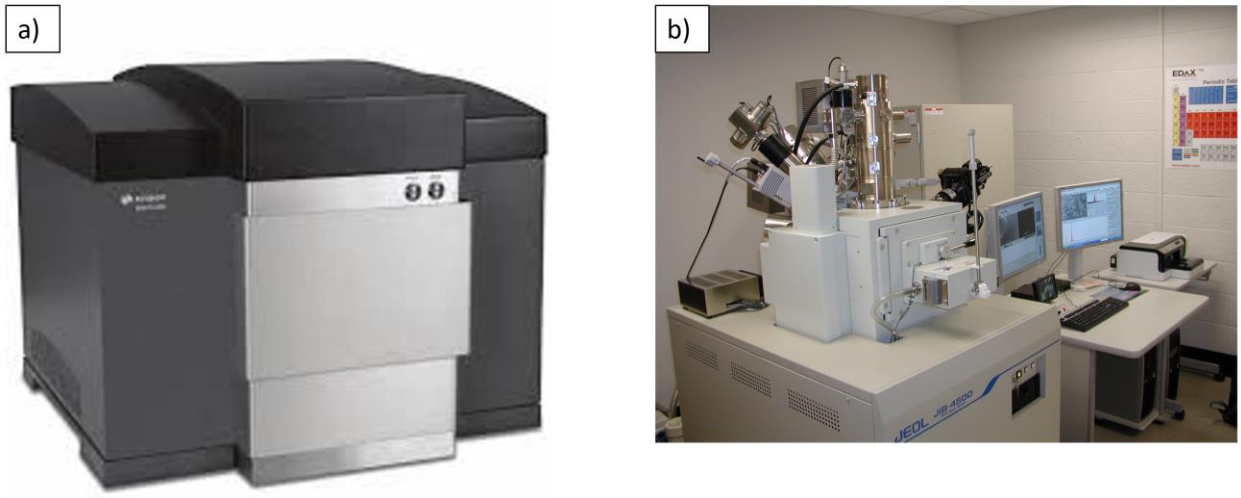

Figure A16: Scanning Electron Microscope. (a) Keysight FE-SEM. (b) JEOL JIB-4500 multi beam SEM [7].

A2.9.2.1. Focused Ion Beam (FIB)

Focused Ion beam is a technique similar to SEM with the only difference that it uses an ion beam instead of an electron beam. The ion beam is used to obtain images as well as for micromachining. Typically, secondary electrons generated from Ga are used in this system with a gas unit for activating the beam. A two-lens unit consisting of a condenser and an objective lens is used to define the beam so that a precise rastaring area with high intensity ion spot is generated. In practice, spot size and aberration are the two problems that users face to focus the beam without noise. This technique is used for several purposes like sample heating, sample imaging and sample micromachining [10, 11]. In this research, a JEOL JIB-4500 SEM equipped with FIB was used to prepare TEM samples out of Material jetting printed ZrO_2 samples. The unit is equipped with Ga ion generation activated by W and C gas injection systems. This unit was also used to micromachine and weld the samples to the TEM sample holder. A refined needle, Omniprobe nano manipulator was used to pick the tiny samples (ranging from 1nm to 10 nm).

A2.9.3. Transmission Electron Microscopy

Transmission Electron Microscope (TEM) is a powerful microscope used to analyze thin samples. The working principle of the TEM is similar to that described by the light microscope except that it uses electrons instead of light. The interaction of electrons on the sample surface creates the image showing the finest details like crystal structures, and grain morphology. The main components in the TEM are an electron gun, condenser lens, objective lens, a fluorescent screen and an image display unit (see figure 17a). The electron beam generated is focused on the condenser lens and then angled so that the beam is transmitted through the sample to reflect the image on the fluorescent screen. Hence, it is necessary that the sample is electron thin. The objective lens and apertures can be adjusted to enhance and contrast the features of the sample by deflecting the electron beam angles to obtain high-resolution images.

A TEM can also be used for obtaining a diffraction pattern of the samples since the electron beam is transmitted and an electrostatic potential is created in the sample. A focal point is created from the electron beam spot and the electrons are scattered from one point to another in the image plane creating a diffraction pattern.

In this research a JEOL 2100 Scanning/Transmission Electron Microscope was used to analyze the samples prepared on the SEM-FIB unit (see figure 17b).

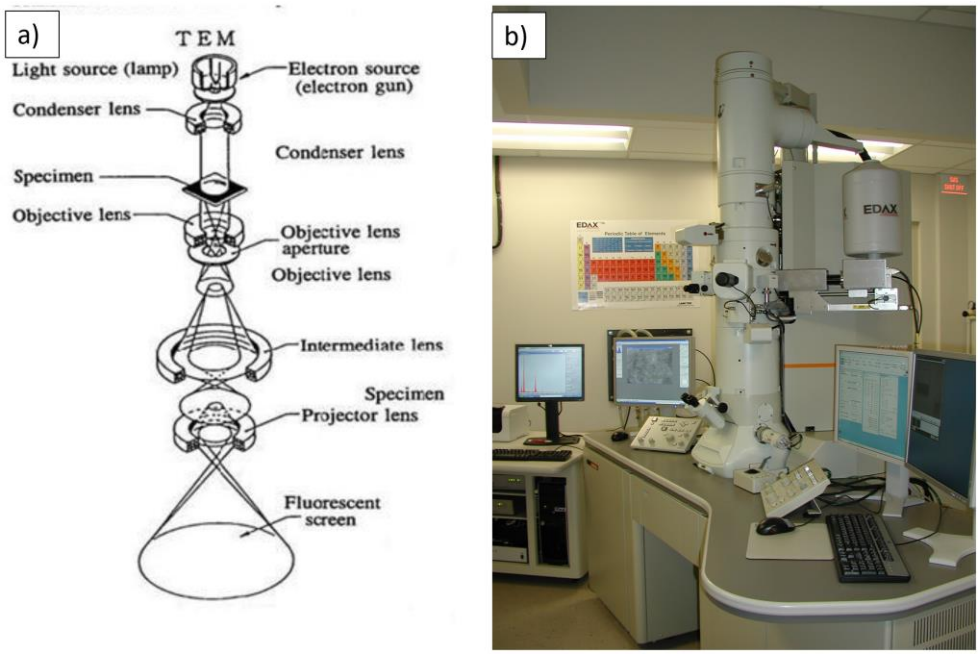

Figure A17: Transmission Electron Microscope. (a) Working principle of TEM [12]. (b) JEOL 2100 Scanning/ Transmission Electron Microscope [7].

A2.10. Energy Dispersive Spectroscopy

Energy Dispersive Spectroscopy (EDS) is an analytical technique used for the elemental or chemical analysis of a sample. In this technique, characteristic X-rays interact with the sample, which produce an excitation of electrons resulting in an unique emission spectrum related to each element. The main components in an EDS unit are the X-ray beam source, X-ray detector, pulse processor and an analyzer. Si (Li) detector and silicon drift detectors are the most commonly used detectors operating in controlled atmospheric conditions. This method is used for elemental mapping, elemental detection and quantitative analysis in the sample. This research used a Keysight FE-SEM equipped with and EDS gun.

A2.11. Contact Angle Measurement

A Kruss Drop Shape Analyzer, DSA 100E was used to understand the contact angles and drop shapes of the binder systems in this research (see Figure 18 a). The unit expels a particular liquid from a controlled syringe head on a flatbed which is then used for analyzing the stream of ink

droplets in terms of drop formation, volume, speed and behavior. An automated image generated by the ADVANCE software is used to make the measurements. The drop wetting the bed is reflected on an in-built camera, and it provides video-images of the nozzle and the drop formation. This image helps in measuring the contact angle and length of the drop with the aid of a reference frame. A sessile drop technique was used in this research to determine contact angle (see Figure 18 b).

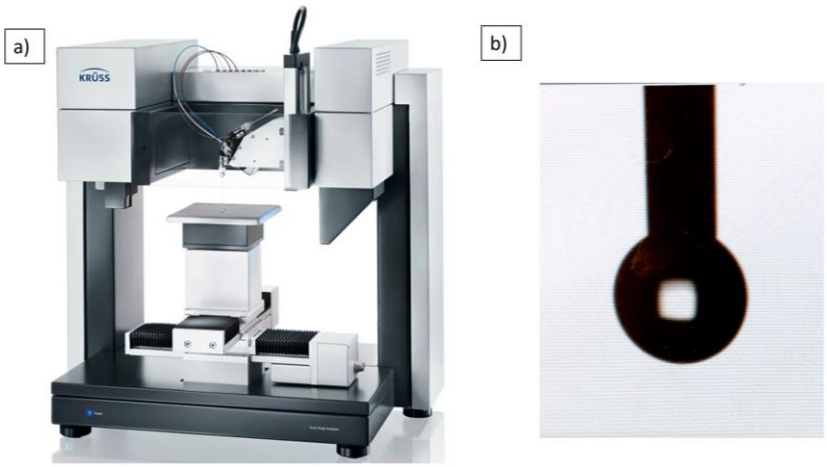

Figure A18: Surface measurements taken in this research. (a) KRUSS Drop Shape Analyzer [13]. (b) A sessile drop formed from the syringe.

A3. Mechanical Characterization

A3.1 Universal Testing Machine (UTM)

A Universal Testing Machine (UTM) is a unit used to determine the material's mechanical properties like compressive, tensile, and flexural strength. An UTM is mainly composed of a load frame, load cell, cross head, extensometer, and a computer to program the conditions for testing. The cross head is operated either electromechanically or by hydraulic systems to adjust traverse velocities for the mechanical testing. The frame is equipped with a load cell and an extensometer which is essentially a gauge to measure the length changes (see figure 19). In this research an Instron Universal Testing Machine with 10 kN and 150 kN load cells was used (see Figure 20). A quasi-static testing with a cross head speed of 0.5mm/min or 1mm/min was used. The force and

displacements of corresponding testing were recorded by a Bluehill 3 software that has been developed by Instron. A force vs displacement curve was plotted to further calculate the stress-strain diagram for the tested material.

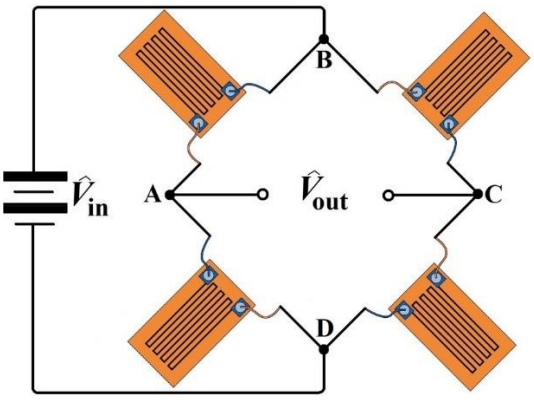

Figure A19: Wheatstone bridge construction for load cell.

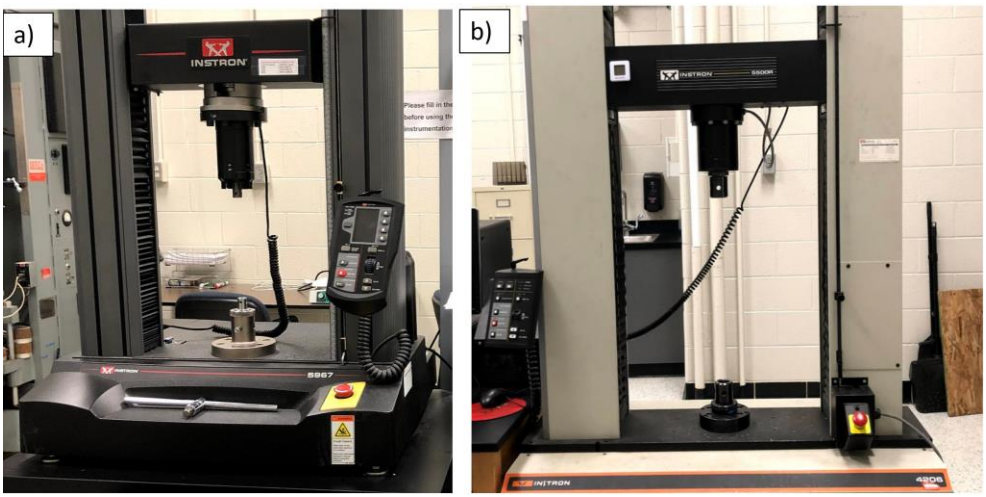

Figure A20: UTMs used in this research. (a) Instron with a load cell capacity of 10kN (Model : Instron 5967). (b) Instron UTM with a load cell capacity of 150kN (Model: Instron 5500R).

A3.1.1. Compressive Testing

Compressive Strength is the resistance of a material to fracture under compression. Compressive strength of any material can be performed in a uni-axial compression where two flat plate fixtures move in the opposite direction applying force on the sample (see figure 21). The materials are exposed to force until they are squished or crushed and a force- displacement diagram is plotted.

The compressive strength is calculated by using Equation 3, where σ is the compressive strength (MPa), F is the force (N) and A refers to the surface area under force application (m^2). This research used the ASTM 1424 and ASTM C364 to test the solid ceramic and lattice structures, respectively. The stress-strain curve plotted from the force vs displacement curves are used to calculate the yield stress, ultimate compressive stress, and fracture points.

$$\sigma = \frac{F}{A} \qquad (3)$$

Figure A21: A compression testing set up.

A3.1.2. Flexural Testing

Flexural strength of a material can be defined as the ability to withstand the bending deformation before failure. Flexural test is used to determine flexural strength and flexural modulus of the material. This test can be performed either by 3-point bending or 4-point bending methods (see figure 22). As in the compressive testing, the force vs displacement along with stress vs strain graphs were used to determine the strength and modulus of the tested system.

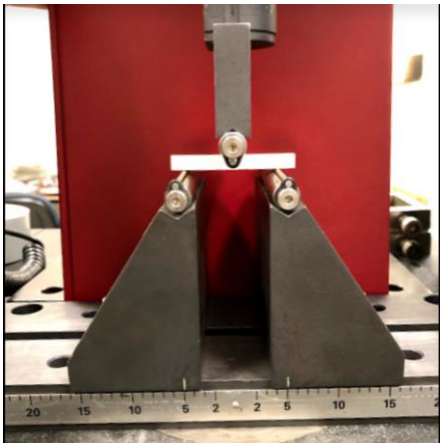

Figure A22: A 3-point bending test set-up with the fixtures.

In this research, 3-point bending under quasi-static testing was used and the stress and strain were calculated using Equation 4,5, where σ_{flex} is flexural strength (MPa), F is force (N), L is the length of support span (mm), b is width (mm), d is thickness of the sample (mm) and D is maximum deflection in the force direction (mm).

$$\sigma_{\text{flex}} = \frac{3FL}{2bd^2} \qquad (4)$$

$$\epsilon_{\text{flex}} = \frac{6Dd}{L^2} \qquad (5)$$

In this research, ASTM C1161, C 1674 testing standards were used for testing the bulk and lattice flexural samples.

A3.1.3. Fracture Toughness

Fracture toughness is the ability of a material to resist the propagation of fracture. A built-in or artificially introduced notch is included in the samples to use as a fracture initiator in the test. A 3-point bending, or 4-point bending set-up is used here to investigate the toughness of the samples. The fracture toughness, K, is calculated from the force applied, specimen size and the pre-crack size (see Equation 6). A normalized crack ratio and function of this ratio play a critical role in obtaining fracture toughness as the introduced notch is associated with the indentation. In this research, a single edge notch is used for all the ceramics following the ASTM C1421. The function of crack ratio was calculated individually depending upon the crack size (see Equation 7).

$$K = g\left[\frac{P\,S_o}{BW^{\frac{3}{2}}}\right]\left[\frac{3\frac{a}{W}^{\frac{1}{2}}}{2[1-\frac{a}{W}^{\frac{3}{2}}]}\right] \qquad (6)$$

$$g\left(\frac{a}{W}\right) = A_o + A_1\left(\frac{a}{W}\right) + A_2\left(\frac{a}{W}\right)^2 + A_3\left(\frac{a}{W}\right)^3 + A_4\left(\frac{a}{W}\right)^4 + A_5\left(\frac{a}{W}\right)^5 \qquad (7)$$

Where K = fracture toughness (MPa √m)

$g\left(\frac{a}{W}\right)$ = function of ratio $\left(\frac{a}{W}\right)$

P = force (N)

S_o = outer span (m)

B = width of the specimen

W = thickness of the sample without notch

a = crack length (m)

A_0, A_1, A_2, A_3, A_4, A_5 = coefficients of polynomial for 3-point flexural testing

In this research, a single edge notch was artificially introduced in the samples for testing.

A3.2. Hardness Measurement

Hardness is the resistance of material towards plastic deformation. Hardness measurements were made by introducing an indentation by a sharp tool. The force used to indent, and the shape of indentation are critical in calculating hardness of the material. A plane surface of the solids is chosen for testing hardness. In this research, Vickers hardness test was used following the ASTM C1327. A Nanovea nano-hardness machine with a diamond (Berkovich) tip and United Hardness testing equipment with a diamond tip with a 10 kg weight were used in this research. The units of hardness were determined by the indenter shape and applied force.

A4. Thermal Characterization

A4.1. Coefficient of Thermal Expansion (CTE)

Coefficient of Thermal Expansion (CTE, α) is a material property that depends on the material composition. This determines the expansion of materials along the temperature change. The

principle behind the determination of CTE is that the material has a natural tendency to expand due to the kinetic energy developed in the material. Such energy is quantified as CTE. The CTE determined for all the ceramics in this research was governed by Equation 8, where α is the CTE (μm/m)/°C) and l is the initial length (m) of the sample and $\frac{dl}{dT}$ is the change in length along the temperature change.

$$\alpha = \frac{1}{l(\frac{dl}{dT})} \qquad (8)$$

In this research, a TA- Q400 EM thermochemical analyzer (see Figure 23) was used to measure the CTE and thermo-mechanical (visco-elastic) properties of materials. The ASTM E831-06 standard was used in this research work.

Figure A23: TA Q400 EM thermo-mechanical analyzer used in this research.

A5.References

1. Blazir - ShenpazShenpaz. https://shenpaz.com/blazir/. Accessed 14 Dec 2020

2. Laser Diffraction. https://www.sympatec.com/en/particle-measurement/sensors/laser-diffraction/. Accessed 15 Feb 2021

3. Zhang G, Yin H, Lei Z, Reed AH, Furukawa Y (2013) Effects of exopolymers on particle size distributions of suspended cohesive sediments. J Geophys Res Ocean 118:3473–3489

4. ADV - FungiLab –. https://fungilab.com/product/rotational-viscometers/viscolead-

series/adv/. Accessed 15 Feb 2021

5. Reichert Abbe Mark II Plus Refractometers | General Laboratory Supply, Inc. https://www.gogenlab.com/equipment-instruments/refractometers/accessories-reichert-abbe-refractometers/reichert-abbe-mark-9. Accessed 25 Feb 2021

6. Wubet W, Abdisa B (2018) Green Synthesis of CuO Nanoparticles for the Application of Dye Sensitized Solar Cell.

7. Chemistry Facilities | YSU. https://ysu.edu/academics/science-technology-engineering-mathematics/facilities/chemistry-facilities. Accessed 25 Feb 2021

8. Major Hardware Advancements [LENS / STAGE / CAMERA] High-Accuracy 4K Digital Microscope VHX-7000 Series | KEYENCE America. https://www.keyence.com/ss/products/microscope/lp_vhx-7000/. Accessed 8 Jul 2021

9. Scanning Electron Microscopy - Nanoscience Instruments. https://www.nanoscience.com/techniques/scanning-electron-microscopy/. Accessed 8 Jul 2021

10. Melngailis J (1998) Focused ion beam technology and applications. J Vac Sci Technol B Microelectron Process Phenom 5:469

11. Volkert CA, Minor AM Focused Ion Beam Microscopy and Micromachining The FIB Instrument.

12. Transmission Electron Microscopy (TEM). https://warwick.ac.uk/fac/sci/physics/current/postgraduate/regs/mpagswarwick/ex5/techniques/structural/tem/. Accessed 9 Jul 2021

13. Drop Shape Analyzer-DSA100E | KRÜSS Scientific. https://www.kruss-scientific.com/en/products-services/products/dsa100e. Accessed 8 Jul 2021

Appendix B: Silicon Carbide

A preliminary study on 3D printed silicon carbide was carried out in this work. The following section shows the preliminary results of this effort.

B1: Objectives

Silicon Carbide was printed via BJ-AM in order to investigate the effect of the bimodal and trimodal printing variations in the density of the manufactured materials.

B2: Printing Methodology

Amorphous Silicon Carbide (SiC) powder from Washington Mills (New York, USA) with different particle sizes (60 µm, 40 µm, 12 µm) and an irregular morphology was used in this research work. The powder particles were mixed in various proportions to produce bimodal and trimodal printing (see Table B1). All the powders were mixed with 5% alumina before printing and sieved before printing. The printing parameters for the bimodal and trimodal process were: 70% of binder saturation, a roller- traverse speed of 2 mm/s, 8s for the binder set time, and 30s for the binder drying time. Cylindrical parts according to ASTM C1462 were printed to measure shrinkage, density and compressive strength. All the samples were printed in Z direction.

Table B1: Powder proportions used for printing.

Printing style	Particle size	Ratio of mixing
Bimodal	60 µm, 40 µm	3:2
Trimodal	60 µm, 40 µm, 12 µm	5:3:2

The printed samples were cured at 180˚C for 6 hours to obtain the green parts. The samples were cured upto 400˚C in the Argon atmosphere to measure the densities at various ramp rates (2˚C/min, 3˚C/min and 5˚C/min). The obtained samples were referenced as “brown parts”. At

least three samples were cured at each ramp rate. The green and brown parts were measured for densities using Archimedes principle with water as medium

B3: Results and Discussion

Particle size and morphology of powder particles printed in BJP play a major role in the final property acquisition. As previously mentioned, irregular shaped SiC particles were printed in bimodal and trimodal variations using a binder saturation of 70%, and a roller traverse speed of 2 mm/sec. These two printing parameters were chosen from the previous research work on fused silica where the binder saturation values between 60% and 80% provided relatively good mechanical properties, and the slower roller-traverse speeds resulted in adequate prints [1]. A 5 wt% of alumina powder was added to the silicon carbide powder to assist the consolidation of parts during the heating stage to produce the "brown" samples. Previous works have shown that alumina powder aids sintering at lower temperatures (~ 1000˚C to 1300˚C) to avoid high sintering temperatures commonly used to obtain final parts from Silicon carbide [2, 3]. Alumina particles generally start fusion at around 1200˚C, helping to keep the SiC particles together during liquid phase sintering [4, 5]]. A weight loss in samples has been observed in some cases when the samples were sintered at higher temperatures with oxide additives [4, 6]. This can be avoided when samples are sintered along with pressure [7]. Some other additives that assist on liquid phase sintering of SiC as reported from literature were Y_2O_3, Dy_2O_3, Yb_2O_3, MgO [7][4].
The shrinkage and density of the produced green and the brown specimen was here evaluated. Figure B1 shows the shrinkage in X and Z directions after cooking the samples to 400˚C at different ramping rates. Similar shrinkages were observed in the SiC preforms when the binders were burnt out from the printed samples [8]. It was observed that the shrinkage was higher in the case of bimodal printed parts when compared to the parts with three different particle sizes aka trimodal prints. From the figure, it is observed that the smaller sized particles in the trimodal print (~12 μm) settled in the voids created by the other two particle sized powders. This aided in

reduction of the shrinkage of the samples when subjected to higher temperatures. Additionally, a reduction in the shrinkage can be observed when the ramp rates were slower. The green samples had exhibited a porosity of 33% and 31% when a graythresh MATLAB program was used on the optical images where the voids were indicated as 0's and the particles as 1's [9–11].

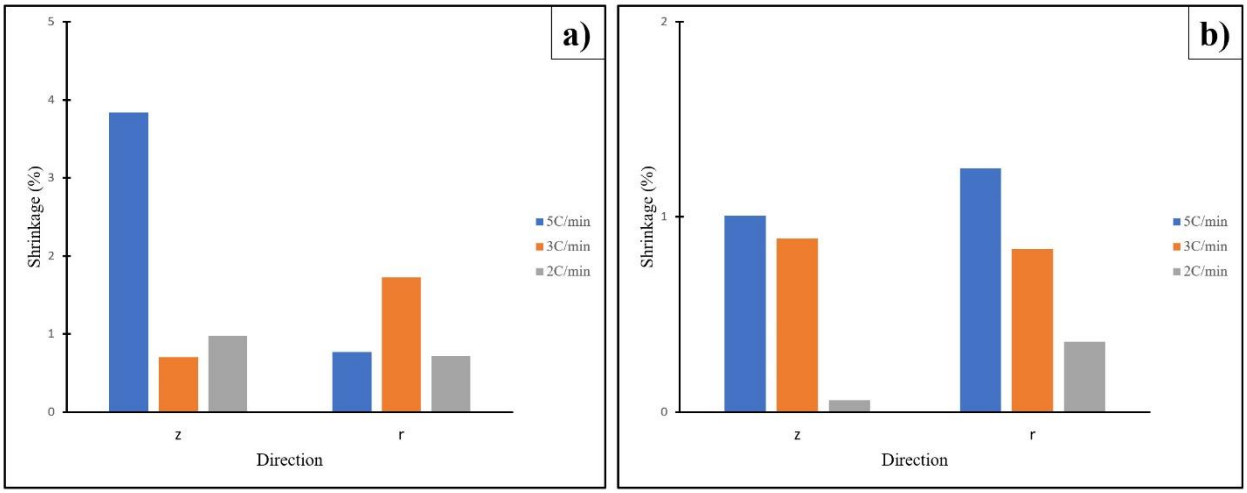

Figure B1: Shrinkage observed in the brown parts when subjected to higher temperatures at different ramp rates. (a) Shrinkage in bimodal samples. (b) Shrinkage in trimodal samples.

The samples were then tested for density and were compared to the green parts density. From figure B2, it was observed that the density of green specimens in bimodal and trimodal prints were relatively similar (1.51 g/cc and 1.55 g/cc, respectively). The densities of the printed samples were comparable to the SiC samples printed using other additive manufacturing technologies such as Stereolithography, and fused filament deposition (FDM), robocasting, and direct ink writing (DIW) where post-processing is required [12–14]. It is worth to be noted that in many AM techniques, the powder particle size plays a critical role in the density of the built parts [12, 15–17]. A similar density value for the green parts was seen when bimodal samples were printed via BJAM by Du et al [18]. A further reduction of density was observed when cooking the samples at 400˚C in an Argon atmosphere. At 400˚C, it is believed that the furan binder is evaporated leaving behind spaces between the particles. A similar pattern in the reduction of density was observed by Húlan et al [19, 20] when fly ash particles were sintered.

However, it can be observed that the samples cooked at slower ramp rates attained higher densities in both the cases. The figure also shows that the samples in the trimodal constitution resulted in a higher density rather than bimodal prints. It is expected that an additional sintering process will result in an increase in density due to the consolidated process governed by the self-diffusing mechanism. Table B2 shows the increase of density in SiC parts after being subjected to different post-processing conditions.

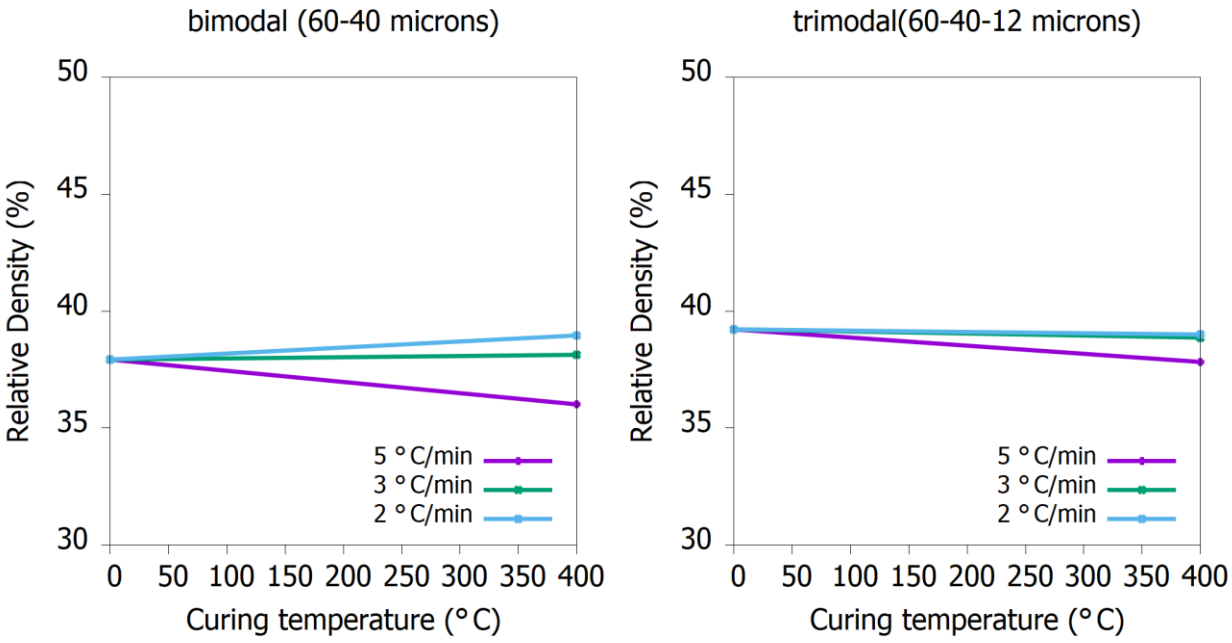

Figure B2: Density Vs Sintering temperature in the bimodal and trimodal printed green and brown specimens.

Table B2: Summary of some of the studies made on SiC using different post-processing techniques.

Manufacturing method	Powder Morphology, Particle size (μm)	Green Density (g/cc)	Post-processing method	Final Density (g/cc)	Reference

Binder Jetting Printing	Irregular, 15.92	1.2	Polymer impregnation (PIP) in vaccum	2.33 ± 0.08	[25]
Binder Jetting Printing	Irregular, ~23	-	Carbon Vapor Infiltration (CVI)	2.95	[27]
Binder Jetting Printing	Irregular, 38.3	1.34	SiC fibers with SiC powder and SMP-10	2.52	[28]
Binder Jetting Printing	Spherical, 49.5	0.72	SiC fibers with SiC powder and SMP-10	2.21	[28]
Binder Jetting printing	Irregular, ~31.15	-	SMP-10	2.15	[29]
Binder Jetting Printing (3DP)	16.2	1.1	Pressureless Si infiltration	2.54	[30]
Uniaxial Pressing	75	-	Additives Al2O3, Y2O3 sintered at ~1850˚C	3.24	[31–33]
Dry pressing	0.5	1.99	Multiple PIP cycles	2.13	[34]
PIP preforms	13.3	2.42	Pyrolysis	2.34	[35]
Perforation of Graphite	11	-	CVI with methyltrichlorosilane	2.48	[36]
C/C-SiC preforms	-	1.3	Reactive Melt Infiltration	2.33	[37]
Preforms from Chemical Vapor infiltration	0.7	-	Capillary infiltration	2.52	[38]

An SEM image of the bimodal and trimodal specimens is shown in Figure B3. As expected, at these post-processed temperatures, the loss of binder results in unbound particles.

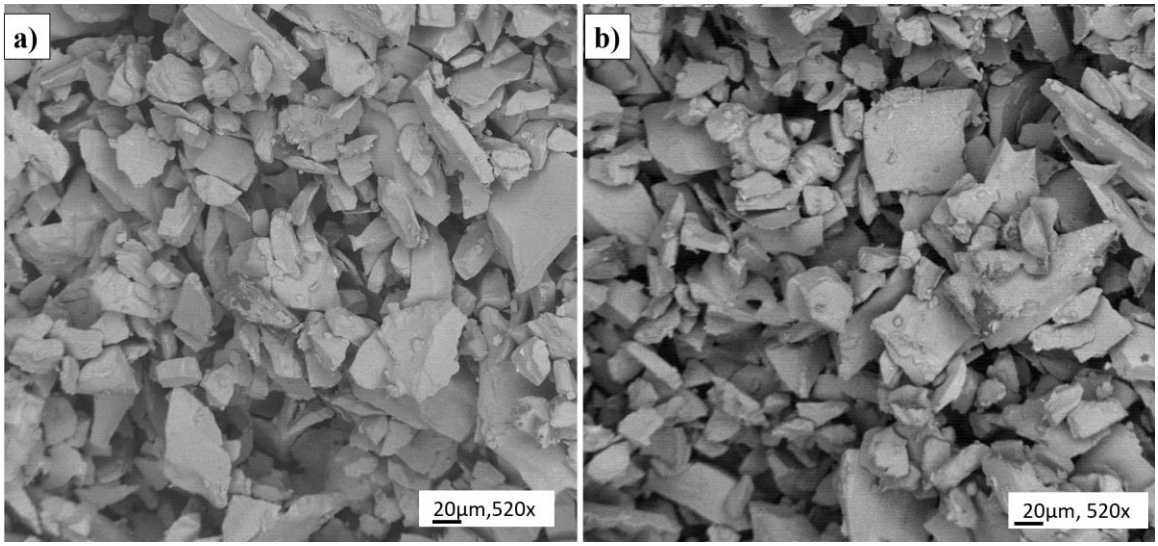

Figure B3: SEM images of the cured samples. (a) Bimodal sample. (b) Trimodal sample.

Some of the other techniques used to increase the density in the final structures is by adding fiber-reinforcements, or using precursors for infiltration, using either CVD, or LPS, or HIP, PIP, or polymer pyrolysis [8, 21–25] . Krenkel et al [26] demonstrated building SiC-C structures for launch vehicles that displayed good abrasive and tribological properties when the samples were melt infiltrated with liquid Silica.

B4: Conclusions

A tri-modal and bimodal printing of SiC was successfully completed using binder jetting. The printed samples displayed relative green densities of 37% and 39% in the bimodal and trimodal prints, respectively. A study on ramp rates was also performed on the investigated samples, and it was shown that a slower ramping rate resulted in denser parts. A decrease in the densities was observed at the brown stage than at the green stage, due to the gasification of the binder. Additionally, a higher shrinkage in the Z- direction was observed in the printed samples. A future study in this research, is the inclusion of additives in order to sinter 3D printed SiC at low temperatures achieving high densities. The infiltration process of the SiC to yield high

temperature cermets will be of interest to the aerospace sector where high-performance materials based on complex and unique geometries are required.

B5: References

1. Miyanaji H, Orth M, Akbar JM, Yang L (2018) Process development for green part printing using binder jetting additive manufacturing. Front. Mech. Eng. 13:504–512

2. Randall M. German (1996) Sintering Theory and Practice | General & Introductory Materials Science | Subjects | Wiley

3. German RM (1996) Wiley: Sintering Theory and Practice -. Wiley-Interscience

4. Pulgarín HLC, Albano MP (2015) Sintering and Microstrusture of Al2O3 and Al2O3-ZrO2 Ceramics. Procedia Mater Sci 8:180–189. https://doi.org/10.1016/j.mspro.2015.04.062

5. Baud S, Thévenot F, Pisch A, Chatillon C (2003) High temperature sintering of SiC with oxide additives: I. Analysis in the SiC-Al2O3 and SiC-Al2O3-Y2O3 systems. J Eur Ceram Soc 23:1–8. https://doi.org/10.1016/S0955-2219(02)00067-5

6. Gadalla A, Elmasry M, Kongkachuichay P (1992) High temperature reactions within SiC-Al2O3 composites. J Mater Res 7:2585–2592. https://doi.org/10.1557/JMR.1992.2585

7. Ribeiro S, Ribeiro GC, De Oliveira MR (2015) Properties of SiC ceramics sintered via liquid phase using Al2O3 + Y2O3, Al2O3 + Yb2O3 and Al2O3 + Dy2O3 as additives: A comparative study. Mater Res 18:525–529. https://doi.org/10.1590/1516-1439.311314

8. He R, Ding G, Zhang K, et al (2019) Fabrication of SiC ceramic architectures using stereolithography combined with precursor infiltration and pyrolysis. Ceram Int 45:14006–14014. https://doi.org/10.1016/j.ceramint.2019.04.100

9. Myers K (2016) Structure-Property Relationship of Binder Jetted Fused Silica Preforms to Manufacture Ceramic-Metallic Interpenetrating Phase Composites. Youngstown State University

10. Andreassen E, Andreasen CS (2014) How to determine composite material properties using numerical homogenization. Comput Mater Sci 83:488–495. https://doi.org/10.1016/j.commatsci.2013.09.006

11. Mummareddy B, Maravola M, MacDonald E, et al (2020) The fracture properties of metal-ceramic composites manufactured via stereolithography. Int J Appl Ceram Technol 17:413–423. https://doi.org/10.1111/ijac.13432

12. Hu C, Chen Y, Yang T, et al (2021) Effect of SiC powder on the properties of SiC slurry for stereolithography. Ceram Int 47:12442–12449. https://doi.org/10.1016/j.ceramint.2021.01.101

13. Griffith ML, Halloran JW (2005) Freeform Fabrication of Ceramics via Stereolithography. J Am Ceram Soc 79:2601–2608. https://doi.org/10.1111/j.1151-2916.1996.tb09022.x

14. Cai K, Román-Manso B, Smay JE, et al (2012) Geometrically Complex Silicon Carbide Structures Fabricated by Robocasting. J Am Ceram Soc 95:2660–2666. https://doi.org/10.1111/j.1551-2916.2012.05276.x

15. Bai X, Ding G, Zhang K, et al (2021) Stereolithography additive manufacturing and sintering approaches of SiC ceramics. Open Ceram 5:100046. https://doi.org/10.1016/j.oceram.2020.100046

16. Tian X, Li D Rapid manufacture of net-shape SiC components. https://doi.org/10.1007/s00170-009-2109-5

17. Ding G, He R, Zhang K, et al (2020) Dispersion and stability of SiC ceramic slurry for stereolithography. Ceram Int 46:4720–4729. https://doi.org/10.1016/j.ceramint.2019.10.203

18. Du W, Singh M, Singh D (2020) Binder jetting additive manufacturing of silicon carbide ceramics: Development of bimodal powder feedstocks by modeling and experimental methods. Ceram Int 46:19701–19707. https://doi.org/10.1016/j.ceramint.2020.04.098

19. Húlan T, Štubňa I, Ondruška J, Trník A (2020) The influence of fly ash on mechanical properties of clay-based ceramics. Minerals 10:1–12. https://doi.org/10.3390/min10100930

20. Haase V, Kirschstein G, List H, et al (1985) The Si-C Phase Diagram. In: Si Silicon. Springer Berlin Heidelberg, pp 1–5

21. Koyanagi T, Terrani K, Harrison S, et al (2021) Additive manufacturing of silicon carbide for nuclear applications. J Nucl Mater 543:152577. https://doi.org/10.1016/j.jnucmat.2020.152577

22. Zhang H, Yang Y, Hu K, et al (2020) Stereolithography-based additive manufacturing of lightweight and high-strength Cf/SiC ceramics. Addit Manuf 34:101199. https://doi.org/10.1016/j.addma.2020.101199

23. Xu T, Cheng S, Jin L, et al (2020) High-temperature flexural strength of SiC ceramics prepared by additive manufacturing. Int J Appl Ceram Technol 17:438–448. https://doi.org/10.1111/ijac.13454

24. Lu ZL, Lu F, Cao JW, Li DC (2014) Manufacturing properties of turbine blades of carbon fiber-reinforced SiC composite based on stereolithography. Mater Manuf Process 29:201–

209. https://doi.org/10.1080/10426914.2013.872269

25. Cramer CL, Armstrong H, Flores-Betancourt A, et al (2020) Processing and properties of SiC composites made via binder jet 3D printing and infiltration and pyrolysis of preceramic polymer. Int J Ceram Eng Sci 2:320–331. https://doi.org/10.1002/ces2.10070

26. Krenkel W, Berndt F (2005) C/C-SiC composites for space applications and advanced friction systems. Mater Sci Eng A 412:177–181. https://doi.org/10.1016/j.msea.2005.08.204

27. Terrani K, Jolly B, Trammell M (2020) 3D printing of high-purity silicon carbide. J Am Ceram Soc 103:1575–1581. https://doi.org/10.1111/jace.16888

28. Polozov I, Razumov N, Masaylo D, et al (2020) Fabrication of Silicon Carbide Fiber-Reinforced Silicon Carbide Matrix Composites Using Binder Jetting Additive Manufacturing from Irregularly-Shaped and Spherical Powders. Materials (Basel) 13:1766. https://doi.org/10.3390/ma13071766

29. NASA Technical Reports Server (NTRS). https://ntrs.nasa.gov/citations/20150023455. Accessed 16 Apr 2021

30. Fu Z, Schlier L, Travitzky N, Greil P (2013) Three-dimensional printing of Si-SiC lattice truss structures. Mater Sci Eng A 560:851–856. https://doi.org/10.1016/j.msea.2012.09.107

31. She JH, Ueno K (1999) Densification behavior and mechanical properties of pressureless-sintered silicon carbide ceramics with alumina and yttria additions. Mater Chem Phys 59:139–142. https://doi.org/10.1016/S0254-0584(99)00039-5

32. MULLA MA, KRSTIC VD (1991) Low-temperature pressureless sintering of β-silicon

carbide with aluminum oxide and yttrium oxide additions. Am Ceram Soc Bull 70:

33. Zhang N, Ru HQ, Cai QK, Sun XD (2008) The influence of the molar ratio of Al2O3 to Y2O3 on sintering behavior and the mechanical properties of a SiC-Al2O3-Y2O3 ceramic composite. Mater Sci Eng A 486:262–266. https://doi.org/10.1016/j.msea.2007.09.052

34. Iveković A, Dražić G, Novak S (2011) Densification of a SiC-matrix by electrophoretic deposition and polymer infiltration and pyrolysis process. J Eur Ceram Soc 31:833–840. https://doi.org/10.1016/j.jeurceramsoc.2010.11.021

35. Luo Z, Zhou X, Yu J, Wang F (2014) High-performance 3D SiC/PyC/SiC composites fabricated by an optimized PIP process with a new precursor and a thermal molding method. Ceram Int 40:6525–6532. https://doi.org/10.1016/j.ceramint.2013.11.105

36. Sun X, Yin X, Fan X, et al (2018) Oxidation resistance of SiC/SiC composites containing SiBC matrix fabricated by liquid silicon infiltration. J Eur Ceram Soc 38:479–485. https://doi.org/10.1016/j.jeurceramsoc.2017.09.004

37. Tong Y, Bai S, Liang X, et al (2016) Reactive melt infiltration fabrication of C/C-SiC composite: Wetting and infiltration. Ceram Int 42:17174–17178. https://doi.org/10.1016/j.ceramint.2016.08.007

38. Marchais A, Roger J, Le Petitcorps Y (2016) Capillary infiltration of hexadecane in packed SiC powder and in SiC/SiC preforms: Pore description and calculation of molten Si infiltration. Ceram Int 42:7774–7780. https://doi.org/10.1016/j.ceramint.2016.01.203